Phenotypic Monitoring of Cell Growth and Motility using Image-Based Metrics and Lensless Microscopy

Valentin Stierle

München 2018

Phenotypic Monitoring of Cell Growth and Motility using Image-Based Metrics and Lensless Microscopy

Valentin Stierle

Dissertation
an der Fakultät für Physik
der Ludwig–Maximilians–Universität
München

vorgelegt von
Valentin Stierle
aus Ulm

München, den 14.09.2018

Erstgutachter: Prof. Dr. Joachim Rädler
Zweitgutachter: Prof. Dr. Bjoern Menze
Tag der mündlichen Prüfung: 05.12.2018

ZUSAMMENFASSUNG

Mit zunehmender Rechenleistung entwickelt sich die automatisierte Bildanalyse zu einem leistungsfähigen Werkzeug für die phänotypische Charakterisierung lebender Zellen in Wirkstoffscreenings, der biologischen Forschung und neuen Therapieansätzen. In jüngster Zeit sind alternative und unkonventionelle Zellmikroskopietechniken wie die linsenlose Mikroskopie (LM) entstanden. Während herkömmliche Mikroskope Linsen zur Abbildung von Objekten verwenden, setzen die meisten LM-Techniken dazu stattdessen einen Computeralgorithmus ein. Dazu rekonstruiert der Algorithmus die Amplitude und Phase des Lichtfeldes in der Objektebene aus einer digitalen Aufnahme des durch die Probe transmittierten Beleuchtungslichts.

Diese Arbeit behandelt zunächst das experimentelle Design eines alternativen LM-Systems, das keine digitale Rekonstruktion zur Abbildung von Zellen erfordert; als Zweites die Entwicklung von Metriken und Berechnungsmethoden zur Quantifizierung von Zellwachstum und Motilität aus den Bilddaten; und drittens, die Überwachung von Zellwachstum und Motilität in der Zellkultur und in Wirkstoffanalysen.

Die Pixel moderner Bildsensoren sind um eine Größenordnung kleiner als Zellen. Werden Zellen nahe genug über dem Bildsensor platziert und in Transmission beleuchtet, ähneln die Formen der aufgenommenen Interferenzmuster denen der Zellen, vergleichbar mit der Aufnahme des Schattens eines Objekts. Daher ermöglicht diese Aufnahmegeometrie die Extraktion von Informationen über Zellwachstum und -motilität direkt aus den Interferenzmustern, anstatt dazu zuerst ein fokussiertes Bild für die nachfolgende Bildanalyse zu rekonstruieren.
Der erste Teil dieser Arbeit konzentriert sich auf das experimentelle Design von LM-Aufbauten, um die Bildgebung von Zellen zu ermöglichen, ohne ein fokussiertes Bild zu rekonstruieren, das heißt rekonstruktionsfreie linsenlose Mikroskopie (RFLM). Die Kohärenz der Lichtquelle und der Proben-Sensor-Abstand wurden so optimiert, dass die RFLM-Aufnahmen die Detektion der Zellen sowie die Extraktion von Informationen über deren Position und Form ermöglichen. Die Wärmeübertragung von der Elektronik des Bildsensors auf die Zellen wurde minimiert, um optimale Umgebungsbedingungen für die Zellen sicherzustellen.
Ziel des zweiten Teils ist die Entwicklung von Bildanalysemethoden zur Erkennung und Lokalisierung der Zellen, zur Verfolgung ihrer Bewegung und zur Bestimmung der zellbedeckten Substratfläche. Die Trajektorien der Zellen wurden als Irrfahrt behandelt, um auf der mittleren quadratischen Verschiebung basierende Metriken für die Motilität zu berechnen. Die Verdoppelungszeiten wurden aus der Zunahme der zellbedeckten Substratfläche als Wachstumsmetrik bestimmt. Weitere bildbasierte Metriken wurden für die Geschwindigkeitsfelder von kollektiv migrierenden Zellen sowie für die Größenverteilung von Zellclustern berechnet. Die Richtigkeit der Analyse wurde mit konventioneller Mikroskopie bestätigt.
Im dritten Teil wird die Technik zur Messung von Zellwachstum und -motilität während der Zellkultivierung und in Wirkstoffanalysen verwendet. Wachstum und Motilität von Zelllinien wurden in einem Inkubator überwacht, eine Anwendung für die herkömmliche linsenbasierte Mikroskope aufgrund ihrer Größe schlecht geeignet sind. Es wird gezeigt, dass eine lineare Diskriminanzanalyse der vorgestellten bildbasierten Metriken es ermöglicht, einzigartige Profile der phänotypischen Eigenschaften verschiedener Zelllinien zu erstellen. Zudem wurden die bildbasierten Metriken verwendet, um mittels parallelisierter Messungen die Änderung von Zellwachstum und -motilität mehrerer primärer und etablierter Zelllinien als

Reaktion auf verschiedene Konzentrationen verschiedener biochemische Substanzen zu untersuchen

Die vorgestellte Technik, die auf RFLM und bildbasierten Metriken basiert, bietet eine attraktive Plattform, um quantitative phänotypische Informationen über Zellen während der Kultivierung und in zellbasierten Assays für Wirkstoffscreenings zu erhalten.

SUMMARY

With increasing computational power, automated image analysis is becoming a powerful tool for phenotypic characterization of living cells in drug screening, biological discovery, and novel therapeutic approaches. Recently, alternative and unconventional cell microscopy techniques such as lensless microscopy (LM) have emerged. While conventional microscopes use lenses to image objects, most LM techniques replace these lenses with a computer algorithm to generate images. To this end, the algorithm reconstructs the amplitude and phase of the light field in the object plane from a digital recording of the illumination light transmitted through the sample.

The scope of this thesis is first, the experimental design of an alternative LM system that does not require digital reconstruction to image cells; secondly, the development of metrics and computational methods to quantify cell growth and motility from the image data; and third, the monitoring of cell growth and motility in cell culture and in drug screening experiments.

Recent image sensors have pixels that are one order of magnitude smaller than cells. Thus, if cells are placed sufficiently close to the image sensor and illuminated in transmission mode, the shapes of the recorded interference patterns resemble the shapes of the cells, similar to the recording of an object's shadow. Therefore, this recording geometry facilitates the extraction of information on cell growth and motility directly from the interference patterns instead of first reconstructing an in-focus image for successive image analysis.
The first part of this thesis focuses on the experimental design of LM setups to achieve imaging of cells without reconstructing an in-focus image, i.e., reconstruction free lensless microscopy (RFLM). The coherence of the light source and the sample sensor distances were optimized such that the RFLM-recordings allow the detection of the cells as well as the extraction of information on their location and shape. The heat transfer from the electronics of the image sensor to the cells was minimized to ensure optimized environmental conditions for the cells.
The aim of the second part is the development of image analysis methods to detect and locate the cells, to track their movement, and to determine the cell covered substrate area. The trajectories of the cells were interpreted as random walks to calculate metrics for the motility that are based on the mean squared displacement. The population doubling times were derived from the increase in cell covered substrate area as a growth metric. Further image-based metrics were calculated for the velocity fields of collectively migrating cells and the size distribution of cell clusters. The accuracy of the analysis was validated with conventional microscopy.
The third part focuses on using the technique to measure cell growth and motility during cell culturing and in drug screening experiments. Cell growth and motility of cell lines were monitored inside a cell culture incubator, a setting for which conventional lens-based microscopes are not well suited due to their size. It is shown that using the presented image-based metrics for a linear discriminant analysis allows generating unique profiles of the phenotypic traits of different cell lines. Secondly, the image-based metrics were used to study the dose-dependent changes in cell growth and motility as a reaction to different biochemical agents in parallelized measurements of multiple primary and established cell lines.

The presented technique that is based on using RFLM and image-based metrics provides an attractive platform to obtain quantitative phenotypic information of cells during culturing and in cell-based assays for drug screening.

Table of Contents

1 Introduction

The advancement of novel medical treatments such as tissue engineering, stem cell therapy, and personalized cancer therapy is the subject of enormous efforts in current biomedical research. These new treatments have in common that they rely heavily on growing cells *in vitro*[1] [1–3]. Likewise, *in vitro* cultured cell lines play pivotal roles in drug discovery [4, 5] and cancer research [6]. The increasing use of cell culture over the last decades [7] has led to rising demand for suitable analysis techniques for cell-based experiments. In this respect, image-based cell-analysis is becoming an increasingly powerful tool due to the dramatic advances in the power of computational methods and digital image sensors [8–11]. Examples include super-resolution techniques that allow imaging inside living cells with a resolution of tens of nanometers [12], light-sheet microscopy which is capable of three-dimensional imaging of hundreds of thousands of living neurons simultaneously [13] and digital holographic microscopy which enables label-free three-dimensional cell imaging with sub-wavelength axial resolution [14]. One particular application is the analysis of cellular phenotypes [15]. In this regard, image-based analysis of cells has several key advantages: it allows studies on the single cell level, it can be used for time-resolved measurements, and multiple phenotypic parameters such as cell growth and motility can be extracted from the image data simultaneously.

Cell Types and Characteristic Phenotypic Traits

Cells, the fundamental building blocks of every multicellular organism, exhibit a broad spectrum of phenotypic differences. Cells can be as different as neurons and liver cells and vary in shape, function, and social behavior. The human body contains more than 200 different named cell types [16], and a recent study identified 39 distinct populations in mouse retinal cells [17]. These different cell types are characterized by specific phenotypic traits. Fibroblasts, for example, are migratory and exhibit an elongated shape, whereas epithelial cells have compact shapes and grow in colonies in close contact with each other [18]. ***Figure 1.1*** illustrates several fundamental phenotypic parameters such as cell motility, growth, clustering, and morphology. Alterations of these parameters often play pivotal roles in pathologies like cancer: The characteristic traits of cells which underwent the transition from a normal cell to a cancer cell include increased proliferation, motility, and altered morphology [19–22]. Using

[1] i.e., outside of the living organism

image analysis on microscopy images of cells allows the determination of imaged-based metrics to assess phenotypic parameters and to create phenotypic profiles for classifying different cell types [23, 24] and assessing drug response [25, 26].

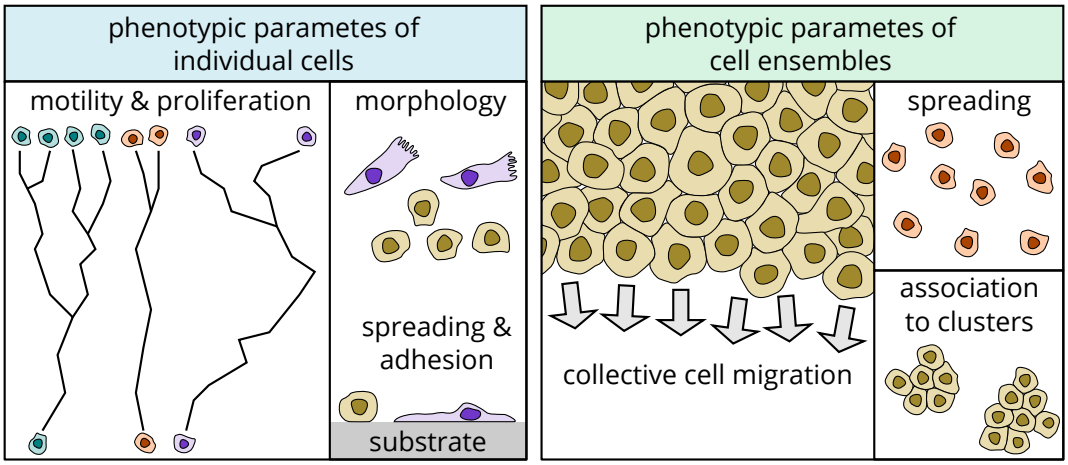

Figure 1.1: Crucial phenotypic parameters of cells. Phenotypic differences can be observed in individual cells, for example in their rate of proliferation, their motility, morphology, and tendency to adhere and spread on substrates. Different cell types also exhibit phenotypic differences when observed as an ensemble, e.g., their capability for collective cell migration and tendency to grow in close contact with neighboring cells or dispersed as individual cells.

Cell Line Characteristic Traits under Culture Conditions

Unlike *in vivo* studies, *in vitro* experiments with cultured cells have the advantage that they can be repeated several times under the same conditions in a controlled environment. In general, cells in culture exhibit differences in their properties and behavior compared to their counterparts in their natural microenvironment in the organism [27]. Nevertheless, cultured cell lines typically retain characteristic traits that are representative of their tissue of origin and provide valuable model systems [6, 28–30]. However, awareness grew over the last decades that cells can undergo substantial changes during culturing, resulting in loss of the critical phenotypic traits that initially characterized the cellular model system [27, 31–34]. Genetic and phenotypic instability can lead to genetic and phenotypic heterogeneity even in clonal populations [18, 35–37]. These subpopulations are subject to selective pressure during serial passaging, resulting in genetic and phenotypic drift. The culture conditions, including factors such as cell density, are a critical factor in the selection process and in causing phenotypic heterogeneity [38–44]. ***Figure 1.2*** illustrates the role of these processes in the change of characteristic phenotypic traits during culturing. Likewise, the culturing history, phenotypic parameters like the growth rate, and the cellular environment also play crucial roles in drug screening assays since they can affect the drug response of the cells [31, 45–51].

Since a routine detailed genotypic and proteomic characterization of cell lines to monitor the consistency of cell line specific characteristic traits is currently not feasible [52], the current best practice in cell culture is the routine visual inspection with a microscope to assess morphology, cell health, current growth phase and cell density. Cells are usually counted manually to

determine and track growth rates over passages. [18]. The shortcomings of the manual visual examination include that it is subjective, can only provide information for one specific time-point, and misses dynamic phenotypic parameters such as the motility entirely.
Therefore, a technique that allows the non-invasive, continuous, and quantitative determination and tracking of critical phenotypic parameters during culturing is highly desirable. While there is still a lack of suitable monitoring equipment that is compatible with standard cell culture containers and CO_2 incubators, substantial progress has been made over the last years both on the instrumental as well as on the computational side. Automated label-free microscopy combined with image analysis is able to determine a wide range of phenotypic parameters such as proliferation and cell motiliry [53–57]. This method can in principle be used to assess cell health and monitor critical parameters like confluency and the growth pase of cell cultures [58–62]. However, the geometry of the optical components and the associated trade-off between resolution and field of view (FOV) [63] limit the miniaturization of conventional lens-based light microscopes, and therefore their capability for parallel monitoring of many cell cultures inside standard cell culture incubators.

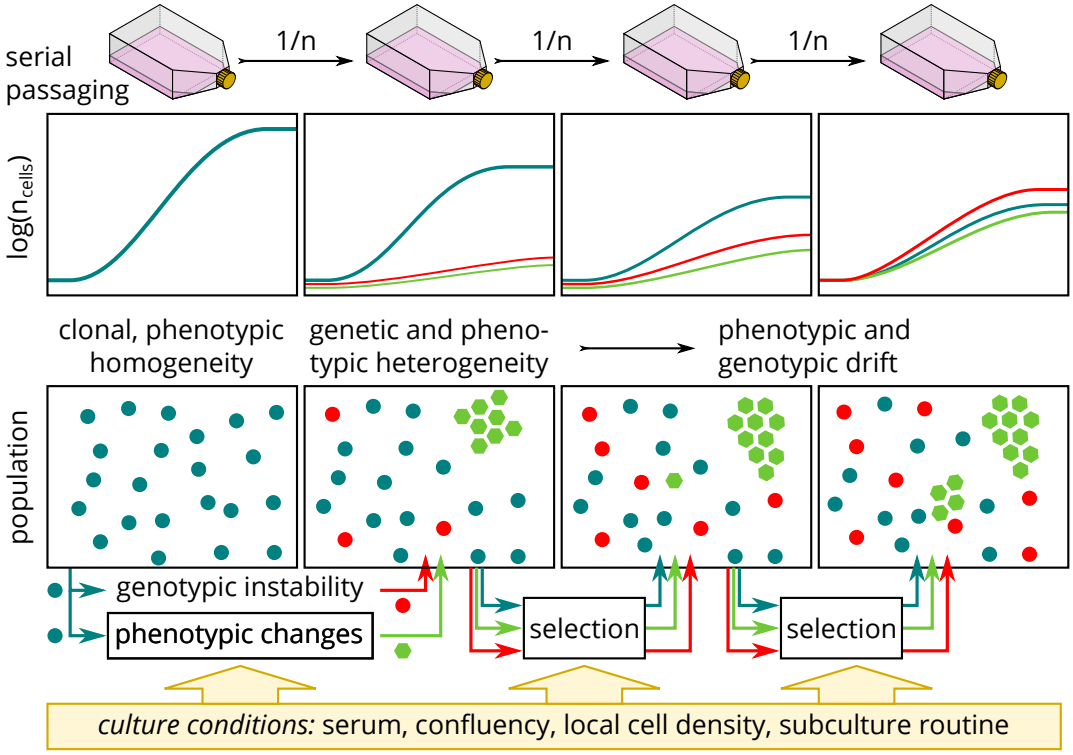

Figure 1.2: The emergence of changes in cells during culturing. Serial passaging consists of repeated cycles of cell growth inside culture flasks and transfer of a fraction of the cell population to a new flask upon reaching a specific population size. Due to genetic instability and phenotypic changes that can be caused by the culture conditions, genetic and phenotypic heterogeneity can emerge in an initially clonal and uniform population. Subsequently, repeated rounds of selection during serial passaging can cause significant phenotypic and genotypic drift in the culture. In this process, the culture conditions and the different growth rates of the subpopulations act as critical selection factors.

Lensless Microscopy

In this regard, lensless microscopy (LM) has emerged as a versatile, attractive alternative imaging technique. LM allows extremely compact and versatile instrumentation since it foregoes the use of lenses entirely and decouples the achievable resolution from the FOV [64]. Consequently, LM has been used for applications like label-free live-cell imaging inside standard CO_2 incubators [65]. Although the principle of LM was already studied decades ago, the use of LM for compact cell microscopy became possible only recently due to several crucial technological breakthroughs.
Holography with electrons was the first form of LM and originally invented by Dennis Gabor to improve the resolution of electron microscopes in 1948. ***Figure 1.3 a*** shows Gabor's original configuration and illustrates the principle of holography. A wavefront that is diffracted by an object interferes with a reference wavefront. Thus, the record of the interference pattern (the hologram) contains phase and amplitude information of the object wave. Therefore,

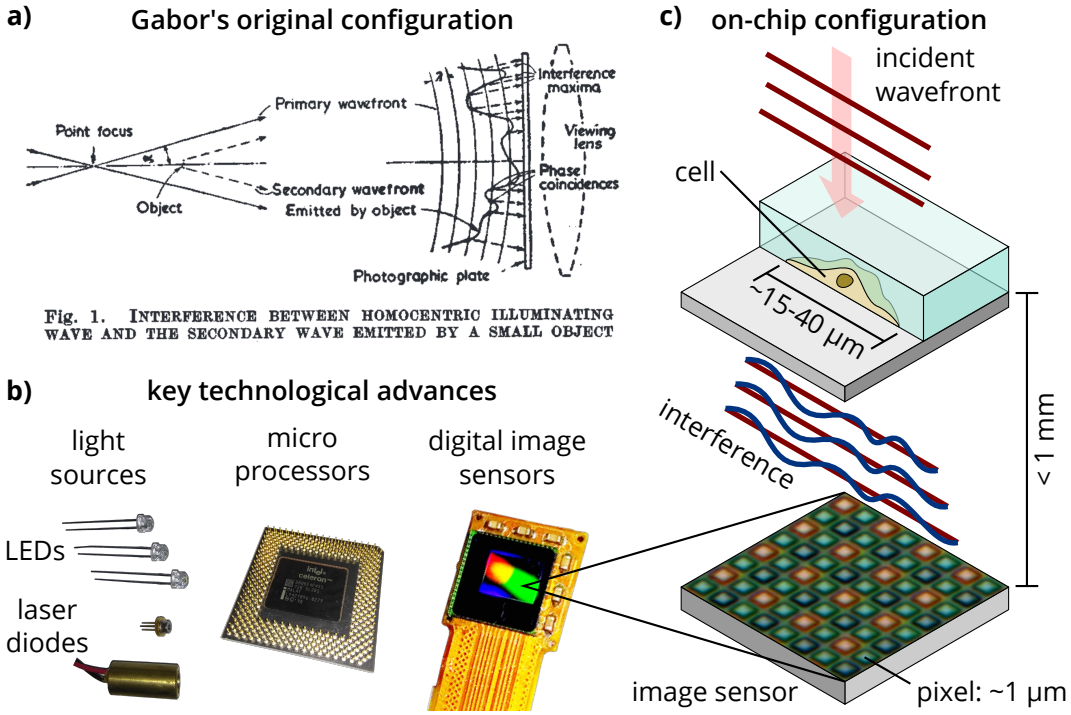

Figure 1.3: Technological advancement of LM. **a)** Gabor's original figure[2] illustrates the configuration for electron holography: A wavefront is diffracted by an object and interferes with a reference wavefront. The recorded interference pattern (hologram) contains amplitude and phase information of the object's light-field. **b)** The photos depict key technological inventions and advances that made LM with light feasible. The development of mass-produced and commercially available compact light sources and digital image sensors was crucial for on-chip LM. **c)** Schematic and dimensions of an on-chip LM configuration using visible light: A fraction of an incident wavefront is scattered, while the remaining light passes the sample unperturbed. The resulting interference pattern is recorded by a digital image sensor for processing with a computer.

[2]The permission to reproduce the figure was kindly granted by Springer Nature.

the hologram allows reconstructing the original object field. For light microscopy, however, the technique only became feasible for practical applications after the invention of the laser as a sufficiently coherent light source, substantial advances in computing power, and the development of digital image sensors (***Figure 1.3 b***). The pixel size of image sensors decreased dramatically over the last decade, and pixels as small as 1 µm have been achieved [66]. This facilitated lensless cell microscopy in an on-chip LM configuration, which is schematically illustrated in ***Figure 1.3 c***. A sample with cells is placed on top of the image sensor, typically in contact or in proximity. The sample is illuminated from above in transmission mode. A fraction of the light passes the sample unperturbed and serves as the reference wave, whereas the other fraction is scattered by the sample and serves as the object wave. The resulting interference pattern is recorded by the image sensor. The shape of the interference pattern resembles the shapes of the cells since the dimension of a typical cell is one order of magnitude larger than the dimension of the pixels and the cells are placed in such proximity to the sensor. Therefore, the technique was initially called "shadow imaging" [67]. The first reported use of "shadow imaging" for cell microscopy was in 2007 by Ozcan and Demirci [68]. Subsequent studies focused on using light sources with higher coherence in combination with computational methods to digitally reconstruct in-focus phase and amplitude images from the recorded interference patterns. This approach is based on digital holographic microscopy (DHM), and its resolution and capabilities have been enormously improved over the last ten years. DHM-based LM has since gained popularity and has matured into a versatile and powerful technique with a wide range of applications in biomedical imaging [65, 69–71]. However, it is also possible to forego the computational reconstruction and instead analyze the "cellular footprint" in the recorded interference patterns directly. This approach for extracting phenotypic information of the cells from the recorded interference patterns remains an attractive alternative to DHM-based LM due to the experimental simplicity and low computational costs [70, 72, 73].

This Work

The scope of this thesis is the development of LM setups and the introduction of computational methods to quantify cell growth and motility using the recorded image data. The goal is to achieve a comprehensive phenotypic cell analysis that can be used for measuring drug-response and for helping to ensure the consistency of cell line characteristic traits during the culture period. To this end, the LM setups must be capable of label-free in-situ live cell imaging. Furthermore, multiple image-based metrics for cell growth and motility must be extracted from the recorded low-coherence interference patterns of the cells.

Following this introduction, ***Chapter 2*** provides relevant background information on the principles and the state of the art of lensless microscopy. The chapter then gives a short overview of some fundamental properties of cells, growing cells in culture, and critical characteristic phenotypic traits of cultured cell lines.
Subsequently, ***Chapter 3*** presents the experimental design of the lensless microscopy setups. First, it is investigated how the images are formed and how much information the images contain with regard to automated image analysis. Then, the capabilities for parallelized in-situ live-cell imaging are demonstrated. Critical environmental parameters such as the temperature during imaging inside the incubator are examined to guarantee optimum conditions for the cells. Especially the heat generation of the electrical components was analyzed to avoid

adverse effects on the cells.
Chapter 4 introduces image analysis methods to show that the recorded images allow the determination of image-based metrics for cell growth, single cell motility, collective cell migration, cell covered substrate area, and cell clustering. Results from reference methods are presented to demonstrate the accuracy of the image-based metrics. Finally, the question is addressed how the presented image-based metrics can be used for (1) obtaining a phenotypic profile of the characteristic traits of different cell lines, and (2), for assessing critical parameters like confluency and growth rates during the culture-period by monitoring cell cultures.
Chapter 5 focuses on using the technique to quantify the phenotypic cellular response to perturbations for cell-based assays. Therefore, the capability of the technique to address several critical aspects of measuring drug response in a reproducible fashion is investigated. These aspects include time-dependent drug response, multiplex readout, variations in cell density, and cell quality. Furthermore, a variety of different established and primary cell lines are used to study their response in multiple phenotypic parameters to the exposure to numerous different biochemical agents.
Chapter 6 explores the adaption and extension of the presented image-based metrics for the analysis of bacterial microcolonies and in ***Chapter 7*** the technique was used to study the cellular response to engineered substrates for the purpose of developing a nanostructured micropattern for cell migration studies.

2 Theory and Background

This first half of this chapter provides an overview of the essential functions and properties of cells, the fundamentals of culturing eukaryotic cells *in vitro*, and the use of cultured cell lines as model systems in biomedical research. The critical parameters for phenotypic profiling of cell lines are presented, followed by a short introduction to prokaryotic cell growth and antimicrobial susceptibility. The second half of the chapter introduces the physical background of holographic and lensless microscopy and gives an overview of applications of state-of-the-art digital holographic microscopy and lensless microscopy in biomedical imaging.

2.1 Cells in Biomedical Research

Cells are the smallest living units of all organisms[1]. Cells can live as individual unicellular organisms as well as in multicellular organisms as organized, social communities. In complex multicellular organisms such as humans, cells can form tissues, i.e., cell-ensembles with the capability to perform specific functions. To be considered living, one criterion is that an organism must be able to reproduce, meaning it can produce new individual living organisms. Every multicellular organism originates from a single cell which reproduces by cell division. Thus, all cells of the organism have the same genotype, meaning identical genetic information encoded in their DNA. However, these cells can exhibit significant variations of their form and function, e.g., neurons and liver cells. Cells with the same genotype can have different phenotypes, i.e., observable characteristics, due to their capability to control and regulate gene expression.
The arrangement of cells with specific functions in specific patterns during development of multicellular organisms is based on four fundamental processes: (1) cell proliferation, i.e., the increase in the number of cells through cell division; (2) cell differentiation, i.e., the specialization to cells with specific characteristics; (3) cell-cell-interactions; and (4) cell migration, i.e. the movement of cells. Development begins with the first pluripotent cells of an organism, which have the potential to develop to all cell types of the adult organism. Each differentiation of a cell along one of the different available specialization branches limits the available options for further successive differentiation. Terminal differentiation of a cell into a highly specialized cell type ends the differentiation process. Undifferentiated cells with the capability

[1] This short introduction to cell biology is based on the textbook by Alberts et al.[16]

of both indefinite division as well as differentiation are called stem cells. Specialized cells retain their characteristic traits defined by their specific gene expression patterns through so-called cell memory. In cell memory, cells can store information on their past without changing the genome itself, for example by methylation of the DNA. Free-living cells compete to survive. In contrast, cells in complex multicellular organisms like humans are social and collaborate to ensure the survival of the whole organism. The most dramatic example is the self-sacrifice a cell undergoing terminal differentiation, which is usually associated with the loss of the capability to divide and therefore results in the eventual death of the cell. To maintain homeostasis, most tissues in humans continually replace old terminally differentiated cells with freshly differentiated cells supplied by a reserve of stem cells.

These briefly outlined fundamental properties of cells play crucial roles in biomedical research. Disruptions of cellular functions and mechanism cause a vast number of pathologies in humans, for example, cancer. Gaining insights into these cellular functions and mechanisms provides new options for therapies, for example by developing drugs targeting the underlying molecular mechanisms. Furthermore, the development of new treatment methods such as stem cell therapy or tissue engineering advances with the knowledge of cellular processes and behavior.

2.1.1 Cell Culture and *In Vitro* Experiments

In biomedical research, experiments with cells can be carried out *in vivo*, which means in the complex environment of the living organism[2]. In contrast, experiments conducted outside of the living organism, e.g., in a test tube, are called *in vitro* experiments. *In vitro* experiments with cells offer the advantage of a controlled environment and accessibility to a higher number of analysis methods. For *in vitro* experiments, cells are typically grown and maintained as so-called tissue or cell cultures. Cells can grow as adherent cultures on a substrate or as suspension cultures. Cell cultures created by taking cells explanted from tissue directly into culture are called primary cultures. Typically, primary cell cultures derived from healthy tissue are finite, meaning that the cells stop dividing after a finite number of cell divisions. This process is referred to as replicative cell senescence and reached after 25-40 divisions for normal human fibroblasts [16]. So-called immortalized or established cell lines have the potential for an unlimited number of cell divisions. Inactivation of the protective mechanisms which prevent uncontrolled and unlimited proliferation can result in immortalization. In rodent cells, immortalization can happen spontaneously due to genetic changes during culturing. Human cancer cells can acquire immortality through mutations of genes which regulate these protective mechanisms. Finite cell lines can often be immortalized through the artificial introduction of cancer-promoting genes. Immortalized cell lines are invaluable for biomedical research as they provide clonal cell populations and allow theoretically limitless repetitions of experiments through cryopreservation.

The goal of cell culture is to create an environment for the cells which is as similar as possible to their *in vivo* environment. To this end, cells are kept in a culture medium inside so-called cell culture flasks or dishes. These containers are usually placed in an incubator, which regulates

[2]The introductory part of this section is based on the textbooks by Mather and Roberts [40], Freshney [18], and Alberts et al. [16]

the environment. The culture flasks provide a surface for cell attachment and protection from contaminants. Cell culture flasks typically have treated or precoated plastic surfaces to promote cell attachment. The culture medium provides amino acids, fatty acids, sugars, ions, trace elements, vitamins, and ions as nutrition for the cells. Culture media also contain a buffering system to keep the pH constant since the cells' metabolism produces lactatic acid as a by-product. The medium must also provide the right osmolarity, which like pH is another critical factor affecting cell growth and function [40]. Animal serum, typically Fetal Bovine Serum (FBS) is a widely used media supplement. FBS provides hormones, growth factors, and a wide variety of other substances of which many are still unknown [74]. However, it is an ill-defined substance, and commercially available sera can exhibit significant lot to lot variance [40, 74, 75].

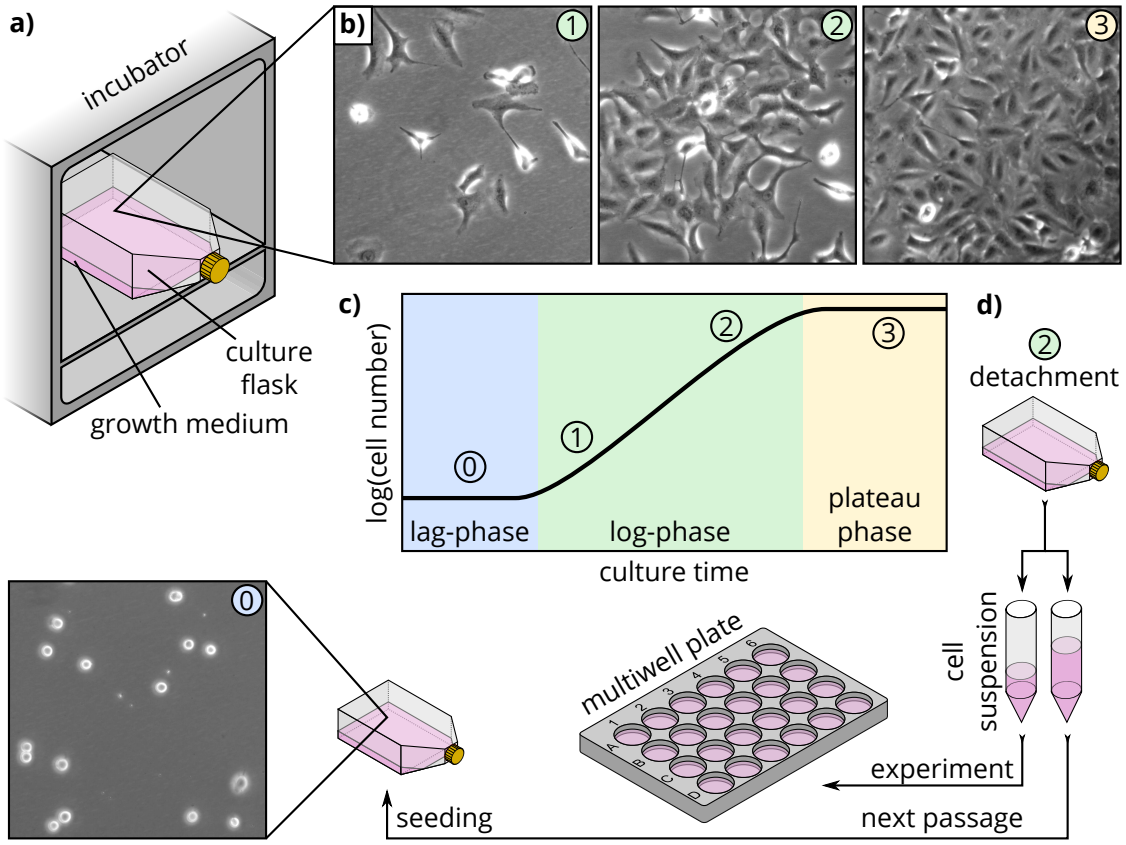

Figure 2.1: Illustration of the steps in subculturing adherent cell cultures. **a)** Culture flasks with cells and medium are placed in a CO_2 incubator. **b)** Phase contrast microscopy images of a culture of A549 cells. As the cells proliferate, they cover increasingly more of the available substrate area: (1) low confluency (2) high confluency (3) fully confluent cell layer. **c)** Idealized growth curve of a cell culture, consisting of the lag-phase (0), the log-phase of exponential growth (1-2), and the plateau-phase of reduced growth due to depletion of nutrients and/or substrate area (3). **d)** Ideally, the cells are detached and suspended from the surface before reaching the plateau-phase. A fraction of the cell suspension is transferred into a flask with fresh medium as a new passage of the culture. The surplus suspension is available for experiments, e.g., drug screening in multiwell plates. Initially, after seeding, the cells are still in suspension and rounded up, as shown in the bottom-left (0). During the lag phase, the cells sediment, adhere, spread out on the substrate, and subsequently re-enter the log-phase.

For most mammalian cell cultures, the incubator is set to a temperature of 37 °C and 5 % CO_2 for buffering the medium. The incubator also maintains a saturated humidity to prevent changes of osmolarity due to evaporation of the culture medium. Rapid changes of these environmental conditions can shock cultured cells and cause apoptotic death [40].

Figure 2.1 illustrates several key aspects of culturing adherent cells. Adherent cells which grow as monolayers cover increasingly more of the available substrate area as they proliferate. The fraction of the total available substrate area which is covered by the cells is called the confluency. As cell number and confluency increases, the amount of available nutrients decreases. Simultaneously, dead cells and metabolic by-products accumulate. Reaching high confluency can also cause significant changes in cellular behavior, which is discussed in more detail in chapter 4. Therefore, the cells are usually detached from the substrate before the culture reaches high confluency, e.g., by trypsinization. Subsequently, a fraction of the detached cells is re-seeded with fresh medium in the same or a new culture flask. The remaining fraction can be used for cell-based experiments like drug-screening, for cryopreservation, or for creating further cultures of the cell line, which is called expansion. The transfer of a fraction of the cells into fresh growth medium is called passaging or subculturing. The passage number specifies how often this procedure was performed and the splitting ratio specifies the fraction of cells transferred to the new passage [40, 74].

Cell number and confluency of cell cultures typically follow a growth curve with three different phases (illustrated in ***Figure 2.1 c***). The first phase is the lag phase, in which the cells recover from the transfer step, attach to the substrate, and subsequently spread on the substrate (see also ***Figure 2.2 a***). Low seeding densities can prolong the lag phase [77]. After the lag phase, the cells enter the so-called log phase of growth, in which the cell number increases exponentially. Cells for use in experiments are optimally harvested from the log phase, as this is the cultures most reproducible form [78]. Cell growth occurs in a specific sequence of events, the cell cycle. The cell cycle is illustrated in ***Figure 2.2 c*** and consists of the interphase and the M-Phase. The interphase contains the gap phase G_1, the synthesis phase S in which the cell replicates its DNA,

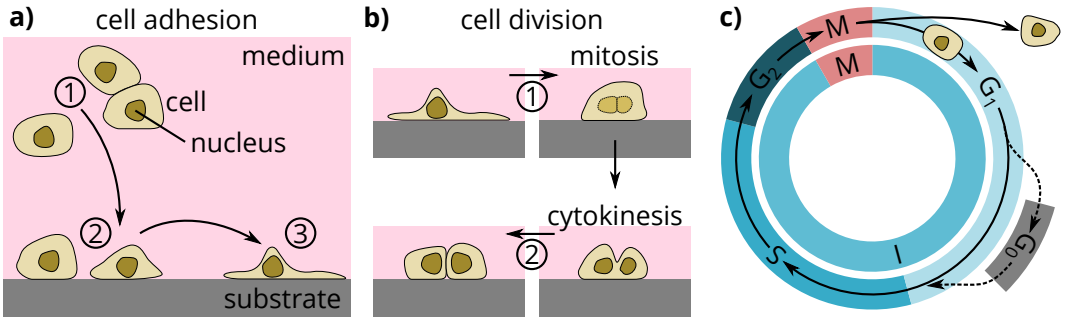

Figure 2.2: Cellular processes during culturing **a)** Cell adhesion. After plating, the cells are initially in suspension (1). Subsequently, the cells sediment and adhere to the substrate (2). After adhesion, the cells can spread out on the substrate (3). **b)** Cell division: The first morphological change during division is that the cells round up before mitosis (1). During cytokinesis, the cell splits into two separate cells. **c)** The cell cycle is divided into the interphase (I) and mitosis (M). The interphase consists of the S-Phase, where the DNA copy is synthesized and two gap phases G_1 and G_2. The cells can also reversibly enter a rest phase G_0 from the G_1 phase (based on [76]).

and another gap phase G_2. The M-phase consists of mitosis and cytokinesis. During mitosis, the cellular apparatus segregates the replicated chromosomes, and during cytokinesis, the cell is cleaved into two daughter cells (see also ***Figure 2.2 b***). With a duration of approximately 1 h the M-phase is the shortest phase of the cell cycle [76]. Typically, for human cell lines in culture, the total duration of the cell cycle is about 24 h [16]. If cells are not proliferating, however, they can reversibly enter the quiescent resting state G_0 for prolonged periods of time. During the M phase, the cells also undergo pronounced morphological changes. The cells reduce adhesion to the substrate, round up to a spherical shape, and increase in height. After cytokinesis, the two daughter cells spread on the substrate [79]. Proliferation in a culture decreases and eventually stops due to nutrient depletion of the medium or due to contact inhibition of proliferation. This phase corresponds to a plateau in the growth curve [18, 78]. While 2D substrates are frequently used for culturing adherent cells, they can also be embedded in hydrogels and grown as 3D cultures. Generally, 3D cell culture has the advantage of mimicking the *in vivo* conditions more closely than 2D cell culture [80, 81].

2.1.2 Essential Phenotypic Traits of Cell Lines

Generally, cultured cells exhibit functions and properties which are representative of their tissue of origin [16]. Therefore, they provide valuable model systems to gain insights into cellular mechanisms [6, 29] and for drug-screening [30]. To obtain meaningful results, it is thus crucial that a cell line maintain its type and its characteristic phenotypic traits during culturing. In practice however, misidentification and cross-contamination remain serious problems although already in the 60s it was found that a majority of the used continuous cell lines in the US were cross-contaminated with HeLa cells [18]. In addition to these problems, the environmental conditions and genetic instability of cultured cells can lead to significant changes in cell lines during cultivation, which is discussed in more detail in Chapter 4. For these reasons, cell line authentication and characterization plays a critical role in cell culture and quality control [52]. To this end, a variety of techniques are available, such as DNA profiling, immunostaining, and measuring enzyme activity or RNA and protein expression [18].
Complementary to a full characterization of a cell line, observation of the cells with microscopy allows the assessment of a variety of a cell lines' characteristic phenotypic traits. The analysis of phenotypic parameters is a routine task in the establishment of cancer cell lines since their characteristic properties and functions deviate significantly from those of cells obtained from healthy, functional tissue [19]. In general, transformed cell lines, i.e., cell lines which underwent a permanent phenotypic change due to a heritable change in DNA and gene expression can show substantial alterations from normal cells [18]. These examples demonstrate that it is essential to asses during the establishment of cell lines, but also during culturing, to what degree a cultured cell line is still representative of its origin. The following presents several of the most critical phenotypic traits for such an assessment.

Cell morphology is a frequently assessed phenotypic parameter. It is a standard measure to categorize cells into fibroblast-like types and epithelium-like types. Subconfluent fibroblast-like cells tend to migrate and exhibit bi- or multipolar shapes with an aspect ratio of more than 2. At reaching confluency, they typically assume bipolar shapes and form characteristic parallel arrays and whorls. In contrast, epithelium-like cells often assume regular polygonal shapes and tend to grow in discrete patches. Morphological features are an important characteristic

in cancer cell lines [82] and stem cells [83]. Frequently used metrics to quantify morphology include the cells' area, perimeter, circularity, and aspect ratio [84].

Cell proliferation is another key parameter to quantify the characteristic behavior of a cell line [85]. Enhanced proliferation is one of the hallmarks of cancer [19]. Therefore, the determination of the growth characteristics is usually part of establishing a new cell line [86, 87]. Cell proliferation also serves as a quantitative indicator to assess senescence and potency in stem cells [88, 89]. A standard measure for cell proliferation is the population doubling time (PDT). Fitting the log phase of a growth curve allows obtaining the PDT [90, 91]. A variety of more complex mathematical models such as logistic growth models [92] are available for a more detailed analysis of growth curves, especially to model tumor growth [93].

Cell migration & motility, likewise, are characteristic traits of cells. An upregulated motility is frequent in cancer cells and directly related to invasiveness and formation of metastasis of tumors [19]. It has also been suggested that cell migration can serve as an indicator to assess the multipotentcy of mesenchymal stem cells [94]. There are two distinct modes of motility: individual cell migration and collective cell migration [95]. The exhibition of different migration pattern depends on intrinsic factors as well as external cues such as cell-cell interactions, and the chemical and physical environment [96]. Individually migrating cells exhibit an asymmetric morphology with a leading edge with actin-rich protrusions or lamellipodia. Intrinsic regulation and adhesion to the substrate influence the randomness and persistence of individual cell migration [97].
Unlike immune cells, tissue forming cells typically move in groups in a coordinated fashion. A defining criterion of collective cell migration is that the cells must move together while being at least temporarily in contact with each other and affecting each other [98]. Stricter definitions require that the cells remain physically and functionally connected, that during movement the cell-cell junctions must be kept intact, and the actin cytoskeleton needs to exhibit multicellular polarity and supracellular organization[3]. While using 2D tissue culture to study cell migration is far from the physiological *in vivo* environment, it is still in widespread use due to providing a range of technical advantages such as high-quality imaging [98]. Examples include the scratch-wound assay, a frequently used model for wound healing in epithelial sheets. Different cell lines can show distinct differences in their collective cell migration, e.g., different length scales of the correlations in the velocity fields in moving cellular monolayers [102]. An important concept in the emergence of collective cell migration and spatial arrangements such as cellular clusters is the interplay between cell-cell-attraction as an attractive force and contact inhibition of locomotion as a repulsive force [103, 104].

Cell colonies & clusters: The cells ability to form colonies is frequently used in the colony-forming assay to establish monoclonal cell lines [105]. Vice versa, the cell scatter assay is based on the inverse process, i.e., the fragmentation of small cell colonies, which is typical for a transition from epithelial to mesenchymal characteristics [106]. The efficiency of colony formation has been linked to cancer stem cell markers and metastasis-associated genes in cancer cell lines [107, 108]. Furthermore, the morphology of stem cell colonies provides a valuable indicator of stem cell quality and health [109, 110]. Different cell lines also exhibit characteristic differences in the dynamics of cell cluster aggregation during colony formation [111].

[3] An overview of collective cell migration phenomena can be found in reviews, e.g., [98–101]

The **Population dynamics** of cells are the result of a complex interplay between proliferation, motility, cell density, cell-cell interactions, and environmental cues, e.g., from the substrate [112]. Examples include contact inhibition of proliferation, where cell division stops once the local cell density reaches a critical value [113] and tissue mechanics [114]. Mechanical cues can play a critical role in increased differentiation along the borders of stem cell colonies [115]. Due to their fundamental role in cell population dynamics, the key parameters proliferation, motility, and cell density are also at the core of computer models of cell population dynamics [116–120]. When cells undergo inheritable changes, they usually affect several of their characteristic traits simultaneously. An example is the epithelial-mesenchymal transition (EMT), which is an essential program in tissue repair and pathologies [22]. Cells that undergo EMT typically exhibit alterations of their morphology, migration, and proliferation [20, 121]. ***Figure 2.3*** schematically illustrates an example of two cell populations with different dynamics.

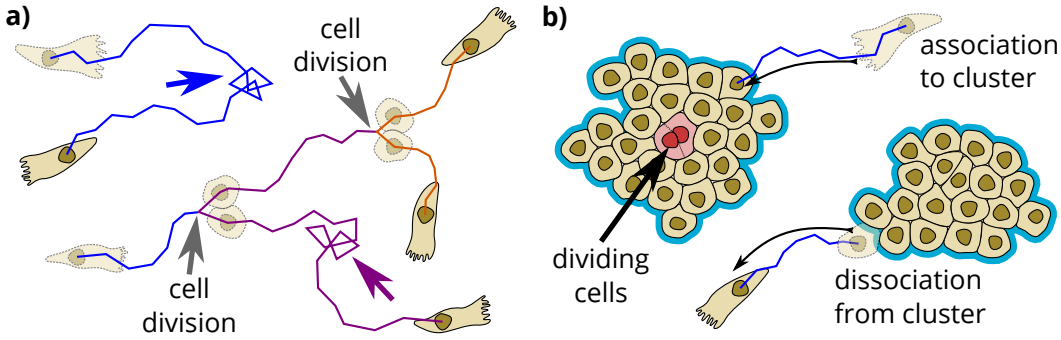

Figure 2.3: Different population dynamics of adherent cells with different characteristic traits: **a)** depicts a population of migratory cells that avoid cell-cell contact. Cells migrate and divide on the substrate. Typical trajectories, drawn as colored lines, exhibit phases of directionally persistent movement and phases of random reorientation (indicated by colored arrows). **b)** depicts a population of cells which prefer to grow in close contact with each other. Colonies/clusters of cells can grow through cell division and through association of migrating cells to the cluster. Cells can also dissociate from clusters and migrate as individual cells, depending on the cell type.

2.1.3 Bacterial Growth and Biofilm Formation

The previous section focused on fundamental properties and functions of cells in complex multicellular organisms such as eukaryotic mammalian cells. Eukaryotes store their DNA in the nucleus, a distinct membrane-enclosed intracellular compartment [16]. Prokaryotes, in contrast, lack a distinct nuclear compartment for DNA storage. They typically exhibit a rod-like or spherical shape, measures a few micrometers in size, and are often enclosed by a cell wall. Most prokaryotes live as independent individuals. However, they can also show social behavior and organize in communities. Like populations of eukaryotic cells, such bacterial communities from different types and strains can exhibit profound differences in their appearance, social behavior, and response to external perturbations.

The role of bacterial infections is of paramount importance in clinical pathology [122]. While antibiotics are highly effective in treating bacterial infections in humans, the emergence of multi-resistant bacterial strains together with the slow pace in the discovery of novel antibiotics poses an enormous challenge [123–125]. New methods for bacterial susceptibility testing, i.e., measuring the response of bacteria to antibiotic agents, play a vital role in finding new antibiotics [126, 127]. Amongst other mechanisms, bacteria can acquire resistance to antibiotics through random mutations and natural selection. Bacteria can pass an acquired resistance to other bacteria through horizontal gene transfer [128, 129]. In addition to acquired resistance, bacteria can also exhibit increased tolerance to the exposure to antibiotic agents or other hostile environments through the formation of biofilms. The individual (planktonic) bacteria can form such a protective biofilm by embedding themselves in a self-produced biopolymer matrix consisting of exopolysaccharides, extracellular DNA, proteins, and lipids [130, 131]. Cells in biofilms differ in some critical aspects from their genetically identical planktonic counterparts: They are physiologically heterogeneous and are significantly less susceptible to antimicrobial agents. Mechanisms contributing to antibiotic tolerance and resistance in biofilms include nutrient gradients, intercellular interactions such as quorum sensing, and persister cells. However, a variety of outstanding questions concerning antibiotic resistance in biofilms are still the topic of ongoing research [130].

2.2 Holographic and Lensless Microscopy

2.2.1 Conventional Microscopy

Ever since the discovery of cells as the basic unit of life, light microscopy has played a crucial part in cell biology and research. Since microscopy allows the direct visualization of cells, it is an excellent tool to study a broad variety of the aspects of cellular behavior outlined in the previous section. The challenge in imaging animal cells, which typically have a diameter of 10–30 µm is that they are mostly colorless and translucent [14, 16]. Today, a plethora of microscopy methods are available for biomedical imaging. Bright-field microscopy is the oldest transmitted light microscopy technique and based on differential light absorption. However, to enhance the comparably poor contrast, biological samples are often stained by incorporating dyes with increased absorption selectively into specific regions of the specimen [132]. In dark-field microscopy, only light scattered by the cells is used to form the image. While cells only weakly absorb light passing through them, they typically cause a significant phase shift due to differences in the Refractive Index within the cell and with respect to the surrounding medium [133, 134]. Phase-contrast and differential-interference-contrast microscopy make use of this phase shift by converting it into an amplitude modulation for enhanced contrast in the resulting image. However, this phase to amplitude conversion is non-linear, and these techniques thus do not allow Quantitative Phase Imaging (QPI) [135].
Fluorescence microscopy is based on using fluorescent dyes, which absorb light of a wavelength λ_1 and emit light with a wavelength $\lambda_2 > \lambda_1$. As the excitation light with wavelength λ_1 can be filtered out, only the light emitted by the dyes is used for image formation. The advantage of fluorescence microscopy is the high sensitivity, which allows imaging of minimal amounts or even single dye molecules against a dark background [16, 136]. Today, a broad variety of fluorescent dyes with a wide range of wavelengths are available. Specific molecules and structures within

cells can be selectively labeled with fluorescent dyes by coupling them to antibodies [16] or by using dyes which bind to specific molecules, for example, the Hoechst and DAPI dyes which target the DNA [137, 138]. The discovery of the green fluorescent protein made it possible to introduce the genetic sequence for fluorescent proteins directly into the DNA of the specimen [139]. Thus, the dye does not have to be brought inside the cell, as the cell produces it directly inside of itself. Fluorescent proteins can be used as fusion proteins to label specific proteins and to monitor gene expression by using it as a reporter molecule. However, the introduction of fluorescent labels can affect cellular function, behavior and metabolism [140–142], was well as the binding behavior of proteins [143]. Especially phototoxicity is often underestimated [144].

A fundamental property of an optical imaging system is its maximum achievable resolution. Diffraction limits the lateral resolution of a conventional lens-based optical microscopes with a numerical aperture NA[4] to $d = 1.22\frac{\lambda}{2NA}$ according to the Rayleigh criterion [145]. The axial resolution is limited to $d \approx 2\frac{n\lambda}{NA^2}$ [146]. However, modern fluorescence microscopy can circumvent the diffraction limit by employing a variety of superresolution techniques [12]. Another characteristic of an optical imaging system is the total amount of information the optical system is capable of transferring. While a detailed treatment requires to consider the signal-to-noise ratio (SNR), the space-bandwidth product (SBP) is a frequently used measure of information transfer capacity. The common definition is SBP $= A/d^2$ where d is the resolution and A the total image area [147].

2.2.2 Principles of Holographic and Lensless Microscopy

In addition to conventional lens-based microscopy methods, cells and other microorganisms can also be imaged with microscopy methods that do not require any lenses for image formation and as a consequence offer some unique advantages. These methods are commonly referred to as lens-free or lensless microscopy. They are either based on or closely related to holography. Dennis Gabor introduced Holography in 1948 as "a new microscopic principle" to improve resolution in electron microscopes [148], for which he received the Nobel price in 1971.
The principle of holography consists of interfering light originating from an object (object wave) with a reference wave and recording the resulting interference pattern (objects hologram). The principle of holography is also illustrated in ***Figure 2.4***. Generally speaking, a hologram is a recording of the wave field information of an object as an interference pattern. In contrast to an image of an object which only contains amplitude information recorded as the intensity of the field, a hologram hence additionally contains the phase-information of the field. Therefore, holography allows reproducing the objects original light-field, either through a suitable illumination of the recorded hologram or computationally (see also ***Figure 2.4 c***). The name hologram was motivated by the fact that it contains the full three-dimensional information on the object and originates from the greek words holos (whole) and graphe (drawing) (graph). However, holography only found widespread use in microscopy after some critical technological breakthroughs [149]. These include the development of lasers as powerful and highly coherent light sources in the 60s, sufficiently fast microprocessors in the 90s, and high-resolution

[4]The NA is defined as NA=$n\sin(\vartheta)$ where ϑ is the maximal half-angle of the light-cone that can enter the objective and n is the index of refraction of the medium.

electronic image sensors in the 2000s. Especially the possibility to record holograms with digital optoelectronic array detectors such as charge-coupled device (CCD) sensors [150] has led to countless applications. The following sections give an overview of the theoretical principles of Digital Holographic Microscopy (DHM) and lensless microscopy (LM) as well as their applications in biomedical imaging.

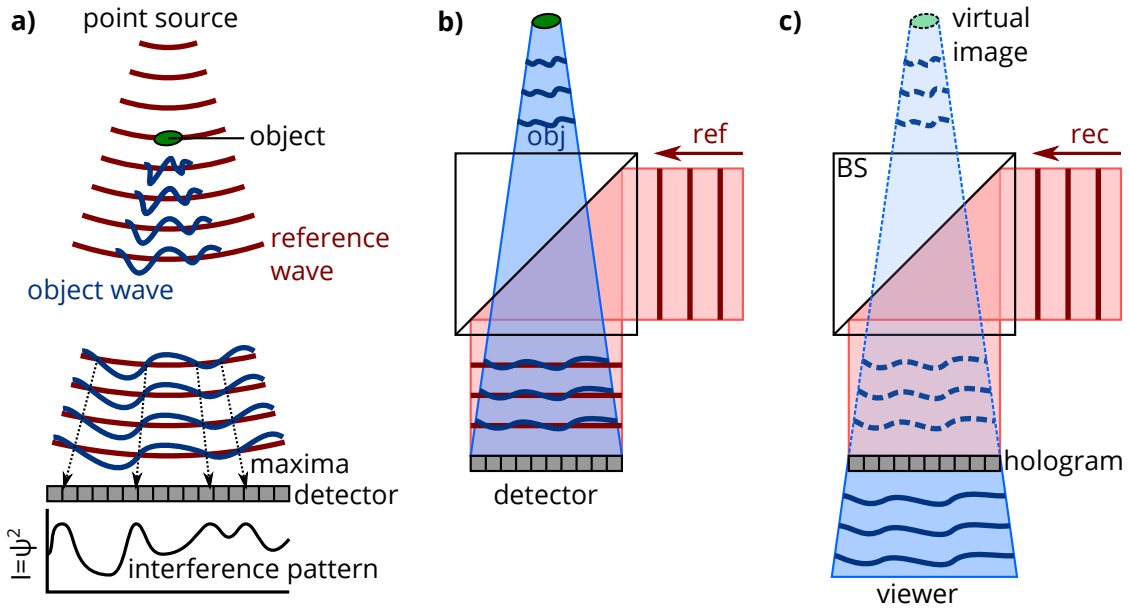

Figure 2.4: Principle of holography **a)** Gabor's original inline configuration: Spherical wavefronts from a point source are incident on the object. A fraction of the wavefront passes the object unperturbed and serves as the reference wave while the scattered fraction forms the object wave. The object wave interferes with the reference wave, and the objects hologram is recorded as the intensity I of the fields complex amplitude ψ squared. **b)** Alternatively, a beam splitter (BS) allows using a reference wave (ref) that does not pass through the sample for interference with the object wave (obj). **c)** Reconstruction scheme: Illuminating the hologram with a reconstruction wave (rec) recreates the original object wavefront, thus providing a three-dimensional virtual image for a viewer.

Scalar diffraction theory

The theoretical and mathematical description of lensless imaging and DHM is based on diffraction theory. The propagation of the wavefront after scattering by the imaged object is treated as diffraction of an incident wavefront by a corresponding aperture. A plane wave with an amplitude A hits an aperture described by a transparency function $T(x, y)$ at the plane $z = 0$. The initial condition for this case is given by the complex amplitude of the field $\psi_{p0}(x, y, z = 0)) = A \times T(x, y)$. Its Fourier transform $\mathcal{F}\{\psi_{p0}\} = \Psi_{p0}$ is also known as the *angular plane wave spectrum*. To derive an expression for the complex amplitude of the field $\psi(x, y, z, t)$ describing the diffracted wave at an output plane located at z, one can start with the Fresnel-Kirchhoff diffraction formula as in [135] or with the wave equation as in [151], which

is followed here. The scalar wave equation is given by

$$\nabla^2\psi = \frac{1}{\nu^2}\frac{\partial^2\psi}{\partial t^2} \tag{2.1}$$

The Ansatz $\psi(x,y,z,t) = \psi_p(x,y;z)\, e^{i\omega_0 t}$ for the solution of the field ψ at a plane at a distance z from the object can be used to derive the following solution describing the propagation of the diffracted wave

$$\psi_p(x,y;z) = \frac{1}{4\pi}\iint_{-\infty}^{+\infty} \Psi_{p0}(k_x,k_y)\exp\left(-ik_0\sqrt{1-k_x^2/k_0^2-k_y^2/k_0^2}z\right)e^{-ik_x x}e^{-ik_y y}dk_x dk_y \tag{2.2}$$

with the wavenumber k_0. The derivation of this and the further equations is explained in detail in ***Appendix 1.1***. Under the paraxial approximation, i.e., $k_x^2+k_y^2 \ll k_0^2$, this equation becomes the *Fresnel diffraction formula*

$$\psi_p(x,y;z) = e^{-ik_0 z}\frac{ik_0}{2\pi z}\iint_{-\infty}^{+\infty}\Psi_{p0}(x',y')\exp\left\{-\frac{ik_0}{2z}\left[(x-x')^2+(y-y')^2\right]\right\}dx'dy' \tag{2.3}$$

$$= \psi_{p0}(x,y) * h(x,y,z) \tag{2.4}$$

with the *spatial impulse response in Fourier optics*

$$h(x,y,z) = e^{-ik_0 z}\frac{ik_0}{2\pi z}\exp\left[-\frac{ik_0}{2z}\left(x^2+y^2\right)\right] \tag{2.5}$$

If the condition $\frac{k_0}{2}\left[(x')^2+(y')^2\right] \ll z$ is fulfilled for the far field, the *Fraunhofer diffraction formula*

$$\psi_p(x,y;z) = e^{-ik_0 z}\frac{ik_0}{2\pi z}\exp\left[-\frac{ik_0}{2z}\left(x^2+y^2\right)\right]\times\mathcal{F}\{\psi_{p0}(x,y)\}_{k_x=\frac{k_0 x}{z},k_y=\frac{k_0 y}{z}} \tag{2.6}$$

can be used to approximate the Fresnel diffraction.
The numerical calculation of the field $\psi(x,y,z)$ at a position z for a given field distribution $\psi_0(x,y,z=0)$ is commonly refered to as numerical diffraction. It can be carried out efficiently with the Fast Fourier Transform (FFT). To this end, equations 2.2 and 2.3 can be expressed in terms of the Fourier transform:

$$\psi_p(x,y;z) = \mathcal{F}^{-1}\{\mathcal{F}\{\psi_{p0}(x,y)\}\times\mathcal{H}(k_x,k_y;z)\} \tag{2.7}$$

$$\psi_p(x,y;z) = \frac{ik_0 e^{-ik_0 z}}{2\pi z}e^{-\frac{ik_0}{2z}(x^2+y^2)}\times\mathcal{F}\left\{\psi_{p0}(x,y)\exp\left[-\frac{ik_0}{2z}\left(x^2+y^2\right)\right]\right\}_{k_x=\frac{k_0 x}{z},k_y=\frac{k_0 y}{z}} \tag{2.8}$$

Using equation 2.7 for numerical diffraction is called the *Angular Spectrum Method* (ASM) and requires two Fourier transforms. Numerical diffraction according to equation 2.8 is referred to as the *Fresnel diffraction method* and requires only one Fourier transform. There are further methods such as Huygens convolution, each with specific restrictions, advantages, and disadvantages which are discussed elsewhere [151].

Recording and reconstruction of holograms

To discuss the hologram recording, we consider the geometry that is illustrated in ***Figure 2.5 a***. An object is placed at a position $z = -z_0$, which is a distance z_0 away from the recording plane at position $z = 0$. The object is illuminated with a plane wave with an amplitude a that propagates along the z-axis. The detector records the intensity distribution of the superposition of the object wave ψ_o and the reference wave ψ_r. If we express the hologram in terms of the transparency function $T_h(x, y)$, it contains the following terms:

$$T_h(x,y) = |\psi_r(x,y) + \psi_o(x,y)|^2 \propto \psi_r^2 + \psi_o^2 + |\psi_r|\,|\psi_o|\,(x,y) \tag{2.9}$$

Using Fresnel diffraction according to equation 2.3 for a point aperture, this equation becomes (see also ***Appendix 1.2***):

$$T_h(x,y) = a^2 + \left(\frac{k_0}{2\pi z_0}\right) + a\frac{ik_0}{2\pi z_0}\left\{\exp\left[-\frac{ik_0}{2z_0}\left(x^2+y^2\right)\right] - \exp\left[\frac{ik_0}{2z_0}\left(x^2+y^2\right)\right]\right\} \tag{2.10}$$

$$= A + B\sin\left[\frac{k_0}{2z_0}\left(x^2+y^2\right)\right] \tag{2.11}$$

Equation 2.11 illustrates that the hologram contains three-dimensional information, as the distance z_0 of the object to the recording plane determines the period of the diffraction fringes. If ψ_o and ψ_r were to propagate over a distance $2z_0$ from the object to the position $z = z_0$, one would obtain a field denoted with $\hat{\psi}$. ***Figure 2.5 a*** shows that $\hat{\psi}$ propagated backwards over a distance z_0 from $z = 2z_0$ to the detector plane at $z = 0$ would result in the same transparency function $T_h(x, y)$ as in the case above. This symmetry will play an important role in the following discussion, as it gives rise to the so-called twin-image.

The original field can now be reconstructed from the hologram, by illuminating it with a reconstruction wave ψ_{rec} that has the same properties as the wave initially used for illumination of the object. This reconstruction geometry is illustrated in ***Figure 2.5 b***. For the hologram of the point aperture, the propagation of the field ψ_{rec} from the hologram at $z = 0$ over a distance z, can be written mathematically according to Fresnel diffraction as

$$\begin{aligned}\psi_{rec}T_h(x,y) * h(x,y;z) = \psi_{rec}\Bigg\{&\left(a^2 + \frac{k_0^2}{(2\pi z_0)^2}\right) - a\frac{ik_0}{2\pi z_0}\exp\left[\frac{ik_0}{2z_0}\left(x^2+y^2\right)\right] \\ &+a\frac{ik_0}{2\pi z_0}\exp\left[\frac{-ik_0}{2z_0}\left(x^2+y^2\right)\right]\Bigg\} * h(x,y;z)\end{aligned} \tag{2.12}$$

This term corresponds to three waves emerging from the hologram. The first term is proportional to $\psi_{rec}\left(a^2 + \frac{k_0^2}{(2\pi z_0)^2}\right)$ and corresponds to a plane wave that passes the hologram without diffraction and is called the *zeroth-order beam* in holography. In the general case of a complex object, the zeroth-order beam is however not uniform. The second and third terms are proportional to

$$\pm\frac{k_0^2}{4\pi^2 z_0 z}\exp\left[\pm\frac{ik_0}{2(z_0-z)}\left(x^2+y^2\right)\right] \tag{2.13}$$

respectively, and correspond to spherical waves. The plus-case is for $z < z_0$ a converging spherical wave and for $z > z_0$ a diverging wave. For $z = z_0$ the wave is focused to a single

point, which corresponds to the original object given by the delta function, i.e., it is a real image. The minus-case is a field that propagates identically to the original object wave. As this is a diverging wave with a virtual point source at $z = -z_0$, i.e., the original position of the object, this wave corresponds to a virtual image. Hence, the light-field reconstructed for the original position of the object at $-z_0$ is the superposition of the original light-field and the light-field of a point source at $z = z_0$. This second contribution is commonly referred to as the *twin image* and is the consequence of the symmetry in the recording geometry in ***Figure 2.5 a***. In the general case of multiple objects in the object plane, equation 2.9 will contain terms corresponding to interference between the object waves, which upon reconstruction will lead to noise in the image. Thus, the amplitude of the reference wave needs to be significantly bigger than the amplitude of the scattered waves for making the interference terms quadratic in the object waves negligible [152]. The twin-image and zeroth-order contributions can be eliminated by using an off-axis configuration where the reference wave is tilted with respect to the object wave. However, this comes at the cost of reducing the information content to one-quarter of the pixel count. Gabor's inline configuration does not have this restriction but requires special techniques to remove twin-image contributions. Furthermore, the sample must be transmissive and only weakly scattering in order to maintain a sufficiently clear reference wave. Although in some cases a distinction is made whether the reference wave is a spherical or a plane wave, both can be used for inline holography [153].

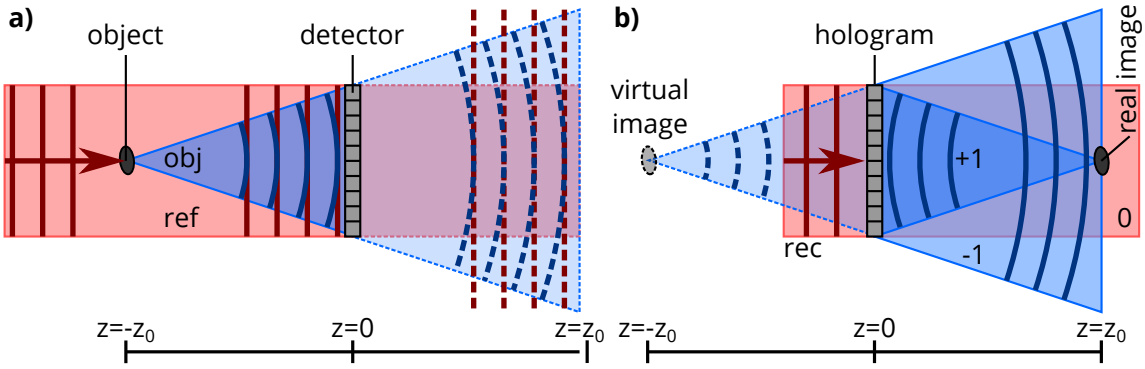

Figure 2.5: Inline holography **a)** Recording: A plane wave propagating along the positive z-direction is incident on an object at $z = -z_0$ and the resulting interference pattern of the scattered object wave (obj) and unscattered reference wave (ref) is recorded as the hologram on a detector at $z = 0$. In the absence of the detector, the field would propagate further along the positive z-direction and reach $z = z_0$. Due to time symmetry, the propagation of the field distribution at $z = z_0$ in negative z-direction would result in the same hologram in the detector plane. **b)** Reconstruction: Illumination of the hologram with a plane reconstruction wave (rec) results in an unscattered zeroth-order wavefront (0), a converging wavefront (+1) forming a real image at $z = z_0$, and a diverging wavefront (-1) forming a virtual image at $z = -z_0$. The diverging wavefront is identical with the original object wavefront in the recording geometry in a). Each of the two images contains the contribution of its respective $2z_0$ out of focus twin-image counterpart.

Digital holography

In digital holography, an optoelectronic sensor array such as a CCD or a complementary metal-oxide-semiconductor (CMOS) sensor is used as the detector to record the hologram as a digital image. The reconstruction of the light-field of the original object from the recorded hologram is then carried out by numerical diffraction. In the case of digital holographic microscopy (DHM), this means a computer algorithm replaces the image-forming lens used in traditional microscopy. One significant advantage of DHM is that due to the three-dimensional information content of the hologram, the light-field can be reconstructed at any distance from the hologram plane. Hence, different planes of the sample can be focused numerically. The reconstructed light-field allows calculating an amplitude image as well as a phase image of the sample. The phase image shows the phase shift induced by the object. Therefore, DHM is a technique for quantitative phase imaging (QPI). DHM has been successfully used to measure differences in optical thickness with nanometer accuracy [135].

Resolution and digital sampling: The image sensor imposes several restrictions due to its finite extent and the discrete pixels, as the resolution is determined by the sensor's capability to resolve the interference fringes. The maximum achievable resolution is determined by the wavelength λ and the coherence of the used light, the numerical aperture NA given by the size of the image sensor as well as the pixel pitch p, and the dynamic range of the image sensor. The lateral resolution is given by $\delta_{lat} = \frac{\lambda}{2NA}$ and the axial resolution as $\delta_{ax} = \frac{\lambda}{2(NA)^2}$ [153]. If f_{sigal} is the spatial frequency of the interference fringes, then according to the Nyquist-Shannon sampling theorem the sensor must sample the signal with a sampling frequency $f_{sampling} \leq 2f_{sigal}$ to faithfully recover the signal [151]. This means the pixel pitch must be less than half the period of the interference fringes to avoid aliasing. The maximum number of observable interference fringes is furthermore determined by the spatial and temporal coherence of the light source. The coherence length describes the length scale over which coherence is lost and is given by the spectral width of the light source whereas the spatial coherence is given by the spatial extent of the light source [151]. Lasers are frequently used as light sources in DHM due to their long coherence lengths. He-Ne-lasers typically have a coherence length of 20 cm. Light-emitting diodes (LED) have a coherence lengths of about 10 µm [135], which for Gaussian power spectral densities can be calculated according to $l_c = \sqrt{\frac{2\ln(2)}{\pi}}\frac{\lambda_0^2}{\delta\lambda}$ [154]. Despite their relatively low coherence length, LEDs can provide suitable light sources for DHM applications [155]. While the resolving power may be reduced, speckle noise and noise due to multiple reflections is minimized. The resolution limit of DHM and the critical parameters of digital image sensors impacting it are discussed in more detail in [156–159].

Twin-image removal and further numerical techniques: If the phase shift introduced by the sample exceeds 2π, the phase image will contain discontinuities. Phase-unwrapping algorithms must be employed to remove these discontinuities. Optical phase unwrapping increases the robustness of the algorithms by using two different illumination wavelengths [135]. To obtain time-lapse series of high contrast in-focus images, the optimum distance for the numerical diffraction in the reconstruction must be determined with algorithms for numerical autofocusing [160]. In the inline configuration, the zeroth-order and twin-image contributions must be removed from the reconstructed in-focus image. These contributions can be removed or reduced with a variety of experimental and computational means [161]. In phase-shifting holography, for example, additional phase shifts are introduced between the object and reference waves.

Recording several holograms with different phase shifts allows complete elimination of twin-image and zeroth-order contributions [135]. A suitable recording geometry can also be used to minimize twin-image artifacts by increasing the length scale of their spatial frequencies to the size of the image [152]. A commonly used approach for twin-image removal is to employ phase-retrieval [162], for which a wide range of techniques and algorithms are available due to the relevance in, e.g., coherent diffraction imaging [163].

Direct analysis of interference patterns: While the previous sections focused on the reconstruction of a high-quality image from the recorded hologram, it is noteworthy, that crucial information on the sample can also be extracted by analyzing the hologram directly without using digital reconstruction. For colloidal particles, the interference pattern can be fitted with the Lorenz-Mie scattering model to determine their radius and refractive index with high precision and track them with nanometer precision [164]. A comparison of this tracking strategy with using the reconstructed images to track particles showed that directly analyzing the holograms provides a viable option for particle tracking [165].

2.2.3 Biomedical Imaging with DHM and LM

First applications of DHM and LM for biomedical imaging and cell microscopy emerged in the 2000s. Initially, DHM was used by modifying conventional light microscopes. While this approach relies on using a microscope objective, the image is formed by an algorithm instead of the lenses and that objective is only used to magnify the hologram. ***Figure 2.6 a*** shows a schematic of DHM using objective lenses.
In contrast, biomedical imaging can also be achieved with configurations that forgo the use of lenses altogether, which is the configuration that is referred to as LM within this thesis. In LM, the sample is typically placed close to the image sensor, as schematically illustrated in ***Figure 2.6 b***. Due to the proximity of the sample to the image sensor, this configuration is frequently referred to as *on-chip*. On-chip LM configurations can be used as a DHM setups by digitally reconstructing an in-focus image. Alternatively, the reconstruction can be omitted, and the interference pattern analyzed directly. This reconstruction free LM (RFLM) is also often referred to as *shadow imaging*. In conventional microscopy, there is an inherent trade off between achievable image resolution and FOV which limites the achievable space-bandwith product to several megapixels [63]. In contrast, the on-chip approach operates under unit magnification, effectively decoupling FOV from resolution and enabling the space-bandwidth product to scale with the size of the image sensor [64].

DHM using objective lenses: In 2005 it was for the first time shown that DHM using objective lenses allows QPI of living cells in culture [14] and that digital reconstruction with the angular spectrum method allows imaging cells with 0.5 µm diffraction-limited lateral resolution and an accuracy of 30 nm in the measured optical path length. It has subsequently been shown that the technique allows label-free determination of the cell density, confluency, cell shape, as well as cellular optical thickness of adherent cells directly in cell culture vessels [54]. Generally, DHM using objective lenses has found widespread use in biomedical imaging applications such 3D-tracking of living cells [167], studying the morphology of cells [168], red blood cell analysis [169], cell death detection [170], analysis of cell cycle and neural activity [171], and cell division monitoring [172]. By using elaborate illumination schemes like in 2π-DHM, an accuracy of 2 nm in variations of the optical path length combined with a lateral resolution below 200 nm

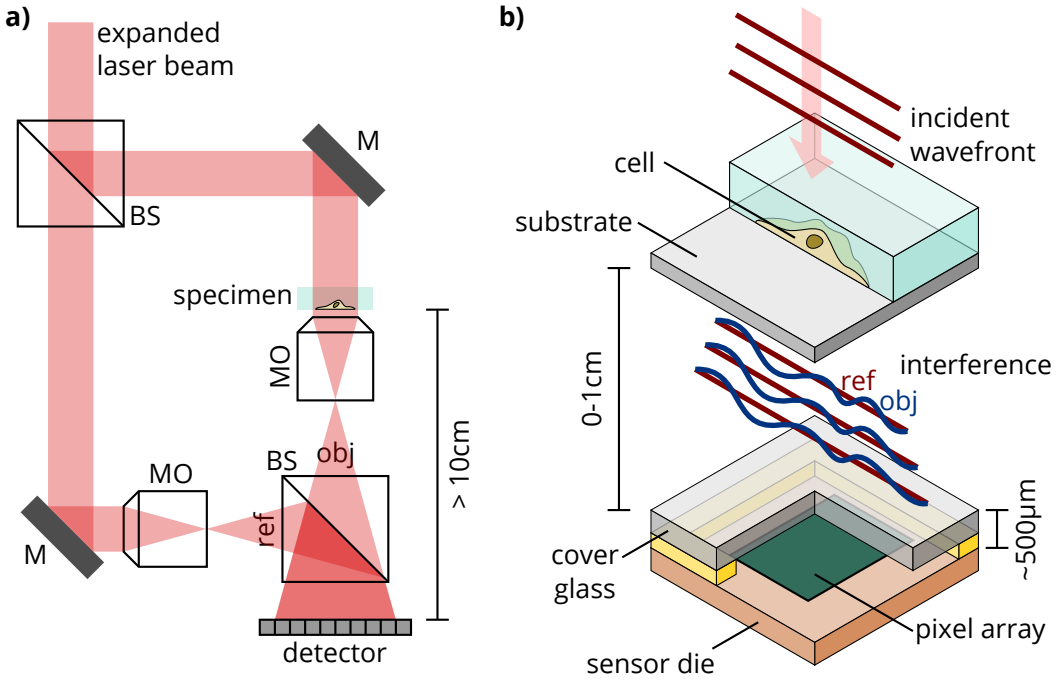

Figure 2.6: Configurations and typical dimensions of DHM using objective lenses and LM. **a)** Schematic of a DHM setup using objective lenses in an interferometric configuration (adapted from [166]). The beam splitter (BS) creates one beam which serves as the reference wave (ref) and one beam for illumination of the sample from the laser light source. The microscope objective (MO) captures the scattered object wave (obj). The reference beam also passes a MO to match the curvature of the object beam. A second BS combines object and reference wave, and the detector records the hologram. **b)** Geometry of on-chip LM: A plane wave is incident on an object, here illustrated as a cell in medium. A digital optoelectronic sensor array records the resulting interference pattern of the scattered wavefront, i.e., the object wave, and the unscattered part of the wave, i.e., the reference wave.

have been achieved [173]. DHM using objective lenses has also been used to perform kinetic cell proliferation assays inside cell culture incubators. This allowed obtaining growth curves and rates multiple parameters such as the cell number, confluence, as well as the average cell volume. The growth curves can then be used to calculate IC_{50} values for growth-inhibiting drugs, i.e., the inhibitory concentration at half maximum effect [174].

The history of LM in biomedical imaging: Lensless DHM was first used in 2001 for biological applications by imaging diatoms and the head of Drosophila Melanogaster. However, in contrast to later on-chip designs, the sample was placed much closer to the light source than to the image sensor to magnify the hologram [175]. The first use of RFLM was to image the nematode C.Elegans in a compact on-chip design in 2005. The used image sensor only had a resolution of only 320 × 240 pixels with a pixel pitch of about 10 µm. Nevertheless, the system successfully acquired "shadow images" of the worms, which have a typical circumference of about 60 µm [67]. Successive RFLM designs included microfluidics and an aperture mask between the sensor and the sample to improve the resolution to 800 nm [176]. Ozcan and Demirci were the first to image cells with an on-chip configuration in 2007 [68]. While the pixel pitch was 9 µm, the FOV was 37 mm × 26 mm and therefore substantially larger than with conventional

microscopy. They used an incoherent white light source and had to remove the sensors cover glass. Based on these pioneering works, LM has since matured into a versatile and powerful technique for a wide range of applications for biomedical imaging [65]. For example, lensless fluorescence microscopy with a resolution of up to 1.2 µm has been achieved by using the Talbot effect for structured illumination [177]. However, the scope of the following sections is focused on the use of LM for label-free cell microscopy.

Image sensors for LM: The development and the feasibility of on-chip LM techniques were closely related to the advancement of digital optoelectronic image sensors. Current CCD and CMOS image sensors are based on using a photodiode as the photodetector for each pixel. The photodiode creates a photocurrent I_{ph} that is proportional to the photon flux $\Phi(\lambda)$ of the incident light. The diodes quantum efficiency $\eta(\lambda)$ determines the photocurrent according to $I_{ph} = q \int_{\lambda} \Phi(\lambda)\, \eta(\lambda)\, d\lambda$ [178], where q is the elementary charge. On overview over CMOS and CCD image sensor technology is given in [179]. Typical consumer-product image sensors consist of the sensor die containing the pixel array and a cover glass to protect the die, see also ***Figure 2.6 b***. Current designs follow the System on a Chip (SOC) design, where a single die includes the pixel array and further circuitry such as analog-digital converters (ADCs). ***Figure 2.7*** shows a typical current CMOS sensor SOC design. Over each pixel, there is a microlens to focus the light onto the photodiode, which only corresponds to a fraction of the surface of the pixel. A red, blue, or green color filter is placed between the microlens and the photodiode of each pixel to enable color imaging. The color filters are usually arranged in the bayer pattern. The blue intensity value for a red pixel is interpolated from the surrounding blue pixels through interpolation in a process called *demosaicing*. State-of-the-art CMOS image sensors follow stacked SOC designs, where a layer beneath the pixel array contains the circuitry for ADCs and other functions. These stacked designs allow extremely compact designs, where the majority of the area fraction of the uppermost die is used for the pixel array. Currently Stacked CMOS image sensors with >20 MP resolution and a pixel pitch below 1.0 µm are being developed [66].

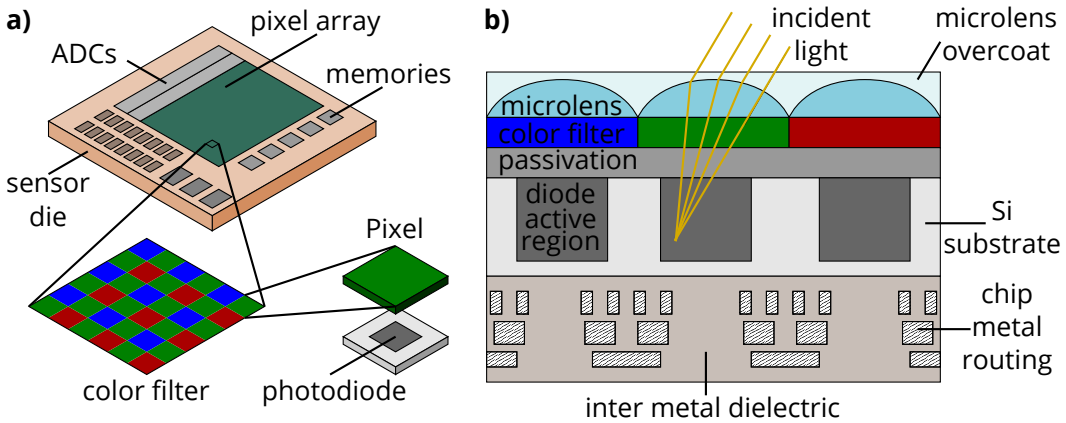

Figure 2.7: Architecture of a current CMOS Sensor (based on [179, 180]) **a)** The sensor die contains circuitry such as ADCs, memories, and the pixel array itself. Each pixel contains a photodiode and is covered with a color filter. **b)** Cross section of a CMOS sensor. Microlenses focus the light into the active region of the photodiode. In a back-illuminated sensor, the circuitry for electrical readout of the diode is located in a layer beneath the diode layer.

DHM-based LM: DHM-based LM enables QPI, 3D imaging and the acquisition of high resolution in-focus images that allow visualizing fine morphological features of cells. However, a basic lensless on-chip DHM setup consisting of just a coherent light source and an image sensor has several limitations: the resolution is limited by the pixel size of the sensor, the presence of the twin-image artifacts, and the scattered wave must be weak compared with the reference wave, which restricts such setups to relatively sparse samples [65] (see also section 2.2.2).
The resolution restriction posed by the pixel size can be circumvented by employing pixel-superresolution techniques [181]. In these techniques, several versions of the sample's holograms are acquired, each with a spatial shift of a fraction of the pixel pitch in the sensor plane. Typically, a shifting light source or an array of light sources are used to this end. From these shifted holograms, a high-resolution hologram with smaller virtual pixels than the physical pixel size can be numerically synthesized, which allows reconstructing nearly diffraction limited images [65]. However, as the photodiode constitutes only a fraction of a pixel's area, the spatial responsivity - the pixel response function - must be either known or determined for optimum performance of these pixel-superresolution approaches. Compared to classical microscopy, DHM-based LM with pixel-superresolution provides the advantage of decoupling resolution from FOV. Here, space-bandwidth products in the gigapixel range have been achieved, which is significantly higher than classical microscopy with typically around 10 MP [64].
To minimize twin-image artifacts and to enable imaging of dense samples where no clean reference wave is available, additional information must be employed for image reconstruction in on-chip DHM [65]. Iterative phase recovery algorithms can use for example restrictions on the field outside of the objects in the sample plane [182]. The optical field is then propagated between the sample and the sensor plane until a self-consistent solution is found. However, the automated detection of the objects' boundaries in the images containing the twin-images can pose a challenge to this approach. Phase recovery approaches that do not require prior knowledge of the object's boundaries are based on acquiring holograms at several sample-sensor distances [183], or at several different illumination angles [184]. Alternatively, several holograms acquired with different illumination wavelengths can be used [185, 186]. Reducing the number of required holograms as well as experimental and computational costs for phase recovery remains an active field of research [187, 188], e.g., by non-iterative phase recovery schemes [189–191].
Lensless on-chip DHM has been successfully used for a wide range of applications, e.g., tomography by using multiangle hologram acquisition to acquire 3D sections of C.Elegans with a lateral resolution of $<1\,\mu m$ and an axial resolution of $<3\,\mu m$ [192]. Other applications include cell migration studies [193], the formation of microvascular networks in 3D culture [194], imaging pathology slides [195], and monitoring critical parameters such as motility and cell number of cell cultures within standard incubators [196]. A more detailed discussion of the design principles and applications for biomedical imaging of LM can be found in reviews, e.g., [65, 69–71].

RFLM: As the simplest form of LM, RFLM remains an attractive choice for research since it allows to build highly versatile, extremely compact, and cost-effective systems which do not require the computational costs of DHM based LM [70]. The key is that with suitable image analysis methods, relevant parameters can be extracted directly from the recorded interference pattern without computationally reconstructing an in-focus image. RFLM has been primarily used for cytometry applications, where identification of specific particle and cell types, counting them, or discriminating between them is the primary goal, such as in blood cell counts and

blood cell analysis [197–199]. However, the technique also allows the continuous monitoring of living samples, e.g., for tracking human sperm [200] or automated tracking of murine 3T3 cells [201]. While RFLM typically cannot resolve single cells in dense or 3D samples, it allows, for example, distinguishing larger structures like spheroids from acini [202], measuring the beating rate of cardiomyocytes [203], or monitoring bacterial microcolonies [204]. Analyzing various parameters of the diffraction patterns of individual cells such as fringe contrast, fringe dispersion, intensity, and further measures allows the identification of different states like alive, dead, spread-out, or mitotic of individual cells within living cultures due to the different morphologies [73, 205–208]. In principle, the resolution of RFLM can be improved by using custom specially fabricated image sensors [72] to sub-micron levels or with superresolution schemes to about 660 nm [209]. However, these improvements required the removal of the cover glass, color filter, and micro-lens layer. The pixel superresolution algorithm also required the acquisition of 15x15 images for each position in combination with a shifting light source to obtain the high-resolution image.

3

Experimental Design of Lensless Microscopy Setups

The previous chapter provided background on the principles of LM, state of the art techniques, and applications in biomedical imaging. The compact instrumentation is one key advantage of LM and facilitates label-free live-cell imaging inside standard incubators. On-chip DHM is capable of QPI and provides amplitude images showing minuscule morphological features of cells. However, the technique is computationally complex since it requires algorithms for image reconstruction, numerical focusing, and suppression of twin image artifacts. For high image quality, DHM-based lensless microscopes typically use pixel super-resolution and acquire multiple holograms for different illumination wavelengths, illumination angles, or sample-sensor distances. Despite being used less frequently than on-chip DHM, RFLM remains an attractive alternative LM technique due to the experimental simplicity and low computational costs. Although the low-coherence interference patterns recorded in RFLM do not allow a direct visual assessment of cell morphology, they still allow the extraction of vital phenotypic information of the cells.

This chapter presents the experimental design of RFLM setups that were developed in the context of this thesis to demonstrate that in-situ live-cell imaging with RFLM in combination with image-based metrics allows analyzing growing cell populations in great detail. A further goal was to show that RFLM facilitates the quantitative analysis of key aspects and processes in cell culture.
To enable the measurement of critical phenotypic parameters like cell growth and motility with RFLM and image-based metrics, a variety of different microscopy setups and methods were used. The design of the setups requires to address the following issues for making the technique suitable and useful for a broad range of experiments with living biological samples: First, for time-lapse experiments, it is crucial that the technique allows the continuous observation of the specimen without having a significant effect on its behavior or environment. Second, the technique must image the cells in a fashion that facilitates the use of image analysis for the automated and robust quantification of phenotypic traits. Furthermore, the instrumentation should be cost-efficient, versatile, and have high-throughput capabilities. This following sections present the experimental methods employed to develop, characterize, and validate RFLM-based instruments which meet these requirements.

3.1 Hardware Considerations

As detailed in ***Section 2.2.2***, the two essential components of a lensless microscope are the optoelectronic image sensor and the light source. Besides the image sensor itself, the circuit boards of commercially available cameras contain electronic components for controlling the image sensor and for the data exchange and communication with a host computer. ***Figure 3.1 a&b*** shows two different camera boards that are suitable for RFLM setups. The first one (b) is an XR-IC2MHD (Shenzhen Xinray Opto-Electronic Tech Co Ltd; Shenzhen, Guangdong, China). Earlier RFLM setups designed for this thesis used this camera. All shown setups use the second camera (a), which is a custom design from Global Digital Star Limited (Shenzhen, Guang Dong, China). The figure illustrates some critical features of the cameras for their use in RFLM

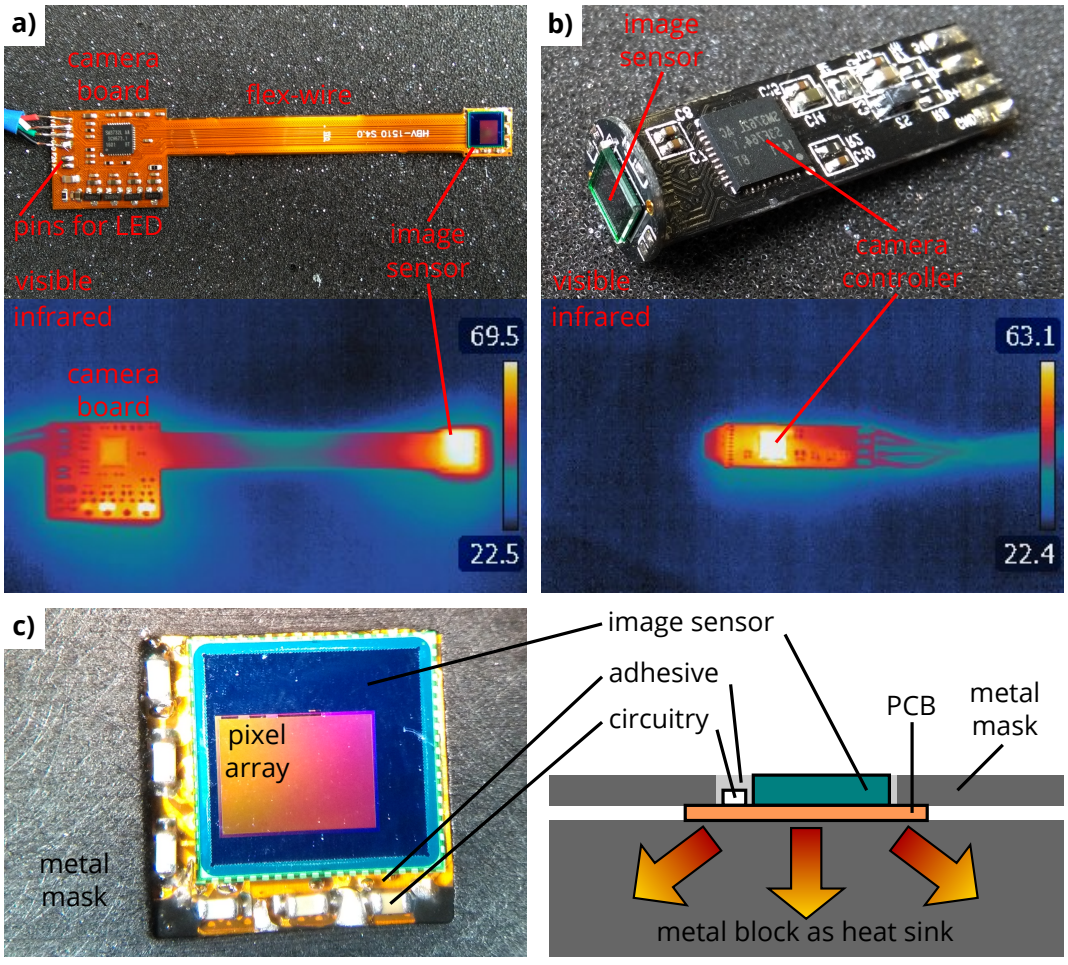

Figure 3.1: Camera board geometry and heat dissipation. **a)** Image of the used camera (custom design). The image sensor is spatially separated from the camera board. The bottom panel shows an infrared image of the camera and illustrates the heat generation during continuous image acquisition. **b)** XR-IC2MHD camera board. The image sensor is directly attached to the camera board. The infrared image shows that the camera controller chip on the printed circuit board (PCB) generates significant heat. **c)** In most setups, the PCB of the image sensor of the camera was incorporated into a metal mask to provide a flat surface for sample placement. The bottom of the PCB was attached to a larger metal block, which served as a heat sink.

setups: The image sensor must be accessible to allow the placement of sample chambers on top of the image sensor and the camera should require only a minimum of space. The figure also shows that the active components of the camera board generate and dissipate heat during operation. Due to the proximity of the image sensor to the biological sample in RFLM, minimization of the heat transfer from the electronic components to the sample is essential. Therefore, the image sensor is spatially separated from the other heat generating components of the customized camera board via a flex wire, as ***Figure 3.1 a*** illustrates. ***Figure 3.1 c*** depicts the geometry of the image sensor in the live cell imaging setups. Connecting the back of the image sensor to a heat sink significantly reduced heating of the sample. Integration into a thin metal mask provided a flat surface to place standard sample containers on top of the image sensor and helped to distribute the heat dissipated by the image sensor further.
The cameras were connected to a PC via USB. An Arduino microcontroller controlled the power supply of the camera boards by switching the +5V line of the USB connection via a p-channel transistor. The cameras were switched on only during image acquisition to minimize heating due to the electronic components. Three consecutively acquired frames were averaged to minimize the pixel noise of the sensor. The resulting image was then stored on the PC. A custom program written in C++ automatically acquired images at specified intervals by switching the camera on, calling the program *fswebcam* to record the three frames, and switching the camera back off again. On average, the camera needed (3962 ± 49) ms to acquire the first frame and (488 ± 2) ms for the subsequent frames. A more detailed analysis of the times required for the individual steps during image acquisition is provided in ***Appendix 2.1***. This analysis shows that using a camera that requires less time to have the first frame ready for transfer to the PC could potentially lead to a significant reduction in heat generation.

As presented in ***Section 2.2***, the properties of the image sensor and the light source determine the quality and features of the acquired lensless microscopy images. The custom camera uses an OmniVision OV5640 CMOS sensor (OmniVision, Santa Clara, USA). The OV5640 has a pixel size of 1.4 µm, an active array containing 2592x1944 pixels, an image area of 3674 µmx2738 µm, and a cover glass thickness of 445 µm. The samples were illuminated with a Kingbright L-9294SECK LED (Kingbright Electronic Co, New Taipei City, Taiwan (R.O.C.)). The LED has a peak wavelength of 610 nm, a spectral line half-width of 29 nm and was used in all shown setups. An important characterization for an RFLM system is the Fresnel number $N = \pi D^2/(4z\lambda)$, with the illumination wavelength λ, the diameter of the imaged object D, and the sample-sensor distance z [68]. In the Fraunhofer regime (N<1), the shadow diameter increases with increasing z and λ. In the Fresnel regime, the shadow diameter increases linearly with D and has only a weak dependence on z. A sample container with a standard No. 1.5 coverslip with a thickness of 180 µm placed directly on the image sensor results in $z_{min} = 625$ µm. As can be seen in ***Table 3.1***, the Fresnel number is below one for cell-sized objects imaged in an on-chip geometry using the components that were described above.

Table 3.1: Fresnel number for different object sizes and sample-sensor distances (λ=610 nm)

	D=10 µm	D=20 µm	D=40 µm
$z = z_{min}$ =0.625 mm	0.21	0.82	3.30
z =1.0 mm	0.13	0.52	2.06
z =2.0 mm	0.06	0.26	1.03

The customized camera board has two pins to directly power the LED used for illumination. The pins provide a voltage of 2.8 V during image acquisition, thus automatically switching the LED on during image acquisition. The LED has a forward voltage of 2.1 V and was used with a 10 kΩ current limiting resistor. Thus, the power consumed by the LED during operation is 150 µW, which corresponds to light dose below 1 mJ mm^{-2}. This light dose is orders of magnitude below the light doses which typically induce phototoxic effects in cells [210]. Since the OV5640 CMOS sensor records color images, illumination with the red monochromatic light from the LED results in pronounced differences in the brightness of the three color channels. The auto-functions of the camera adjusted the exposure such that the red channel was overexposed and that the blue channel was mostly dark, see also ***Figure 3.2 a***. In contrast, the green channel provided a

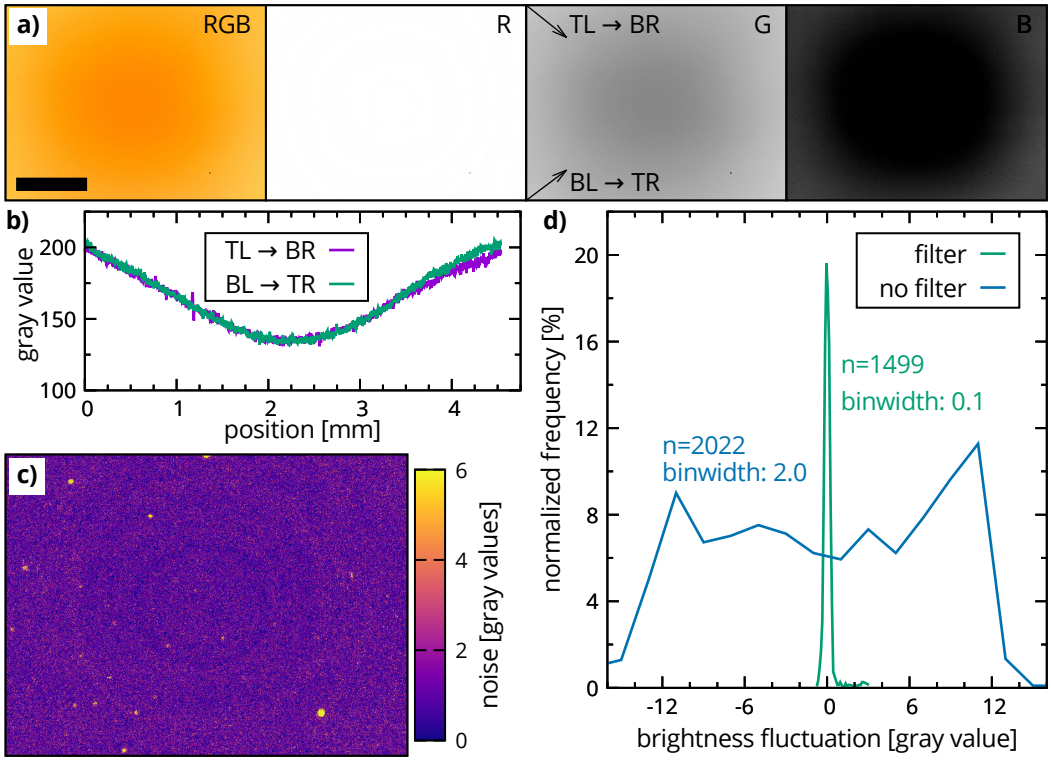

Figure 3.2: Sensor illumination **a)** RGB image and individual color channels recorded by the sensor when the LED was centrally placed 4.5 cm above the sensor. The red channel is overexposed (R), the blue channel underexposed (B), and the green channel (G) provides a reasonable dynamic range. **b)** Brightness profiles along the two diagonals of the green channel showing the increase in brightness towards the periphery of the sensor. **c)** Spatial distribution of pixel noise. The *mean* filter of ImageJ was applied with a radius of 20 pixels to the green channel. The plot shows the difference between the filtered and the original image and indicates a homogenous distribution of the noise. 99 % of the pixels deviate less than four brightness values from the mean. The bright spots are caused by dust particles on the cover glass of the image sensor. **d)** The plot shows the frequency distribution of the temporal fluctuations in brightness for one setup with and one setup without an ND filter placed on top of the image sensor, respectively. The frequency distributions were created by calculating the deviation of the mean brightness of each image from the mean brightness of the whole image series. The results show that the ND filter reduced the fluctuations by one order of magnitude.

sufficient dynamic range for cell-imaging. ***Figure 3.2 b*** shows that central illumination with the LED resulted in a non-uniform brightness profile. Surprisingly, the brightness decreased towards the central areas of the sensor and increased towards the periphery of the sensor. This pattern can be attributed to using the sensor in a lensless configuration: Lenses in cameras for the consumer market typically cause a decrease of the intensity from the center towards the periphery of the image sensor, which is known as lens shading [211]. The 1.4 µm BSI series of CMOS image sensors from OmniVision show a 20 % intensity decrease from the center to the edges when used with lenses [212]. The SOC designs of CMOS sensors for consumer electronics usually contain a built-in Image Signal Processor (ISP) unit which performs various image-processing functions such as automatic lens shading correction [213]. According to the datasheet, the ISP of the OV5640 has a built-in lens correction function, which corrects each pixel by applying a gain to compensate for the non-uniform intensity distribution caused by the lens curvature. In the absence of a lens, this built-in correction most likely causes the observed intensity distribution. ***Figure 3.2 c*** shows that the measured pixel noise is uniform over the sensor area. The averaging of three frames reduces the background noise to only a few gray values. However, when the system is placed inside a CO_2 incubator, the laser of the infrared CO_2 sensor caused fluctuations of the recorded intensities. Therefore, several setups were equipped with a custom neutral density (ND) filter consisting of 45 nm chromium evaporated onto a type I borosilicate substrate (Paul Marienfeld GmbH & Co. KG, Lauda-Königshofen, Germany). Placing this filter between the sample and the sensor reduced the recorded intensity fluctuations by one order of magnitude. In this case, a current limiting resistor of only 47 Ω was used to increase the ratio between the intensity of the LED illumination and the intensity of the background light.

Figure 3.3 shows a typical RFLM image of a sample of A549 epithelial cells in a standard culture dish and a corresponding brightfield (BF) microscopy image for comparison. The LED was centrally placed 45 mm above the image sensor, and the dish with a bottom thickness of 180 µm (μ-Dish 35mm, high; ibidi GmbH, Martinsried, Germany) was placed directly on top of the image sensor, resulting in a total sample-sensor distance of 625 µm. The comparison with the brightfield microscopy image shows that the cells are imaged as their low-coherence interference patterns. The first order intensity maximum is typically visible as a central bright spot surrounded by the first order intensity minimum. The interference patterns of cells which are rounded up, e.g., cells before and during division, usually have more interference fringes in the RFLM images than the interference patterns of cells which are spread out, where the higher order intensity maxima and minima appear washed out in the RFLM images. While minuscule morphological features of the cells are not directly visible in the RFLM images, some morphological information such as orientation, elongation, and spreading is still evident in the RFLM images. While cells in layers are hard to discern individually, isolated cells are clearly distinguishable from the background. ***Figure 3.4*** shows that the intensity variations caused by individual cells correspond to a signal to noise ratio (SNR) of approximately 10.

In summary, the combination of the presented components allows flexible usage in RFLM setups. The properties of the obtained images suggest that they contain a broad variety of phenotypic information. Furthermore, the presented findings suggest that the images facilitate the quantitative analysis of this phenotypic information with suitable image analysis.

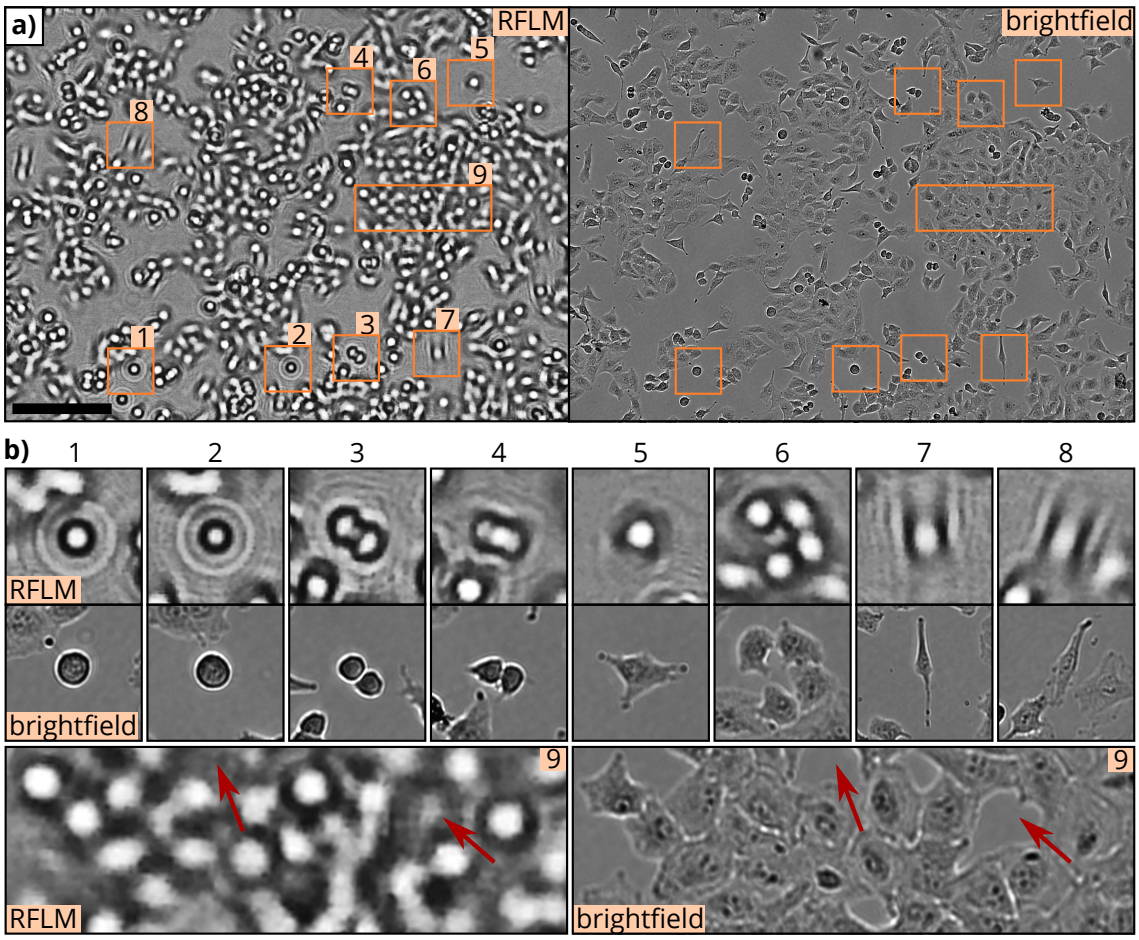

Figure 3.3: Characteristic features in RFLM images of cells **a)** Comparison between an RFLM image showing A549 cells and a corresponding brightfield microscopy image. Scale bar: 250 µm. Both images show the same section of the sample. Cells appear as their low coherence interference pattern in the RFLM image. The central maxima of the diffraction patterns are clearly discernible from the background. Unlike in the brightfield image, minuscule morphological features are not visible in the RFLM image. **b)** Enlarged RFLM and corresponding brightfield images of the regions highlighted in a). Distinct differences in cellular morphology are represented in the interference pattern. The round cells from regions 1&2 have a circular interference pattern. Cells shortly after division (regions 3&4) exhibit characteristic interference patterns which are symmetrical along the axis of cell division. Spread out cells with an aspect ratio close to one (regions 5&6) have circular interference patterns, but with fewer interference fringes as the non-spread out cells from the regions 1&2. The interference pattern of elongated cells like in the regions 7&8 are oriented along the longer axis of the cells. If the cells form a layer like in region 9, the interference patterns of the individual cells overlap, preventing a precise identification of cells. Small holes in the cell-layer are also hardly discernable in the RFLM image. However, accurate segmentation of the cells is also not feasible in the brightfield image, as some of the borders between the individual cells are not discernible by eye.

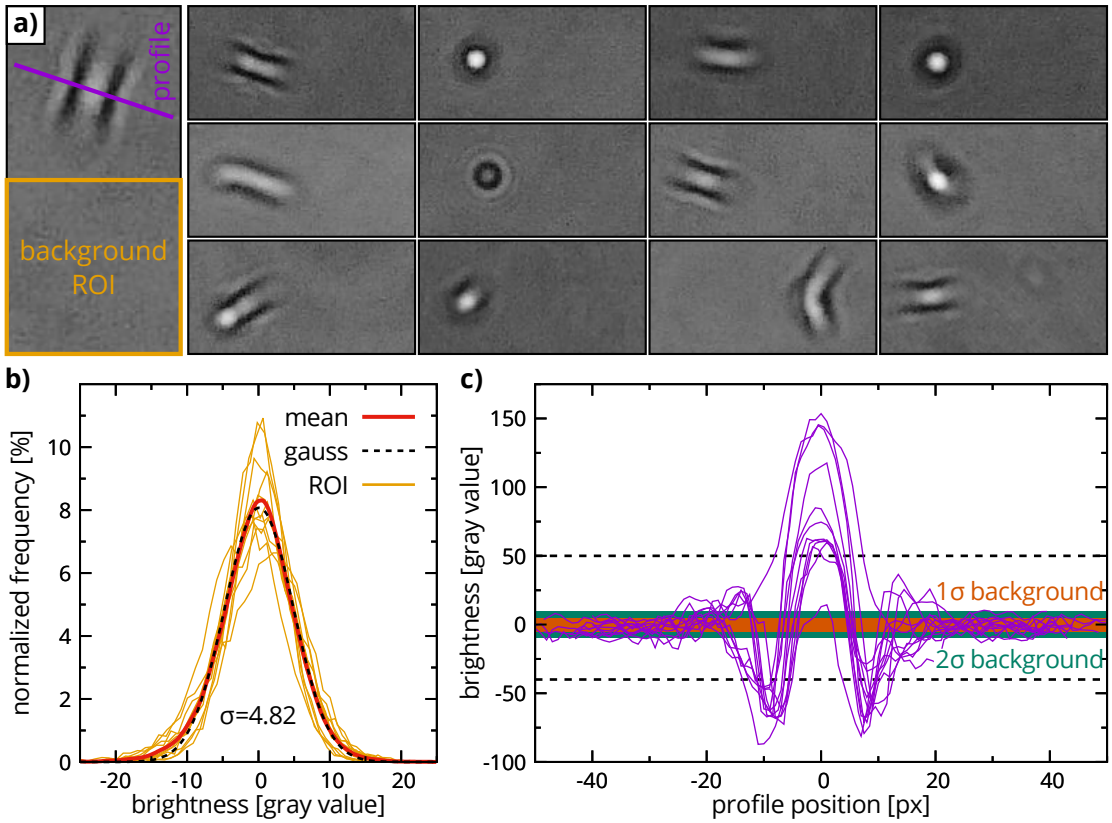

Figure 3.4: Signal to noise in the obtained RFLM images. **a)** The panel shows 12 160 pixel×80 pixel regions of an unprocessed RFLM image. Each region contains one individual NIH-3T3 cells. A 80 pixel × 80 pixel cell-free region is used to calculate the background noise in each section. For each cell, an intensity profile is determined. **b)** The plot shows the frequency distributions of the brightness in all background regions. The frequency distributions were centered around their respective mean. Calculating the mean of the frequency distributions shows that the noise is consistent with white noise and fitting it with a Gaussian gives $\sigma = 4.82$. **c)** The plot shows the brightness along the profiles through the cells together with the 1σ and 2σ intervals of the background noise. The background intensity was set to zero. The cells typically cause intensity variations of more than +50 and -40 brightness values with respect to the background intensity. These brightness variations correspond to a signal to noise ratio of $SNR_+ = \frac{50}{4.8} = 10.4$, and $SNR_- = \frac{40}{4.8} = 8.3$.

3.2 Validation Setups

3.2.1 Combined RFLM and DHM setup

For a comparison of images obtained with RFLM live-cell imaging with corresponding images captured with a reference method, here a lensless microscopy setup was designed to achieve combined RFLM and DHM image acquisition. ***Figure 3.5*** shows a schematic of the setup, which consists of an RFLM unit and a lensless DHM unit. A motorized XYZ-Scanning stage (Prior H101P1F, FB206, PS3H122R, H31, Prior Scientific, Inc., Rockland, USA) allows automated translation of samples between the RFLM and the DHM unit. The whole setup was placed inside an incubator (Binder KB115, Fa. BINDER GmbH, Tuttlingen, Germany) to keep

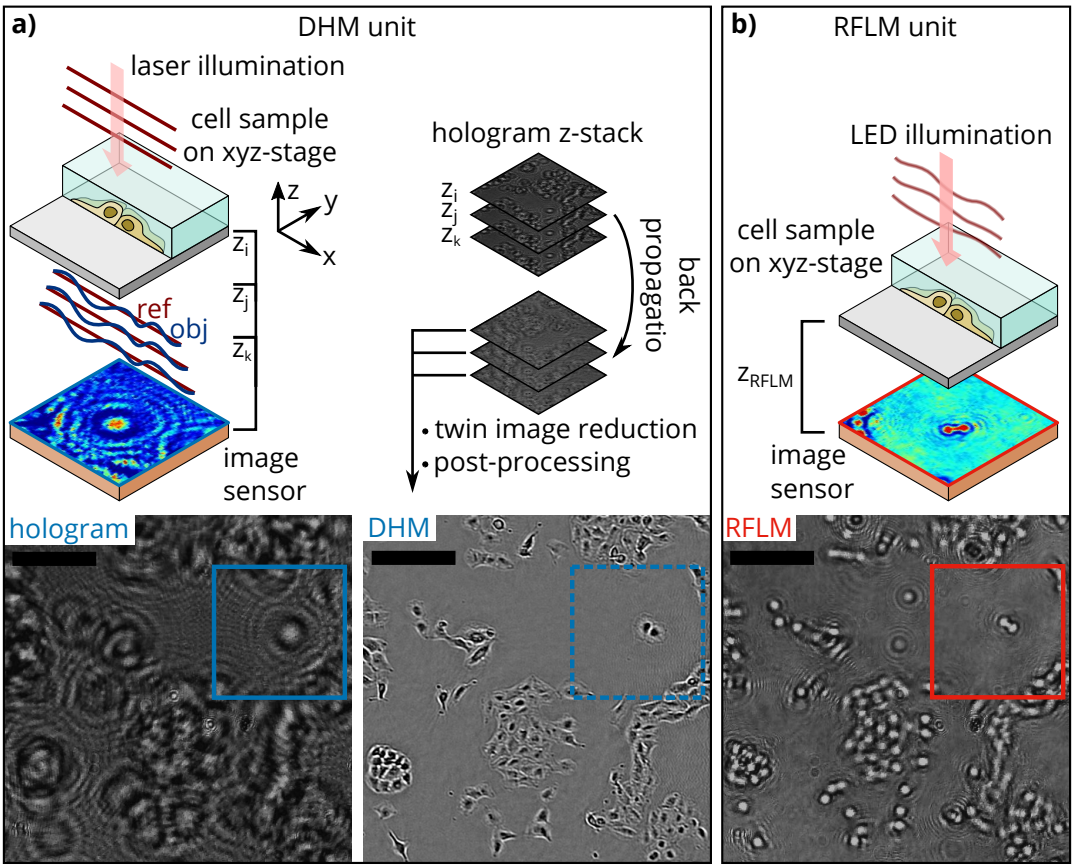

Figure 3.5: Setup for combined RFLM and DHM acquisition. **a)** DHM unit: A sample of cells is mounted on a motorized XYZ-Stage and illuminated with coherent light from a laser. The image sensor records the hologram. The stage is used to record a stack of holograms at various sample-sensor distances $\{z_i, z_j, z_k\}$. The bottom panel shows a section of a recorded hologram of A549 cells (Scale bar: 200 µm). For each hologram, an in-focus image is reconstructed computationally. The in-focus images are averaged to remove twin image artifacts. The result is then post-processed to obtain the DHM amplitude image, shown at the bottom. **b)** The stage moves the sample to the RFLM unit. Here, a LED illuminates the sample with partially coherent light, and the image sensor records the RFLM image of the cells. The image in the bottom shows the recorded RFLM image. It can be seen that the imaged region is the same as in the DHM amplitude image shown in a).

the sample at 37 °C. The image acquisition interval for the time-lapse experiments with this setup was 90 min for each of the two imaging units. The acquired DHM amplitude images and RFLM images show the same region of the sample, thus allowing a direct comparison between the images.

DHM acquisition: A diode laser (Coherent CUBE 405-100C, Coherent Inc., Santa Clara, USA) with a wavelength of 405 nm was used as the light source. An ND filter was used to reduce the intensity of the laser beam to an energy density of less than 40 nW mm^{-2} on the cell sample. The sample was mounted on a XYZ-scanning-stage (Prior H101P1F, FB206, PS3H122R, H31, Prior Scientific, Inc., Rockland, USA) to acquire holograms at different heights. For each image, 70 holograms were acquired with the sample-sensor distance being equidistantly varied from 2.7 mm to 12.7 mm. This sample sensor distance includes the cover glass of the sensor

as well as the bottom of the cell culture container. From each hologram, an in-focus image of the sample was reconstructed with a python program using the implementation of the angular spectrum method described by Poon and Liu [151]. The reconstructed in-focus images were averaged to reduce twin image artifacts. A highpass bandpass filter (*ImageJ*) and nonlocal means denoising (*openCV*) were applied to the averaged image to obtain the final image.
RFLM acquisition: The RFLM unit consisted of the camera and the 610 nm wavelength LED. The automated stage allowed a variation of the distance between the sample slides bottom and the image sensor of 18 mm. The distance between the LED and the sample could also be varied between 35 mm and 70 mm.
The setup and associated computational methods are described in greater detail in [214].

3.2.2 Combined RFLM, Brightfield, and Fluorescence Microscopy

For the acquisition of further RFLM image sequences that are complemented with additional external reference information, a conventional fluorescence microscope was modified to allow imaging samples with RFLM and fluorescence microscopy simultaneously. To this end, one of the customized camera boards was mounted on an objective of a Nikon Eclipse TI microscope (Nikon Corporation, Tokyo, Japan). The microscope has a custom-built heating box to keep the samples at 37 °C. The objective revolver was controlled with the NIS-Elements software to automatically switch between the objective with the CMOS sensor and a CFI Plan Fluor DL 4x objective for fluorescence as well as brightfield image acquisition, see also ***Figure 3.6***. Fluorescence, brightfield, and RFLM images were acquired every 10 min. Brightfield/fluorescence and RFLM micrographs were scaled and aligned with a custom program based on *openCV*. The user marked pairs of corresponding points in the different micrographs. The program then calculated the rotation and scaling between the two images, used a quadratic minimization to determine the translational shift, and subsequently superimposed the coinciding image regions.

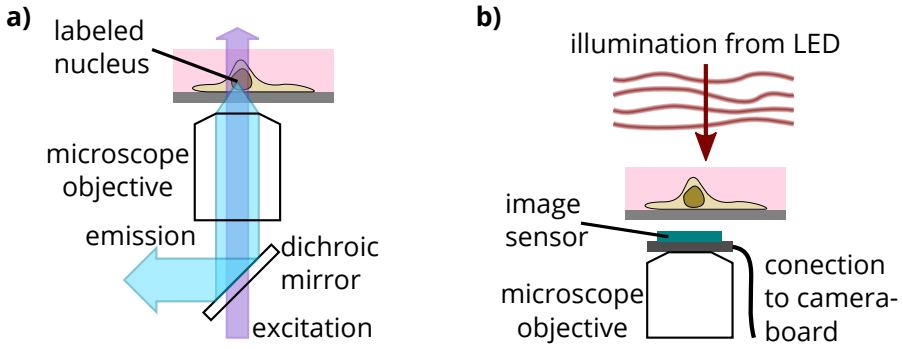

Figure 3.6: Combined RFLM, brightfield, and fluorescence acquisition. Automated control of the microscope objective revolver allowed to image the same section of the sample in fluorescence mode, as schematically shown in **a)**, and RFLM mode, as schematically shown in **b)**. To this end, the image sensor of the camera was mounted on top of a dummy microscope objective.

3.2.3 Setup for Scanning Culture Flasks

To image larger substrate areas such as the complete area of T75 culture flasks, an image sensor was mounted on an x-y linear translation stage (C-Beam Linear Actuator Bundle; Openbuilds, Monroeville, USA). The stage has a 8 mm lead screw which is rotated by a stepper motor (ST5909X2508-B; Nanotec Electronic GmbH & Co. KG, Feldkirchen, Germanys) with a step angle of 0.9°, resulting in a linear step size of 20 µm. This step size corresponds to 0.5 % and 0.7 % of the size of the image sensor in x and y-direction, respectively. For scans of entire culture flasks, the stage translated the image sensor in an S-shaped pattern in multiples of the dimensions of the imaged area to obtain images of the whole substrate area, as shown in ***Figure 3.7***. For flasks with a non-rectangular bottom, the angled outlines were imaged by translating the image sensor by an offset of half the size of the image area. The acquired images were then tiled into their quadrants. The centers of these tiles form a rectangular grid with a period of 1.84 mm and 1.37 mm, respectively.

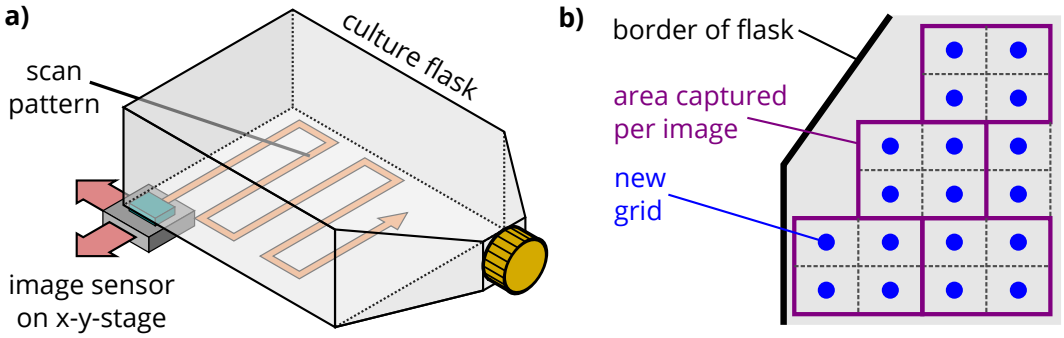

Figure 3.7: Flask scanning setup **a)** Acquisition scheme: The image sensor is mounted on a motorized x-y-stage which moves the sensor beneath the culture flask in an S-shaped pattern. The step sizes were set to be equal to the dimensions of the image (an offset of a half step can be applied to image an angled area like in b)). After a target position is reached the camera acquires an image and moves to the next position. **b)** Each image is cut into four quadrants (indicated with gray lines). The centers of the quadrants now form a rectangular grid. This allows creating a map of the flask, by assigning each position of the grid a quantity determined by analyzing the corresponding quadrant image, e.g., the confluency. Hence, the flask is sampled with half the dimensions of the active area of the image sensor with respect to the corresponding directions.

3.3 In-Situ Live-Cell Imaging Setups

Live-cell imaging requires a system for environmental control to provide optimal conditions for the cells. To this end, the compact RFLM setups have the advantage that they can be placed inside standard CO_2 cell culture incubators. ***Figure 3.8*** shows the regulation of CO_2, temperature, and humidity inside a standard incubator (Incumed 246; Memmert GmbH + Co.KG, Schwabach, Germany) in response to the change in environmental conditions caused by opening the door of the incubator. For this purpose, three temperature sensors with a resolution of 0.034 °C and an accuracy of ±0.1 °C (TSIC 506; B+B Thermo-Technik GmbH,

Donaueschingen, Germany) measured the temperature. After data recording, the measured values of each sensor were corrected so that the mean temperature after equilibration matched the set-temperature of the incubator. The CO_2 concentration was measured with an MH-Z16 infrared CO_2 sensor (Sandbox Electronics, Liaoning, China). Relative air humidity (RH) was measured with three different humidity sensors with a resolution of 0.1 %RH and an accuracy of ±2 %RH (DHT22; Aosong Electronics Co.,Ltd, Guangzhou, China). The measured relative humidity of the sensors in the incubators was corrected so that the mean humidity after equilibration matched the relative humidity of 95 % displayed by the incubator. These results demonstrate that the incubator provides a sufficiently stable environment for live cell imaging, even if the door is occasionally opened. However, care might be necessary if the measurement is sensitive to variations caused by a temporally decreased humidity.

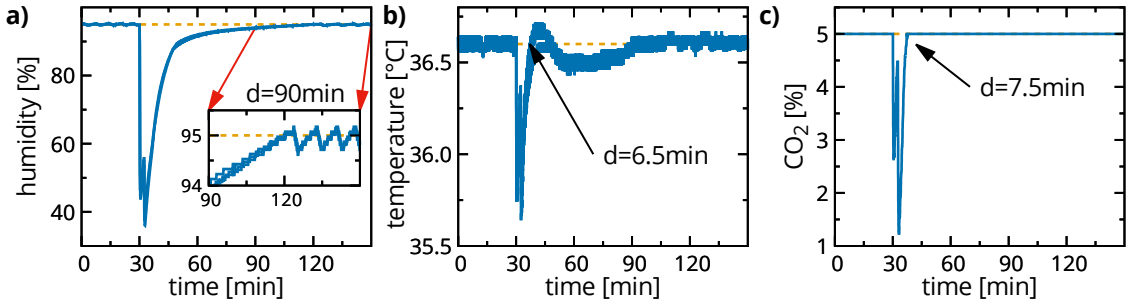

Figure 3.8: Control of environmental conditions for live cell imaging inside a standard CO_2 incubator. The graphs show the progression of environmental parameters in response to opening the door twice (at around 30 min) in three minutes, corresponding to a typical event in cell culture, e.g., taking a flask out of the incubator for experiments. **a)** shows the relative humidity, measured by three humidity sensors. The humidity fell below 50 % after opening the door. The incubator needed about 90 min to restore the humidity to 95 %. The inset shows the periodic variations in the humidity due to the heating cycles of the incubator. **b)** shows the temperature, measured by three temperature sensors. The temperature drop caused by the door opening was less than 1 °C. While the incubator restored the initial temperature in about 6.5 min, the response overshot by about 0.1 °C and stable temperature levels were reached after 60 min. **c)** shows the CO_2 levels, measured by one sensor. The CO_2 concentration dropped from 5 % to 2 % following the opening of the door. The incubator regulated the CO_2 concentration back to a stable level of the initial concentration in 7.5 min.

3.3.1 Setup for Cell Culture Monitoring in Flasks

Achieving a continuous measurement of critical phenotypic parameters of cells during culturing with RFLM required the development of setups that allow the acquisition of time-lapse image series of cells growing inside standard culture flasks. ***Figure 3.9*** shows two types of RFLM setups that were designed for this purpose and used for monitoring cells growing inside culture flasks directly inside the incubator. The distance between the sample and the LED was 45 mm for both setup types. In the first setup type, the flasks were placed directly on top of the image sensor, whereas in the second setup type, a chromium ND filter was placed between the bottom of the flask and the image sensor. The horizontal dimensions of the setups were determined by

the size of the sample container. ***Figure 3.9*** illustrates that the size of the setups is comparable to the size of the cell flask, showing that RFLM allows extremely compact instrumentation.

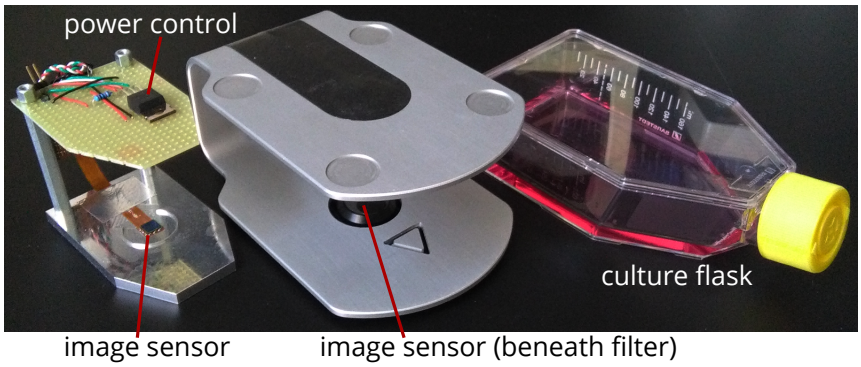

Figure 3.9: RFLM Setups for the continuous monitoring of cell cultures inside standard cell culture flasks. The left side shows a setup without an ND filter. The transistor to control the power supply of the camera can be seen on top of the setup. The middle shows a setup type using an ND filter. The right side shows a T75 culture flask for size comparison.

3.3.2 Setup for 8-chamber Slides

Since the previously presented setups were only capable of measuring one sample per setup, the next goal was to build RFLM setups with increased throughput and the capability to perform parallelized measurements. To this end, an RFLM setup for imaging cells inside the chambers of an 8-chamber slide was built. This setup is equipped with eight cameras and shown in ***Figure 3.10***. The cameras were connected via three USB hubs (975100 4 Port USB 2.0-Hub; Conrad Electronic SE, Hirschau, Germany) to the PC. The power supply of each camera was controlled individually via transistors and an Arduino microcontroller. For imaging one of the chambers of the slide, only the camera corresponding to that chamber was switched on for the image acquisition. An LED was placed with a vertical distance of 45 mm centrally over each camera. The cameras were arranged in a pattern such that each camera was able to image a part of the area of one of the chambers of an 8-chamber slide. The flexibility of the RFLM components offered the possibility to add further features to the setup in a convenient fashion. Several of the 8-chamber slide setups were equipped with additional LEDs for experiments with photoswitchable molecules. Therefore, eight LEDs with a wavelength of 380 nm (RLS-UV380; Roithner Lasertechnik GmbH, Vienna, Austria) were placed next to the red LEDs that were used for imaging. An Arduino microcontroller switched the additional UV LEDs of and on and ensured that they were switched off during image acquisition.
It is critical for live-cell imaging that the system provides a constant stable environment for the cells [215]. A custom build 8-chamber slide was used to assess the effect of the image sensors on the environment inside the chambers of the slide. One TSIC 506 temperature sensor (B+B Thermo-Technik GmbH, Donaueschingen, Germany) was attached to the bottom of each chamber. This temperature measurement slide is shown in ***Appendix Figure 2.2***. The chambers were filled with deionized MilliQ-Water to measure the temperature in each chamber with high precision under realistic conditions. One of the eight temperature sensors was read

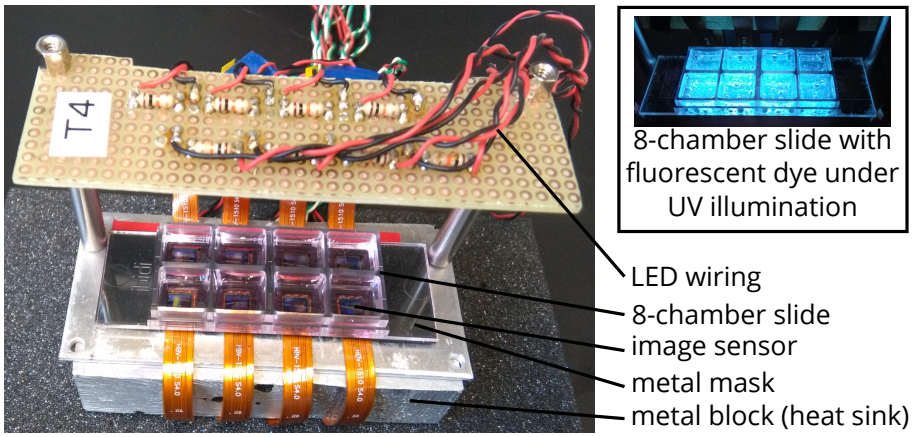

Figure 3.10: Setup for parallelized live cell imaging using 8-chamber slides. The slides were placed on top of a metal mask which contained the image sensors and provided a level surface. One image sensor and one LED were placed beneath and above each sample chamber, respectively. The photo shows a metal block attached to the bottom of the setup, which served as a heatsink. Right panel: The 8-chamber slide setups can be easily equipped with further LEDs for illumination of the samples with additional wavelengths, which was used in experiments with photoswitchable molecules. The photo shows an 8-chamber slide filled with a solution containing quinine, placed on the setup, and illuminated with eight UV LEDs. The bright fluorescence light demonstrates that the UV LEDs provided sufficient excitation illumination.

out every 200 ms, resulting in a sampling of 1.6 s for each temperature sensor. The incubator (Incumed 246; Memmert GmbH + Co.KG, Schwabach, Germany) was set to a temperature of 36.6 °C to counteract the heating due to the cameras. The slide was placed on the setup, and after thermal equilibration, the temperature was measured over a 12 h interval while the setup was in an inactive state. The temperature sensors were calibrated to the incubators set-temperature by applying a constant offset. Subsequently, image acquisition was started with an imaging period of 4 min for each position. Image acquisition was distributed temporally equidistant between the sensors, meaning that every 30 s a different sensor acquired an image. ***Figure 3.11*** shows that the average temperature increase due to the setup was about 0.2 °C, which can be compensated for by adjusting the incubator set-temperature. During image acquisition, the temperature sensor in the corresponding chamber measured a heat spike, which subsequently subsided. After about 30 s the heat was mostly dissipated and the temperature had reached almost the pre-acquisition level. The average peak of the temperature with respect to the average temperature was (0.24 ± 0.06) °C. This temperature variation is in the same range as the overshoot of the temperature by the incubator, which was measured after opening the incubator door (***Figure 3.8***). Except for temporary temperature increases caused by camera errors, the maximum measured temperature was less than 37.2 °C. While the exact effect of the periodic temperature variations on cellular behavior might require further study, these results demonstrate that the setup meets the stability requirements for live cell imaging.

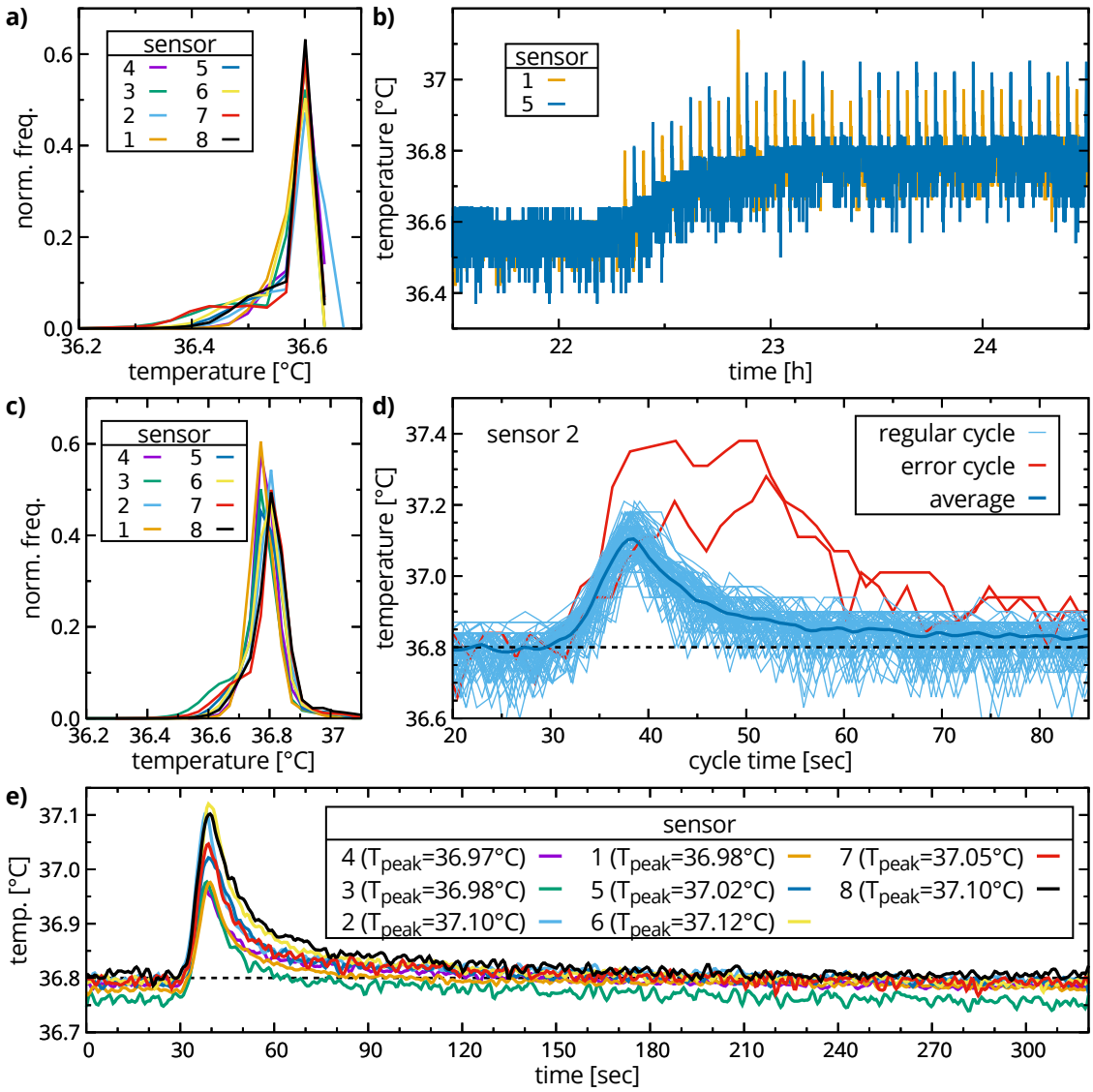

Figure 3.11: Temperature in the 8-chamber slide setup. One TSIC temperature sensor was integrated into each well of an 8-chamber slide to assess the temperature development during live-cell imaging. **a)** The offset of the T-sensors was set such that the median temperature matched the set-temperature of 36.6 °C of the incubator. The plot shows the frequency distribution of the measured temperatures for each T-sensor. The temperature was measured after thermal equilibration over a 12 h interval while the setup was inactive. **b)** Subsequently, at t=22.3 h, image acquisition was started. The plot shows the development of the temperature in two of the chambers. The average temperature increased after image acquisition. Furthermore, sharp spikes can be seen in the plot, corresponding to a temporary increase in temperature when the respective camera acquired an image. **c)** Frequency distributions of the temperature for the eight sensors after image acquisition was started, measured over a 12 h interval, beginning at t=24 h. The average temperature was about 36.8 °C, hence about 0.2 °C higher than the set-temperature of the incubator. **d)** The plot shows the temperature development during 100 acquisition cycles for Sensor 2 and the mean of these curves. The image acquisition caused a temperature-peak of about 0.3 °C, which decayed in about 30 s. An increased generation of heat was measured in a few cycles, when the camera experienced errors during image acquisition. **e)** The plot shows the average temperature of 100 acquisition cycles in all eight chambers. For the largest part of the acquisition cycle, the temperature was equal to the average temperature of 36.8 °C. The average peak height with respect to the baseline temperature of 36.8 °C was (0.24 ± 0.06) °C.

3.3.3 Setup for Multiwell Plates

To increase the throughput with respect to the previously presented 8-chamber slide setup the next goal was to build a setup that allows in situ measurements with standard multiwell plates. Therefore, four image sensors were mounted on a linear translation stage. The image sensors were aligned in a line, see ***Figure 3.12***. The distance between the cameras was the same period as the distance between the wells of the 24-well plates in row-direction. Two different linear translation stages were used for this setup type. The first linear translation stage has a resolution of 1.3 µm (ET-150-12; Newmark systems, inc., Rancho Santa Margarita, USA). The second linear translation stage (C-Beam Linear Actuator Bundle; Openbuilds, Monroeville, USA) used an 8 mm lead screw which was rotated by a SKU 518 stepper motor (Openbuilds, Monroeville, USA) with a step angle of 1.8°, resulting in a linear step size of 40 µm. The six rows of wells of the plate were imaged consecutively by moving the row of sensors along the column direction of the 24-well plate. The stage needed less time to move from one acquisition position to the next than the 5.2 s required by *fswebcam* to acquire an image. Therefore, the *opencv* API for cameras is used to control the cameras and to acquire the images in the live-stream mode to reduce the total time required for imaging all wells. The power supply of each camera is only switched on during the acquisition of images in the corresponding row. While it is in principle possible to acquire images for all rows simultaneously, the rows of the plate were imaged in serial. Simultaneous streaming of all four cameras would require specialized hardware capable of handling the high data transfer rates. Furthermore, a multithreaded acquisition program would be required for storing the images from the different live-streams. However, the setups still provided sufficient time-resolution since the time needed to image all wells was only a few minutes. A more detailed description of the system can be found in [216].

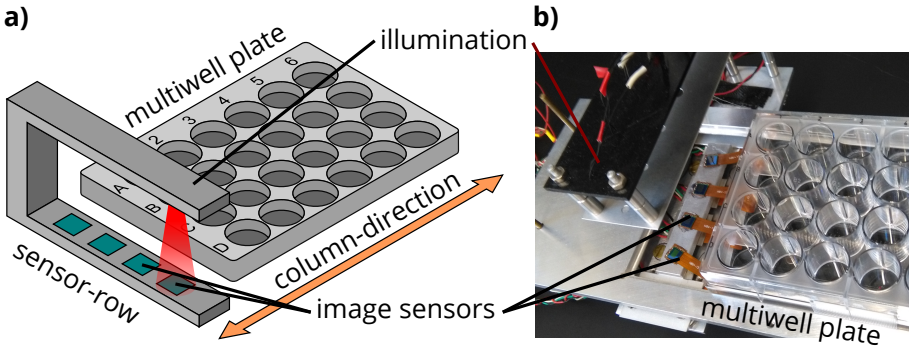

Figure 3.12: Schematic (a) and photo (b) of a setup for in situ RFLM imaging of cells in 24-well plates. Four image sensors were attached in a row on a support, which was mounted on a motorized linear translation stage. The stage translated the sensor-row beneath the 24-well plate along the column-direction, thus allowing all wells to be imaged. Once an acquisition cycle is completed, the camera row is moved to the side from the 24-well plate to avoid unwanted heating of the sample from underneath.

4 Image-based Metrics for Phenotypic Profiling and Monitoring of Cells

4.1 Introduction

In vitro experiments using cultured cells are an invaluable tool in cell biology and medical research to study cell behavior and physiology and to explore biochemical networks in cancer and drug development. As presented in ***Section 2.1***, cultured cell lines provide cellular model systems that facilitate conducting experiments in a controlled environment, in contrast to studies in the complex *in vivo* environment. Results obtained from clonal cell lines are expected to provide consistency and reproducibility. Cells are cultured in the same medium, serum, and supplements, to ensure the persistence of characteristic traits of the cell lines. Over the last decades, however, awareness arose that cells undergo changes even in stable culturing conditions due to intrinsic factors, and that characteristic traits of cell lines can change over the culturing period. Even in clonal cell lines, the culturing history plays a pivotal and sometimes underestimated role [31, 33, 34, 51, 60].
These changes can be caused by genetic and epigenetic instability and drift, as well as by phenotypic instability. Significant genetic and epigenetic instability has been reported in the case of cultured stem cells [35, 36], and an increased genetic instability is characteristic for cancer [37] as well as for transformed cell lines [18]. This genetic instability leads to genetic heterogeneity even in initially clonal populations. The genetic changes are subsequently subject to genetic drift, i.e., the differential selection of subpopulations from the genetically heterogeneous population. This drift can cause a stem cell culture to be overgrown with abnormal, culture-adapted cells that exhibit a decreased differentiation capacity [36]. Serial passaging and selective pressures can result in significant phenotypic changes like morphology, growth rate, growth pattern, and adherence [217, 218] up to the point where a cell line no longer resembles the original cell line [27] and experimental results become hard to compare [32, 33]. Phenotypic changes of cells in culture are often related to dedifferentiation and are - unlike genetic changes - often reversible [219]. It has been reported that significant phenotypic drift can occur even during as few as four passages in cultured tenocyte cells [220].
The culture conditions [39] and the subculture routine [40] are critical extrinsic factors of the selection pressure that the genetically heterogeneous cellular populations are exposed to. The cellular microenvironment is another sensitive factor, as high confluencies and cell densities can

select cells with a decreased contact inhibition of proliferation [41] or increased growth rates [221]. Confluency and plating density also impact cell differentiation [42] and proliferation potential [222], as well as cellular phenotype [43, 44] and the heterogeneity of phenotypes [38]. In general, the population context of a cell affects phenotypic parameters such as proliferation, cell shape, and motility. Vice versa, the behavior of the individual cells resulting from these parameters defines the population context for the other cells, forming nonlinear feedback mechanisms with intrinsic stochasticity [223].

With the intention of addressing these issues and enhancing reproducibility, efforts are currently increasing in biomedical research to establish standardized and optimized protocols and quality control (QC) in cell culture [48, 52, 224–227]. For this purpose, a comprehensive genomic, proteomic, and phenotypic analysis can in principle be used for a complete cell line characterization, consequently allowing the assessment of genotypic as well as phenotypic drift and heterogeneity. However, this elaborate analysis is currently considered too costly for this purpose. As an invasive end-point measurement, this approach also provides no information on the cellular microenvironment - such as confluency - in the culture. Current best practice recommendations in cell culture include the routine visual inspection of the cell cultures with an optical microscope to assess morphology, signs of possible contamination, and the current growth phase, e.g., sparse, subconfluent, confluent or dense. Keeping photographic records of the inspected cultures is suggested to detect morphological changes over time. Cells ought to be counted to determine growth rates, which is usually performed manually using a hemocytometer, and the resulting PDT information along with the passage numbers should be tracked and included in reports [18, 52, 227]. However, such a manual visual examination of cell cultures is perturbative, subjective, misses dynamic parameters such as the motility entirely, and can only provide information for one specific time-point.

These examples broadly demonstrate the need for a method that is complementary to a full genomic and proteomic analysis and allows the non-invasive, continuous, and quantitative determination and tracking of critical phenotypic parameters during culturing for ensuring the consistency of cell line characteristic traits, for cell culture QC and optimization as well as for an assessment of cell culture health. One reason, why a phenotypic analysis during the culture period is still unusual in conventional experiments, is the lack of suitable monitoring equipment that is compatible with standard cell culture containers and CO_2 incubators.
In the last years, however, enormous progress has been made both on the instrumental as well as on the computational side. Phase contrast microscopy and QPI combined with image analysis provide non-invasive, label-free, high-throughput methods for an automated determination of cell count, proliferation, motility [53–55], cell morphology [56], and colony morphology [57]. Hence, these techniques in principle provide tools for cell culture QC [58–62]. However, conventional light microscopes are bulky, and thus, their capability for monitoring many cell cultures in parallel within an incubator is limited. These microscopes can be miniaturized to a certain degree [228, 229]. However, this comes at a trade-off due to the relationship between resolution, the FOV and the geometry of the optical components. Unconventional microscopy techniques can circumvent this restriction [230], but ultimately, the dimensions of the lenses pose a limit for miniaturization.

As detailed in ***Section 2.2.3***, LM has emerged as a versatile alternative imaging technique in this context. Since LM foregoes the use of lenses entirely, it allows extremely compact instrumentation and has consequently been used for applications like label-free live-cell imaging

inside standard CO_2 incubators. Further advantages of LM include a wide FOV and being cost-effective. In ***Chapter 3*** it was shown that the RFLM setups developed in the context of this thesis are exceptionally compact and compatible with standard cell culture containers and incubators. Furthermore, it was shown that the acquired images contain a broad range of phenotypic information. The presented setups provide the advantage of experimental simplicity and reduced computational cost since no in-focus image is reconstructed.
This chapter presents image analysis methods to obtain a multitude of image-based metrics for a quantitative phenotypic cell-analysis that can be used for multiparametric cell line monitoring and to determine distinct phenotypic profiles for different cell lines. These image analysis methods for RFLM were developed to be capable of simultaneously determining the key culture parameter confluency as well as the critical phenotypic parameters proliferation, motility, and cell-clustering over an extensive range of culture conditions. Several different image-based metrics are calculated, and the results are compared with conventional DHM, brightfield microscopy, and fluorescence microscopy to validate the accuracy of the approach. Furthermore, the broad potential of the technique for cell culture QC applications and phenotypic cell line profiling is shown. The technique is used to monitor proliferation and motility of different cell lines during subculturing. Parallelized measurements of cells from several different cell lines in 8-chamber slides are performed to use the image-based metrics to determine a unique phenotypic profile for each cell line.

4.2 Cell Covered Area

The detection of the cell covered substrate area does not only allow the determination of the confluency but also the calculation of metrics for cell cluster morphology and clustering dynamics. Therefore, this section presents image analysis methods for the automatic detection of the cell covered substrate area in RFLM images. However, the RFLM images only contain the low coherence interference of the cells. The first step of the subsequently presented solution is the automatic detection of the foreground area in the RFLM images, i.e., the area corresponding to intensity variations caused by the cells. The setup capable of acquiring both RFLM as well as DHM images that was presented in ***Section 3.2.1*** is then used to record time-lapse image series of growing cell cultures of different cell lines for the second step. The automatically determined RFLM foreground area in these image series is related to the real cell covered substrate area determined in the corresponding DHM images to obtain a relation between the two areas. This relation finally allows the determination of the cell covered substrate area from the detected RFLM foreground area alone.

4.2.1 Area Detection Algoritms

To detect the foreground area in the RFLM images, as a first step, a custom computer program converts the raw color images into grayscale images, applies a correction for the inhomogeneous brightness distribution, and then enhances the contrast. ***Appendix 3.1*** describes the details of this preprocessing procedure and the implementation. A computer program written in C++ was developed to subsequently determine the RFLM foreground area in the preprocessed images. The program uses the open computer vision library *OpenCV* (version 2.4 [231]). The algorithm

is based on applying a combination of geometrical filters to the RFLM image to obtain a raw foreground mask and subsequent post-processing of this foreground mask. ***Figure 4.1*** illustrates the different steps of the algorithm. In addition to the geometric filters, the algorithm also takes temporal aspects of growing cell populations into account. For each frame, the following masks are calculated after the application of the *GaussianBlur* function for a reduction of pixel noise:

M1 The spatial variance within a kernel of variable size is calculated. This variance map is converted into the binary mask M1 with the *adaptiveThreshold* function.

M2 The spatial gradient is calculated with the *Sobel* function in x and in y direction. This gradient map is converted into the binary mask M2 with the *threshold* function.

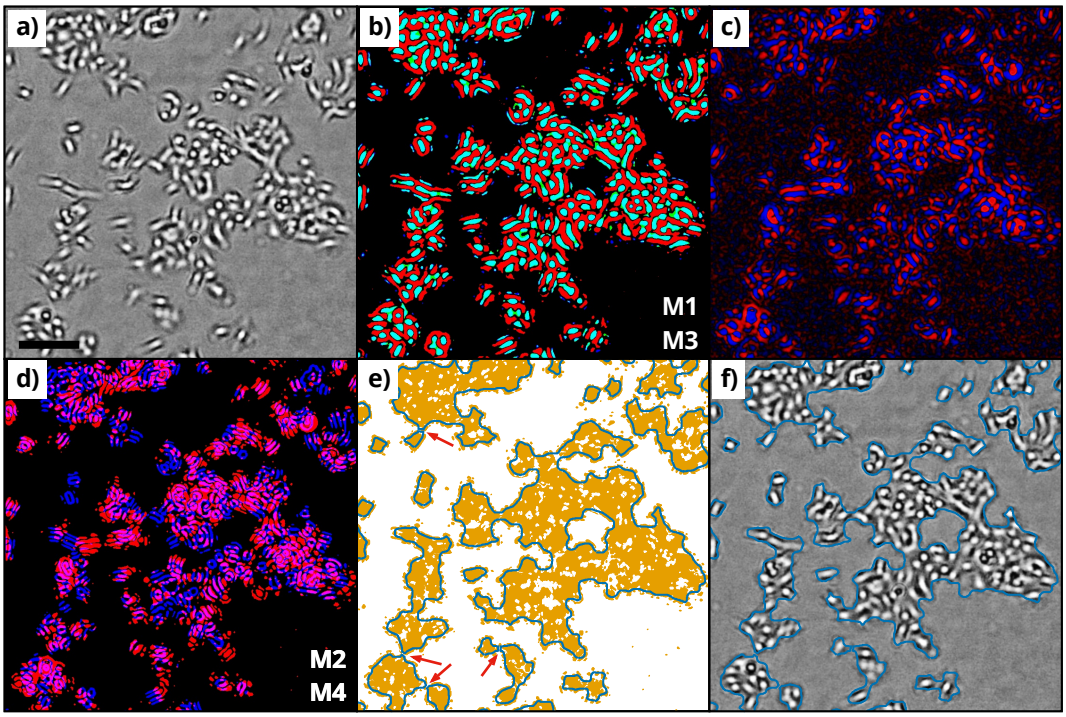

Figure 4.1: Automated foreground detection in RFLM images. **a)** shows a section of an RFLM image. Scale bar: 200 µm. **b)** The image shows the result of the geometrical filters applied to the image section from a). Areas drawn in green/red correspond to pixels with gray values above/below the threshold from mask M3. Areas drawn in blue correspond mask M1. If more than one condition is fulfilled for a pixel, its color corresponds to the superposition of the respective colors. **c)** The image shows the temporal activity map of the sample, corresponding to the net gray value loss (blue) and gain (red) calculated over several frames (see text for details). **d)** The image shows the binary masks M4 (red channel) and M3 (blue channel), calculated for the image section from a). **e)** The masks from b) and d) are combined with *bitwise_or*, which gives the yellow area. This area is post-processed by filtering out isolated areas below a certain size, filling holes, smoothing the outlines, and applying a watershed segmentation. The blue lines show the outlines of the final result of the foreground area. The red arrows highlight were blocks of foreground area were disconnected by the watershed segmentation. **f)** Shows the raw image from a) with the outlines of the detected foreground area drawn as blue lines.

M3 The binary mask M3 is calculated by selecting pixels with gray value levels above and below a chosen threshold with the *adaptiveThreshold* function.

M4 Temporal activity: for every frame, a stack containing the frame itself and its n successive and n previous frames is built. For each pair of consecutive frames in this stack, the pixel-wise gray value difference is calculated to obtain a stack of difference-maps. Then the pixel-wise sum of all difference maps is calculated. This sum is then converted into the binary mask M4 by applying the function *threshold* to the absolute value of the sum.

For each of the masks M1-M4, background noise is reduced with a morphological opening. The masks M1-M4 are then combined with *bitwise_or* to the foreground mask of the frame. The time evolution of the growing cell patches is taken into account with the following procedure:
A moving average foreground map of the final foreground masks of the individual frames is calculated with the *accumulateWeighted* function. This moving average foreground map is converted into a binary mask with the *threshold* function. This mask is shrunk with a morphological opening operation and subsequently added with *bitwise_or* to the foreground mask of the current frame.
To obtain the final foreground mask for the current frame, the following post-processing steps are applied:

- Connection of foreground areas: The function *distanceTransform* is applied to the inverted foreground mask. If the distance of a background pixel to the closest foreground pixel is below a given threshold, then its value in the inverted mask is set to zero. Subsequently, a morphological dilation with a kernel size equivalent to the distance transform threshold is applied to the inverted mask. Finally, the inverted mask is inverted back again.
- removal of background and closing of holes: foreground areas with an area below a given size are removed from the foreground mask. If the foreground area has "holes" with a size below a given threshold, they are closed by setting the value of the corresponding pixels to one.
- smoothing of borders: The function *Gaussian Blur* is applied to the foreground mask, followed by application of the *threshold* function.
- watershed segmentation: The segmentation is performed with the *watershed function*. The seeds for the segmentation are determined by applying a morphological erosion to the foreground mask. The kernel for the erosion is chosen to match approximately half the size of the foreground area corresponding to a single cell.

The result in ***Figure 4.1 f*** shows that the presented image analysis is capable of distinguishing the RFLM foreground area from the background. Likewise, a second similar algorithm[1] was used for the automatic detection of the cell covered substrate area in the DHM images. In the following, the accuracy and the performance of the algorithms are assessed in more detail. Therefore, three researchers with several years of experience in cell culture used the program GIMP to manually and independently segment the foreground area A_{FG} in seven RFLM micrographs and their seven corresponding DHM micrographs. As shown in ***Figure 4.2***, if two out of three researchers segmented a pixel as foreground, it was considered ground truth (GT)

[1]Described in more detail in the master's thesis of Pärr [214]

foreground area A_{GT}. The micrographs used for this purpose were taken from a time-lapse measurement of HeLa cells growing from less than 10 % to 100 % confluency. Subsequently, A_{GT} was used to determine the relative error of the area detection by the algorithms as a function of the detected foreground area A_{FG}. The relative error of both algorithms is less than 8 % for

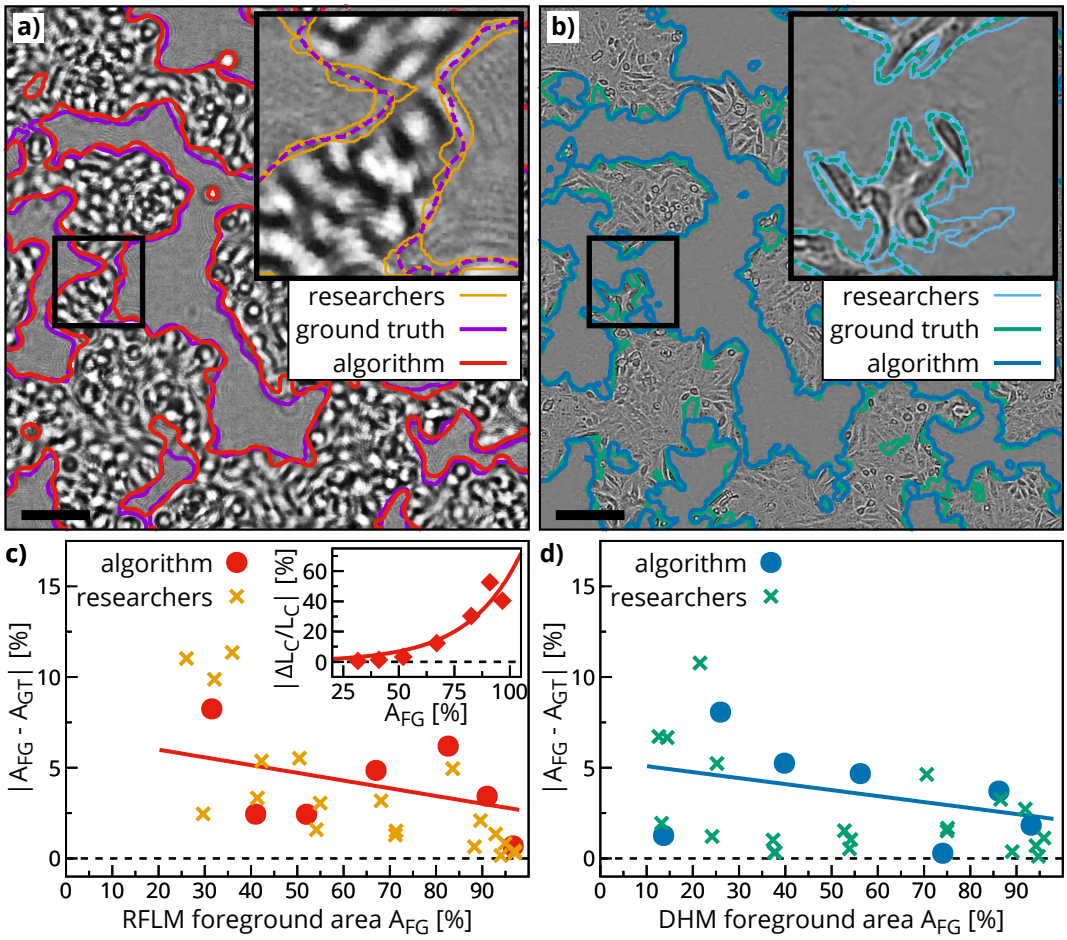

Figure 4.2: Determination of the error of the automated area detection. **a)** shows a 1024x1024 pixel section of an RFLM image of HeLa cells. The outlines of the automatically detected foreground area A_{FG} and the ground truth foreground area A_{GT} are drawn as lines. Inset: enlarged view of the highlighted region, illustrating the manual segmentation by the individual researchers and the resulting A_{GT}. Scale bar: 200 µm. **b)** shows the DHM image of the region shown in a) and illustrates the results of the corresponding segmentation analogously to a). Scale bar: 200 µm. **c)** The graph shows the absolute value of the relative difference between A_{FG} and A_{GT} plotted against A_{GT} for the RFLM images. The data is from seven manually segmented images and shows the performance of the algorithm as well as the individual researchers with respect to the ground truth. The performance of the algorithm is comparable to the performance of the researchers. A linear fit to the data is used to determine the relative error of the algorithm. The inset shows the absolute value of the relative error of the contour length of the outlines of the RFLM foreground area detected by the algorithm plotted against A_{GT}. An exponential fit to the data is used to determine the relative error of the contour length. Note that the absolute error of the contour length approaches zero as the foreground area approaches 100 %. **d)** shows the same plot as in c) for the detection of the area in the corresponding DHM images.

all measured values of A_{FG}. Furthermore, the relative error of the manual segmentation by the individual researchers with respect to the GT foreground areas was calculated. The comparison shows that the performance of the automatic segmentation by the algorithms is comparable to the performance of the manual segmentation by the researchers. The performance of the algorithms was further evaluated with the commonly used performance metrics precision and recall. Precision is defined as $\frac{TP}{TP+FP}$ and recall is defined as $\frac{TP}{TP+FN}$. The GT maps were used to determine the true positive (TP), false positive (FP), and false negative (FN) areas, as shown in ***Figure 4.3***. Both precision and recall are above 0.9 for the majority of the analyzed images. Only for two RFLM micrographs with less than 30 % foreground area, the precision was less (0.68 and 0.86 respectively). This can be attributed to the more pronounced interference fringes at the beginning of the measurement when the cells tend to be more round and separated.

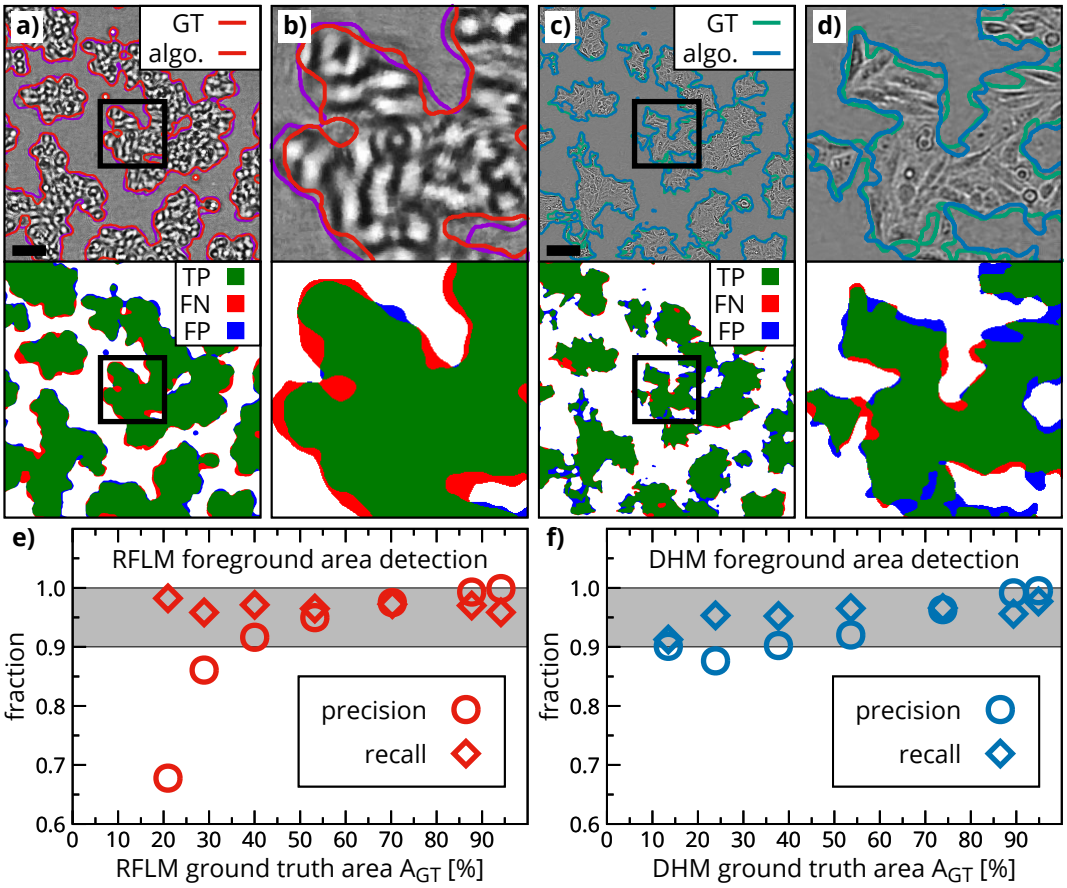

Figure 4.3: Evaluation of automatic area determination. **a)** Top: 1024x1024 pixel section of an RFLM image with the outlines of the ground truth foreground area A_{GT} and the foreground area A_{FG} detected by the algorithm drawn as colored lines. Bottom: Same section from the image above, illustrating the result of the algorithm in terms of true positive (TP), false negative (FN), and false positive (FP) areas. Scale bar: 200 µm. **b)** Enlarged view of the region highlighted in a) by the black rectangle. **c&d)** Show the analogous results for the DHM images. Scale bar: 200 µm. **e,f)** The graph shows precision and recall of the respective area detection algorithms. Over a wide range of A_{GT}, the values for both algorithms are between 0.9 and 1.0, indicating good performance.

4.2.2 Area Correlation

After the development of the algorithms for the automatic area detection, the next step was to find a relationship between the RFLM foreground area A_{RFLM} and the corresponding cell covered substrate area A_{DHM} detected in the DHM images. This relationship is required to work reliably for different cell lines during all phases of cell growth. To find this relationship, the setup capable of both DHM and RFLM time-lapse live cell imaging was used to acquire time-lapse image series of growing cell populations. The cells were seeded out in standard cell culture flasks at low densities corresponding to less than 15 % confluency and subsequently grew over several days up to 100 % confluency. To be capable of imaging the dense cell layers when the culture approaches confluency, the DHM unit of the setup used a multi-height based twin image suppression approach. The motorized stage varied the sample-sensor distance and for each sample-sensor distance, the hologram of the sample was recorded and the corresponding amplitude image reconstructed. The light field reconstructed for the sample plane is identical for all sample-sensor distances, whereas the twin image is different for each sample-sensor distance. Hence, averaging the reconstructed amplitude images reduced the twin image artifacts substantially. Due to the high number of sampled distances, the obtained DHM micrographs showed high contrast even for dense samples with confluent cell layers, see ***Appendix Figure 2*** for an example.
To demonstrate cell type independence, three different cell lines were used to relate the automatically detected RFLM foreground area A_{RFLM} to the automatically detected cell covered area A_{DHM} from the corresponding DHM images. To this end, A549 and HeLa cells were used as epithelial cell lines and NIH-3T3 cells as a fibroblast cell line. ***Figure 4.4 a*** exemplarily shows the detected DHM and RFLM foreground areas from HeLa cells at low, medium, and high confluency. These examples illustrate that the differences between A_{DHM} and A_{RFLM} occurred predominantly along the borders of the cell patches. ***Figure 4.4 b*** shows one growth curve of the foreground area for each cell line. The results show that A_{RFLM} was higher than the corresponding A_{DHM}, especially for lower confluencies. Since the differences between A_{DHM} and A_{RFLM} were found to be close to the borders of the detected areas, the relationship between $\Delta A = A_{RFLM} - A_{DHM}$ and the border length of the cell patches was analyzed. The plot of the difference of the detected areas $\Delta A = A_{RFLM} - A_{DHM}$ against the RFLM foreground area border contour length L_C indicates a linear correlation between the two quantities (see inset ***Figure 4.4 b***). Therefore, A_{DHM} is estimated from the measured A_{RFLM} by calculating a contour corrected area A^C_{RFLM} with the formula

$$A_{DHM} \approx A^C_{RFLM} = A_{RFLM} - \mu_A L_C \tag{4.1}$$

The correction factor μ_A is obtained by fitting the relation between ΔA and L_C with a linear function. For the used culture flasks and geometry of the presented setup, this gives a correction factor of $(19.2 \pm 0.2)\,\mu m$. The uncertainty was calculated from the fit, which used the relative error of the algorithm in determining A_{RFLM}, L_C, and A_{DHM}. While A_{RFLM} overestimated the cell covered substrate area by up to 20 percentage points, A^C_{RFLM} gave an unbiased estimate of the cell covered substrate area, as ***Figure 4.4 c*** shows. There only remained a small bias in the confluency range below 20 %. In addition, the growth curves for A^C_{RFLM} also coincided with the growth curves of A_{DHM}, as the inset of ***Figure 4.4 c*** shows. Thus, A^C_{RFLM} can be used to determine the cell covered substrate area of cell ensembles and cell clusters. In general, the value of the correction factor μ_c depends on the sample-sensor distance z_{RFLM}

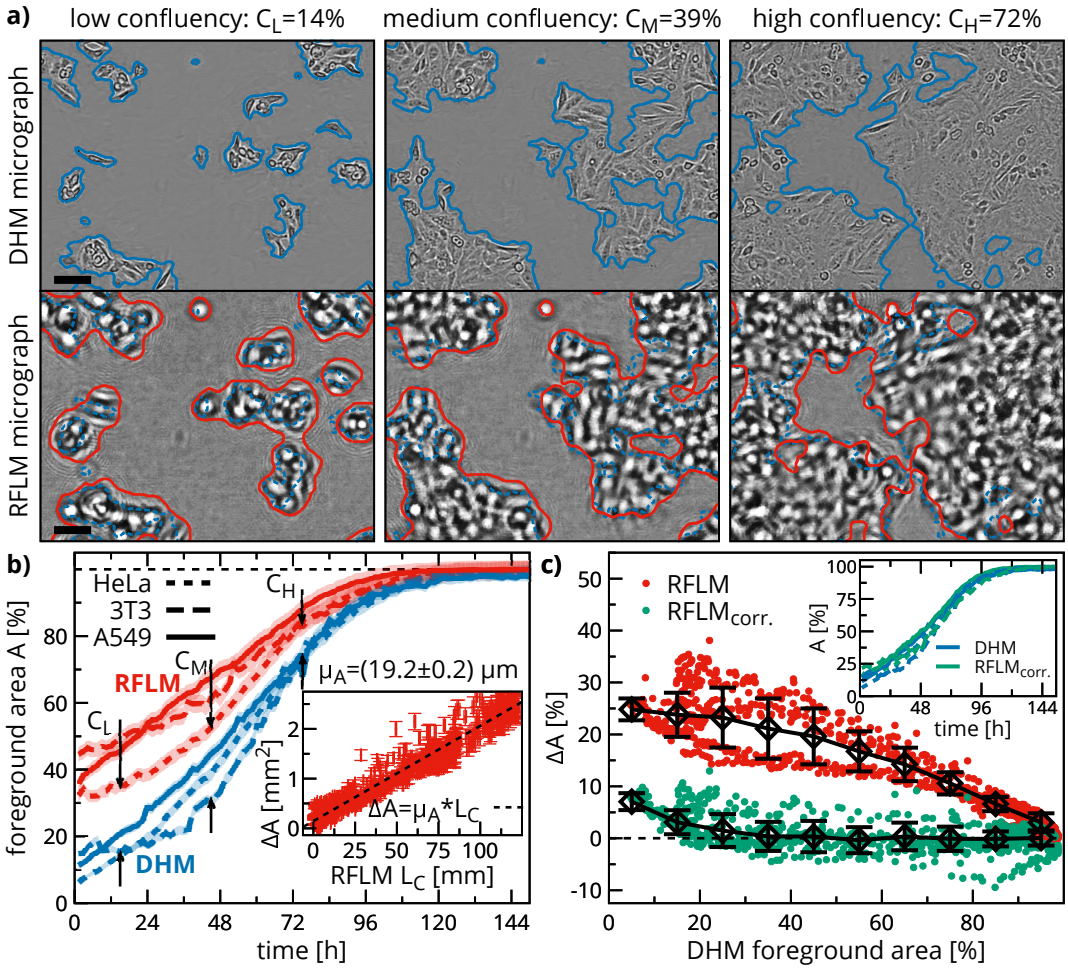

Figure 4.4: Automated determination of the cell covered substrate area from RFLM images. **a)** The upper row shows sections of DHM images from a time-lapse measurement with HeLa cells at low, medium, and high confluency. Scale bar: 100 µm. Blue lines indicate the outlines of the automatically detected foreground area A_{DHM}, i.e., the cell covered substrate area. The bottom row shows the identical region in corresponding RFLM images. Red lines indicate the border of the automatically detected foreground area A_{RFLM}. The outlines of the respective A_{DHM} are included as dashed blue lines. The images show that the deviations between the different foreground areas occur predominantly along the borders of the cell patches. Scale bar: 100 µm **b)** Foreground area fraction from measurements with three different cell lines plotted against time. Red lines correspond A_{RFLM}, blue lines to A_{DHM}. The error intervals of the detection are indicated by the colored transparent background, respectively. Inset: The difference ΔA between the RFLM and the DHM foreground area is plotted against the contour length of the outlines of the RFLM foreground area. A linear fit allows the introduction of a contour length dependent correction of A_{RFLM}. **c)** The difference between the DHM foreground area and the corrected and uncorrected RFLM foreground area is plotted against A_{DHM}. The black rhombuses with error bars indicate the mean and standard deviation of all data points from eight time-lapse measurements binned into 10 % foreground area fraction intervals. While the uncorrected RFLM foreground area overestimates the true cell covered area, the contour corrected RFLM foreground area fraction agrees with the true foreground area fraction. Inset: DHM and corrected RFLM foreground area plotted against time. The excellent agreement between the curves shows that the contour corrected RFLM foreground area gives the correct cell covered area and can hence be used to determine the confluency.

and the exact parameters of the image analysis used to detect A_{RFLM}, as ***Figure 4.5*** shows. The diffraction pattern spreads with increasing z_{RFLM} and as a consequence the ratio between the detected area A_{RFLM} and the length of its borders L_C changes, which ultimately results

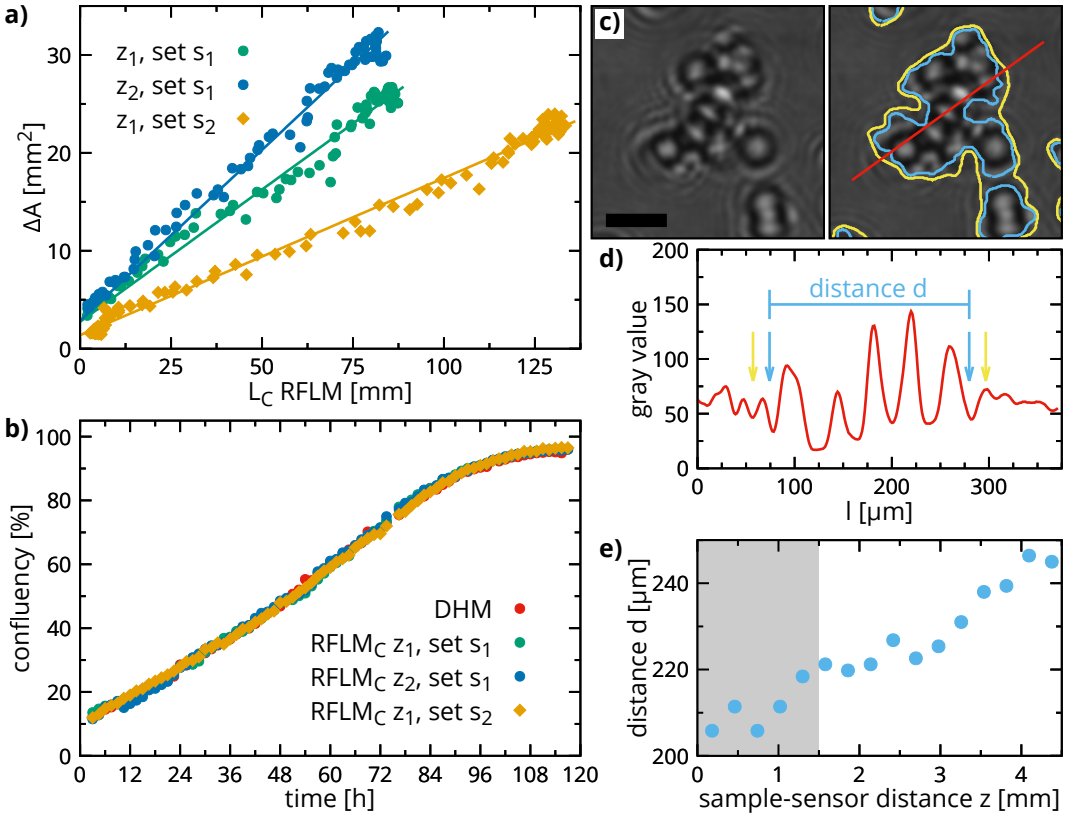

Figure 4.5: Correction factor for different geometries and settings. **a)** shows a plot of the area difference $\Delta A = A_{RFLM} - A_{DHM}$ against the contour length L_C of the border of A_{RFLM} for a measurement with A549 cells. Data is shown for two different sample-sensor distances z_1 and z_2 ($\Delta z = 300\,\mu m$) where a parameter set s_1 was used for image analysis, and the sample-sensor distances z_1 analyzed with a parameter set s_2. In all three cases, the relationship between ΔA and L_C is linear, and the corresponding correction factor μ_c can be obtained with a linear fit. **b)** shows a plot of the confluency growth curve for the detected DHM cell covered substrate area and the corrected RFLM area. The DHM confluency growth curve is recovered in all cases, indicating the validity of the approach for different parameter settings and sample-sensor distances. **c)** illustrates how different parameter sets result in different values for the correction factors μ_c. The left side shows an RFLM micrograph of a cell cluster. Scale bar: 100 µm. The right side shows the outlines of the detected area A for two different parameter sets, resulting in a different ratio of A to L_C, and consequently in different values for the correction factor μ_c. The brightness profile along the red line is shown in **d)** and the arrows indicate the borders of the detected areas. The blue arrows show that the detected area for the used parameter set is determined by minima in the intensity profile. **e)** shows a plot of the distance d between the minima in the intensity profile from d) against the sample-sensor distance z, which was varied with a motorized stage. It shows that d increases as z increases, hence leading to a different correction factor μ_c. The area highlighted in gray corresponds to the sample-sensor distance range of the RFLM-setup geometries used in this thesis.

in a different μ_c. The parameters of the image analysis used to detect A_{RFLM} also affect this ratio. Therefore, the relationship between ΔA and L_C was additionally determined for different sample-sensor distances and different analysis parameter sets. The results in ***Figure 4.5*** show a linear correlation between ΔA and L_C for both cases. Hence, the correction factor approach can recover the cell covered substrate area in all tested cases. The correction factor μ_c was determined for several sample-sensor distances to extrapolate it for arbitrary sample-sensor distances, see ***Appendix Figure 7***. Thus, in summary, the area correction approach is robust towards the specific details of the area detection and applicable to different recording geometries, e.g., due to different bottom thicknesses of the sample containers. Therefore, recording only one set of RFLM and corresponding in-focus images for an RFLM setup is sufficient to enable the determination of the cell covered substrate area with that setup by using the area correction approach.

4.3 Cell Motility

As discussed in more detail earlier and in ***Section 2.1.2***, cell motility is a crucial phenotypic trait in cell line characteristics and plays a critical role in development and pathology. In the following, image analysis methods are presented to obtain quantitative measures for the motility of individual cells from time-lapse sequences of RFLM images.

4.3.1 Single Cell Motility

To obtain measures of the single cell motility, the trajectories of individual cells must be tracked through time. The recorded RFLM images are well suited for cell tracking since the RFLM micrographs show single isolated cells as their blurred diffraction patterns with the first order maxima being clearly distinguishable from the background. However, simple thresholding is insufficient to detect the cells robustly, since the surrounding second order maxima can easily lead to false positive detections. Therefore, a cell detector based on fully convolutional networks (FCN) and residual learning was used to generate probability maps for the locations of the cells from the RFLM images. The network was trained with manually annotated sequences and with annotations generated from fluorescence microscopy images. A probabilistic model based on moral lineage tracing (MLT) uses the probability maps as input to generate trajectories and lineages of the cells. MLT has the advantage of explicitly handling multiple detections and temporal successor hypotheses. Benchmarking against annotated datasets showed F1 scores above 95 % for the detection of the cells in the individual frames and global scores for the determination of the entire lineage (MODA, MOTA) above 95 %, indicating high-quality detection and tracking of cells in sequences of RFLM images. The methods of the detection and tracking approach, as well as the evaluation of their performance against the training sets, are discussed in greater detail in the corresponding publications [232, 233].
The following presents a comparison of the FCN cell detection and the MLT cell tracking output with reference results obtained with conventional fluorescence microscopy. The microscopy setup capable of parallel RFLM and fluorescence acquisition (see ***Section 3.2.2***) was used to generate image series for comparison and evaluation. The nuclei from different cell lines (A549, HuH7, NIH-3T3) were fluorescently labeled with Hoechst 33342 and the *ImageJ* plugin

TrackMate was used to obtain the cells trajectories from the fluorescence microscopy images. Although the position of the first order maximum of the diffraction pattern of a cell does not necessarily need to correspond to the position of its nucleus, the cells positions determined in the RFLM micrograph coincided very well with the positions of the nuclei of the cells, as ***Figure 4.6*** illustrates. The reason for this good agreement might be that the nucleus gives a key contribution to the light scattering of cells [234]. The comparison between the cell trajectories determined with MLT and the reference trajectories determined with fluorescence microscopy that is shown in ***Figure 4.6*** demonstrates that not only the positions but also the trajectories coincided very well. These results confirm that the FCN detection in combination with the MLT tracking allows the reliable generation of cell trajectories from RFM image sequences.

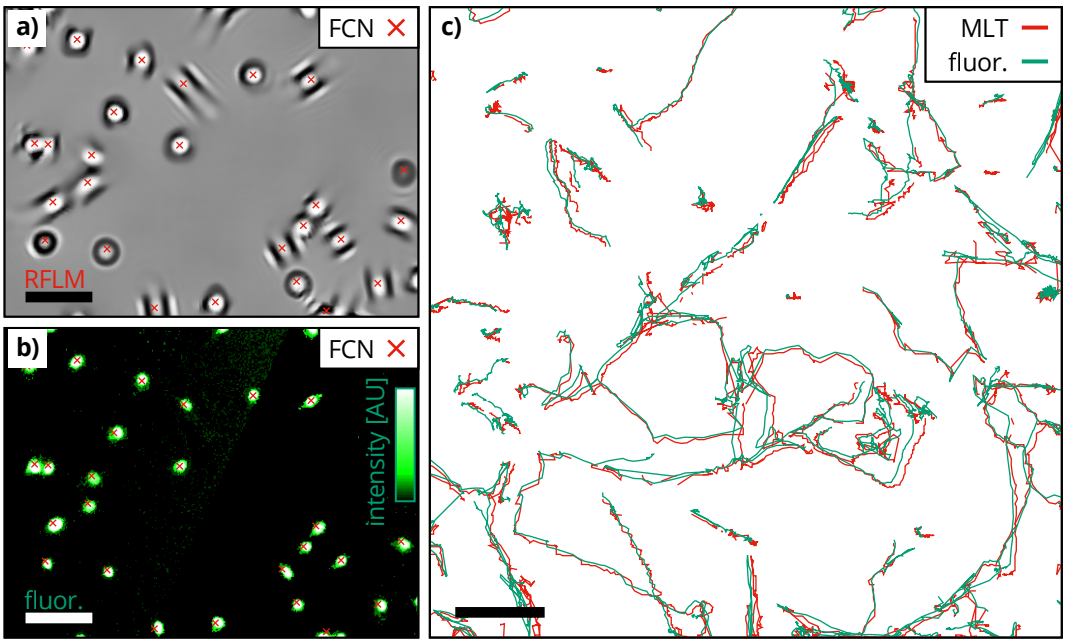

Figure 4.6: Determination of single cell motility with FCN cell detection and MLT tracking. **a)** The image shows a section of an RFLM image of NIH-3T3 cells. The red crosses indicate the automatically determined positions of the cells, based on the FCN detection. Scale bar: 100 µm. **b)** Fluorescence microscopy image of the same section as in a). The results of the cell localization in the RFLM image using the FCN detection is in good agreement with the positions of the cells nuclei. **c)** Cell trajectories obtained from RFLM images with MLT and trajectories obtained from fluorescence microscopy images, showing good agreement between both methods. The scale bar corresponds to 100 µm in a)-c)

The obtained tracking data allows calculating a variety of different measures to characterize the motility of the cells [235, 236]. Such calculations typically are based on the individual trajectories or tracks of the cells, for which ***Figure 4.7 a*** shows an example. Important measures of a track are the duration t, the total traveled distance d_{tot}, the net traveled distance d_{net}, and the confinement ratio $r_{con} = \frac{d_{net}}{d_{tot}}$. Cell speed is another commonly used motility measure, however, a more detailed analysis than simply dividing d_{net} by t is typically useful. Cells usually do not travel along straight lines and their motion is often characterized intermediary pause phases. Thus, the cell speed determined from trajectories that have been generated from image

sequences depends on the time interval used for image acquisition and the interval used for the calculation of the speed. In general, longer intervals lead to higher errors. The frequency distribution of the measured speeds like in ***Figure 4.7 b*** can be used to asses the dynamics of the motility of individual cells as well as of cell populations.

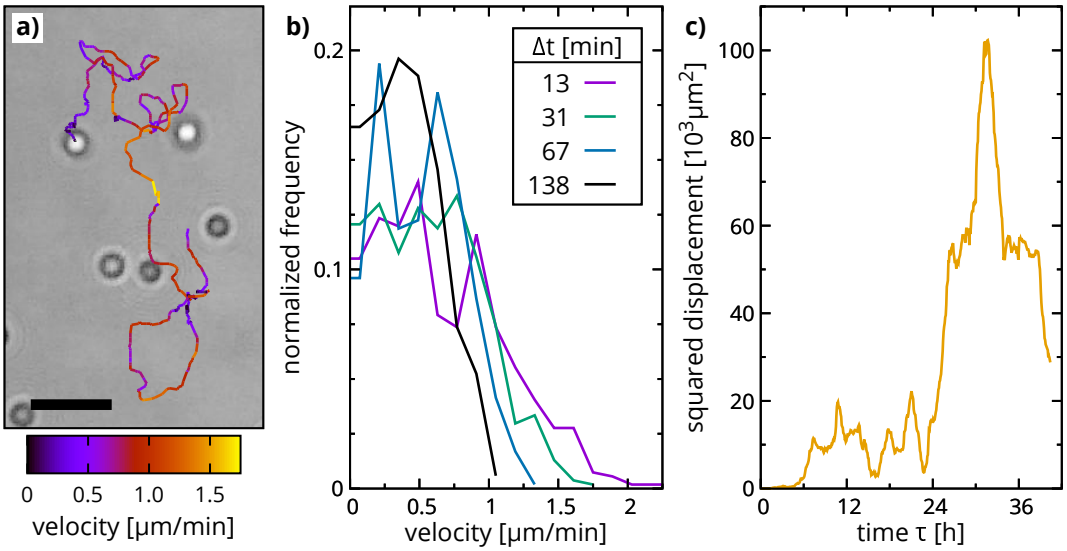

Figure 4.7: Calculation of cell motility measures **a)** Track of a NIH-3T3 cell obtained from an RFLM image sequence. The color of the track corresponds to the cells velocity at that position, where the velocity is calculated over an interval of 31 min. The track shows the random motion of the cell, with different periods of lower and higher speeds. The cell covered a total distance of 1886 µm and a net distance of 170 µm in 40.4 h. The confinement ratio is 0.09. Scale bar: 100 µm. **b)** Frequency distribution of the speed at different time points of the track. The velocity has been calculated over different time intervals Δt. The average velocities are v=0.7 µm min^{-1}, v=0.6 µm min^{-1}, v=0.5 µm min^{-1}, and v=0.4 µm min^{-1} in order of increasing Δt, indicating the influence of changes of the direction in the movement. **c)** Squared displacement of the cell with respect to the time and location of origin of the track.

A common approach is to treat cell motility as random motion [237]. Here, the movement of the cells is treated as the anomalous diffusion of particles [238] which can be analyzed using the mean squared displacement (MSD) calculated from the individual tracks [239]. The squared displacement (SD) of a single track is shown in ***Figure 4.7 c***. Motility measures based on the MSD are sensitive to the reliability of the tracking and artifacts in the generated tracks. In long-term live cell experiments tracks can begin and terminate due to tracking errors, cells entering or leaving the FOV, cell division, and detachment from the substrate (see also ***Appendix Figure 8***). The time of the beginning of a track is denoted as τ in the following. ***Figure 4.8 a*** shows the SD of 538 tracks of NIH-3T3 cells of a typical tracking experiment conducted with the in situ 8-chamber slide setup. The tracks are obtained from one quadrant of the image sensor, corresponding to a size of 1814 µm×1361 µm. Cells were tracked for 60.9 h, and the average length of the obtained tracks was 9.9 h, which is only about half of the cells doubling time. In the initial frame, 64 cells were counted manually, and the FCN detector found 73 cells. In the final frame, 335 cells were counted manually, and the FCN detector found 293 cells. The number of the automatically detected cells hence deviated about 14 %

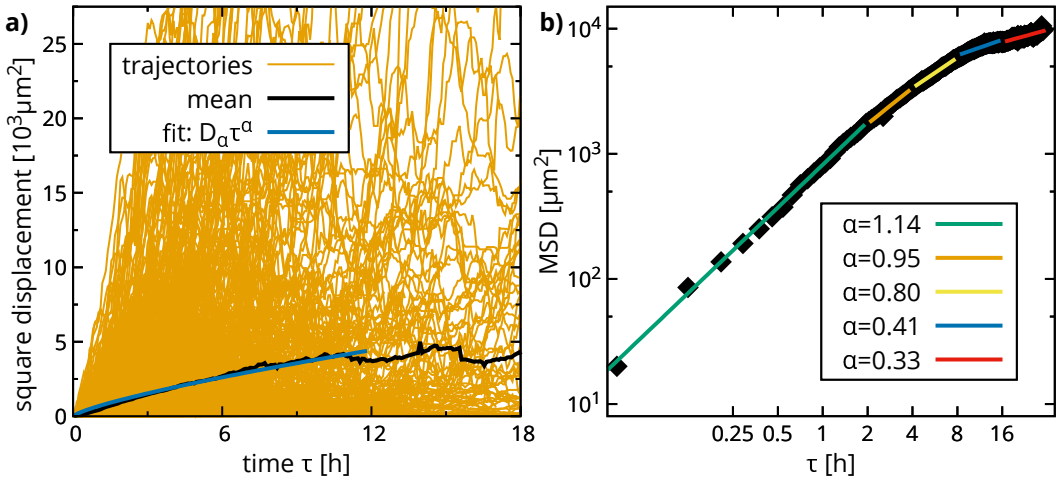

Figure 4.8: Cellular motion as anomalous diffusion **a)** The plot shows the squared displacement of 515 individual tracks of NIH-3T3 cells obtained from one quadrant of the image sensor. The average track length is 9.9 h, resulting in a lower number of tracks at longer times τ. The individual tracks are averaged to obtain the MSD, which is fitted with the anomalous diffusion equation $MSD(\tau) = 4 \times D_\alpha \tau^\alpha$. The fit interval is 12 h. **b)** Timescales of cellular diffusion: The graph shows the average MSD of four measurements with NIH-3T3 cells. The function $MSD(\tau) = 4 \times D_\alpha \tau^\alpha$ is fitted to the data over different intervals of $\Delta\tau$. The colored lines show the results of the fits in the corresponding fit interval. The values determined for α indicate that on short timescales the cells behave like super-diffusive particles ($\alpha > 1.0$), whereas they behave like sub-diffusive particles on larger timescales ($\alpha < 1.0$).

from the manual determination in this experiment. Thus, the detection and tracking errors are not negligible for tracking cells over an extended period. However, due to the large FOV, one such tracking experiment with the 8-chamber setup generates around 17×10^3 tracks, which allows to studying cell motility with ample statistics.
To analyze the diffusive motion of the cells, the MSD was calculated by averaging the SD of all individual tracks. The MSD is then fitted with the anomalous diffusion equation

$$MSD(\tau) = 4D_\alpha \tau^\alpha \tag{4.2}$$

Here, D_α is the generalized diffusion coefficient. This diffusion coefficient D_α, obtained by using a fit interval of 12 h, is later used as a measure of single cell motility to compare the characteristic phenotypic traits of different cell lines and to create distinct phenotypic profiles for these cell lines. In general, the cells can exhibit different types of diffusive behavior over different timescales. The exponent α can be obtained from the slope of the MSD in a log-log-representation and is used to distinguish between subdiffusive behavior, normal diffusion, and super-diffusive behavior. To analyze how the diffusive behavior of the cells changes on different timescales, the anomalous diffusion equation is fitted to the measured MSD over different intervals of τ, see ***Figure 4.8***. In the conducted experiments, the NIH-3T3 cells showed super-diffusive behavior on short timescales ($\tau < 2$ h) and highly sub-diffusive behavior on larger timescales ($\tau > 8$ h). This transition appears to be plausible since Podestá et al. also reported such an eventual transition into a sub-diffusive regime on longer timescales for MDCK cells [240].
Typically, cells have doubling times of around 20 h, which is the same order of magnitude as

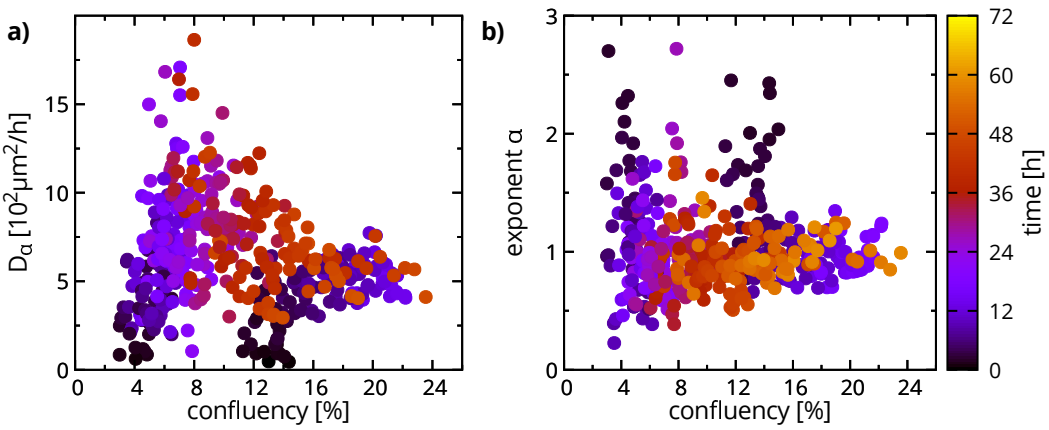

Figure 4.9: Dynamics of the diffusive motion for NIH-3T3 cells determined in two repetitions of parallelized tracking experiments. **a)** The graph shows the diffusion coefficient D_α plotted against the confluency. The MSD was fitted over 6 h intervals, after setting the current position of the tracks to zero after every hour of the measurement time, which is indicated in the plot as the color of the dots. Initially, during adhesion, D_α is lower due to the reduced movement of the cells. For the measurements starting at lower confluencies, D_α first increased and subsequently decreased to the values determined in the measurement starting at higher confluencies. **b)** The graph shows the exponent α from the same experiments plotted against the confluency. For the 6 h interval, α scattered mostly around 1, with no apparent change over time. The exception are the first hours of the experiment where the cells still adhere and the determined values for α are significantly higher. However, the determined values for D_α are significantly below the average during this period.

the duration of the longer tracks. Thus, the environmental conditions for the migrating cells can change significantly during the experiment due to an increase in cell-cell-interactions and a decrease in available area. The following approach allows an assessment of changes in the diffusive behavior of the cells that might occur over the course of the measurement. In one hour intervals, the current position of each active track was set as its new position of origin, and the MSD of all tracks over the subsequent six hours was first calculated and the fitted with the anomalous diffusion equation to obtain D_α and α. Two repetitions of tracking experiments with NIH-3T3 cells showed that α and hence the diffusive behavior of the cells showed no significant change during the experiment, with the only exception of the first few hours, when the cells were still attaching to the substrate (see also ***Figure 4.9***). However, the confluency remained below 25 % during the experiments, and a further increase in confluency might be more likely to cause a change in the diffusive behavior.
A simpler measure to track changes of cell motility during the experiment is to set the current position of the track to zero and then calculate the MSD after one or, e.g., three hours (MSD_{1h} / MSD_{3h}) with respect to the current frame for each frame of the image series, see also ***Figure 4.10 a***. Calculating such time-dependent measures of the cell motility both for the tracks obtained with RFLM and fluorescence microscopy shows that both methods give similar results despite the use of different tracking algorithms, as ***Figure 4.10 b*** shows. For both methods, the same trends in the change of the motility over time can be observed. However, comparing the MSD_{1h} measured with both methods for 14 time-lapse measurements showed that the MSD_{1h} determined from the MLT data tends to be lower than the MSD_{1h} determined from the

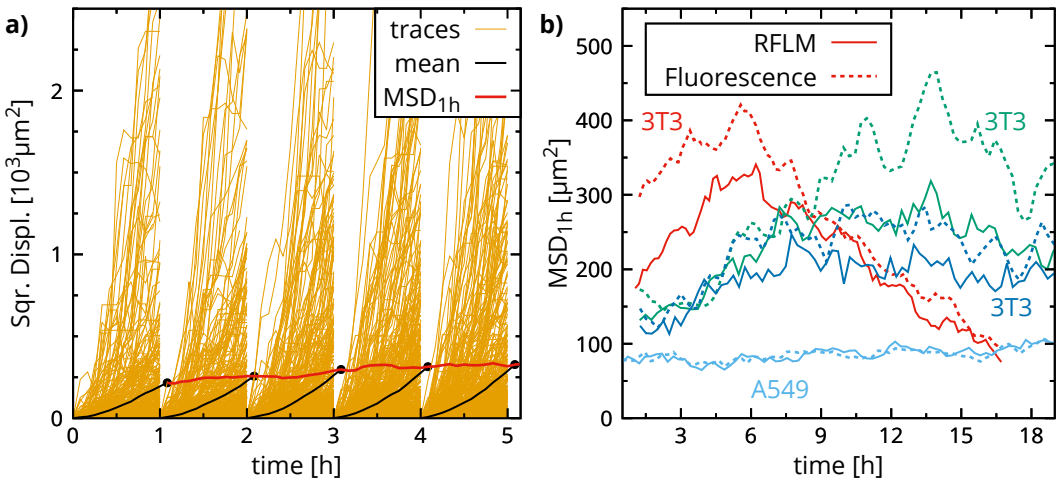

Figure 4.10: Dynamic measures of cell motility based on the MSD **a)** Plot of the SD of all tracks of NIH-3T3 cells in the FOV against time. Every hour, the current position of each cell is set as its new position of origin. The black lines show the MSD of the trajectories and the black dots the values of the MSD after one hour. Calculating the MSD after one hour (MSD_{1h}) for each frame (red line) gives a time-dependent measure of cell motility. Likewise, such dynamic measures can also be calculated over longer time intervals, e.g, over 3 h to obtain the MSD_{3h}. **b)** Plot of the MSD_{1h} calculated both from fluorescence and corresponding MLT tracking data, respectively, against time, for different cell lines. The results from both methods agree well, and qualitatively show the same trends in the changes of cell motility over the time course of the measurement.

fluorescence data (see also ***Appendix Figure 10***). On average, the MSD_{1h} determined from the fluorescence was 23 % higher for the NIH-3T3 cells, 24 % higher for the HuH7 cells, and 9 % lower for the A549 cells. This deviation might occur if the fraction of dirt particles that are erroneously recognized as cells is higher in the RFLM images than in the fluorescence images. The deviation might also be introduced by a possible bias of the MLT to lose fast-moving cells, as the deviation was lower for the slow-moving A549 cells.
Tracking cells with MLT does not only allow the calculation of the presented motility measures but also provides the whole lineage of the cells. ***Figure 4.11 a*** shows an example of lineages of NIH-3T3 cells. The lineage illustrates how the cells move and divide into daughter cells, which subsequently move and divide themselves. Therefore, the lineages allow studying proliferation on a single cell level, instead of providing only population ensemble averages. In practice, the input parameters for the MLT must be fine-tuned with respect to the application: a parameter set optimized for high tracking accuracy can decrease the correct linking to generate the lineages and vice versa.

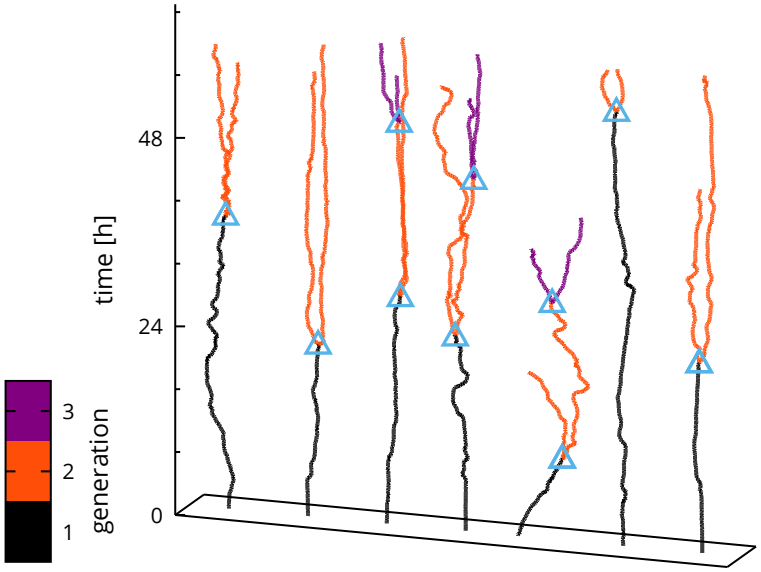

Figure 4.11: Determination of cell lineages **a)** Visualization of example cell lineages determined with MLT for NIH-3T3 cells. The lineages illustrate the spatial movement of the cells through time, their divisions (cyan triangles), and the generation of the cells (color-coded). Such cell lineages allow studying migration and proliferation on a single cell level, in contrast to ensemble measurements. The shown lineages illustrate the variance in the time between cell divisions within the population as some cells divide twice in less than 24 h and other cells undergo just one division in more than 48 h.

4.3.2 Collective Cell Migration

In the previous section, it was shown that the FCN cell detection and the MLT facilitate the reliable tracking of sparse cells in RFLM image sequences. The tracks then enable the calculation of various measures of the single cell motility. The extension of the presented single cell motility analysis with measures for collective cell migration requires suitable image analysis and image-based metrics, is are the scope of this section.
When the cell density increases, the cells typically become harder to track individually. The proximity of the cells makes it more difficult to distinguish the cells from each other and increases the probability of tracking artifacts like switching errors. However, with increasing cell density, the movement of the cells typically also becomes increasingly correlated and the movement of the cell transitions from individual cell migration to collective cell migration. Particle Image Velocimetry (PIV) provides an invaluable tool to analyze collective cell migration [102]. Therefore, PIV has been used in a wide range of studies on collective cell migration phenomena [241–243]. Instead of determining the paths of individual cells PIV provides the velocity field for patches of neighboring cells. The velocity field is determined by calculating the correlation between subwindows of consecutive frames.

To show that the analysis of RFLM image series with PIV allows a faithful quantification of collective cell migration, the results obtained with PIV were compared to manually tracked trajectories and reference velocity fields obtained by analyzing bright field microscopy images. To this end, a time-lapse image sequence of a layer of confluent MDCK cells was analyzed

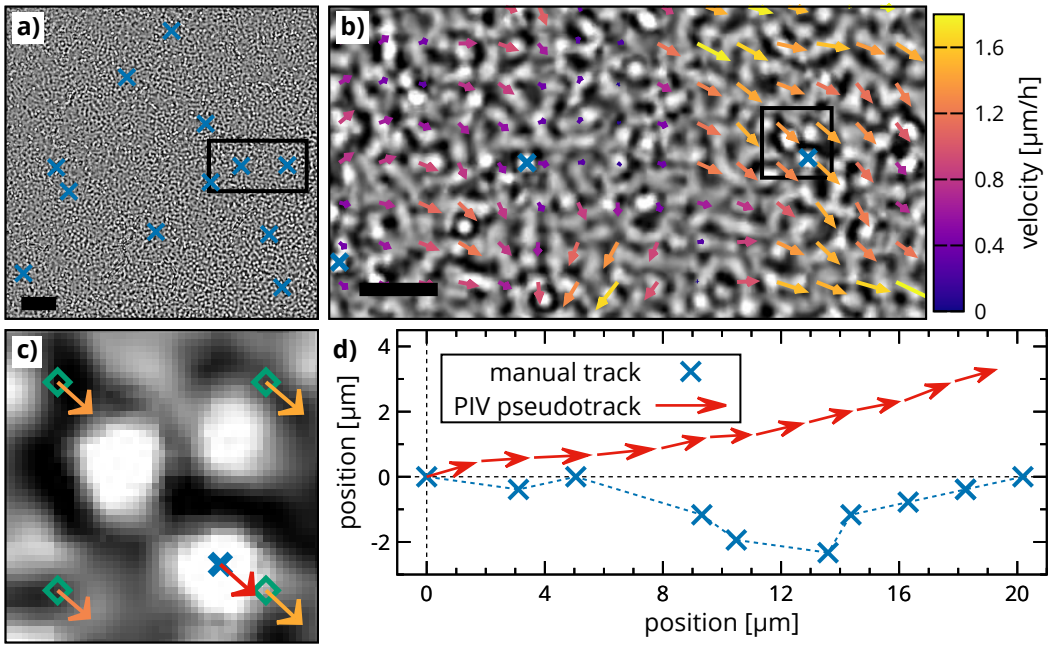

Figure 4.12: Determination of collective cell migration with PIV and generation of PIV pseudotrajectories. **a)** The image shows a closed layer of MDCK cells. The blue crosses indicate the initial positions of 12 manually tracked cells. Scale bar: 250 µm **b)** Enlarged view of the section highlighted in a). Additionally, the velocity field determined with PIV is drawn as a vector field with color-coded arrows and shows the correlated movement of the cells within the layer. Scale bar: 100 µm **c)** Enlarged view of the section highlighted in b). PIV calculates the velocity field as velocity vectors for a regular grid of positions. The depicted region contains four of these grid-points, drawn as green diamonds together with the corresponding velocity vectors. The velocity for the location of the manually tracked cell was calculated from the gridded data with bilinear interpolation. The resulting velocity vector is indicated with a red arrow. **d)** Generation of PIV pseudotrajectories: The velocity vector $\vec{v}_0$ for an initial position $\vec{x}_0$, here the first position of the manual track, is calculated by interpolation. For the next frame, the velocity vector $\vec{v}_1$ for the position $\vec{x}_1 = \vec{x}_0 + \vec{v}_0$ is calculated. Repetition of this procedure yields PIV pseudotrajectories which can be compared to the tracks obtained by manual tracking.

with PIV to determine the velocity fields corresponding to the collective cell migration, see ***Figure 4.12***. For comparison, 12 cells with a diffraction pattern exhibiting a clearly distinguishable maximum were additionally tracked manually in the image sequence. The velocity field at the starting position of the tracked cell was determined through bilinear interpolation of the gridded velocity field. The endpoint of this velocity vector is then used as the position for interpolation of the velocity field in the consecutive frame. Repetition of this procedure generates an extrapolated PIV pseudotrajectory for the cell, which can then be compared to the manually determined actual track. ***Figure 4.13*** shows the comparison between the 12 manually determined tracks and the corresponding extrapolated PIV pseudotrajectories. The comparison indicates that the PIV pseudotrajectories deviate from the manual tracks with respect to the track lengths and exact locations of the cells but qualitatively agree in the sense that they exhibit the same direction of movement and similar changes of direction. The total traveled distance of the cells in the PIV pseudotrajectories is only about half of the total net traveled distance determined from the manual tracks. However, the net traveled distance cal-

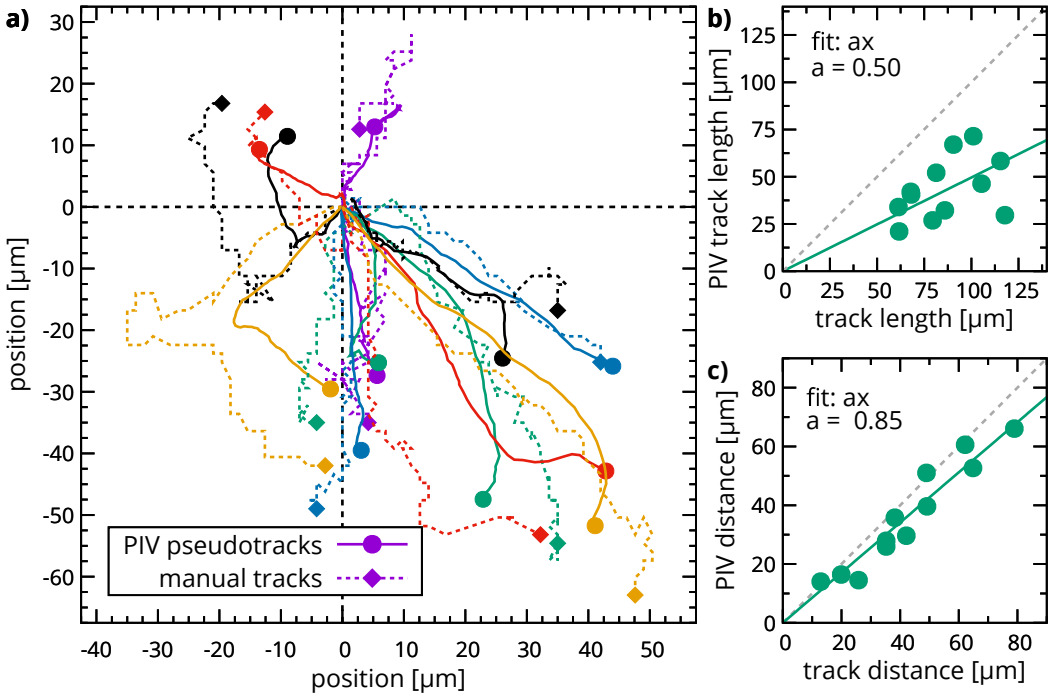

Figure 4.13: Comparison of PIV pseudotrajectories with manually determined tracks. **a)** The plot shows 12 manually determined tracks and the corresponding PIV pseudotrajectories, with the initial position of each track set to zero. The same direction of movement and similar turns can be observed in both the manual tracks as well as in the corresponding PIV pseudotrajectories. **b)** The plot shows the total covered distance of the cells determined from the PIV pseudotrajectories plotted against the total covered distance determined from the manual tracks. A linear fit to the data shows that the individual cells covered about twice as much total distance as the PIV pseudotrajectories suggest. **c)** The plot shows the net covered distance of the cells determined from the PIV pseudotrajectories plotted against the net covered distance determined from the manual tracks. For the net covered distance, the agreement between the results from the two different methods is substantially higher than for the total covered distance. However, the net covered distance determined from the PIV pseudotrajectories tends to underestimate the net covered distance from the manual tracks by about 85 percent.

culated from the PIV pseudotrajectories is 85 % of the net traveled distance determined from the manual track, therefore showing significantly better agreement. Thus, although the results obtained by PIV analysis of RFLM images miss some features of the motion of the individual cells, the approach successfully quantifies essential properties of the collective motion of the cells. Two corresponding brightfield microscopy and RFLM time-lapse image sequences of NIH-3T3 cells growing to confluence each showing the same section of the sample were used for further validation. PIV analysis was used on both image sequences. The agreement of the PIV results is excellent both for the velocity fields in the individual frames as well as for the change of the mean field strength over time, see ***Figure 4.14***.
In summary, these results demonstrate that PIV can be used on RFLM image sequences to obtain the velocity fields corresponding to the collective cell migration reliably and accurately. The velocity fields allow the calculation of PIV pseudotrajectories and averaged quantities such as the mean speed for quantification of the collective cell migration.

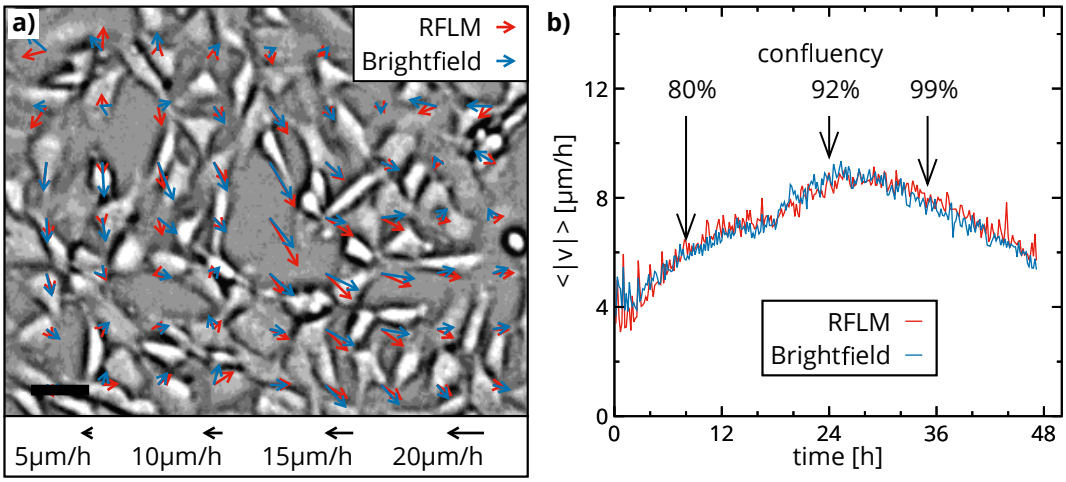

Figure 4.14: Comparison of PIV results from RFLM and brightfield microscopy **a)** Determination of correlated cell movement with Particle Image Velocimetry (PIV). The background shows a section of a brightfield (BF) microscopy image of NIH-3T3 cells. The velocity fields determined with PIV from the BF images and from the RFLM images is illustrated with arrows. The velocity vectors of both fields are in good agreement. Scale bar: 50 µm **b)** The graph shows the average absolute velocity of the field plotted against time both for the PIV analysis of the BF images and the corresponding RFLM images. The agreement of the evolution of the mean velocity field strength is excellent between the two methods.

4.4 Multiparameter Analysis of Population Dynamics

The previous sections demonstrated that the acquisition of RFLM image sequences in combination with suitable image analysis methods enables the determination of the cell covered substrate area and various image-based metrics for single cell motility and collective cell migration. Hence, the next goal was to achieve a multiparameter analysis that is capable of examining the complex population dynamics of adherent cells in more detail. To this end, the previously presented image analysis methods were extended with an analysis of cell clustering. Finally, all analysis methods were combined to achieve a phenotypic cell analysis that provides an extensive set of image-based metrics in order to capture a broad variety of phenotypic traits.

4.4.1 Cluster Size Analysis

Besides the relevance for stem cell culturing and the colony forming assay, analyzing cell clusters and their dynamics provides further image-based metrics for the assessment of cell line characteristic traits and phenotypic profiling. In this context, for example, cell cluster size distributions were analyzed to quantify the clustering behavior of cells [244]. The large FOV of the used RFLM system facilitates the determination of the distribution of cell cluster sizes with good statistics. ***Figure 4.15 a*** shows cell clusters detected in an RFLM image of A549 cells. At 30 % confluency one FOV typically contained more than 100 individual cell clusters. Following the approach of Mendes et al. [244], exponential and power law functions were used to analyze the size distributions. To this end, the cluster size distribution was automatically

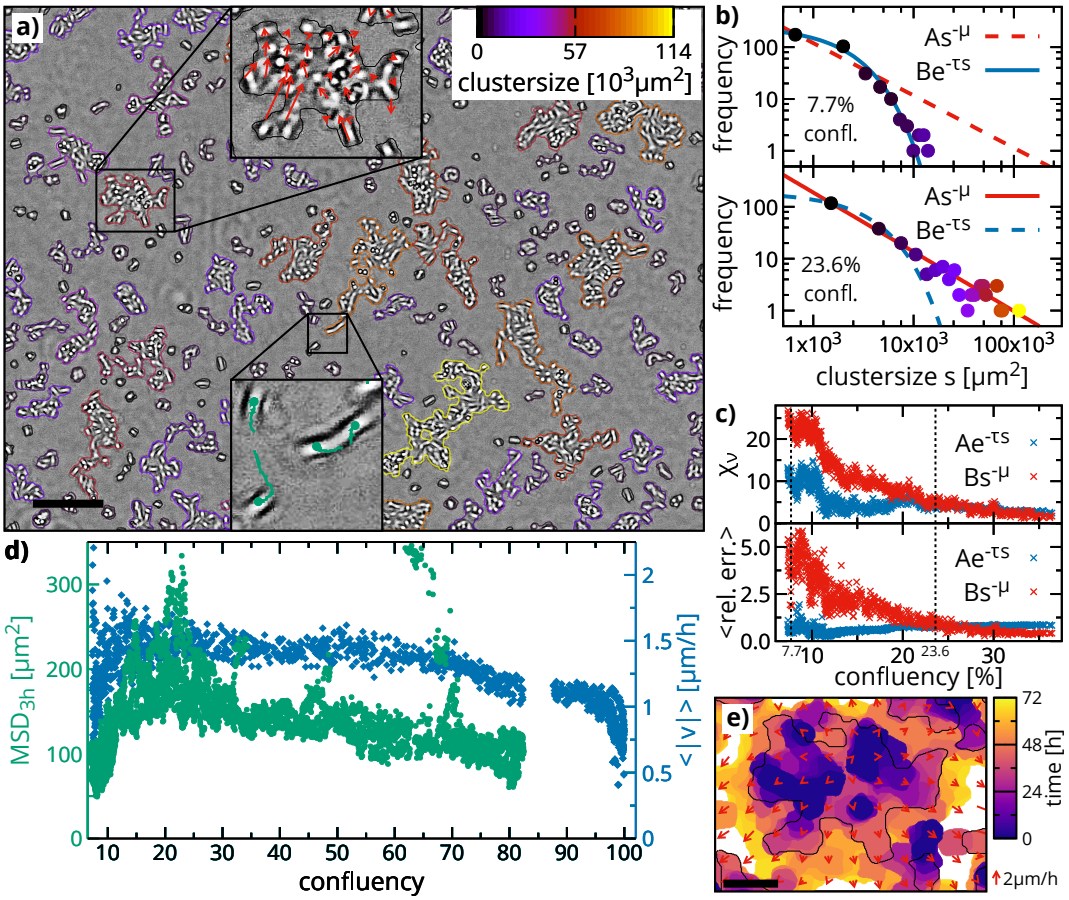

Figure 4.15: Multiparameter analysis of cell populations. **a)** RFLM micrograph showing a population of A549 cells at 23.6 % confluency. Scale bar: 400 µm. The outlines of the detected foreground area are drawn as colored lines, with line colors corresponding to the cluster size. Larger clusters can be analyzed with PIV (region enlarged at top). Isolated cells can be tracked with MLT (region enlarged at bottom). **b)** Cell cluster size distributions for two different confluencies. A power law and an exponential curve are fitted to each distribution. **c)** Shows plots of two fit quality measures against the confluency. The upper graph shows the reduced chi-square χ_ν for both fits. The bottom graph shows the average relative difference between both fits and the data. The shown data indicates a transition from an exponential to a power law decay at around 25 % confluency. **d)** The graph shows the MSD_{3h} as a measure of single cell motility and the PIV mean velocity field strength $<|v|>$ as a measure of collective cell migration plotted against the confluency. The data is from four identical measurements with A549 cells. Both motility measures show a similar development as the confluency increases. The interval on the right shows PIV data from 4 additional samples that were seeded with a higher cell density. The mean velocity decreases as the cells reach confluency. **e)** Correlation of cluster growth with the velocity field. The area of the cell cluster highlighted in a) is drawn with different colors for different times of the sequence. The clusters outline from a) is included as a guide to the eye with a black line. Scale bar: 100 µm. The time-averaged velocity field is drawn as red arrows. It can be seen that the direction of the collective cell migration correlates well with the clusters growth and spreading throughout the measurement.

calculated for each frame of the image sequences and subsequently fitted with an exponential and a power law function (***Figure 4.15 b***). To quantify which function better matches the observed size distributions, the reduced chi-square χ^2_ν and the average relative error for both fit functions were calculated (***Figure 4.15 c***). The dominating contribution to χ^2_ν comes from the prevailing smaller clusters, which makes χ^2_ν a suitable measure to describe the quality of the fit with regard to the bulk of the distribution. The average relative error of the fit with respect to the data provides a measure of how well the fit describes the tail of the distribution. For the epithelial cell lines A549 and HuH7 at confluencies below 25 %, the exponential fit outperforms the power law fit for both measures (see also ***Appendix Figure 14***). For confluencies above 25 %, the power law fit performs marginally better in terms of χ^2_ν. However, the relative error is lower for the power law fit. This indicates that the tail of the distribution is described better by the power law. The change of the size distribution of the A549 cells from an exponential decay to a power law decay at around 25 % confluency might hint at a change in the underlying aggregation dynamics. In contrast, the NIH-3T3 fibroblast cell line did not exhibit such a transition. As further metrics for phenotypic profiling, the mean cluster size and the mean of the contour length of the cluster outline divided by the cluster area were calculated (see ***Appendix Figure 13***). In general, the mean cluster size, as well as the transition behavior, depends on the seeding density. However, when the different cell lines are seeded at the same density as in this case for the shown experiments, clear differences in the cell clustering were observed between the three cell lines.

4.4.2 Multiparameter Image Analysis

Next, the analysis methods for the cell covered substrate area, the cell clustering, the single cell detection and tracking, and the collective cell migration were combined into a multiparameter image analysis. This combined analysis is capable of determining various image-based metrics for multiple critical phenotypic parameters in just one measurement, as ***Figure 4.15*** illustrates. The detected foreground area of the RFLM micrographs provided a mask for the motility analysis. Cell clusters above a certain size were analyzed with PIV, and isolated cells that moved individually, were tracked with MLT. This approach enabled the simultaneous determination of measures, both of the single cell motility as well as of the collective cell migration during the same measurement. ***Figure 4.15*** shows the progression of both measures for four measurements of A549 cells, as they grew from low confluency to high confluency. For the A549 and HuH7 cells, the results show that the mean field strength of the velocity field remained relatively constant over a wide range of confluencies, with a tendency to decrease with increasing confluency. In contrast, the velocity field strength decreased continuously for the NIH-3T3 cells (see ***Appendix Figure 12***). At reaching confluency, however, the mean field strength dropped distinctively for all cell lines. While the single cell tracking with MLT was optimized and evaluated for low confluencies, we found that MLT was still able to detect and track isolated individual cells at higher confluencies and even cells within larger clusters, which can also be observed in ***Figure 4.16***. The same observed trend in the mean field strength determined with PIV and the time-dependent motility measure MSD_{3h} indicates that MLT is still able to give a resonable estimate of the single cell motility even at high confluencies. While the ratio between the detected and the total number of cells decreases as the total number of cells increases, the total number of correctly located and tracked cells remains high due to the increase in the total number of cells. Finally, the determined parameters can be correlated with

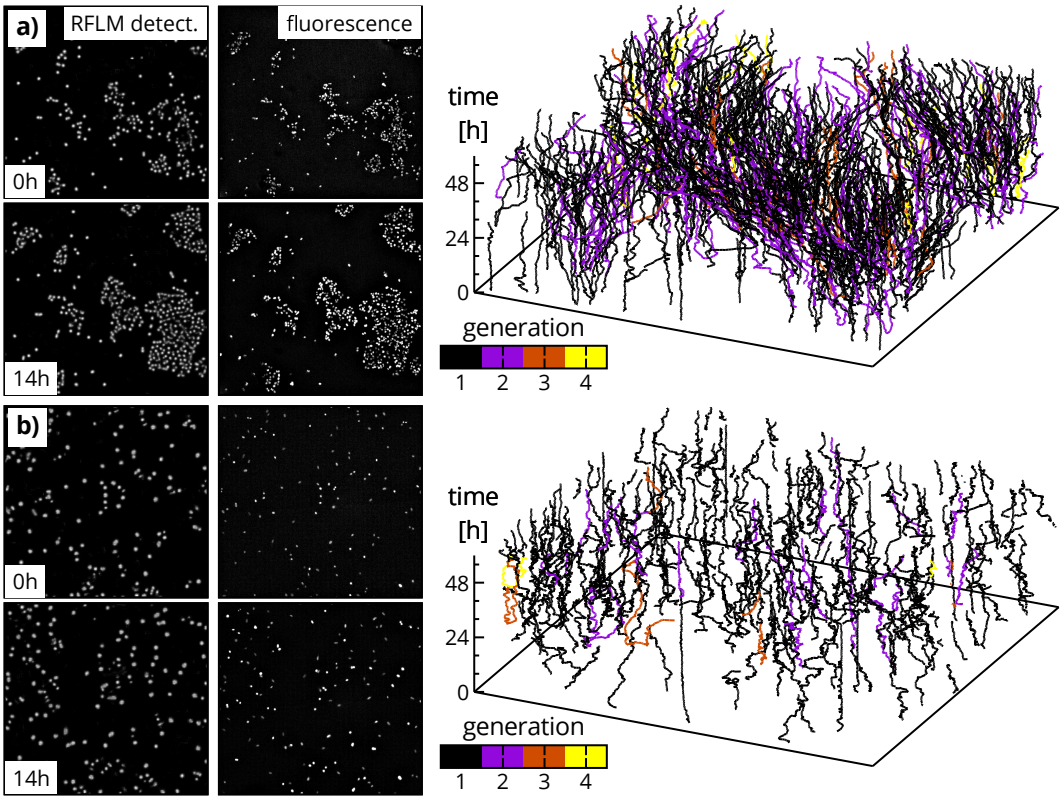

Figure 4.16: Social behavior of NIH-3T3 fibroblasts, illustrated in **a)**, compared to the social behavior of A549 epithelial cells, illustrated in **b)**. The left side shows fluorescence microscopy images and the probability maps as the output of the FCN cell detection in the RFLM images at 0 h and at 14 h of the measurement, respectively. The shown ROI is 1378 µm×1301 µm. The right side shows the MLT cell lineages for this ROI. As the fluorescence images confirm and the lineages illustrate, the two cell lines exhibited notable characteristic differences in their social behavior. The A549 cells did tend to aggregate and grow in clusters whereas the NIH-3T3 cells did prefer to move as individual cells.

each other, e.g., cell cluster growth with collective cell migration, as shown in ***Figure 4.15 e***. Such a correlation between the evolution of the area of cell clusters with the corresponding velocity field has for example been used to study the impact of mechanical constraint on cell proliferation and migration in contact inhibition [113]. The cluster analysis could also be combined with the MLT, as the different clustering behavior of different cell lines is apparent in the lineages obtained with MLT. The lineages shown in ***Figure 4.16*** were obtained by tracking epithelial A549 cells and NIH-3T3 fibroblasts and illustrate notable characteristic differences in the collective behavior between epithelial-like and fibroblast-like cell lines: the A549 cells tend to aggregate and grow in clusters whereas the NIH-3T3 cells prefer to grow and move as individual cells.

In summary, the presented multiparameter image analysis allows the determination of various image-based metrics for a variety of critical phenotypic parameters over a wide range of culture conditions from just one measurement. Thus, the technique can provide detailed insights into the dynamics of a motile and proliferating cell population.

4.5 Phenotypic Profiling and Monitoring of Cell Lines

This section addresses the question if the presented RFLM systems in combination with the presented multiparameter image analysis provide a suitable tool for phenotypic cell line profiling and monitoring of cell line characteristic traits. To this end, it is first shown that the growth curves of the confluency allow the determination of the PDTs as a commonly used measure for cell proliferation. Then, the multiparameter analysis is applied to parallelized measurements of the epithelial cell lines A549 and HuH7 and the NIH-3T3 fibroblast cell line to obtain a variety of image-based metrics. These metrics are subsequently used to create a phenotypic profile for each cell line. Furthermore, two different cell cultures were monitored during the culturing period to investigate the suitability of the technique for the monitoring of critical phenotypic traits.

4.5.1 Determination of Population Doubling Times

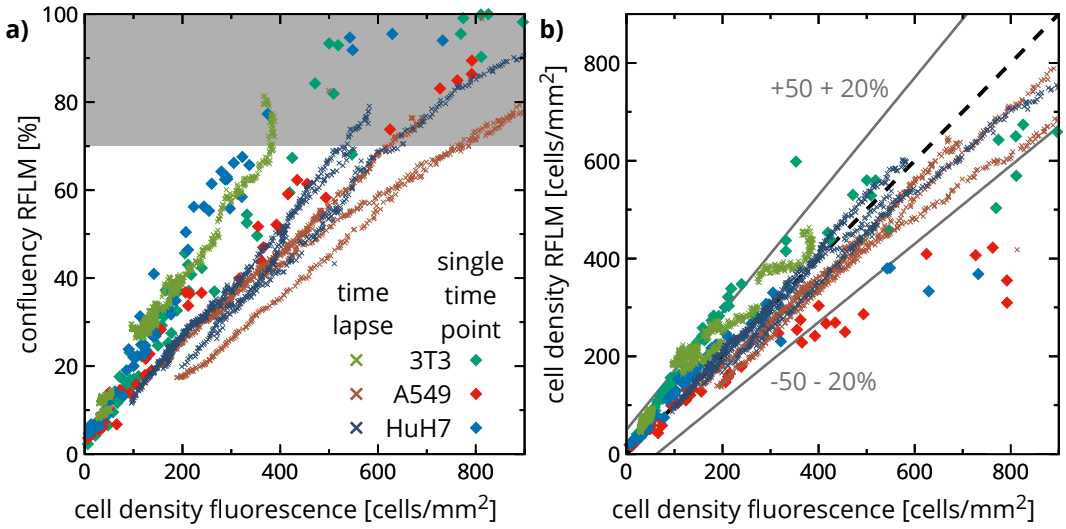

Figure 4.17: Correlation of the cell density with the confluency and the cell number determined with RFLM. **a)** The graph shows the confluency plotted against the cell density. The confluency was determined in RFLM images, the cell density in corresponding fluorescence microscopy images. Data from time-lapse measurements is plotted with crosses, data from single time point measurements with diamonds. The confluency increases linearly with the cell density up to about 70 % and saturates for higher cell densities. For the epithelial cell lines, the confluency at the same cell density is higher for the single time point measurements than for the time-lapse measurements. This is most likely due to cluster formation of the cells of these cell lines in the time-lapse measurements. **b)** Comparison between the cell number determined with RFLM and fluorescence microscopy. The graph shows a high correlation (r=0.97) between the results of both methods. Most measured values lie within an error interval of $\pm 50\,\text{cells}\,\text{mm}^{-2}$ $\pm 20\,\%$. Some of the outliners are the result of inhomogeneous plating, see also ***Appendix Figure 6***. Both graphs demonstrate that the confluency, as well as the cell number determined in the RFLM images, allow the determination of cell proliferation.

For a determination of PDTs as a frequently used measure of cell proliferation, first, the correlation between the determined confluency and the cell number was investigated. Therefore, cells were seeded at different cell densities in a multiwell plate. Then the confluency was determined from the RFLM images. The cell density was determined by acquiring fluorescence microscopy images of the same sample region and subsequently counting the number of fluorescently labeled nuclei. Additionally, time-lapse image series with combined RFLM and fluorescence microscopy acquisition were analyzed in the same fashion. Such measurements were performed for the A549, HuH7, and NIH-3T3 cell lines. For all measured cell lines, the confluency increased linearly with the measured cell density up to about 70 % confluency, see also ***Figure 4.17 a***). These results demonstrate that the confluency is highly correlated to the cell number and hence can be used to assess cell proliferation. Therefore, fitting exponential functions to the log phase of the confluency growth curves allows the determination of the PDTs [90]. The confluency growth curves for several measurements conducted with identical initial conditions are shown for the three cell lines in ***Figure 4.18***. Here, it was found that the HuH7 cells had the slowest growth rate with a PDT of (22.2 ± 0.4) h, followed by the A549 cells with a PDT of (19.9 ± 0.2) h. The NIH-3T3 were the fastest growing cells with a PDT of (18.7 ± 0.7) h. The PDTs from all conducted measurements, also including those with different initial conditions, are shown in ***Figure 4.19 a*** and can also be found in ***Appendix 5.4***. Furthermore, the cell density was also determined with the FCN cell detection and compared to the cell density determined from the fluorescence microscopy data, see ***Figure 4.17 b***. The results from both measurements are highly correlated with a Pearson correlation coefficient of r=0.97. This result demonstrates that in addition to to the confluency growth curves, the cell number determined from the RFLM images with the FCN detector can also be used for a reliable determination of cell proliferation.

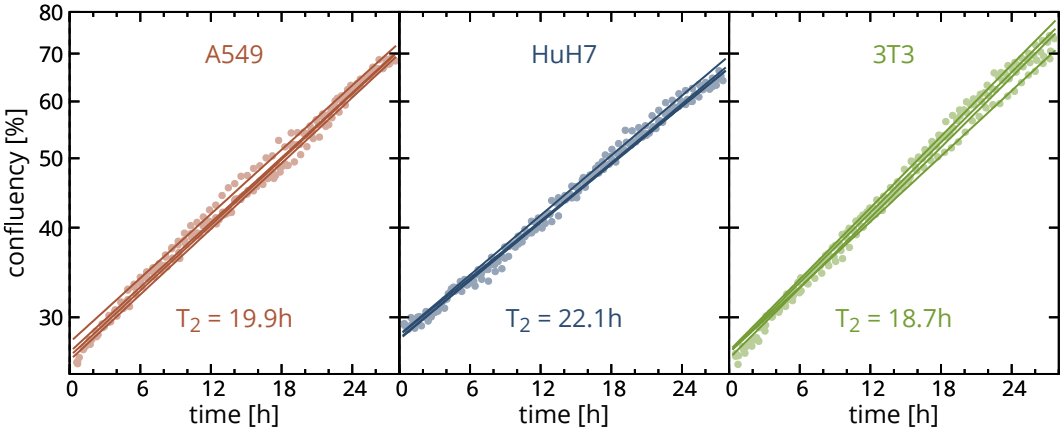

Figure 4.18: Determination of the PDTs from the confluency for three different cell lines (A549, HuH7, NIH-3T3). The graphs show semi-log plots of the confluency against time. The PDT is determined by fitting an exponential function to the data over the range of the log-phase of the growth curves. All plotted growth curves show the log-phase, as they exhibit a linear slope in the semi-log representation. The plots show four growth curves together with the corresponding fits (solid lines) for each of the three cell lines.

4.5.2 Cell Line Profiling

Pooling different metrics of cellular phenotypes for the creation of phenotypic profiles to assess the impact of environmental factors on cells or to discriminate between different cell types is a frequent task in cell-based experiments. Such profiles can be generated from spectral fingerprints of Raman spectra [245, 246], impedance readings [247], image-based morphological features [248], or cell migration patterns [249]. This section investigates the potential of the presented technique to use image-based metrics to create phenotypic profiles for cell line profiling. Therefore, the 8-chamber slide setup was used to conduct parallelized measurements of three different cell lines. Here, the A549 and HuH7 cells were chosen as representatives of epithelial cell lines and NIH-3T3 cells as representatives of fibroblast cell lines. The chambers of the slide were seeded either with a higher cell density to obtain measures for proliferation, clustering, and collective cell migration, or with a lower seeding density to obtain measures for the single cell motility. In some cases, all measures could be determined in a single measurement, if the population grew fast enough from low to high confluency.

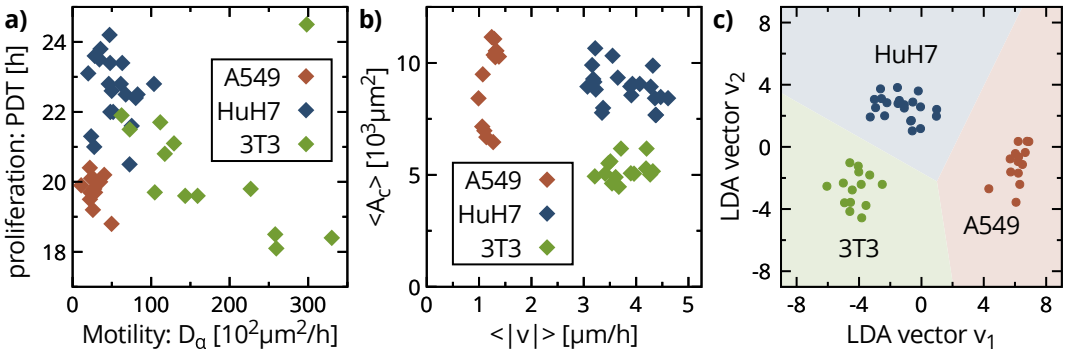

Figure 4.19: Cell line characteristic traits and phenotypic profiling of different cell lines (NIH-3T3, A549, and HuH7). **a)** The graph shows the PDTs plotted against the diffusion constant D_α as a motility metric. The values were determined in several measurements for each cell line. Both metrics quantify the behavior of the individual cells. **b)** Plot of the mean cluster size against the mean speed of the collective cell migration. Both metrics quantify the collective behavior of the cells. **c)** The plots in a) and b) demonstrate that the cells exhibit characteristic phenotypic differences in terms of the used metrics. This plot shows the result of an LDA applied to the results of the measurements from the three cell lines using the metrics from a) and b) together with three additional parameters. The clear separation between the three different cell lines demonstrates that the presented image-based metrics reflect the characteristic traits of the three different cell lines. The metrics are thus well suited for phenotypic profiling or fingerprinting.

The diffusion coefficient D_α and the exponent α were used as image-based metrics to quantify the motile behavior of the different cell lines. These measures were obtained by fitting the anomalous diffusion equation to the MSD over an interval of 12 h (see also ***Appendix Figure 11***). A measure for the collective cell migration was obtained by calculating the average of the mean velocity $<\vec{v}>$ determined with PIV over the confluency interval 50–90 % (see also ***Appendix Figure 12***). To obtain measures of the cell clustering behavior as phenotypic parameters, the average cell cluster size $<A_c>$ was calculated by averaging the measured cell

cluster sizes over the confluency interval 15–30 % (see also ***Appendix Figure 13***). Furthermore, the ratio between the length of the perimeter of the clusters and their respective area was analyzed to obtain two further metrics for colony morphology, which is shown in ***Appendix Figure 13***. ***Figure 4.19 a&b*** show some of the obtained metrics for the three cell lines, namely PDT, D_α, $<\vec{v}>$, and $<A_c>$. These results show that the NIH-3T3 cells exhibited the highest single cell motility, but were slower than the HuH7 cells in terms of collective cell migration. The A549 cells showed the slowest movement both as individual cells as well as collectively. These findings already demonstrate that the three cell lines exhibit distinct differences in the obtained measures. In general, the individual metrics are correlated with each other, as ***Appendix Figure 15*** shows. Therefore, a linear discriminant analysis was used to reduce the high dimensional parameter space to two dimensions while achieving maximum separation between the different classes. ***Figure 4.19 c*** shows that this approach achieves a clear separation between the three cell lines. This result demonstrates that the technique can be used to generate meaningful phenotypic profiles and that it is suitable for phenotypic profiling of cell lines. The obtained image-based metrics appear to capture and reflect the complexity of the cellular population dynamics since the parametrization provides a distinct fingerprint of the cell line characteristic traits.

4.5.3 Cell Line Monitoring

Finally, this section addresses the issue of detecting changes of critical phenotypic traits of cell lines over the culture period and ensuring the consistency of serial passaging. Therefore, the RFLM setup that was designed for imaging cells in culture flasks inside the incubator (see ***Section 3.3.1***) was used for monitoring of a typical procedure in cell culture, namely the thawing and subsequent subculturing of cell lines. Here, the frequently used NIH-3T3 cell line and a primary human melanoma cell line are used as two example cell lines. Standard thawing protocols were followed to transfer the cells from storage in cryovials to a proliferating cell culture in the incubator. Then the RFLM setup was used to monitor confluency, PDTs, and cell migration of both cell lines over the culture period, see ***Figure 4.20***. The cell migration was here measured by calculating the mean of the average absolute velocity field determined with PIV over the confluency range >90 % (see ***Appendix Figure 16*** for details). Both cell lines were cultured in standard cell culture flasks inside a standard CO_2 incubator and passaged before reaching 90 % confluency. The results show that the NIH-3T3 cells reached and subsequently maintained stable levels of growth right after exchanging the culture medium one day after thawing. This medium exchange is usually done to remove any remaining DMSO that has been released by the cells into the medium after thawing. The primary cell line, on the other hand, needed slightly longer to adapt to the new environment and reached a stable level of growth after the first passaging. The results also show that both cell lines exhibited constant cell migration over the passages. Higher fluctuations of the cell migration were measured than for the PDTs. However, this might be due to the dependence of the cell migration on the confluency, especially in the case of the NIH-3T3 cells.

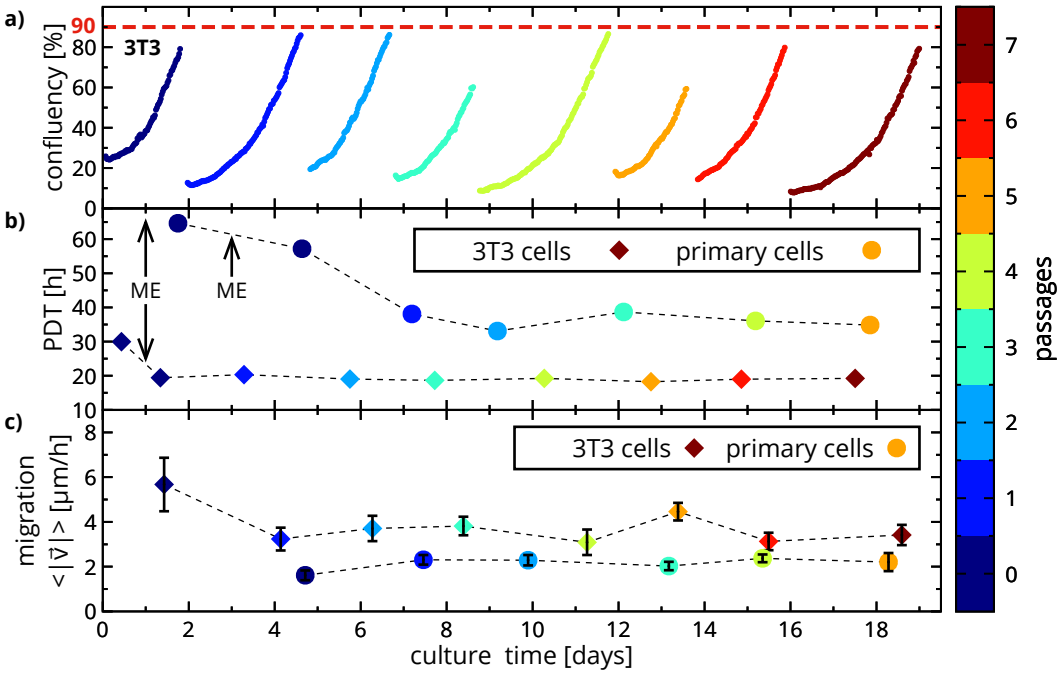

Figure 4.20: In situ monitoring of phenotypic traits with RFLM. A culture of NIH-3T3 cells and a primary human melanoma cell line were used as example cell lines. **a)** shows the development of the confluency of the NIH-3T3 cells during serial subculturing. The data is color-coded with the number of passages after thawing the cell line. The cells were consistently passaged before the culture reached a confluency of more than 90 %. Fitting the log phase of the growth curves with an exponential function allows the determination of the PDTs. **b)** Plot of the determined PDTs against the culture time for both cell lines. The number of passages after thawing is color-coded. The NIH-3T3 cells reached and subsequently maintained a stable PDT of (19.1 ± 0.6) h after the first exchange of culture medium following thawing. The primary cells reached a PDT of (36.1 ± 2.3) h after the first passage, which they maintained over the subsequent passages. **c)** shows the development of the cell migration over the culturing period. To obtain a measure for the cell migration, the average velocity field was determined with PIV and averaged over the confluency range >40 %. The migration remained fairly constant over the culturing period, with the NIH-3T3 cells having exhibited a slightly higher migration that the primary cells.

4.6 Discussion

Techniques for monitoring cell lines during the culture period are highly desirable in cell culture since they facilitate the detection of changes in cell line characteristic phenotypic traits and provide information on the current state of the culture, e.g., its current confluency. Therefore, such techniques provide valuable tools in ensuring the consistency of cell cultures during serial passaging. RFLM is ideally suited in this regard since it allows label-free life-cell imaging inside standard cell culture incubators with a wide FOV. Critical information can be extracted directly from the recorded interference patterns [73, 198, 199, 201, 205, 206] with the advantage of having no associated computational cost for image reconstruction [70] and extremely low experimental demands, which allows compact, cost-efficient instrumentation. However, RFLM has so far not been used to determine the key parameters confluency, as well as cell proliferation, motility, migration, and clustering for phenotypic profiling and monitoring of cell lines.While the scope of ***Chapter 3*** was the design and performance of setups for in situ RFLM live-cell imaging, this section presented suitable image analysis methods to achieve an extensive analysis of cell growth and motility with image-based metrics.

To this end, first, a method to determine the cell covered substrate area of adherent cell populations in RFLM images was presented. For this goal, an algorithm for the detection and segmentation of the area in the RFLM images, which corresponds to the interference pattern of the cells was developed. Second, it was shown that the length of the outlines of the detected RFLM area allows the correction of the detected area to the real cell covered substrate area. The performance of the algorithm was evaluated by calculating the mean precision and the mean recall, which were 0.92 and 0.97, respectively. Similar image analysis problems were studied for automated phase contrast microscopy, where typical values of slightly below 0.8 for the precision and slightly below 0.9 for the recall were reported [60]. For newer algorithms, better scores with a precision of 0.96 and a recall of 0.94 were reported [61]. Thus, the performance of the presented automated image analysis is comparable to the performance of current algorithms for cell covered substrate area detection in phase contrast microscopy. The presented algorithms together with the area correction approach hence allow the robust determination of the cell covered substrate area and the confluency in RFLM images.
The change of confluency over time can be used to assess cell proliferation [60]. Generally, the PDT is the most frequently used quantitative measure for cell proliferation. The PDT is typically determined by measuring the increase of cells during the log phase of growth [90]. Therefore, the next goal was to use the confluency to determine the PDT. For other microscopy methods, a high correlation between the cell number and the confluency has been reported [54, 250]. Therefore, the relationship between cell number and confluency was investigated for RFLM to confirm over which confluency range it is valid for the used setup and analysis. To this end, three different cell lines (A549, HuH7, and NIH-3T3) were used to correlate the confluency determined with RFLM with the cell count determined with fluorescence microscopy. The results confirmed a linear relationship up to about 70 % confluency. The measured growth curves of the three cell lines showed that this confluency range also corresponded to the log phase of cell growth. Thus, the RFLM confluency growth curves allow a determination of the PDTs that is independent of the used cell line.
To verify the measured PDTS, we attempted to compare the results with reference values, however, only in case of the NIH-3T3 and A549 cells, the PDTs were provided by the cell banks the cultures were purchased from. The reference values of about 20 h (NIH-3T3) and about 22 h

(A549) are close to the PDTs of (18.7 ± 0.7) h and (19.9 ± 0.2) h which were measured with the RFLM setups, respectively. Interestingly, even for these frequently used cell lines the used media, supplements, and PDTs reported by different cell banks (DSMZ, BCRJ, ATCC, JCRB) differed substantially by up to 20 hours. It is known for a while now, that there are differences in cellular characteristics, including proliferation, of the same cell lines between different laboratories, e.g., for MCF-7 cells [251]. Nevertheless, a study evaluating the consistency of ovarian cancer cell lines found out that PDTs were reported in only less than 30 % [252]. In this context, it has been suggested to track and report PDTs for cell culture QC [52], and the results of this and the previous chapter showed that the presented technique is ideally suited to improve data quality in this regard since it can determine the PDTs during culturing while requiring only a minimum of computation power and incubator space. Additionally, the automatically obtained PDTs could be combined with Research Resource Identifiers (RRIDs) of the used cell lines [253] and information on media and supplements to improve reporting standards and provide this important metadata in a machine-readable form for online based resource databases such as the Cellosaurus.

After having obtained the PDTs as a measure of the key phenotypic parameter cell proliferation, the next goal was to obtain metrics for the motility of individual cells. Therefore, the trajectories of the cells were determined by tracking them in RFLM image sequences. The tracking method is based on a state of the art machine learning technique and can not only detect the cells in the RFLM images with high accuracy by using an FCN but can additionally determine their whole lineage by employing MLT [232, 233]. Such lineages have the advantage of providing further insights into cell population dynamics, e.g., the heterogeneity of cell populations [254]. To obtain quantitative metrics for the cellular motion, the common approach of treating cell motility as random motion [237] was used to calculate MSD-based measures from the cell trajectories. The performance of the tracking method was evaluated further by comparison with conventional fluorescence microscopy measurements. The results showed that the RFLM cell tracking performs comparably to conventional fluorescence microscopy, but with the advantage of not requiring any labeling of the cells. To compare the single cell motility of different cell lines, the diffusion coefficient D_α was calculated as a commonly used motility measure. Therefore, the measured MSD data was fitted with the anomalous diffusion equation.
For the NIH-3T3 cell line, values between $50\,\mu m^2\,h^{-1}$ and $350\,\mu m^2\,h^{-1}$ were measured for the diffusion coefficient D_α in several parallelized measurements. Similar values have been reported for 3T3 cells in literature, e.g., 183–$410\,\mu m^2\,h^{-1}$ (pyrex substrate of a cell culture flask) [255], 198–$382\,\mu m^2\,h^{-1}$ [256], and $77\,\mu m^2\,h^{-1}$ (glass substrate) [257]. In general, the results depend on the used substrate, the time interval over which D_α is calculated, and the confluency. For example, for 3T3 cells in culture flask a D_α of $180\,\mu m^2\,h^{-1}$ was reported for low cell densities and $D_\alpha = 18\,\mu m^2\,h^{-1}$ for high densities, which is a difference of one order of magnitude [258]. It is noteworthy, that while the presented analysis provides a quantitative measure for the cell motility, using least squares fitting of the anomalous diffusion equation can have its pitfalls [259, 260] and more sophisticated analysis methods [261], as well as cell-type-specific motility models for statistical analysis of cell motility [262], have been reported.

The correlated movement of cells in collective cell migration is another critical phenotypic trait in cell lines. In collective cell migration, the cells are typically in close proximity or contact with each other, which complicates single cell tracking approaches. However, PIV provides an excellent tool to determine a velocity field of the correlated movement of even densely packed cells and has found frequent use in analyzing collective cell migration [102, 241–243]. Therefore,

PIV was used to determine the velocity field in the obtained RFLM image sequences. The average of the absolute velocities $<|\vec{v}|>$ was used as a measure for the collective cell migration. The accuracy of the results obtained by using PIV on RFLM image sequences was verified with corresponding brightfield microscopy image sequences and comparison with single cell tracks. These comparisons confirmed that the PIV analysis of RFLM image sequences provides accurate results and that the velocity fields capture essential features of the cellular motion such as the direction of motion and the net covered distance.

Next, an analysis of cell clustering was introduced to provide a quantification of this important phenotypic trait. RFLM is especially well suited for this type of analysis due to its large FOV. From coagulation models, it is known that the size distribution is the result of the underlying stochastic processes of the aggregation dynamics [263]. For example is the exponential length distribution of polymers the result of constant polymerization and depolymerization [264], whereas the diffusion limited aggregation of particles leads to a power-law distribution of the aggregate sizes [265]. Exponential and power-law distributions of cell cluster sizes, as well as transitions between the two distributions, have both been used to describe the aggregation dynamics of cell clusters [111, 244]. The results indicated that the size distribution of cell clusters of A549, HuH7, and NIH-3T3 cells seeded at a density of $1.2 \times 10^4\,\mathrm{cells\,cm^{-2}}$ (corresponding to a confluency below 10 %) is initially best described with an exponential distribution. At a confluency of about 25 %, the distribution of the epithelial A549 and HuH7 cells transitioned to a power-law decay, while the distribution of the NIH-3T3 fibroblasts did not. While current modeling cannot explain the transition between the distributions, it has been suggested that cell-cell-adhesion might play an essential role in it [266]. The combination of RFLM with the cell-tracking and cluster size analysis might be well suited to shed light on the dynamics of such collective cellular phenomena since the tracking would allow a determination of the aggregation-fragmentation rates of the cell clusters while the size distribution could be determined at the same time with high statistics. Being able to measure cell migration and the expansion of cell clusters over a wide FOV is also beneficial to study a variety of other phenomena of collective cell behavior. This includes e.g. contact inhibition [113], the balance of mechanical forces [267], or the relation between cluster geometry and cell migration [268].

Finally, it was demonstrated that the presented image analysis methods can be combined into a multiparameter analysis that allows obtaining multiple image-based metrics to assess different crucial phenotypic parameters. By combining metrics for proliferation, single cell motility, collective cell migration, and cell clustering distinct phenotypic profiles were created for the three cell lines NIH-3T3, HuH7, and A549 using an LDA analysis. The successful distinction between these different cell lines shows that the presented image-based metrics capture essential characteristic phenotypic traits of the cell lines. Furthermore, the demonstrated in situ monitoring of cell growth and motility during subculturing proves that the presented RFLM setups and image analysis methods facilitate tracking of these critical characteristic phenotypic traits during the culture period.

5 Multiparametric Drug Screening Assays Using RFLM

5.1 Introduction

The quantification of cellular response to perturbations is an essential aspect in cytotoxicity testing, preclinical drug discovery, and studying mechanisms of drug action and resistance. A plethora of different techniques for cell-based assays[1] exist to study viability, cytotoxicity, proliferation, and cell migration. A fundamental property of an assay is its readout method: End-point assays provide one measurement value at a single time point at the end of the assay period. In contrast, kinetic assays provide multiple measurement values at different time-points during the assay period. Single target assays measure a single readout parameter, whereas multiplex assays measure several readout parameters simultaneously.
The goal of cell viability assays is to measure quantities which are related to the survival of cells and maintenance of cell functions. Measuring the accumulated enzymatic turnover of tetrazolium compounds such as MTT and XTT to a final product with colorimetric readout and detecting the amount of cellular ATP are two frequently used methods for viability assays based on metabolic activity. These methods also give an indirect measure of the cell number and hence the proliferation. Classical proliferation assays are based on using the rate of DNA synthesis as a direct measure for proliferation by measuring the incorporation of radioactive ^{3}H-thymidine or base analogs like BrdU and EdU into newly synthesized DNA. Unlike cell viability assays, cytotoxicity assays assess the number of dead cells. Most commonly used cytotoxicity assays are based on measuring membrane integrity. Living cells with intact membranes exclude dyes like trypan blue or red-fluorescent propidium iodide, whereas dead cells include the dyes following the loss of membrane integrity. The most frequently used assay to measure cell migration and invasion is based on determining the number of cells which migrated through a porous membrane in a Boyden chamber. Other migration assays are based on measuring the movement of cells into cell-free areas such as the scratch wound assay and cell exclusion zone assays.
Current developments in cell-based assays aim at overcoming some of the limitations of these established classical assays which usually include being single target assays, being endpoint assays, or being invasive or destructive. In this regard, multiplex assays are becoming more

[1] The following reviews and textbooks provide an overview of cell-based assays: [269–272]

prevalent since the measurement of multiple readout parameters provides a more robust assessment of cellular response [273–276]. Electrical sensing of cells, for example, is capable of measuring morphology, motility, cell proliferation, and cytotoxicity as readout parameters. Furthermore, the technique allows real-time and label-free measurements [277–279].
With the dramatic advancement in the power of computational methods, high content screening based on live-cell imaging and automated image analysis has become a powerful tool for cell-based assays as it offers several key advantages. It is a kinetic assay with high time resolution. Unlike electrical sensing, it is compatible with standard multi-well plates. The images provide information on spatial aspects such as cell density. The technique allows measuring the response on the level of individual cells and is inherently multiparametric as the images contain information on a multitude of phenotypic parameters [280, 281]. In this regard, another advantage is the flexibility in data analysis strategies. From a computational viewpoint, a phenotype can be any vector of metrics calculated from an image sequence. Such vectors can be calculated ad hoc after the experiment, and allow constructing complex phenotypic profiles from hundreds of image-based metrics for the determination of the phenotypic response [26, 282, 283].

However, despite the availability of numerous and sophisticated techniques for cell-based assays and their widespread use, it was found that a significant fraction of preclinical results are not reproducible and the rate of successful translation of findings from preclinical research into approved drugs is low [284–286]. In response, it was recommended to raise standards in biomedical research, e.g., concerning the widespread use of mislabeled cells [287–289]. Furthermore, several studies have focused on minimizing the contribution of cell-based assay techniques to the low reproducibility in preclinical research by identifying sensitive factors that can cause variations in the measurement of cellular drug response, and by developing standards to increase the robustness of the procedures [47, 51].
In ***Chapter 4*** it was shown that the culture conditions and history can cause significant genotypic and phenotypic changes in cell lines. Likewise, the culture history and quality of the cells used for cell-based assays can substantially affect the outcome of drug response measurements [31, 45, 46]. Further sensitive factors affecting the measured drug response and robustness of the assay include the total number, density, and spatial distribution of the plated cells, the cell lines growth rate plus the volume, type and batch of used culture medium and serum, and the substrate [47–51, 290].
Time is another inherently critical factor as growth and drug-response can change over the assay period. If the total assay time is long, the cells in the wells with the control and low doses of antiproliferative drugs can exhibit reduced growth due to depletion of the available medium, pH change, or contact inhibition of proliferation at reaching high confluencies. This results in a seemingly reduced cell viability in these wells. As a consequence, the overall sensitivity of the assay is decreased since the response is typically normalized to the control. As the cellular microenvironment of cancer cells plays an essential role in their drug-resistance [291], the drug effect can change over the assay period due to adaptive resistance [47] or due to density-dependent resistance [292–294].
Therefore, it is essential for the robust and reproducible measurement of phenotypic cellular response to drug exposure, that the assay-conditions are well defined and ensure uniform cell growth during the assay period. In addition, suitable metrics, e.g., normalized growth rates [295], are required for the analysis in order to account for effects caused by a time-dependent response and cellular heterogeneity [296, 297].

In this chapter, it is investigated how different RFLM systems in combination with image-based metrics can be used for obtaining cells with well-defined phenotypic characteristic traits, and for subsequent use of these cells in high-throughput time-resolved measurements of phenotypic drug response with well-known initial conditions. To this end, a method for quantitative analysis of the spatial distribution of the cells in the culture flasks and multiwell chambers is presented in order to facilitate a homogeneous seeding density for cell culture and assays. Next, it is shown how image analysis of RFLM image sequences can be used for kinetic wound healing assays. Subsequently, several drug screening experiments were performed with different established and primary cell lines to determine the dose-dependent response of multiple phenotypic parameters such as cell growth and motility. Finally, the time-dependency of the phenotypic multiplexed drug response (EC_{50}, IC_{50}[2]), as well as the capability to measure dynamic drug response, is investigated.

5.2 Seeding Density and Spatial Homogeneity

The results from ***Section 4.5.3*** demonstrate that the RFLM setup presented in ***Section 3.3.1*** allows the continuous monitoring of confluency, cell growth, and cell motility of cultured cell lines directly in the incubator. This monitoring can be used to ensure the timely passaging of a culture before it reaches high confluency. Furthermore, it is possible to detect possible changes in critical phenotypic traits. However, the presented monitoring gave no insights into the spatial distribution of the cells within the culture flask. A nonuniform cell density could increase the phenotypic heterogeneity of the cell population and entail that the growth curve obtained from monitoring is not representative of the whole population. To address this issue, the RFLM setup presented in ***Section 3.2.3*** was used to map the spatial distribution of the cells over the entire substrate area of the culture flasks.

First, the effect of different seeding techniques on the cell density distribution of A549 cells in T75 culture flasks was investigated. ***Figure 5.1*** shows three spatial cell density maps resulting from different seeding techniques. In the first case, the cell-suspension was simply deposited in the flask with the pipette and the flask subsequently placed in the incubator (***Figure 5.1 a***). In the second and third case, the cell suspension was repeatedly dispensed into the flask and re-aspirated with the pipette to distribute the cells homogeneously. Then, the flask was moved repeatedly in an eight-shaped pattern and subsequently transferred steadily from the tissue culture hood to the incubator. In the incubator, the flask was placed on a slightly tilted surface in the second case (***Figure 5.1 b***), whereas the flask was placed on a level surface in the third case (***Figure 5.1 c***). The flasks were incubated for about 1.5 h to let the cells adhere to the bottom of the flasks. In the first case, substantial variations in the measured cell density were observed. A gradient in the measured cell density was apparent in the flask placed on the tilted surface. The cell density was most uniform in the third case, with variations in confluency of about 20 %. The uniformity of the seeding technique can be quantified by calculating the frequency distribution of the measured confluencies for each flask. The frequency distribution corresponding to the third case is significantly more narrow and symmetrical than the frequency distributions corresponding to the other two cases. ***Table 5.1*** summarizes the sample standard deviation and the skewness for the three different seeding techniques as quantitative metrics

[2] EC_{50}: half maximal Effective Concentration; IC_{50}: half maximal Inhibitory Concentration

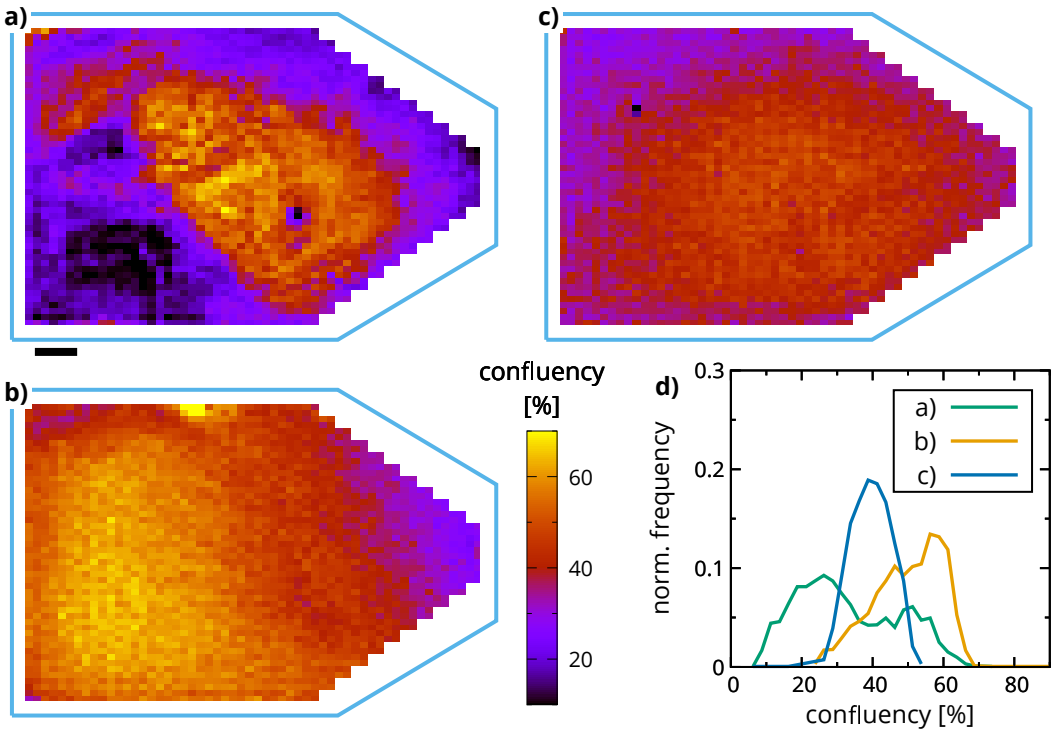

Figure 5.1: Influence of different seeding techniques on the spatial homogeneity of the cell density. **a)** The plot shows the spatial distribution of the cells inside the T75 culture flask after 1.5 h of incubation to let the cells adhere. Each pixel is color-coded with the confluency in a 1.84 mm×1.37 mm area, and the blue lines show the outlines of the cell culture flask. The image shows an inhomogeneous distribution of the cells, with the spatial variations of the confluency exceeding 40 %. Scale bar: 1 cm. **b)** Spatial distribution resulting from a slight tilt of the flask during cell adhesion, resulting in a spatial gradient of the confluence of more than 40 %. **c)** Flask with spatial variations of around 20 %. The cell density is higher in the central areas, and lower towards the periphery. **d)** The plot shows the frequency distributions of the spatially resolved confluencies from a)-c). It can be seen that the variance in a) is the highest. The frequency distribution from b) is significantly skewed. In contrast, the frequency distribution from the flask in c) is symmetrical and substantially more narrow. This finding indicates a significantly more homogeneous cell density than in a) and b). The frequency distributions were created by binning the confluency values of the 2360 pixels into 2.5 % intervals.

to assess the uniformity of the seeding density. It should be noted that the detection of the cell covered substrate area is optimized for adhered cell that are spread out on the substrate. Since the cells are not fully adhered yet after the incubation period of 1.5 h and still exhibit a round morphology, the detection overestimated the confluency, see also ***Appendix Figure 19***. However, while the absolute value of the confluency is slightly biased, the detection of the spatial variations is not significantly influenced by this bias.
In summary, these results demonstrate that the seeding technique has a strong influence on the uniformity of the cell density in the flask. Furthermore, it was shown that the frequency distribution of the confluencies can be used to obtain metrics for the quantitative analysis of this influence.

seeding technique	sample standard deviation	skewness
Case 1	14.3	0.33
Case 2	9.8	-0.37
Case 3	5.6	-0.12

Table 5.1: Metrics for the uniformity of the seeding density shown for the three experiments from ***Figure 5.1***. The best results were obtained for Case 3, as the corresponding confluency distribution exhibits the lowest values for the sample standard deviation and skewness.

Next, the effect of environmental cues on the resulting seeding density was investigated. Here, the flasks were placed on top of different objects after seeding with NIH-3T3 cells. The flasks were incubated for an interval of about 3 h for the cells to adhere to the substrate. ***Figure 5.2*** shows the resulting spatial distribution of the cells in a T25 flask which was placed on top of a metallic object during incubation. The density map clearly shows that the density of adhered cells is distinctively increased in the areas above the object by more than 15 % confluency. Since the cells are seeded into the flask in a sterile cell culture hood, the temperature of the cell suspension inside the flask is significantly lower than the object and air inside the incubator. Therefore, the thermal conductivity and thus the heat transport is substantially higher above the object than in the areas of the flask which are only in contact with the air. Although the exact mechanism for the increased adherence above the object in contact with the flask bottom was not investigated here, this difference in thermal conductance might play a critical role. The example also demonstrates that the occurrence of a non-uniform cell density can have obscure reasons, thereby highlighting the need for quantitative analysis.

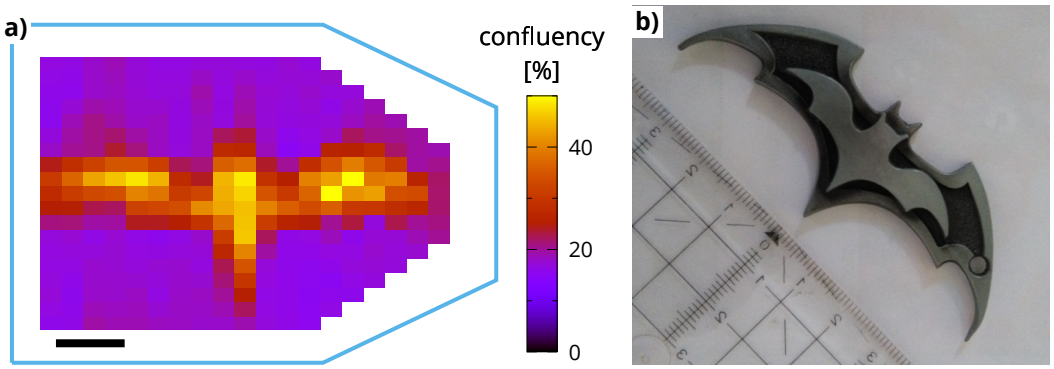

Figure 5.2: Impact of environmental cues on cellular adhesion inside cell culture flasks. **a)** The plot shows the spatial variations of the density of NIH-3T3 cells inside a T25 cell culture flask. The pixels are color-coded with the confluency in a 1.84 mm × 1.37 mm area. The blue lines show the outlines of the cell culture flask, and the scale bar is 1 cm. **b)** Metallic object with an iconized batman shape. The culture flask was placed on top of the object after seeding for an incubation period of about 3 h. Since the cells were seeded into the flask at room temperature, the cell suspension has a lower temperature than the metallic object when they are brought into contact. It can be clearly seen, that the cell density shown in a) is distinctively increased in an area which corresponds to the shape of the metallic object. This result shows that environmental cues can have a substantial impact on the spatial distribution of the cells inside a culture flask.

The introductory section detailed that the number and spatial distribution of the cells inside the wells of a multi-chamber slide or multiwell plate can have a significant effect on the measured drug response and the sensitivity of the drug screening assay. Therefore, the image analysis presented in ***Chapter 4*** is used to obtain metrics to quantify these sensitive factors for control and improvement of the initial conditions of the assay. As a first step, the initial frame of the image sequence is analyzed to obtain the confluency and to detect the cells. The results of the FCN cell detection allow the calculation of the seeding density. Then, the results of the cell covered area analysis are used to extract the value of the confluency in a subwindow of the image (illustrated in ***Figure 5.3 a***). This subwindow is shifted over the whole image, and the local confluency is extracted for each region. Assigning the confluency within the subwindow to the position of its center creates a map showing spatial variations in the confluency (***Figure 5.3 b***). A map of the cell density can be created analogously. These maps visualize the spatial variations in the seeding density and allow to compare the initial conditions in the different wells or chambers in high-throughput experiments to detect potential systematic bias (***Figure 5.3 c***). Calculating the frequency distribution of the local confluencies in the wells provides metrics like sample standard deviation and skewness for a quantitative assessment of the initial conditions (***Figure 5.3 d***). These metrics for that measurement are summarized in ***Table 5.2***. Sample chambers one and two contained small areas with a substantially elevated confluency. Correspondingly, the values of the skewness and sample standard deviation of these chambers were also increased with respect to the other sample chambers.

chamber position	1	2	3	4	5	6	7	8
mean	8.8	12.4	12.7	7.0	10.5	11.6	11.6	9.7
sample standard deviation	7.2	11.4	9.5	5.2	6.6	6.9	7.3	6.3
skewness	1.6	2.3	0.3	0.3	-0.3	-0.6	-0.3	-0.2

Table 5.2: Metrics for the uniformity of the initial confluency for the measurement with NIH-3T3 cells in the 8-chamber slide shown in ***Figure 5.3***.

5.3 Scratch Wound Assay

The scratch wound assay is a popular well-established method to measure cell migration *in vitro* [298]. The assay is based on artificially creating a cell-free gap in a confluent cell monolayer and quantifying the subsequent migration of the cells into the cell-free area. The most frequently employed method to create the cell-free gap is using a pipette tip for scraping the cell monolayer in a straight line, hence the name scratch wound. Then, the scraped cells are removed by rinsing the sample, and an image of the scratch wound is recorded. The rate of migration is measured by comparing this initial image with images acquired at later time points to determine of the area of the cell-free gap which has been closed. A variety of other methods is available to create the cell-free area, for example, the removal of a physical barrier which was applied to the sample substrate prior to cell seeding. This method has the advantage to enable the reproducible generation of a cell-free area with a defined geometry [299].

The closure of the model wound is a complex mechanism and involves several different processes. Due to the contributions of both proliferation and migration, closure of the model wound is

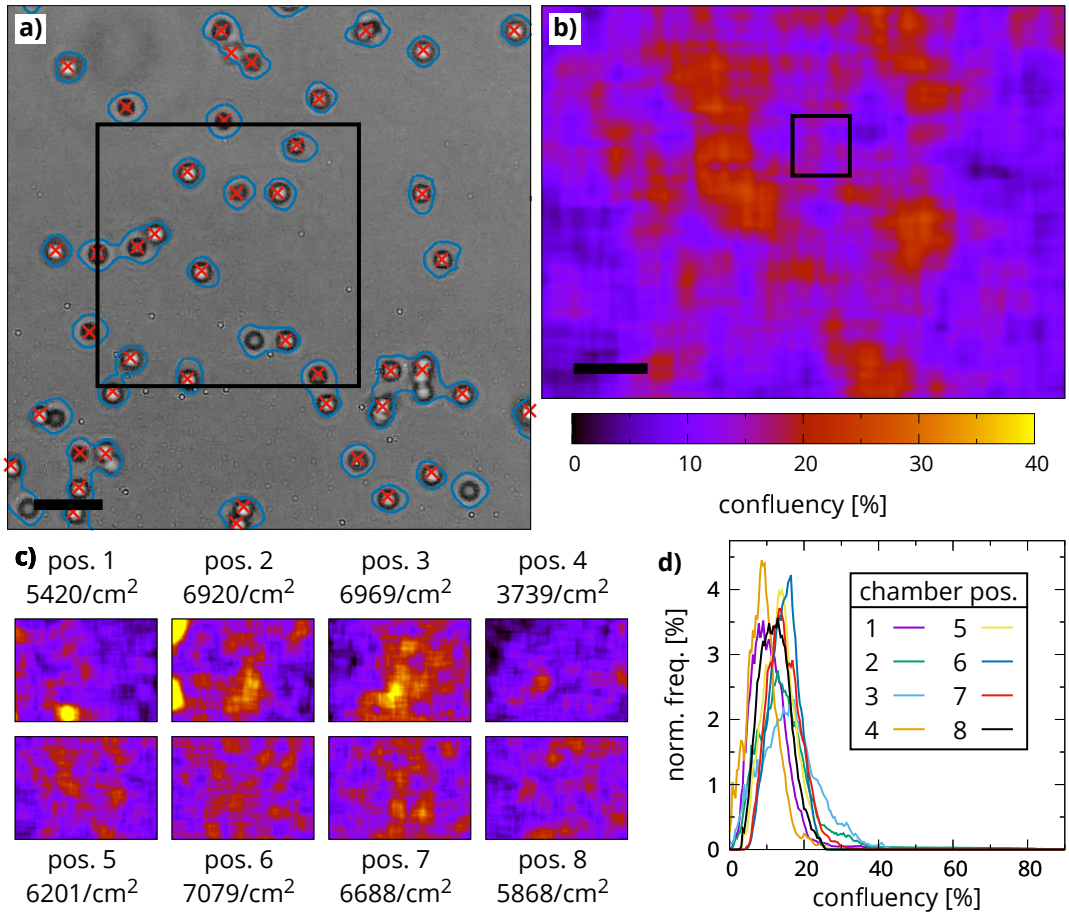

Figure 5.3: Determination of the initial conditions of parallelized RFLM growth measurements. **a)** The image shows the initial frame of an image sequence of NIH-3T3 cells seeded into a chamber of an 8-chamber slide. The results of the cell covered area detection and the FCN cell detection are shown as blue lines and red crosses, respectively. The area is optimized for adhered cells and therefore overestimates the area of the cells during adhesion. The confluency is calculated for a subwindow with a size of 360 µm × 360 µm, which is shifted over the whole image. Scale bar: 100 µm **b)** Map of the confluency within the subwindows. Each pixel is color-coded with the confluency determined in the subwindow that this particular pixel is the center of. The map shows that the confluency varies about 15 % within the image. The black square indicates the size of the shifted subwindow. Scale bar: 500 µm **c)** The graph shows the seeding density and spatial variations of the confluency in the initial images of each chamber of the 8-chamber slide. The map from b) corresponds to the chamber with position five. The results show that the cells are seeded mostly homogeneously inside the wells despite the formation of concave menisci of the cell suspension in the chambers, which tends to lead to an accumulation of cells in the center of the chamber. Chambers one and two contain two small areas with an elevated confluency. **d)** The graph shows the frequency distributions of the local confluency for the eight chambers obtained by binning the confluency values of 3.9×10^6 pixels into 0.4 % intervals. These frequency distributions can be used to calculate metrics such as the mean and the sample standard deviation to assess the quality of the initial conditions of the assay. These metrics are summarized for the shown measurement in ***Table 5.2***.

often modeled as a reaction-diffusion process described by the Fisher-Kolmogorov equation [300, 301]. The equation is given by

$$\frac{\partial c\,(x,t)}{\partial t} = D\nabla^2 c\,(x,t) + \lambda c\,(x,t)\left(1 - \frac{c\,(x,t)}{K}\right) \tag{5.1}$$

and describes the relationship between the cell density $c(x,t)$, the diffusion coefficient D describing the random motion of the cells, the proliferation rate λ, and the carrying capacity density K. It has been reported that the initial conditions defined by a cell density of zero in the cell-free gap and a constant cell density in the remaining areas result in a traveling wave with a speed of $v = 2\sqrt{\lambda D}$. Numerical solutions showed that the cell front initially requires some time to reach the constant speed upon creation of the cell-free gap [301].
This simple model assumes that D and λ are spatially and temporally constant. In practice, however, proliferation and motility of cells depend nonlinearly on the cell density in their surrounding, and the movement of the cells is characterized by long-range correlations [302]. Furthermore, mechanical forces play a critical role, and the cell front typically does not advance uniformly into the cell-free area but has finger-like protrusions which extend into the cell-free area and exhibit increased speeds [303, 304]. Furthermore, different cell lines show different modes of migration during wound closure: Fibroblast-like cells migrate into the cell-free area as a loosely connected population and epithelial-like cells as connected sheets [298].

5.3.1 Analysis of Scratch Wound

To use the presented RFLM setups for scratch wound assays, the detection of the cell covered substrate area was used to automatically detect the converging fronts of the cell layers during wound closure. ***Figure 5.4 a*** shows the cell fronts detected in RFLM images for three different time-points after the creation of a cell-free gap in a monolayer of primary human melanoma cells. This scratch wound assay was carried out in an 8-well chamber slide, and the in-situ 8-chamber live cell imaging RFLM setup (***Section 3.3.2***) was used to acquire a time-lapse image sequence during the closure of the cell-free gap. The results show a good performance of the automatic detection of the cell fronts. A frequently used approach to obtain the front velocity is to plot the segmented gap area against time. Then, fitting a linear function to the data can be used to calculate the front velocity as $v_F = \frac{|slope|}{2L}$, where L is the length of the cell-free gap [305]. ***Figure 5.4 b*** shows a plot of the progression of the fronts for the scratch wound assay with the primary human melanoma cells. For this plot, the mean distance covered by the two converging fronts is calculated as $< W_t - W_0 >= (A_t - A_0)/L$. Here W_0 and A_0 are the initial gap width and area, and W_t and A_t correspond to the current gap width and area. The mean front velocity v_F is then determined by fitting a linear function to the data for $< W_t - W_0 >$ and calculating $v_F = \frac{slope}{2}$. The figure also shows that the fronts require several hours to reach a constant velocity, which is consistent with the reported results of the numerical analysis of the Fisher-Kolmogorov equation [301]. The presented calculation is only valid as long as the gap is not yet closed over a significant fraction of its initial length L. Therefore, the algorithm automatically determines the time-point $t_{50\%}$, when the gap is closed over more than 50 % of L. The range of the linear fit to obtain the front velocity was then restricted to the interval between the time point when the fronts reached a constant velocity and $t_{50\%}$. The perimeter

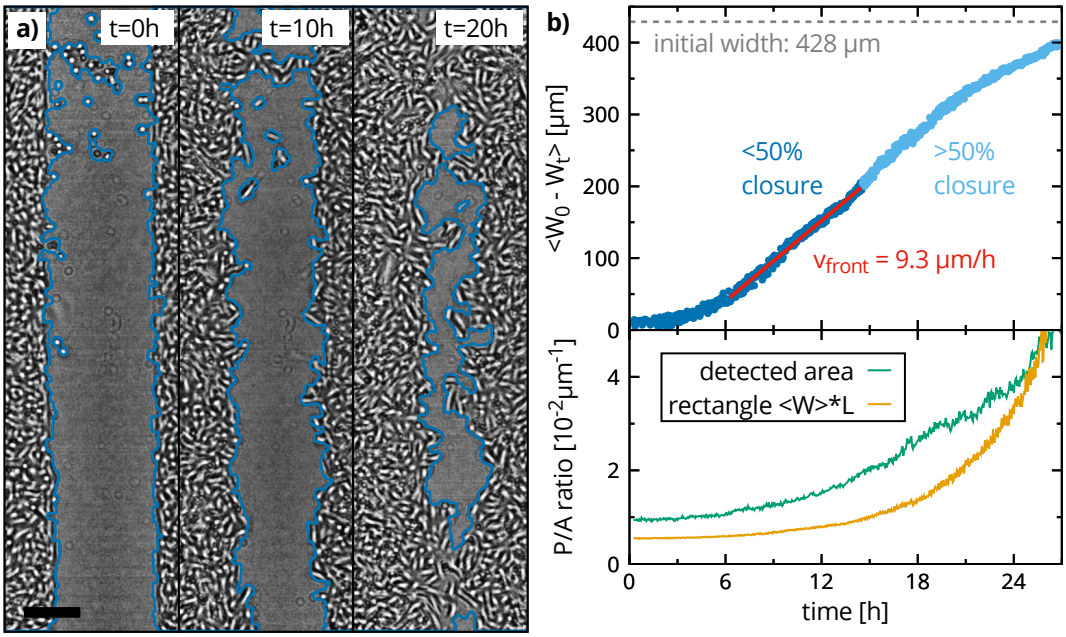

Figure 5.4: Scratch wound assay: Detection and quantification of cell fronts in RFLM images. **a)** The RFLM images illustrate the closure of a cell-free gap in a monolayer of primary human melanoma cells at different time-points. The cell-free gap was created through the removal of a silicone insert. The blue lines show the outlines of the automatically detected cell covered area of the monolayer, corresponding to the two fronts of the converging migrating cell layers. The top of the scratch contains some cells that the rinsing step failed to remove. Scale bar: 250 µm. **b)** The top panel shows a plot of the average distance covered by the cell fronts against time (mean initial scratch-width W_0 - mean current scratch-width W_t). After several hours, the fronts reach a constant velocity, and a linear fit allows to obtain the front velocity. The bottom panel shows the perimeter to area (P/A) ratio for the detected cell-free gap. Additionally, the P/A ratio of the corresponding rectangle with width $<W_t>$ and length L is included, where L denotes the initial length of the scratch. This analysis provides a measure of the uniformity of the cell front. As the gap closes over a significant fraction of its length, the calculation $< W_t >= A_t/L$ becomes invalid, resulting in the crossing of the two curves.

to area (P/A) ratio of the cell-free gap can be calculated as a measure of the uniformity of the cell fronts. The more protrusions a cell-front exhibits, the higher its P/A ratio. A comparison of the P/A ratio of the detected cell-free area with the P/A ratio of a corresponding rectangle with the dimensions $< W_t >$ and L is shown in ***Figure 5.4 b***. The graph for the measurement with the primary human melanoma cells shows that as long as the cell-free gap is not closed over a significant fraction of its initial length, the P/A ratio of the cell-free gap is higher than the one of the corresponding rectangle, but does not diverge with respect to the P/A ratio of the rectangle.

A more detailed analysis of collective cell migration in the scratch wound assay can be achieved by analyzing the cellular motion in the two converging cell layers with PIV [306, 307]. ***Figure 5.5 a*** shows the results of the PIV analysis applied to an RFLM image sequence acquired for a scratch wound assay performed with NIH-3T3 fibroblasts. The converging cell layers exhibit domains with correlated cellular motion and speeds that are significantly higher than

in most of the rest of the cell-layers. The highest speeds are observed directly at the front of the cell layer, as ***Figure 5.5 b*** shows. However, an increased directed motion can be detected in the bulk of the cell layer up to a distance of 450 µm from the front of the cell layer. Therefore, RFLM is an interesting technique to study collective cell migration in the scratch wound assay since the large FOV allows measuring long-range correlations in the velocity fields of the converging cell layers.

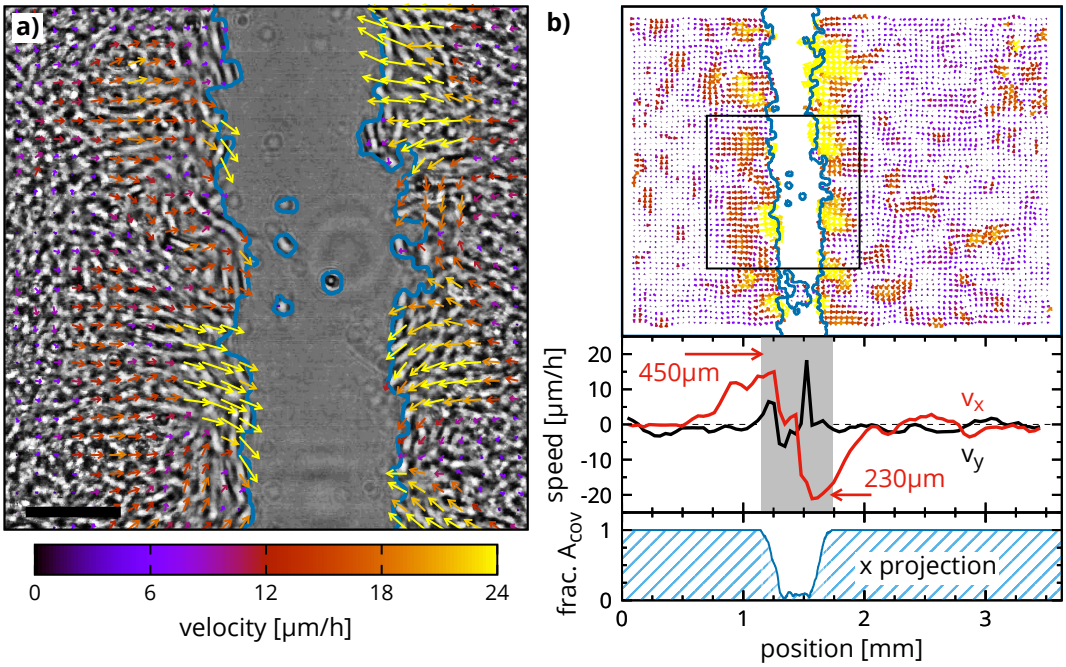

Figure 5.5: Determination of collective cell migration in scratch wound assays using RFLM and PIV. **a)** Section of an RFLM image showing a scratch wound in a monolayer of primary human melanoma cells. The blue outlines show the automatically detected fronts of the converging cell layers and the arrows correspond to the direction and speed of the collective cell migration determined with PIV. The image illustrates the increase in the speed of the cells from the bulk of the layer towards the front. Several domains with elevated levels of speed are visible. Scale bar: 250 µm. **b)** Top panel: The image shows the velocity field in the whole FOV. The region shown in a) is highlighted with a black square. The front of the layer is depicted as a blue line. The velocity field exhibits higher speeds towards the front of the layer. Some domains in the bulk also exhibit increased velocities, however, not necessarily in the direction towards the gap. Middle panel: The plot shows the column-wise average of the x and y components of the velocity vectors. Bottom panel: Column-wise fraction of the pixels which are within the cell layer. The gray area in the middle panel highlights the range in the x-direction that contains the cell-free gap. It can be seen that this region contains the highest values of the column-wise averaged x-components of the velocity vectors ($< v_x >$). The values of $< v_x >$ reach zero in the bulk of the cell-layer at a distance from the front of about 450 µm and 230 µm in the negative and positive x-direction, respectively. The column-wise average of the y-components $< v_y >$ fluctuates around zero along the x-axis.

5.3.2 Impact of Media Supplements on Wound Healing

Preceding this section, it was shown that the presented RFLM systems and image analysis methods can be used for scratch wound assays and provide multiple image-based metrics to determine wound healing efficiency in terms of collective cell migration. In this section, the RFLM system and image analysis are used for parallelized scratch wound assays to investigate the effect of different media supplements on the wound healing efficiency of NIH-3T3 fibroblasts.

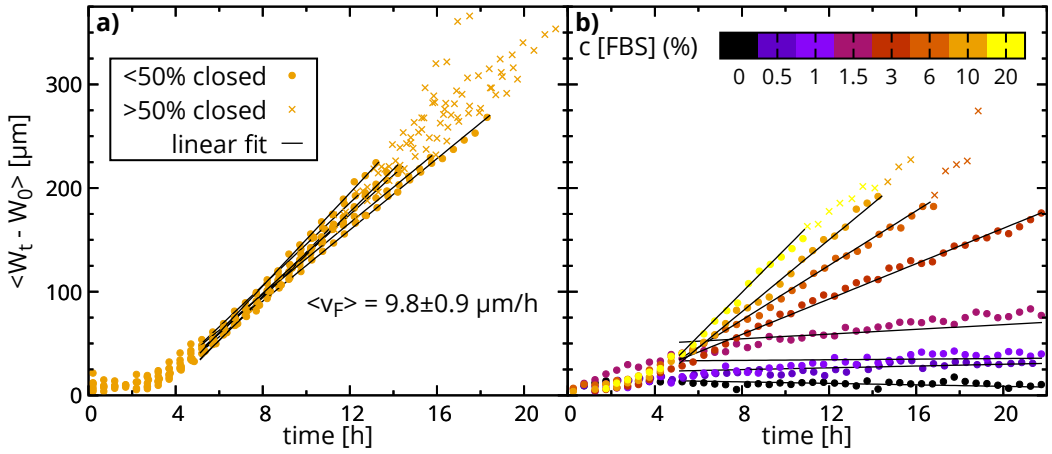

Figure 5.6: Sensitivity of the presented image-based analysis for scratch wound assays. Influence of FBS on the wound healing efficiency. **a)** The graph shows the closure of the cell-free gap as the mean gap distance covered by the cell fronts (mean initial scratch-width W_0 - mean current scratch-width W_t) plotted against time. The shown data is for eight scratch wound assays performed with NIH-3T3 cells simultaneously, and under identical experimental conditions. A linear fit is used to obtain the mean front velocity of $(9.8 \pm 0.9)\,\mu m\,h^{-1}$. The FBS concentration in the medium was 10 %. These results show a variation of about 10 % in the measured speeds under identical conditions, which corresponds to the sensitivity of the method. **b)** The graph shows the results of eight scratch wound assays performed with NIH-3T3 cells simultaneously, but with varying concentrations of FBS in the medium. The mean gap distance covered by the cell fronts is plotted against time. A linear fit is used to obtain the mean front velocity for each concentration. The plot shows that without FBS the gap width remains constant. Below 3 % FBS in the medium, no significant closure of the model wound was observed. To increase visibility, only every tenth datapoint is shown in a) and b).

The first goal was to assess the sensitivity of the technique. To this end, eight scratch wound assays were performed in an 8-chamber slide simultaneously and under identical experimental conditions. The medium was supplemented with 10 % FBS. ***Figure 5.6 a*** shows the results of the measured gap closure. The scratch model wound was closed by the converging cell layers, which migrated with a mean speed of $(9.8 \pm 0.9)\,\mu m\,h^{-1}$ into the cell-free gap. This corresponds to an uncertainty of approximately 10 % for the determination of the front velocity under identical conditions. Subsequently, this uncertainty is used for the front velocities determined with the presented analysis.
Next, the results for the front velocities were analyzed using the Fisher-Kolmogorov equation. According to the supplier, the NIH-3T3 cells have a doubling time of T_2=20 h, which was also

confirmed by the measurements in ***Section 4.5***. Using this doubling time, the measured values of the front velocities and the formula for the velocity of the traveling wave solution $v = 2\sqrt{\lambda D}$, a diffusion coefficient of $D = \frac{T_2 v^2}{4 \ln 2} = 693\,\mu m^2\,h^{-1}$ is obtained. This value is significantly higher than the values between $50\,\mu m^2\,h^{-1}$ and $350\,\mu m^2\,h^{-1}$ that were obtained from the single cell tracking experiments in ***Section 4.5***. Using the Fisher-Kolmogorov equation to obtain the diffusion coefficient of 3T3 cells, values of D=$330\,\mu m^2\,h^{-1}$ have been reported for the scratch assay [258] and D=1500–$2900\,\mu m^2\,h^{-1}$ for a circular barrier array [308]. However, these studies also found that the values reported for similar experiments can vary over more than one order of magnitude. Furthermore, it has also been reported, that the diffusion coefficient obtained from the Fisher-Kolmogorov equation was almost twice as high as the diffusion coefficient obtained by single cell tracking experiments [258]. The possible modification of the substrate with collagen by the cells has been suggested as a possible explanation for this discrepancy. In addition, discrepancies can be caused by variations of the cell density, which can significantly influence the wound healing efficiency and the obtained diffusion coefficients [309].

After the assessment of the sensitivity of the technique, the enhancement of the wound closure speeds due to different concentrations of medium supplements was investigated. ***Figure 5.6 b*** shows the results of a measurement, where the medium contained different concentrations of FBS during the scratch wound assay. FBS concentrations in the medium of 3 % and more clearly caused a substantial enhancement of wound closure. The cells did not migrate into the cell-free gap at all if the medium contained zero percent FBS. ***Figure 5.7 a*** shows the average speeds of the fronts of the cell layers in dependence of the FBS concentration. Two repetitions of parallelized scratch wound assays were performed to assess the possible enhancement of wound healing efficiency by a supplement S_u of unknown composition. The supplement is obtained from milk (unpublished results) as a side-product in the purification of antibodies from bovine milk [310]. For this set of experiments, the medium was supplemented with 0.5 % FBS and varying concentrations of S_u. The dose-dependent response shows that the unknown supplement S_u seems to increase the wound healing efficiency if its volume percentage exceeds 6 % in the medium (***Figure 5.7 a***). However, in the control measurements with 0 % S_u and 0.5 % FBS, a mean front velocity of $(6.5 \pm 2.1)\,\mu m\,h^{-1}$ was measured. This speed is substantially higher than the speed measured in the previous experiment with 0.5 % FBS in the medium. It should be noted, that these experiments were performed with early versions of the setups and analysis. The cultures were not monitored, and unlike in later experiments, the measurements were performed in Leibovitz's L-15 medium. These factors could have contributed to the observed inconsistencies in the measured speeds. To compensate for these experimental inconsistencies, the enhancement of the wound closure efficiency was analyzed by normalizing the measured speeds. To this end, the speeds measured in the FBS concentration series were normalized to the speed measured for the sample containing 0.5 % FBS. The speeds measured in the S_u concentration series were normalized to the speeds of the controls. The normalized enhancement of wound closure is shown in ***Figure 5.7 b***. The results indicate that while FBS is a far more potent supplement for enhancing wound healing, the supplement S_u of unknown composition also enhances the wound healing efficiency by a factor of about two. Although the results are inconclusive due to the experimental inconsistencies, they illustrate that the RFLM system and the analysis provide a suitable tool for kinetic phenotypic screening in scratch wound assays.

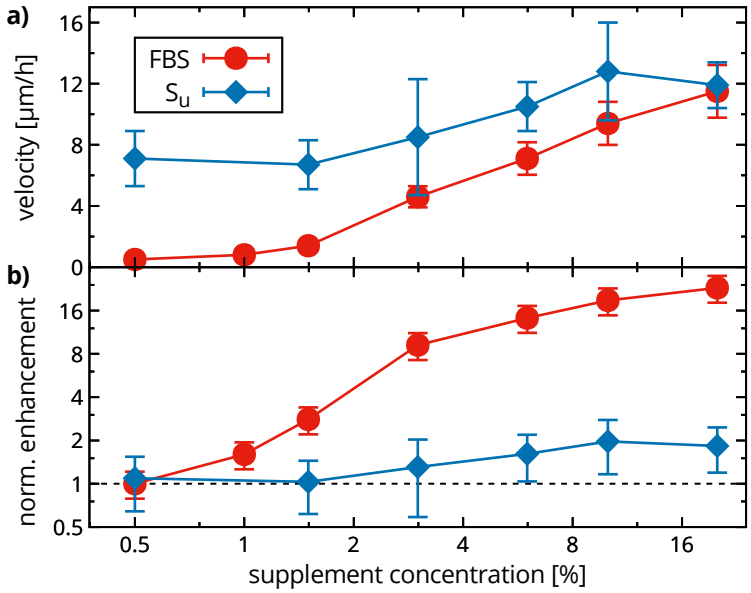

Figure 5.7: Impact of two different medium supplements on wound healing efficiency. **a)** Parallelized scratch wound assays were conducted using 8-chamber slides and NIH-3T3 cells. In the first experiment, the medium was supplemented with varying concentrations of FBS. In the second set of experiments, the medium was supplemented with 0.5 % FBS and varying concentrations of the supplement S_u of unknown composition. The plot shows the average front velocity of the cell layers in dependence of the supplement composition (control for FBS experiment: v=0 µm h^{-1}). For the controls of the second set of experiments with 0.5 % FBS and 0 % S_u, a mean front velocity of (6.5 ± 2.1) µm h^{-1} was measured. This velocity is significantly higher than the velocity at 0.5 % FBS in the first experiment. The plot shows that speed of the cell fronts that are migrating into the cell-free gap increases with increasing concentration of both supplements. **b)** To compensate for the difference in the measured speeds in the controls, the normalized enhancement of the closure speed in dependence of the supplement concentration was calculated. The speeds of the first measurement were normalized to the speed at 0.5 % FBS. The speeds obtained from the second set of experiments were normalized to the speed in the control. The graph shows the resulting normalized enhancement in the speed of the cell fronts due to the medium supplements. The results show that FBS is a far more potent supplement for enhancing wound healing. However, the supplement S_u also significantly increased the wound healing as it increased the mean front velocity of the cell layers by a factor of about two. The high speeds of the control hint at some experimental inconsistency, possibly decreasing the sensitivity of the assay.

5.4 Multiplexed Drug Screening

In the previous section, it was shown that the presented technique can be used to measure the dose-dependent effect of biochemical agents on collective cell migration in the scratch wound assay. The goal of this section is to explore using the simultaneous determination of the dose-dependent inhibition of cell growth and motility for multiplex drug screening assays. Furthermore, the possibility to analyze the recorded interference patterns to assess cytotoxicity is investigated.

5.4.1 Impact of Mitomycin C on Growth and Motility

Mitomycin C is an antitumor drug that inhibits cell proliferation by crosslinking a specific DNA sequence, thereby preventing DNA synthesis [311]. Mitomycin C has also found application in *in vitro* experiments of cell migration, where it has been used to suppress the effects of proliferation [312–314]. The drug concentration where cell proliferation is sufficiently suppressed, but the effect on cell migration is supposed to be as small as possible, is often chosen according to concentrations reported in related studies. Databases such as ChEMBL [315] are very useful in this context as they provide an overview of reported IC_{50} and EC_{50} values for numerous compounds and various cell lines. However, the reported values vary over a wide range of concentrations, even for identical cell lines. Due to the large variations in reported values and the high number of sensitive factors influencing drug response, it can be desirable to determine the optimum concentration for each study individually. To investigate the capability of the presented RFLM system to find such optimized concentrations in a multiplex assay, the response of MDCK cells in cell growth and motility to exposure with different concentrations of Mitomycin C is determined in a parallelized experiment.

Figure 5.8 a shows the growth of MDCK cells exposed to different concentrations of mitomycin C, measured as the increase of confluency over time. The results show significantly reduced growth for the treatment of the cells with a concentration of 1 µM mitomycin C. For higher concentrations, proliferation stops almost completely. Hafner et al. proposed to use the normalized growth rate inhibition (GR) as a metric to quantify drug response since it is largely independent of the assay duration and the growth rate of the cells [316]. Therefore, the measured growth curves are approximated with smooth curves $c_i(t)$ to follow the GR approach. The approximation is described in more detail in ***Appendix 4.2***. The curves $c_i(t)$ approximate the data well, as ***Figure 5.8 a*** shows. Dividing the derivative $\dot{c}_i(t)$ by the y-value of the approximated curve gives the normalized growth rate. For the controls, the normalized growth rates remain constant for 36 h, corresponding to the exponential growth phase, as ***Figure 5.8 b*** shows. The normalized growth rates for higher mitomycin C concentrations are reduced. The normalized growth rates are averaged over the interval from 6 h to 42 h to generate the dose-response curve for cell proliferation. ***Figure 5.9 a*** shows the resulting dose-response curve for the normalized growth rates. Such dose-response curves can be fitted with logistic functions to obtain IC_{50} and EC_{50} concentrations [317]. The IC_{50} obtained from fitting the dose-response curve for the normalized growth rates is $0.37\,\mu g\,ml^{-1}$. MLT was used for single cell tracking in the same image sequences that are used for the determination of the normalized growth rates to obtain a measure for the dose-dependent motility. Here, the average MSD_{3h} was calculated and used to generate the dose-response curve for the motility shown in ***Figure 5.9 b***. Fitting

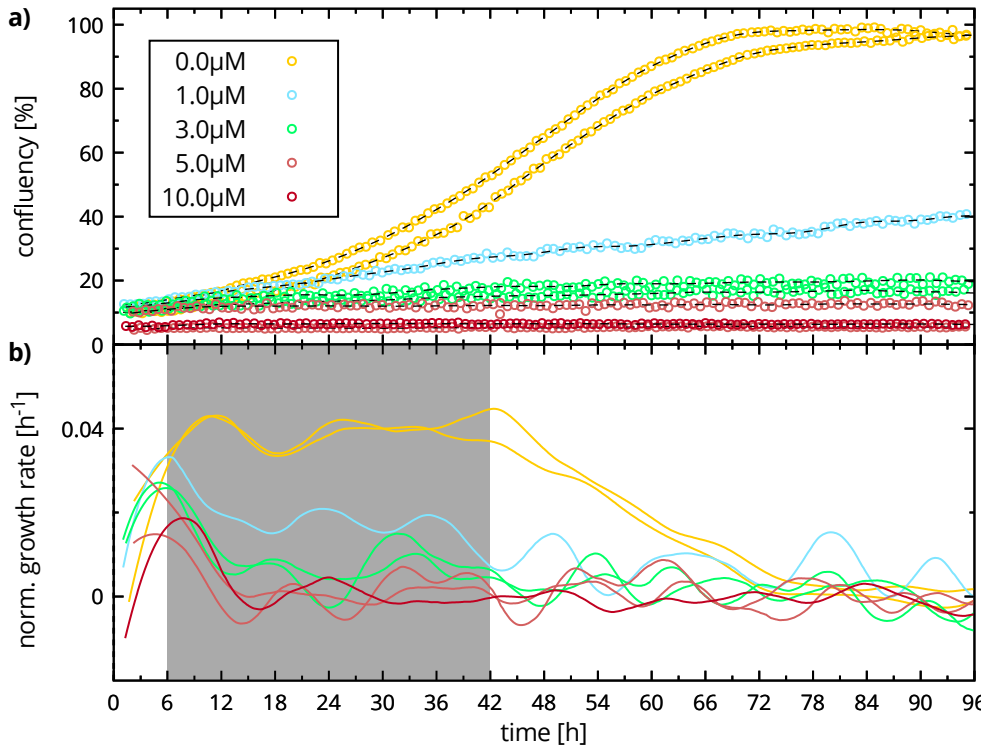

Figure 5.8: Determination of the dose-dependent antiproliferative effect of Mitomycin C on MDCK cells. **a)** The graph shows a plot of the confluency against time for different Mitomycin C concentrations. Growth is substantially inhibited for treatment with 1 µM of mitomycin C, and no significant growth is observed for higher concentrations. The data is approximated with smooth curves, drawn as black dashed lines. **b)** The graph shows a plot of the corresponding normalized growth rates against time. Constant positive normalized growth rates correspond to the exponential growth phase. The normalized growth rates were averaged over the interval from 6 h to 42 h to obtain a measure for the dose-dependent response.

the dose-response curve gives an EC_{50} of 1.6 µg ml^{-1}. The results indicate that at a concentration of about 1 µg ml^{-1} (3 µM), proliferation is strongly inhibited, whereas cell motility is only inhibited weakly. The obtained IC_{50} and EC_{50} concentrations are lower than the concentrations of about 5.0 µg ml^{-1} used in experiments with dense layers of MDCK cells [302, 313]. However, the sensitivity of the cells might be increased due to the low seeding densities that are used for the experiments presented here. It should also be noted, that the exposure to mitomycin C also had a substantial impact on the morphology of the cells (see ***Appendix Figure 17***), which might affect the efficiency of the tracking.

In summary, the results presented in this section show that RFLM live-cell imaging and image-based metric can be used to determine several phenotypic parameters like cell growth and motility in one measurement simultaneously. Therefore, the technique is in principle capable of label-free multiplex cell-based assays. It provides a convenient tool to fine-tune the concentrations of biochemical agents for experiments where it is vital to selectively affect only one of the two phenotypic parameters migration or proliferation.

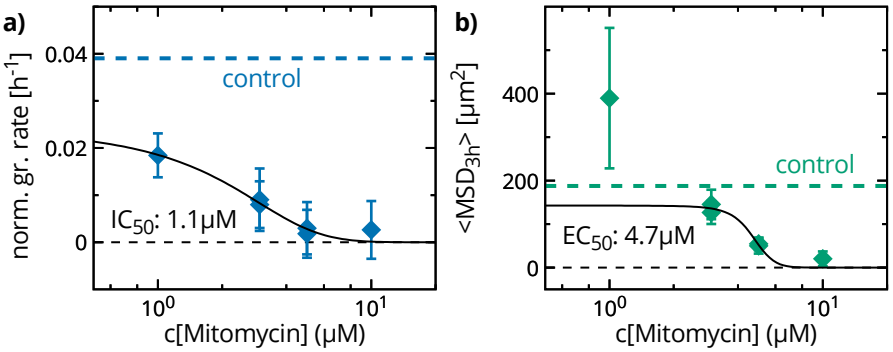

Figure 5.9: Dose-response curves of proliferation and motility for the exposure of MDCK cells to Mitomycin C. **a)** The average normalized growth rate is plotted against different concentrations of Mitomycin C. The error bars correspond to the sample standard deviation of the normalized growth rate in the calculation interval (***Figure 5.8 b***). The solid line shows a sigmoidal fit to the data (to extract the IC_{50}). The function values at positive and negative infinity were fixed to zero, and to the normalized growth rate of the control, respectively. **b)** The graph shows the MSD_{3h} (the average over the interval 0 h to 48 h) plotted against the mitomycin C concentration. The error bars correspond to the sample standard deviation in the calculation interval. Single cell tracking with MLT was used to obtain the MSD_{3h} from the same image sequences that are used for the determination of the normalized growth rates shown in a). With respect to the control, the measured motility is increased for 1 µM and decreased for higher concentrations. The solid line indicates a sigmoidal fit to the data (to extract the EC_{50}). The function values at positive and negative infinity were fixed to zero, and the value of the control, respectively. The value for 1 µM was excluded from the fit.

5.4.2 Cytotoxicity and Validation of Growth Inhibition

In the previous section, the normalized growth rate determined from the measured confluency was used to quantify the antiproliferative effect of mitomycin C on MDCK cells. In this section, two frequently used anti-cancer drugs with different mechanisms of action are used as a reference to assess the reliability of the image-based determination of growth inhibition through comparison with the established MTT assay. Furthermore, the potential of morphology-based and motility-based metrics for cytotoxicity testing is investigated.

In a first set of experiments, HeLa cells were exposed to different concentrations of docetaxel, and the phenotypic response was measured by analyzing the recorded RFLM image series. Docetaxel is a cytotoxic agent which prevents mitosis by disrupting microtubule reorganization, thereby inducing apoptosis and cell death [318]. In a second set of experiments, the effect of etoposide on HeLa cells was investigated. Etoposide acts on the enzyme topoisomerase II and causes it to introduce breaks into the DNA. The accumulated effect of the disruptions caused by these breaks ultimately results in apoptosis [319].

Figure 5.10 shows sections of RFLM images of HeLa cells at different time points after exposure to two different concentrations of etoposide. The effect of the higher dose (500 µM) on the cell number and morphology of the cell population is clearly visible. Here, an earlier version of the cell detection and tracking was used to analyze the images. The cell detection is based on using gray value levels and geometric parameters of the detected areas. The details of this

gray value level (GVL) based analysis are described in ***Appendix 3.4***, together with a comparison with the FCN cell detection and the MLT tracking. Concerning the detection of cells, the performance of the GVL-based analysis is significantly worse than the FCN cell detection. However, the obtained motility measure MSD_{1h} is comparable for both approaches, and unlike the FCN cell detection, the GVL-based analysis provides image-based metrics for assessing morphological changes. The image of the sample treated with 500 µM etoposide (***Figure 5.10***) shows a high number of interference patterns with a circular shape and very pronounced first order intensity minima and central maxima with a significantly reduced brightness. The GVL-based analysis detects cells with a bright central first order intensity maximum and cells with a dark interference pattern separately. Furthermore, the GVL-based analysis was used to calculate the ellipticity of the bright central intensity maximum for each cell to provide a metric for the elongation of the cells.

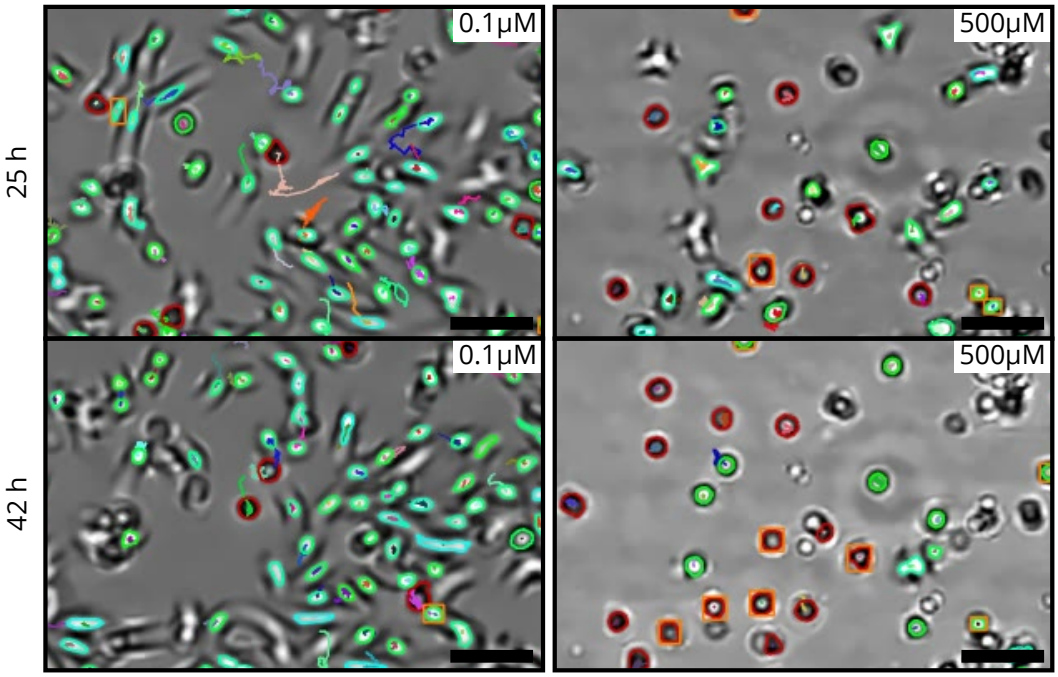

Figure 5.10: Effect of etoposide on proliferation, motility, and morphology. Time-lapse image series were acquired for HeLa cells plated in an 8-chamber slide and exposed to different concentrations of etoposide. The images show sections of the recorded RFLM images 25 h and 42 h after the start of the measurement for treatment with 0.1 µM and 500 µM etoposide, respectively. Unlike for the 0.1 µM sample, no cell growth can be observed for the 500 µM sample, clearly illustrating the antiproliferative effect. The images are superimposed with the results of an earlier version for cell detection and tracking, which is based on gray values and geometry. The analysis shows the outlines of the detected area of the central intensity maxima of the cells. The lines are color-coded with the ellipticity; rounder cells appear more green, more elongated cells more turquoise. Tracked trajectories are drawn as randomly colored lines. The outlines of cells with a circular diffraction pattern and a below-average brightness are drawn with red lines. Cells that are exhibiting only minimal movement are highlighted with orange squares. Although the algorithm fails to detect a significant number of cells, the results clearly illustrate that the sample with 500 µM contains considerably more cells with a dark diffraction pattern as well as non-moving cells. Scale bar: 50 µm.

A comparison between the images of the sample treated with 0.1 µM etoposide and the sample treated with 500 µM etoposide shows that the number of cells with a circular dark interference pattern is considerably increased for the later. This finding suggests that these interference patterns correspond to dead cells, especially since it has been reported that a similar approach allows a dead/alive classification [73]. To achieve a robust dead/alive classification, the trajectories of the cells could be used as an additional indicator of cell death. Therefore, the trajectories of the cells were used to determine for each cell if the standard deviation of its position calculated over 12 consecutive frames is less than 1.1 µm. If this was the case, a cell was classified as immobile. In general, using this motility-based measure for a reliable dead/alive classification

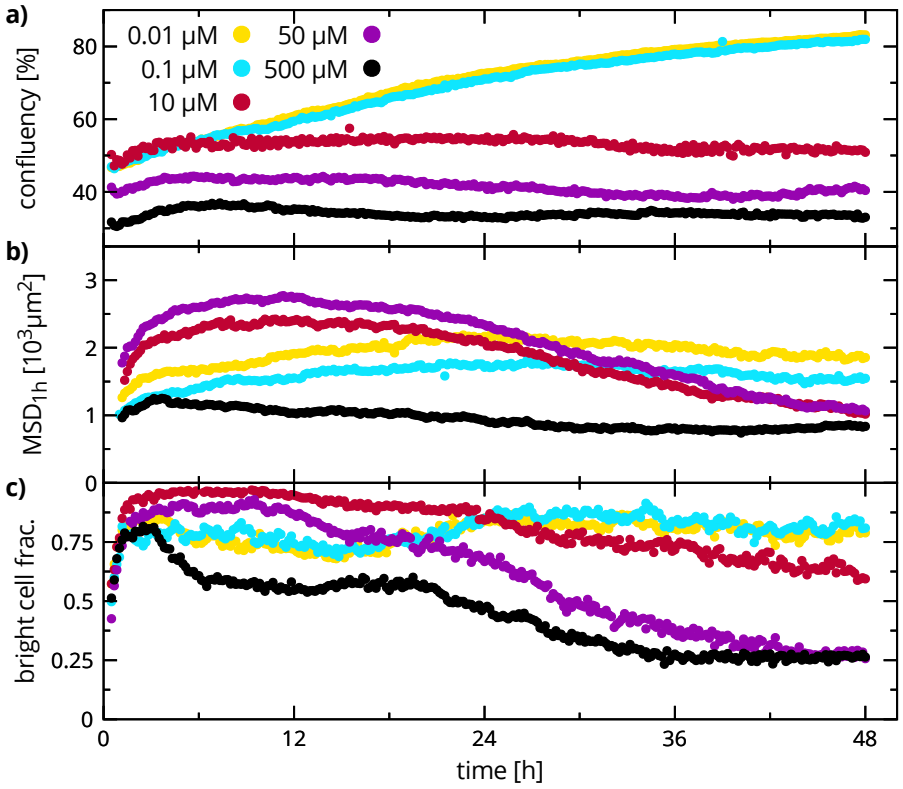

Figure 5.11: Dose-dependent effect of etoposide on proliferation, motility, and the diffraction patterns of HeLa cells. **a)** The plot shows the confluency of the samples against time. An increase of confluency was measured for concentrations of 0.1 µM and less, whereas no increase in confluency was observed for concentrations of 10 µM and higher. **b)** Effect on cell motility, shown as a plot of the MSD_{1h} against time. Interestingly, the cells treated with intermediate concentrations (10 µM and 50 µM) exhibit the highest motilities during the first half of the assay period. However, in the second half of the assay period, the motility decreases below the motility of the samples exposed to the lower concentrations, which show no significant variation of motility over the assay period. The cell motility is substantially reduced for treatment with 500 µM etoposide. **c)** The number of cells with a bright central intensity maximum is plotted against time as the fraction of these cells of the total number of detected cells. For the samples treated with the two highest concentrations of etoposide this fraction decreases with a dose-dependent trend over time to about a quarter. For the two lowest concentrations, the fraction remains mostly constant at around three quarters. Due to a malfunction of the camera imaging the control during this measurement the corresponding curves are missing.

would require further fine-tuning of the parameters to correlate the immobile cells with cell death. However, the increased number of cells classified as immobile in the 500 µM sample shown in ***Figure 5.10*** indicates this might be a feasible approach.

Figure 5.11 shows the evolution of cell proliferation, motility, and morphology of HeLa cells over time for the treatment with different concentrations of etoposide. Here, cell proliferation was assessed using the confluency growth curve (a) and cell motility by calculating the MSD_{1h} (b). The morphology was assessed by calculating the fraction of the number of cells with a bright central intensity maximum (c).
For the cells treated with 500 µM etoposide, the growth curves show that the cells do not proliferate. The motility is substantially reduced, as is evident from the MSD_{1h}. Furthermore, the lowest fraction of cells with a bright central intensity maximum can be observed for this concentration. This fraction drops to about a quarter over the measurement period. The response in these three parameters suggests a strong cytotoxic effect that eventually causes cell death. For the two lowest concentrations (0.01 µM and 0.1 µM), cell growth, a constant motility, and a constant fraction of bright cells of above 0.7 can be observed.
The cellular response to the two intermediary concentrations (10 µM and 50 µM) is more multifaceted. No proliferation is visible in the corresponding growth curves. A slight decrease increase in the fraction of cells with a bright intensity maximum over the measurement time is visible in the case of 10 µM, whereas this fraction drops to the level of 500 µM for 50 µM over the duration of the assay. The cells treated with the intermediary concentrations exhibit the highest motility of all samples during the first half of the measurement. However, the motility decreases during the last two-thirds of the measurement period and eventually drops almost to the level of the cells treated with 500 µM.
These findings suggest that at concentrations starting at about 10 µM, docetaxel has an increasingly cytotoxic effect, especially at prolonged exposure. At 10 µM, the cells do not proliferate, and their motility decreases over time. However, the still comparably high fraction of cells with a bright central intensity maximum suggest that the exposure to 10 µM etoposide does not cause significant cell death.

To assess if the determination of dose-response curves for growth inhibiting agents by analysis of RFLM image sequences provides reliable results, the well-established MTT assay was used as a benchmark. To this end, two sets of dose-response measurements were performed, the first with docetaxel, and the second with etoposide. Each of these sets of experiments consisted of three repetitions of live-cell imaging measurements with RFLM and three repetitions of a simultaneously prepared MTT assay. For the live-cell imaging measurements, the cells were grown in an 8-chamber slide and exposed to different concentrations of docetaxel/etoposide. For the MTT assay, the cells were grown in a 96-well place and exposed to the same concentrations, where each concentration was measured in quintuplicate. A plate reader was used to obtain the normalized viability from the MTT assay. For the RFLM results, the increase in the number of detected cells (GVL-based detection) over the assay period was normalized to the control to obtain a measure that was used as the normalized viability. The resulting dose-response curves and the corresponding sigmoidal fits to determine the IC_{50} are shown in ***Figure 5.12*** for the two drugs.
For docetaxel, the two dose-response curves measured with the two different methods are in good agreement, and the IC_{50} values are comparable (16 nM for MTT, 13 nM for RFLM). In contrast, the IC_{50} of etoposide was 36 µM when measured with the MTT assay, and 4 µM when measured with RFLM live-cell imaging. However, it is known that the type of assay affects

the measured dose-dependent response [51]. Obtaining the dose-response curves from RFLM live-cell imaging data is based on measuring proliferation, which is inhibited completely by etoposide in a concentration range between 0.1 µM and 10 µM as ***Figure 5.11*** shows. The data also suggests that the highest increase of the cytotoxic effect takes place between 10 µM and 50 µM. In contrast, the MTT assay is based on measuring metabolism. However, cells with suppressed proliferation can still be able to metabolize MTT. Therefore, in the MTT assay the cytotoxic affect can have a larger impact on the measured viability than the antiproliferative effect. This difference in the readout method might explain that the IC_{50} from the MTT assay is substantially larger.

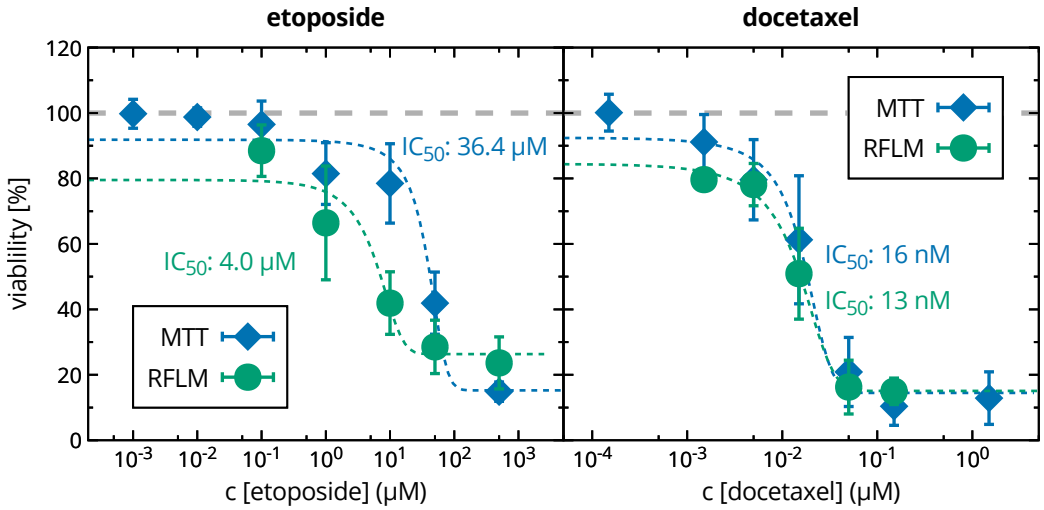

Figure 5.12: Comparison of dose-response curves obtained using the MTT assay and RFLM live-cell imaging. The plots show the effect of different concentrations of etoposide and docetaxel on the viability of HeLa cells. The IC_{50} concentrations were determined by fitting a 3-parameter sigmoidal function to the data. The functions were fixed to 100 % at minus infinity. The resulting best-fit functions are drawn as dashed lines. The IC_{50} values determined by using the two different methods are in very good agreement for docetaxel. In contrast, the IC_{50} for etoposide determined with the MTT assay is almost one order of magnitude higher than the IC_{50} determined from the RFLM image sequences.

In summary, it was shown that live-cell imaging with RFLM can be used to obtain multiple image-based metrics to measure the dose-dependent drug-response of several phenotypic parameters like cell growth, motility, and morphology. The results suggest that depending on the mechanism of effect of a drug the dose-response curves agree well with results obtained with conventional cell viability assays like the MTT assay. Furthermore, it was shown that cytotoxic agents influence the interference patterns of the cells, which suggests that the RFLM images can also be used for cytotoxicity testing.

5.4.3 Primary Melanoma Cells

The previous sections demonstrated the capability of the presented technique to determine cell migration and cell proliferation in parallelized measurements. To this end, well-established

drugs like etoposide and docetaxel, and frequently used established cell lines such as NIH-3T3 fibroblasts and HeLa cells were used. In this section, the phenotypic dose-dependent response of two primary human melanoma cell lines to several biochemical agents is investigated. The first one of the two cell lines is resistant to MAPK[3] inhibitors and the second one is sensitive to MAPK inhibitors. The resistant and sensitive cell lines are referred to as R and S in the following.

First, the effect of the aspartylprotease inhibitor pepstatin A on the collective cell migration of the two cell lines was investigated with parallelized scratch wound assays. ***Figure 5.13*** shows the results of the scratch wound assays for treatment of the two cell lines with 10 µM pepstatin A and respective control measurements. For the assayed concentration, no effect of pepstatin A on the efficiency of scratch wound closure was observed. The R cell line exhibited a higher wound healing efficiency with a mean front velocity of $(12.3 \pm 1.2)\,\mu m\,h^{-1}$ than the S cell line with a mean front velocity of $(7.2 \pm 0.4)\,\mu m\,h^{-1}$.

Subsequently, it was tested if differences can be observed between the two cell lines concerning their respective response in cell proliferation and migration to exposure to different biochemical agents. To this end, live-cell imaging based proliferation and scratch wound assays were performed in 8-chamber slides. Normalized growth rates were calculated from the confluency growth curves and used as a metric for cell proliferation. Cell migration was determined by

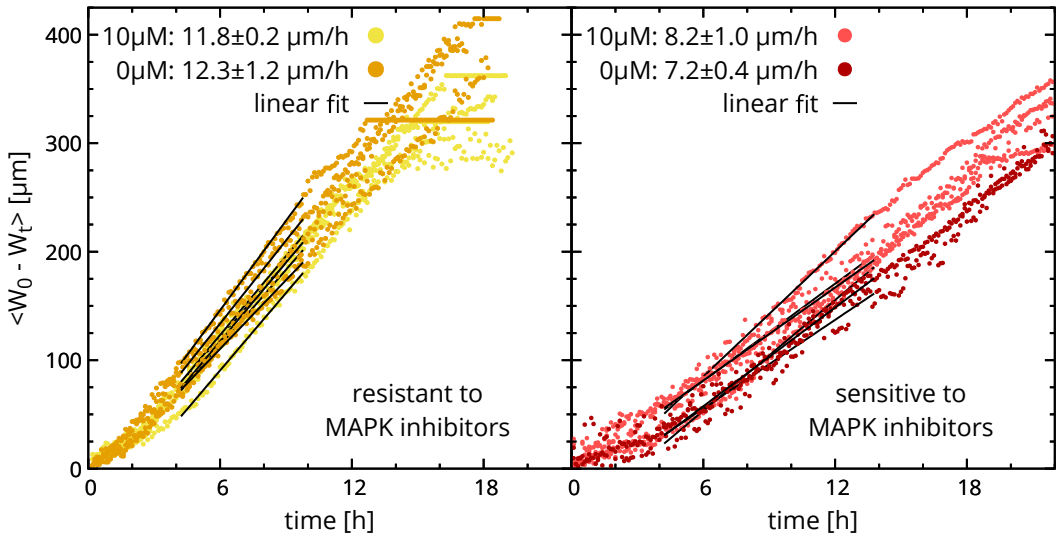

Figure 5.13: Effect of pepstatin A on the wound healing efficiency of a MAPK inhibitor resistant and sensitive primary melanoma cell line. The plots show the average distance covered by the cell fronts against time (mean initial scratch-width W_0 - mean current scratch-width W_t). Linear fits to the data are used to obtain the average front velocities. The cells in four chambers of an 8-chamber slide were treated with 10 µM pepstatin A and the cells in the remaining four chambers were treated with a corresponding control medium. The curves show that the resistant cell line exhibits a higher wound closure efficiency than the sensitive cell line. However, no effect of the treatment with pepstatin A on the wound healing efficiency was observed for either of the two cell lines.

[3]MAPK: mitogen-activated protein kinase

measuring the front velocity of converging cell layers in scratch wound assays. In these experiments, the cells were treated with different concentrations of T-5224, an inhibitor of the c-Fos/activator protein-1 [320], the chelating agent neocuproine, and BMS-754807, an inhibitor of IGF-1R/IR (insulin receptor/insulin-like growth factor receptor 1), which is a target of anticancer drugs [321]. ***Figure 5.14 a*** shows the dose-response curves of wound closure efficiency and ***Figure 5.14 a*** for the proliferation of the two cell lines and the three different agents, respectively. For the tested concentrations, T-5224 has no effect the scratch wound closure efficiency or the proliferation in neither of the two cell lines. In contrast, BMS-754807 and neocuproine both inhibited the proliferation as well as the scratch wound closure efficiency of the MAPK inhibitor sensitive cell line, whereas no noticeable response was observed for the MAPK inhibitor resistant cell line (with the exception of an apparent small antiproliferative effect of BMS-754807).

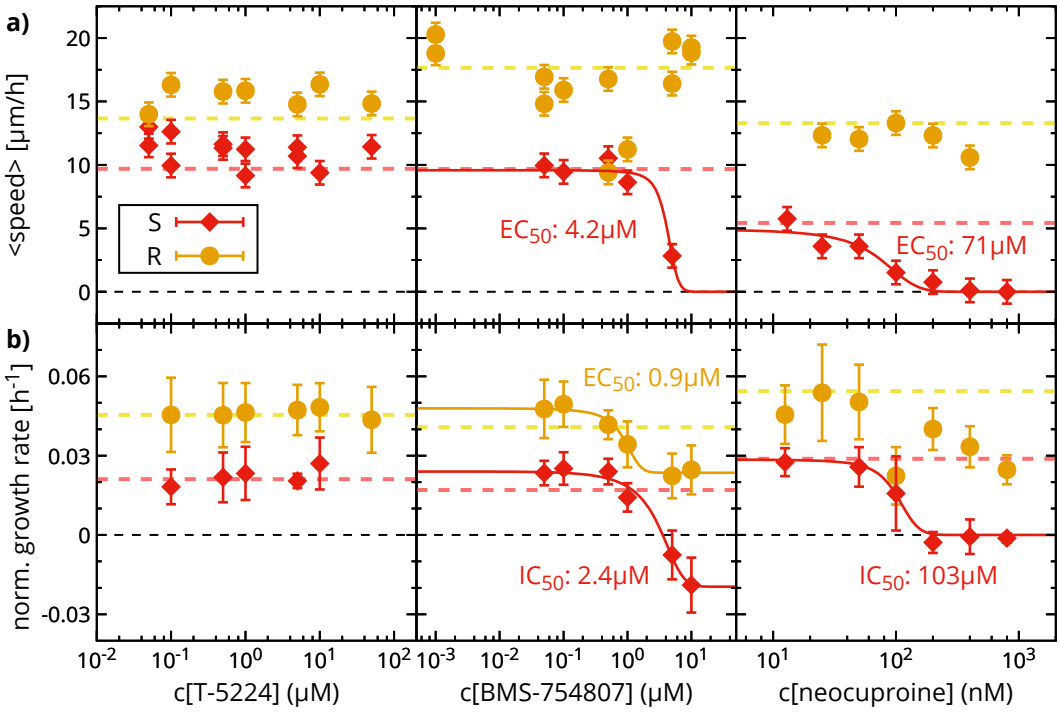

Figure 5.14: Dose-response curves for the MAPK resistant (R) and sensitive (S) primary melanoma cell line for treatment with T-5224, BMS-754807, and neocuproine. **a)** The plots show the efficiency of scratch wound closure, measured as the mean front speed of the cell layers in dependence of drug concentration. **b)** Graphs showing the normalized growth rates in dependence of drug concentration. Dashed lines indicate the value of the control in a) and b). Where applicable, the dose-response curves were fitted with a sigmoidal function that was fixed to zero and the value of the control at positive and negative infinity, respectively. In case of the proliferation assay of BMS-754807, the value at positive infinity was used as a fit parameter, and the value at negative infinity was fixed to the respective maximum relative growth rate. No response in scratch wound closure efficiency or proliferation was observed for treatment with T-5224 for neither of the two cell lines. In contrast, BMS-754807 and neocuproine both inhibited proliferation as well as scratch wound closure of the S cell line, whereas no such response was observed for the R cell line (except for BMS-754807, which appears to reduce the proliferation of the R cell line by about a factor of two).

The typical assay duration of the shown experiments was less than 24 h. Therefore, these results demonstrate that the technique can be used as a fast assay to assess the effect of biochemical compounds on proliferation and cell migration of primary human cancer cells.

5.4.4 High-throughput Cell Viability Assays

All preceding measurements of drug response were performed with the 8-chamber slide RFLM setup. While this setup allowed parallelized measurements, the throughput remained limited. To increase the throughput, a setup that moves a row of cameras with a linear translation stage to acquire images of cells inside the wells of standard multiwell plates was designed and presented in ***Section 3.3.3***.
In the following, first, the increased throughput of the multiwell setup for multiplex viability assays is demonstrated. To this end, the multiwell setup is used to measure the response in proliferation and motility of NIH-3T3 cells to exposure to the previously used mitomycin C. Furthermore, the influence of the assay duration on the measured dose-dependent response is examined. The dose-dependent response is calculated for different assay durations and compared with the results from MTT assays that were performed with different assay durations.

In contrast to the 8-chamber slide setup, the position of the image sensor with respect to the imaged sample region does not remain fixed, and the bottom of the multiwell plate is not in contact with the image sensor. ***Figure 5.15 a*** shows the confluency growth curves for different mitomycin C concentrations, measure with the multiwell plate-setup. The growth curves are smooth, and no apparent differences to the growth curves obtained with the 8-chamber slide setups are visible. This indicates that no artifacts due to the translation of the image sensors between the wells have been introduced and that the same sample region is imaged in each acquisition cycle. As expected, proliferation decreases with increasing mitomycin c concentration. The cell motility was determined by using the MLT and using the tracking data to calculate the MSD_{1h}, which is shown in ***Figure 5.15 b***. The measured cell motility first increases for about 12 h after plating and subsequently decreases for the rest of the assay period. Furthermore, the results show a dose-dependent inhibition of motility.
The experiment was conducted twice, and the obtained growth curves and MSD_{1h} values are used to calculate the dose-dependent normalized viability. To this end, the proliferation rate and the average MSD_{1h} for each concentration are normalized to the values of the control. Here, the growth curves and the MSD_{1h} from the first 48 h of the measurements are used to calculate the proliferation rates and the values for the average MSD_{1h}. ***Figure 5.16 a*** shows the resulting dose-response curves for proliferation and motility. For comparison, the dose-response curve measured with an MTT assay over the same assay duration is included. The IC_{50} and EC_{50} for the inhibition of cell proliferation, motility, and metabolism are determined with sigmoidal fits to the dose-response curves.
For cell proliferation, the obtained IC_{50} of $0.05\,\mu g\,ml^{-1}$ is about seven times smaller than the IC of $0.37\,\mu g\,ml^{-1}$ obtained previously in ***Section 5.4.1*** for the MDCK cells. These findings indicate that the NIH-3T3 cells react far more sensitive to mitomycin C than the MDCK cells. For both the MDCK and the NIH-3T3 cells, the EC_{50} for the effect on cell motility is about three to four times higher than the respective IC_{50} for the proliferation. The IC_{50} for the viability measured with the MTT assay is the highest of all three readout methods. The

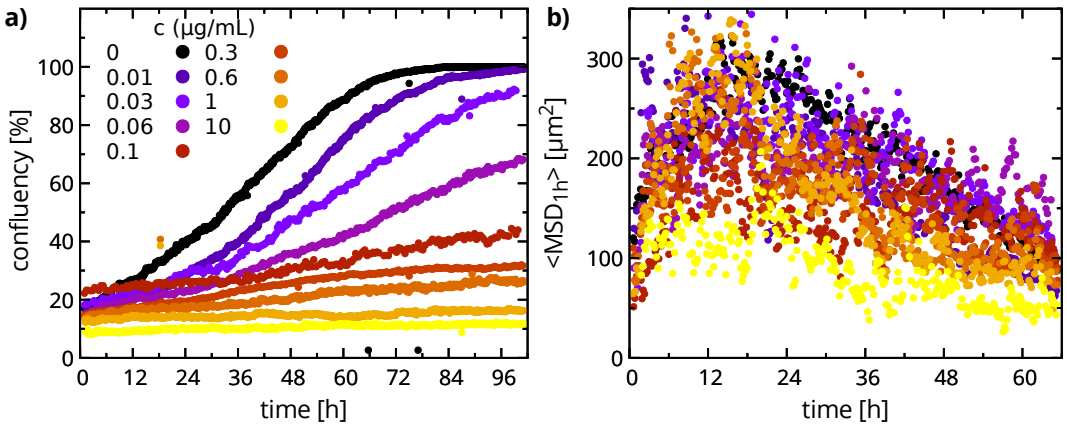

Figure 5.15: High-throughput measurement of the time-resolved response in proliferation and motility of NIH-3T3 fibroblasts to treatment with mitomycin C. **a)** For each of the nine concentrations measured in triplicate, one representative growth curve is shown in this plot as the increase in confluency over time. A dose-dependent proliferation inhibiting effect is clearly visible. The highest concentrations suppress proliferation completely. **a)** The graph shows a plot of the MSD_{1h} as a measure of cell motility plotted against time. The data shows one measurement of each concentration. An increase of the motility can be observed during the first 18 h of the measurement, which is followed by a decrease over the rest of the assay period. The results also show a dose-dependent reduction in motility.

same observation was made in ***Section 5.4.2*** in the comparison between using the proliferation from the RFLM measurement and using the metabolic activity measured by the MTT assay as readouts for cell viability in the case of HeLa cells and the drug etoposide. As discussed in that section, the inter-assay variation of the results can most likely be attributed to the different readout methods instead of experimental errors since non-proliferating cells can still exhibit an intact metabolism.
The next goal was to investigate the impact of the assay duration on the determination of the drug response. To this end, the dose-response curves and IC_{50}/EC_{50} values were calculated over different time intervals to simulate different assay durations. In addition, MTT assays were performed with an assay duration of 48 h, 72 h, and 100 h to obtain dose-response curves for different assay durations. All dose-response curves were fitted with sigmoidal functions to extract the corresponding IC_{50}/EC_{50} values. The dependence of the resulting IC_{50}/EC_{50} on the assay duration is shown in ***Figure 5.16 b***. Using the growth curves measured with RFLM live-cell imaging to determine the IC_{50} provides results that do not vary with different assay durations. RFLM provides fast results for measurements of the inhibition of proliferation since less than 18 h appear to be sufficient for obtaining an accurate IC_{50}. In contrast, the inhibition of motility and metabolic activity appear to depend on the assay time, as the corresponding IC_{50}/EC_{50} values decrease with longer assay durations.

In summary, it was shown that RFLM provides a viable option for high-throughput multiplex viability assays based on label-free live-cell imaging. The technique is compatible with standard multiwell plates and allows fast measurements of the dose-dependent inhibition of cell proliferation since only short assay durations are required to provide accurate results.

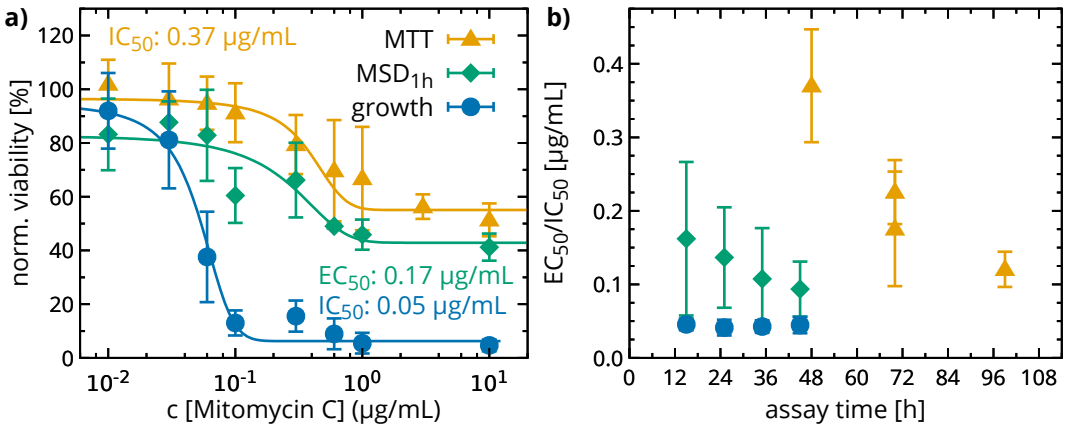

Figure 5.16: Comparison of different readouts and assay periods for viability assessment. **a)** The plot shows the dose-response curves for the proliferation and motility obtained from RFLM live-cell imaging. Furthermore, the plot includes the dose-response curve for the metabolic activity obtained with the MTT assay. The three readouts were determined after an assay period of 48 h, normalized to the respective average of the control, and plotted as a normalized viability against the corresponding concentration. IC_{50}/EC_{50} values were determined with sigmoidal fits fixed to 100 % at negative infinity. The dose-dependent response varies significantly between the three different readouts. Proliferation is inhibited at a lower concentration than motility and metabolic activity, with the latter being the least inhibited readout measure. The shown data contains two repetitions of the assays. **b)** Effect of the assay period on the measured drug response and IC_{50}/EC_{50} values. The IC_{50}/EC_{50} for the motility and proliferation were calculated by adjusting the interval where the growth curves and MSD_{1h} curves shown in ***Figure 5.15*** were analyzed to obtain the relative viabilities. MTT assays were performed using three different assay durations, as the computational adjustment of the assay period is not possible. It can be seen that the IC_{50} determined from the growth curves does not change with different assay times. The EC_{50} for the motility changes with assay time and the inhibitory effect appears to increase over the assay time. For the MTT assay, a decrease in the IC_{50} can be observed with increasing assay time.

5.5 Dynamic Drug Response

Finally, it was investigated if the presented technique is capable to measure dynamic changes in the drug response with high temporal sensitivity. One disadvantage of conventional anti-cancer drugs is the lack of possibilities to target specific locations at specific time-points or over a defined period of time. Therefore, the development of biochemical agents with the possibility to control their effect both spatially as well as temporally are active fields of research. It has been reported that photostatins (PSTs) provide a class of inhibitors that is well suited for this purpose [322]. Light allows switching the PSTs between an inactive state, and an active state in which the PSTs disrupt microtubule dynamics. The delay in the effect on the microtubule dynamics after activation is less than a second. However, in order to achieve the desired antiproliferative effect, the duration and periodicity of the intervals where the PSTs or other temporally controlled agents are active have to be optimized. This section addresses the question if the presented RFLM setups and analysis provide a suitable means to measure the dynamics of the cellular response caused by such novel biochemical agents.

To this end, an experiment was performed where the dynamic cellular response in proliferation was measured by varying the activity of the PST over the time course of the measurement. First, a suitable PST-concentration range was determined. Here, the 8-chamber slide setup with additional UV LEDs (***Section 3.3.2***) was used to control the activity of the PST and simultaneously acquire images of the cells. In this first experiment, the UV LEDs were switched on for 10 s every 4 min. This illumination scheme ensures that the PST is in the active state during the whole measurement period. ***Appendix Figure 18*** shows the obtained growth curves. A PST concentration of 1 µM results in a complete stop of proliferation, whereas no significant inhibition of growth with respect to the control was observed for the exposure of the cells to PST in a concentration of 0.5 µM.
Based on these results, PST concentrations of zero, 0.75 µM, and 1.5 µM were chosen to investigate the sensitivity of the detection of a time-dependent response in proliferation. Each concentration was measured in duplicate. 5 h, 13 h, and 22 h after the start of the measurement, the UV illumination switched the PST into its active state for a duration of 0.3 h, 1 h, and 8 h, respectively. The total dose of UV light was substantially lower than in the previous experiment to avoid a potential cytotoxic influence of the UV light. To this end, only 500 ms pulses were applied every 60 ms to keep the PST in its active state during the corresponding intervals. ***Figure 5.17*** shows the growth curves and normalized growth rates obtained from two repetitions of the experiment using this temporal PST activation scheme. A decreased proliferation of the cells that are exposed to the PST can be seen in the growth curves during the second two activation intervals. During the last activation interval, the relative growth rates of the cells that are exposed to the PST drop to around zero. Subsequently, after the end of the PST activation with UV light, these growth rates return to the previous levels within about 3 hours. In contrast to the PST treated cells, the normalized growth rates of the control samples remain constant.

These findings demonstrate that using live cell imaging with the presented RFLM setups in combination with the analysis of the growth curves facilitates measuring dynamic changes in drug response. A sudden inhibition or enhancement of proliferation can be detected within a few hours as a signature in the growth curve. Therefore, the technique provides a suitable system to study novel biochemical agents that exhibit complex temporal aspects in their effect on cells.

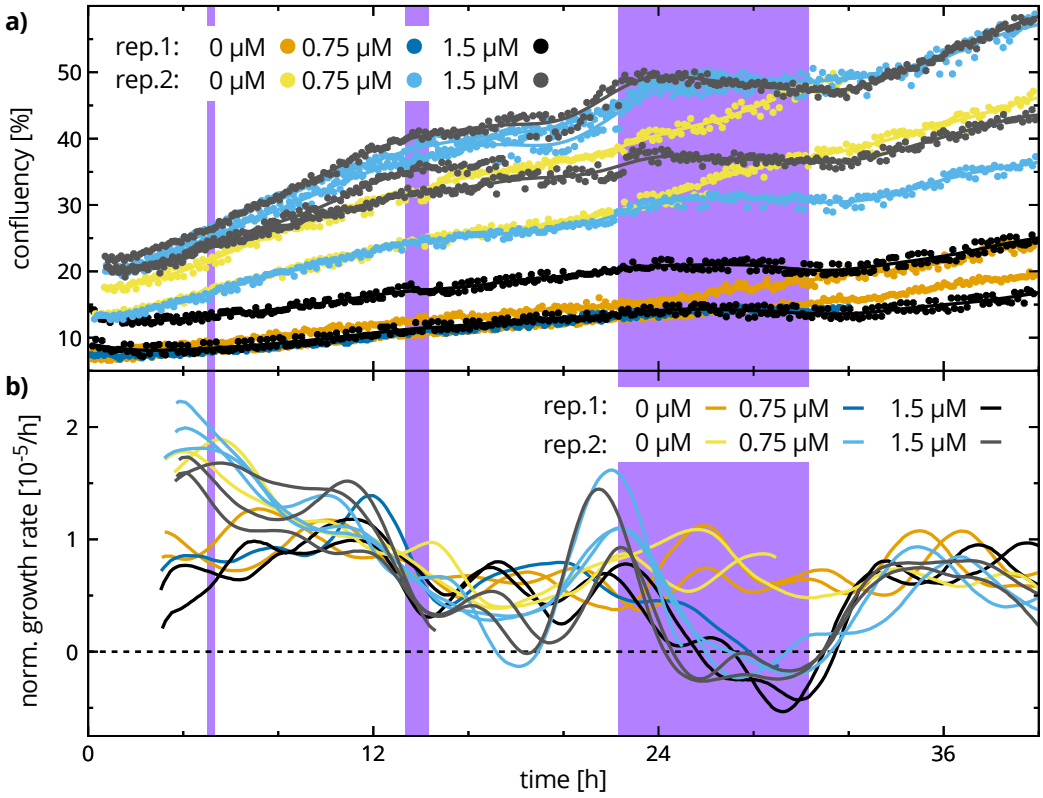

Figure 5.17: Dynamic response in proliferation caused by controlled temporal variation of PST activation. **a)** The graph shows a plot of the confluency against time. The cells were exposed to different concentrations of the PST. The background areas shaded in violet indicate time intervals where the PST was activated with short pulses of UV light. The data includes two repetitions of the experiment, where each PST concentration was measured in duplicate. A few curves terminate before the end of the measurement, which was caused by technical problems of the corresponding cameras. No apparent effect on the proliferation is visible for the first short activation interval. For the subsequent two activation intervals, proliferation is temporarily and reversibly inhibited for the cells exposed to the PST, whereas such behavior cannot be observed for the control. **b)** The normalized growth rates for the curves from a) are plotted against time. Since the cells do not reach stable constant growth before approximately 16 h, no observations can be made for the first two activation intervals. However, it is clearly visible that during the last activation interval the proliferation rate of the cells exposed to the PST drops to around zero, whereas the proliferation rate of the cells in the control remains constant. The proliferation rate of the affected cells returns to the previous levels after about 3 h.

6 Analysis of Bacterial Microcolonies

As briefly outlined in ***Section 2.1.3***, analyzing bacterial growth and the susceptibility to antibiotic substances plays an essential role in drug-development and studying biofilm formation. For antimicrobial susceptibility testing, bacteria are grown in broth or on agar substrates, and a variety of different techniques can then be used to measure the response to the assayed antimicrobial agent [323, 324]. As shown in the previous chapters, the presented RFLM systems can be used to analyze growth and motility of eukaryotic cells. In this chapter, the feasibility of using the presented RFLM system for the analysis of bacterial microcolonies as well for the discrimination between different bacterial strains is evaluated.

The first reports describing LM for bacterial detection used thin wetting films to create microlenses on top of each images bacterium in order to improve image resolution in on-chip LM [325]. LM has also been used to quantify bacterial biofilms by measuring its light absorbance [326]. Jung and Lee showed that on-chip LM can also be used to detect bacterial microcolonies and count them in real-time [327]. Maeda et al. presented a method using LM and a custom sample chamber to measure the growth of bacterial microcolonies on agar substrates and discriminate different bacterial species without removing the cover-glass of the CMOS-Sensor as in the on-chip methods [204]. In this study, seven parameters, which included time dependent-parameters such as colony appearance time and maximum specific growth rate, were used for colony discrimination[1].
The following section addresses the question if the presented high throughput RFLM setup can be used in combination with suitable image analysis algorithms to detect bacterial microcolonies on agar patches inside standard multiwell plates. Furthermore, it is investigated if the technique allows single-shot bacterial strain discrimination.

To this end, the HT RFLM setup (presented in ***Section 3.3.3***) was used to acquire time-lapse image series of bacterial microcolonies growing inside standard 24-well multiwell plates, as ***Figure 6.1 a*** illustrates. The whole setup was placed inside a standard incubator to guarantee ideal growth conditions for the bacteria. The bacterial microcolonies were grown on thin agar patches that were placed inside the wells to provide the bacteria with nutrients. The used agar

[1] Unknown to the author at the time of writing, two weeks before the print of this thesis a follow-up study demonstrating an extended analysis for colony fingerprinting was published [328].

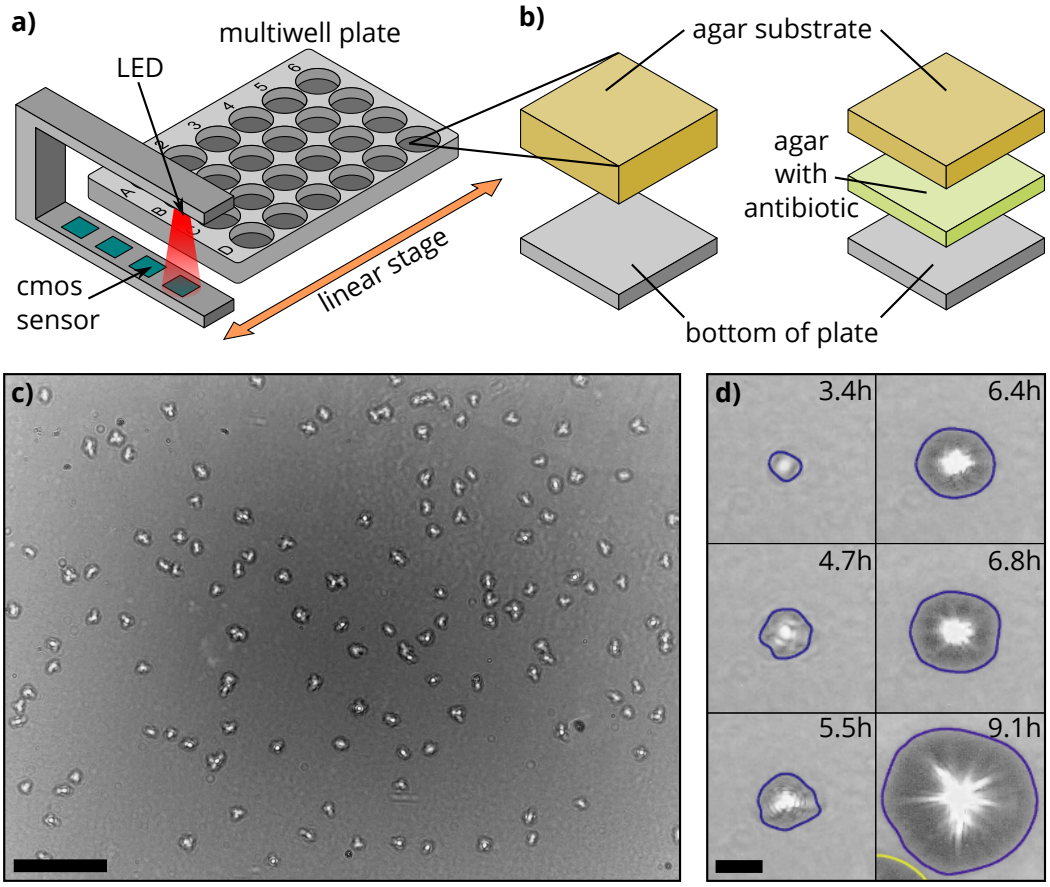

Figure 6.1: High-throughput analysis of bacterial microcolonies with RFLM. **a)** The in situ setup acquired time-lapse image series of bacterial microcolonies growing inside standard 24-well plates by moving a row of four image sensors beneath the plate using a linear translation stage. **b)** The bacterial microcolonies were grown on either single layer or double layer agar patches placed inside the multiwell plates. The double layer arrangement allowed the time-delayed exposure of the bacterial microcolonies to antibiotics included in the bottom agar layer. **c)** Full FOV of the image sensor showing 130 individual bacterial microcolonies of an E. coli strain. Scale bar: 500 µm. **d)** The area of the growing microcolonies can be automatically detected with the developed algorithm despite the change in the appearance of the colony over time. This is illustrated by the outlines of the automatically detected area at various time-points of the measurement. Scale bar: 100 µm

patches[2] were several millimeters thick and consisted either of a single agar layer or of two agar layers, where the bottom layer contained antibiotic agents (see ***Figure 6.1 b***). The double layer patches allow the introduction of a varying time-delay in the effect of the antibiotics on the bacteria by placing the top layer onto the bottom layer at any time-point during incubation. This time-delay facilitates, for example, the measurement of the typical size of a biofilm forming bacterial microcolony at which the colony acquires unspecific antibiotic resistances through biofilm formation. RFLM is well suited for this task since a typical FOV contained more than 100 individual microcolonies, see also ***Figure 6.1 c***. Time-lapse image sequences of growing

[2]The details of the fabrications of the agar patches and their use for bacterial susceptibility testing can be found in the Master's thesis of Lamparter[329].

colonies of the two different bacterial strains E. coli and B. subtilis were acquired to demonstrate the feasibility of this technique for the analysis of bacterial microcolonies. The colonies and their area were automatically detected by an algorithm which is explained in detail in the following section. ***Figure 6.1 d*** illustrates the results of the area detection at various stages of a growing microcolony. The development of the colony area over time can then be used to calculate growth rates, e.g. for growth phenotyping [330].

6.1 Detection of Microcolonies

While individual bacterial cells cannot be resolved due to the limited resolution of RFLM, the diffraction patterns of bacterial micro-colonies, however, are clearly distinguishable from the background in the recorded RFLM micrographs. ***Figure 6.2 a*** shows that the diffraction pattern of a monolayer bacterial microcolony consisting of around 16 individual cells is dis-

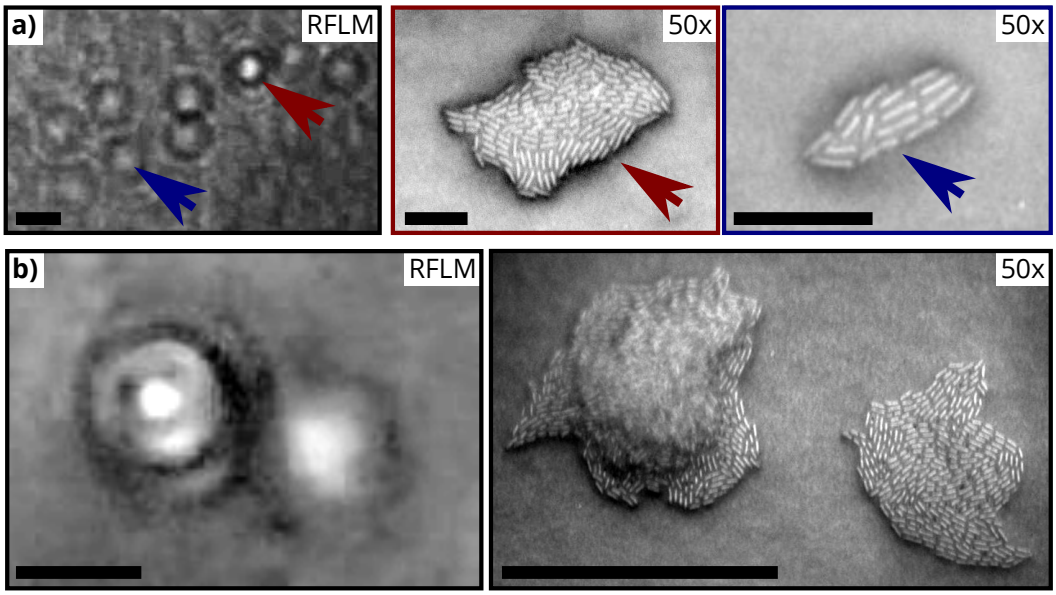

Figure 6.2: Appearance of bacterial microcolonies of the E. coli strain in RFLM images. **a)** RFLM and corresponding 50x brightfield microscopy images of monolayer bacterial microcolonies. The scale bar is 50 µm in the RFLM image and 10 µm in the 50x microscopy images. The maxima of the diffraction pattern of the larger colony highlighted with the red arrow is clearly distinguishable from the background and its signal to noise ratio is sufficient for automatic detection. The diffraction pattern of the smaller microcolony which contains about 16 individual cells is highlighted with a blue arrow. While the diffraction pattern is discernible by eye, the automatic detection of these small microcolonies is not robust enough due to the low contrast. **b)** RFLM and corresponding 50x brightfield microscopy images of two bacterial microcolonies. The brightfield image shows that the colony on the right side is formed by a monolayer of cells while the colony on the left side consists of several vertically stacked layers of cells. The RFLM image shows that the diffraction pattern of the multilayer colony exhibits significantly increased contrast compared to the monolayer colony. The scale bar is 50 µm in both images.

cernible in an RFLM image. However, only larger colonies with a lateral dimension of more than 10 µm provide sufficient signal to noise for automatic detection. ***Figure 6.2 b*** shows that once the microcolonies started to grow in 3D by forming multilayers, the contrast increased further.

The development of the algorithm for the automatic detection of the microcolony area was based on making several key adjustments to the algorithm for the detection of the cell covered area which was described in ***Section 4.2.1***. Likewise, the algorithm was implemented with a custom C++ program. The program uses various functions of the OpenCV library (version 2.4 [231]). In the following section, function names in italic refer to OpenCV functions. Prior to analysis, the raw color RFLM images were preprocessed according to ***Appendix 3.1***. To each used image the *GaussianBlur* function is applied before any further steps are performed to reduce pixel noise. To detect the substrate area covered by the microcolonies, the four

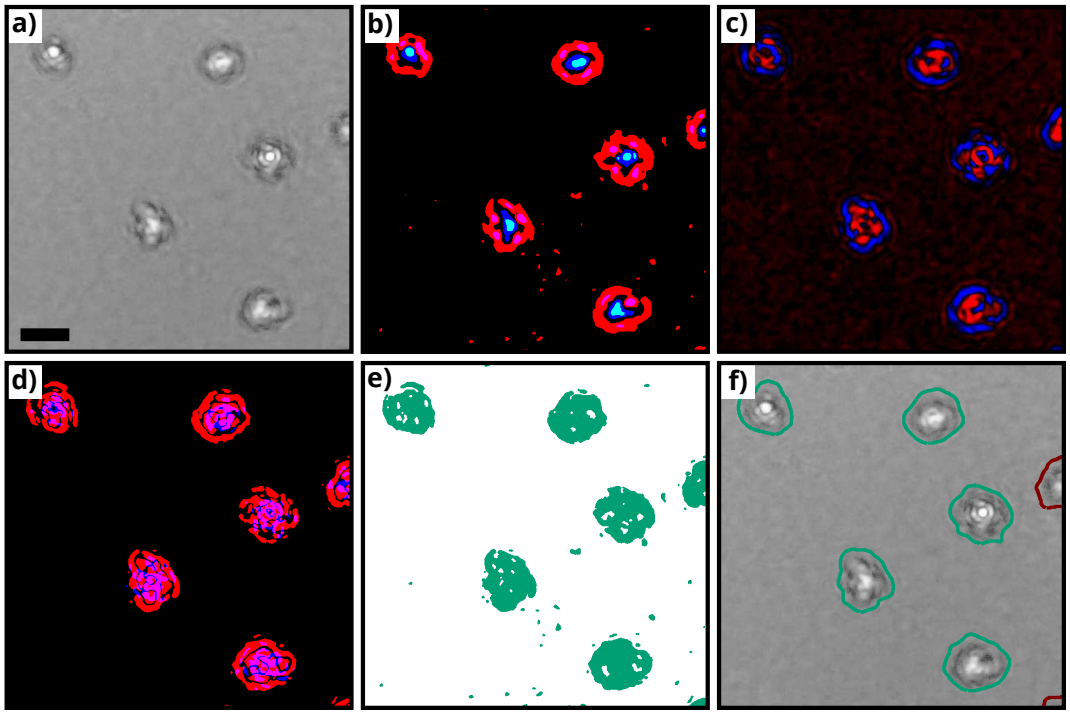

Figure 6.3: Detection of bacterial microcolonies in RFLM images. **a)** RFLM image showing microcolonies of the E. coli strain. Scale bar: 100 µm. **b)** The image shows the result of the image filters corresponding to the binary masks M1 and M3 applied to the image section from a). Areas drawn in green/red correspond to pixels with gray values above/below local thresholds from the binary mask M2, and areas drawn in blue correspond to the binary mask M1. **c)** Temporal activity map of the sample showing the pixel-wise balanced intensity gain (red) and loss (blue), calculated over several frames. **d)** The image shows the binary mask M2 resulting from thresholding the temporal activity map as the blue channel, and the binary mask M4 as the red channel. **e)** The image shows the area resulting from combining the four binary masks M1-M4 drawn in green. **f)** Illustration of the final result of the area detection of the microcolonies drawn as green lines after the post-processing step of the mask obtained in e). The outlines of colonies at the image border are drawn as red lines and the corresponding colonies are discarded from the analysis.

masks M1-M4 used for the automated detection of the cell covered area for the eukaryotic cells (***Section 4.2.1***) were calculated for each frame. ***Figure 6.3*** shows the four masks calculated for an RFLM image of bacterial microcolonies. The obtained binary masks are combined and post-processed identically as in the algorithm for the eukaryotic cells.

However, the temporal evolution of the area of the bacterial microcolonies is incorporated in a different fashion which reflects the growth behavior of the colonies. ***Figure 6.4 a*** illustrates the working principle of the algorithm. Unlike the colonies of eukaryotic cells which show significant fluctuations in their outlines and sizes due to cell migration and association and dissociation from and to the clusters, the bacterial colonies are stationary and exhibit mostly isotropic expansion of their outlines. Thus, in a first step, a coarse-grained segmentation of the colonies is performed by manually selecting the detected microcolonies from a post-processed mask like in ***Figure 6.3 f***. This mask is calculated from one single frame of the sequence where the colonies are clearly detectable by calculating the binary masks M1-M4 and applying the post-processing step. The mask with the manually selected colonies serves as a constraint for

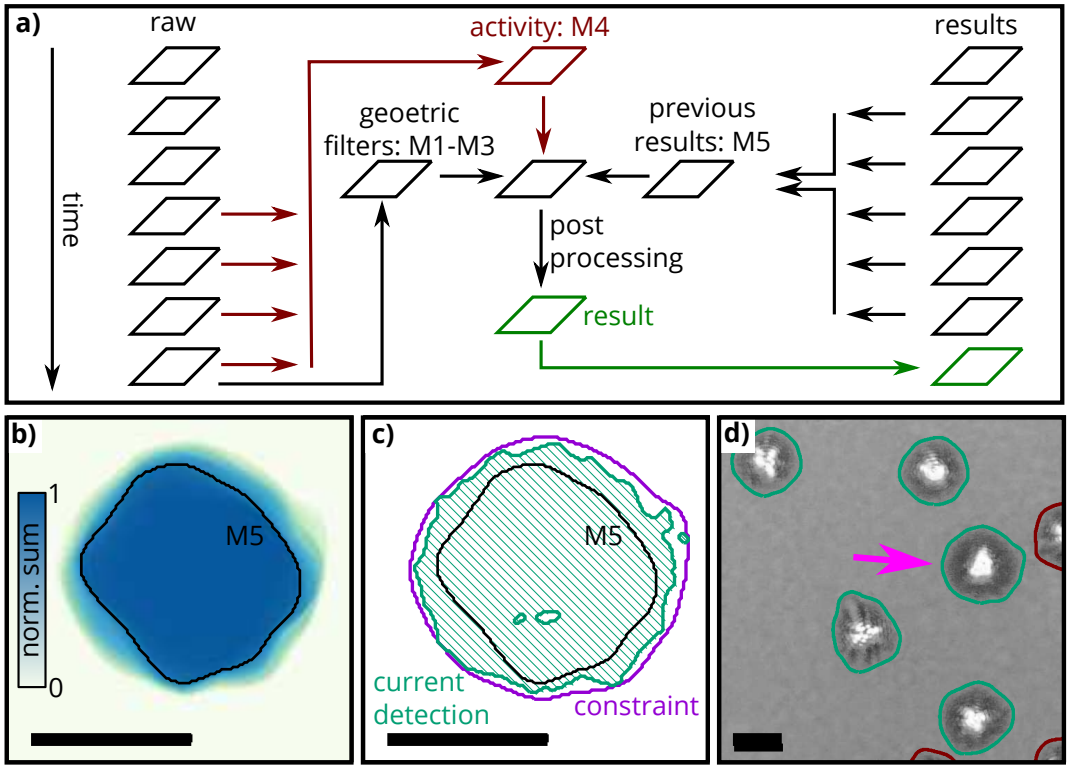

Figure 6.4: Determination of the area of bacterial microcolonies. Scale bar: 100 µm **a)** Scheme of the detection algorithm: For each image of the sequence, the masks M1-M4 are calculated from the activity maps and geometric filters. **b)** The area detected in all previous frames is summed up and thresholded to obtain the binary mask M5. The graph shows the sum and the outline of the thresholded area drawn as a black line. **c)** shows the combined binary masks M1-M4 as the area shaded in green, with the outlines drawn as solid green lines. It furthermore shows the constraint as well as the outlines of M5. It can be seen, that adding M5 fills two small holes in the detected area. The masks M1-M5 are combined and post-processed to obtain the final result of the detected area, which is shown in **d)**. The colony shown in b)&c) is highlighted with an arrow. The image demonstrates the correct detection of the area of the microcolonies.

the segmentation of the colony area in all previous frames. Therefore, all foreground areas detected outside of the manually segmented colonies is discarded. This procedure minimizes the number of detection errors during the beginning of the image sequence when the contrast of the diffraction patterns of the smaller microcolonies is still low. For each frame, the binary masks of the area detected in all previous frames are summed up and thresholded to obtain the binary mask M5, which is then added with *bitwise_or* to the area from the masks M1-M4 calculated for the current frame (see also ***Figure 6.4 b&c***). For all images acquired after the frame that was used for manual selection of the colonies, the mask M5 is expanded by a selectable amount of pixels and subsequently used with *bitwise_and* as a constraint for area detected in the current frame to avoid errors due to background noise. The final result of the segmentation is shown in ***Figure 6.4 d*** and demonstrates the accurate detection of the area of the bacterial microcolonies

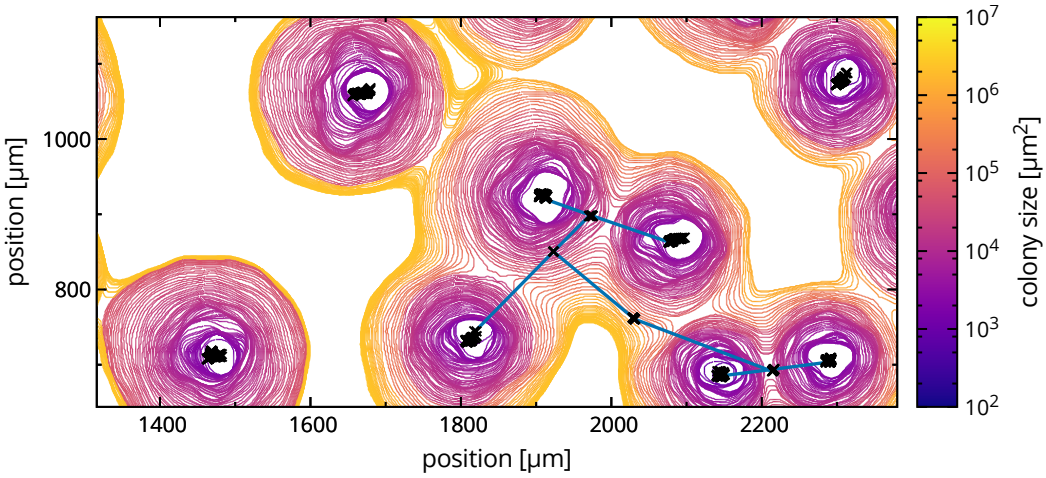

Figure 6.5: Tracking of bacterial microcolonies. The plot shows the outlines of the automatically detected apparent area of several initially isolated bacterial microcolonies in consecutive frames. The outlines are color-coded with the apparent area of the colony. The time between successive frames was 5 min. The center of mass (COM) coordinates of the detected apparent area is drawn as a black cross for each frame. When colonies merge, the COM coordinates exhibits a distinct jump, which is indicated with blue lines for five selected colonies. Since the COM coordinates of the two original colonies must lie within the outlines of the merged colony, a hierarchical tree can be constructed for the merging colonies.

The bacteria are seeded onto the agar patches in a fashion that results in the formation of initially separated isolated microcolonies. However, as the microcolonies grow, the individual microcolonies eventually merge and form larger colonies. ***Figure 6.5*** depicts the expansion of several initially separated microcolonies over time. The analysis of bacterial growth on the level of individual colonies requires to detect and track these merging-events. Tracking the microcolonies corresponds to the inverse problem of cell tracking, where one individual cell divides into two daughter cells and the resulting lineage is a hierarchical tree that branches along the time axis. The eventual merging of the individual microcolonies into one layer that covers the whole substrate area corresponds to a tree where the branches merge along the time axis into one single stem. The merging-event of two microcolonies can be easily detected by using the following information: (1) The center of mass coordinates of the original microcolonies must lie within the outlines of the merged microcolony. (2) There is a distinct jump in the

center of mass coordinates from the original microcolonies to the center of mass coordinate of the merged colony, as ***Figure 6.5*** shows.

6.2 Colony discrimination

In the previous section, it was shown that the presented algorithm allows the automatic detection of bacterial microcolonies with a diameter of more than about 10 µm in the RFLM images. The goal of this section is, to investigate, if the calculation of multiple metrics of the morphology of the detected colonies facilitates single-shot phenotypic profiling. Changes in colony morphology are thought to reflect the adaption of the bacteria to different environmental conditions [331]. Therefore, a single-shot assessment of critical morphological traits of the colonies might provide a suitable tool to assess the phenotypic response in morphology to the exposure to antimicrobial agents.

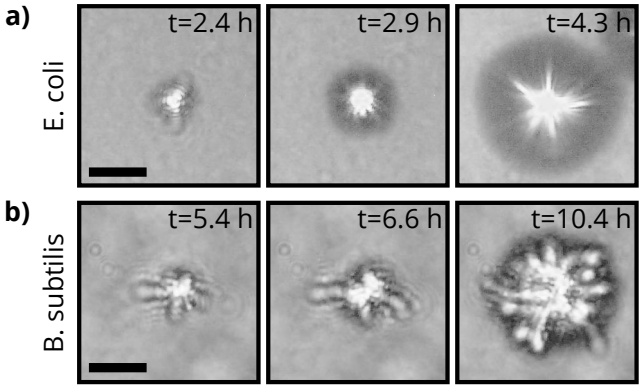

Figure 6.6: Colony morphology: The images show one microcolony of the E. coli strain (a), and one microcolony of the B. subtilits strain (b) at different time-points. The images demonstrate that the microcolonies of the two strains exhibit distinct morphologies. Scale bar: 100 µm

Figure 6.6 illustrates that the microcolonies of the E. coli and the B. subtilis strains exhibit distinct differences in morphology. To achieve an automated single-shot discrimination between the microcolonies of the two different strains, 12 morphological metrics were calculated for each detected colony. The details of the metrics can be found in ***Appendix 3.3***. An LDA using these metrics calculated for 70 colonies of the B. subtilis strain and 110 colonies from the E. coli strain was used for colony discrimination. The result is shown in ***Figure 6.7*** and demonstrates that the selected metrics allow a good automated discrimination between the colonies of the two different strains.

In summary, it was shown in this chapter that the presented algorithm is capable of accurate detection and segmentation of bacterial microcolonies with a diameter of more than about 10 µm. The results demonstrate that the analysis facilitates the measurement of bacterial growth on agar substrates on the level of individual microcolonies. Furthermore, image-based metrics for the morphology of the detected colonies allowed the analysis of further phenotypic parameters. Here, for example, it was shown that the microcolonies of different strains can be discriminated within one frame.

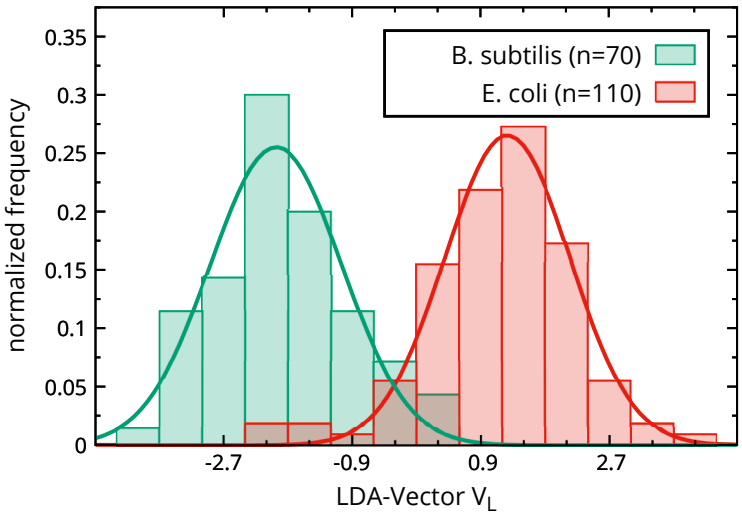

Figure 6.7: Single-shot discrimination of bacterial microcolonies with LDA. 12 different image based metrics of colony morphology were calculated for microcolonies of the bacterial strains E. coli and B. subtilis. These metrics were used for an LDA. The plot shows the normalized histogram of the resulting LDA-vectors of the colonies, binned in 0.6 intervals. Both histograms were fitted with a Gaussian distribution. The low overlap between the two distributions indicates a good discrimination between the microcolonies of the two bacterial strains.

7

Development of a Nanostructured Micropattern

Micropatterned cell culture substrates fabricated by engineering the substrate surface are an effective approach to study critical cell functions such as migration [332], differentiation [333], or apoptosis [334]. Micropatterned environments usually consist of cytophilic (cell adhesion promoting) and cytophobic (cell repellent) areas. For this purpose, numerous patterning techniques are available to fabricate micropatterned substrates [335]. Gold is an attractive choice as an adhesion promoting surface since patterns can be fabricated with electron beam lithography, or the self-assembly of gold nanoparticles, and further functionalization via thiol chemistry is possible, e.g., with thiol-functionalized RGD peptides [336–339]. Gold is often used in combination with a poly-L-lysine (PLL)-polyethylene glycol (PEG) passivation on glass substrates. Polypropylene oxide (PPO) copolymers such as the PEG-PPO-PEG copolymer Pluronic F127 provide excellent and often superior passivation, but require hydrophobic substrates [340]. Cyclic olefin copolymer (COC) substrates are compatible with the pluronic passivation. While the combination of COC substrates and electron beam lithography has been used to create chips with integrated gold electrodes [341], so far it has not been used to create gold micropatterns for cells.

Here, the feasibility of using a nanostructured micropattern based on using gold for the cytophilic areas of the micropattern and the pluronic passivation of the COC substrate for the cytophobic areas of the micropattern is investigated. Atomic force microscopy (AFM) was used to characterize the gold structures of the pattern, and RFLM was used to confirm the long-term stability of the pluronic passivation as well as the preferential adhesion to the cytophilic areas.

Figure 7.1 shows the principle of the developed pattern. A gold layer with a thickness of several nanometers is applied to specific regions of the COC substrate to make these specific regions cytophilic. This thin layer is still transparent for visible light and can be functionalized by attaching molecules via thiol bonds to it, for example, adhesion promoting RGD peptides conjugated with cysteine. The gold-free areas of the COC substrate are passivated with pluronic f127 and serve as the cytophobic areas of the micropattern. Here, the PPO block of the pluronic copolymer adheres to the hydrophobic COC substrate, while the PEG blocks shield the substrate from adhesion of biomolecules. The first step was to evaluate the long-term stability of the cytophilic and cytophobic properties of the fabricated patterns. To this end, a 3 nm thick adhesion layer, followed by 7 nm thick gold layer was applied to the top half of the substrates,

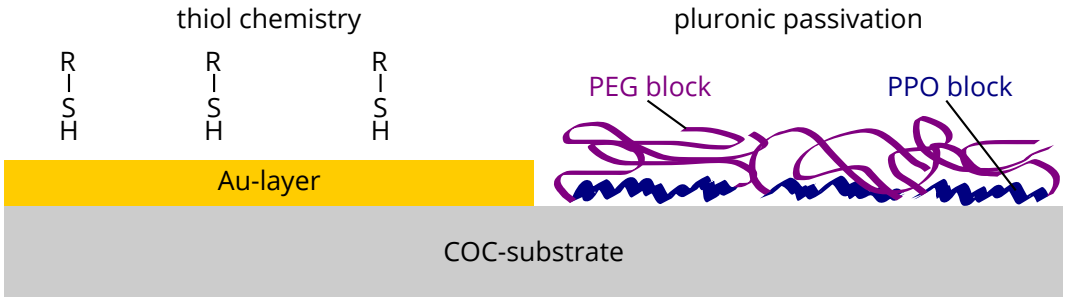

Figure 7.1: Principle of the developed pattern. A thin layer of gold on top of a COC substrate serves as the cytophilic region of the pattern. The gold can be functionalized with thiol chemistry, e.g., by binding cysteine-conjugated peptides to it. The cytophobic region of the pattern is provided by the pluronic passivated regions of the COC substrates which are free from gold. Here, the PPO-block of the pluronic copolymers can adhere to the hydrophobic COC substrate. The PEG blocks shield the substrate area from adhesion of biomolecules.

while the bottom half was left gold-free. Subsequently, the bottom half of the substrate was passivated with pluronic and then cells were seeded onto the sample. The substrate and the cells were monitored with RFLM. ***Figure 7.2*** shows that the cells adhered and proliferated on the gold layer, but did not adhere on the passivated part. The cytophilic and cytophobic properties of the system were stable for more than 24 h. The images also show that the gold layer was still transparent enough to allow imaging of the cells which adhered on top of it. AFM measurements showed that the raw COC substrate had a root mean square surface roughness of 0.7 nm, while the gold layer had a root mean square surface roughness of 1.5 nm. The processes for the application of the gold layer hence increase the surface roughness about a factor of two, but otherwise, no alterations in the surface topology were found.

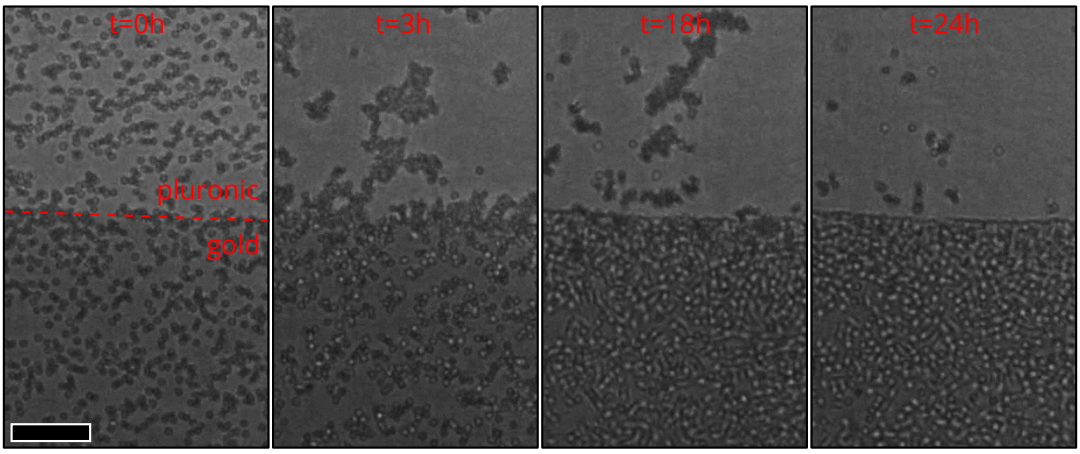

Figure 7.2: Long term stability of the pattern: A549 cells were seeded on a COC substrate. Onto the bottom half of the substrate a thin gold layer was evaporated, while the upper half was passivated with plurinic f127. The area with the gold is slightly darker in the image. It can be seen that on the bottom half cells adhere and grow. On the passivated upper half, the cells can not adhere and float above the substrate as clusters. Between 18 h and 24 h the sample was rinsed to remove dead floating cells. At 24 h the image shows a clear border between the passivated area and the area with the gold, where the cells grow. Scale bar: 250 µm

Finally, the gold-pluronic combination was used to create nanostructured micropatterns with electron beam lithography. ***Figure 7.3 a*** shows a schematic of a linear lane pattern measuring 80 µm in length and 18 µm in width. The lane consists of individual gold circles with a radius of 300 nm arranged in a hexagonal lattice. By changing the lattice constant along the x-axis, a linear gradient of the adhesion area which is available to the cells can be created. As shown in ***Figure 7.3 b***, AFM measurements confirmed that the fabricated structures have the desired height and geometry. Furthermore, the cell repellent properties of the substrate passivation on a nanometric scale were confirmed with scanning electron microscopy (SEM), as ***Figure 7.3 c*** demonstrates. Cells were seeded onto a sample that contained an array of the lane patterns. Time-lapse image series of the cells on the sample were acquired with RFLM, showing that the passivated area repelled the cells, and that the cells adhered only to the lane patterns, as shown in ***Figure 7.3 d***.

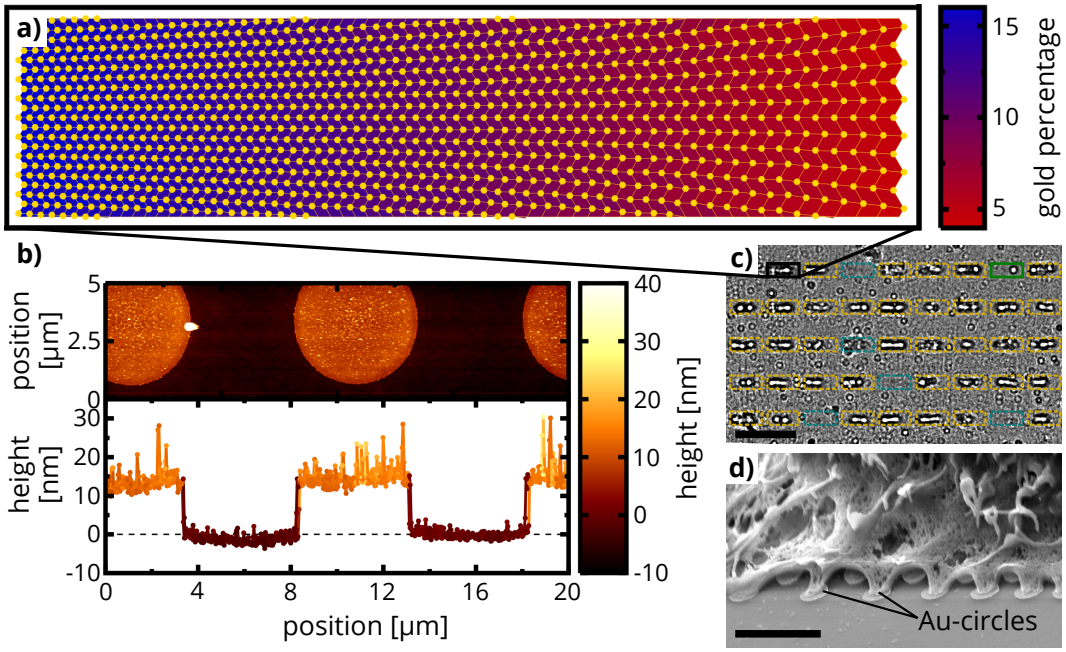

Figure 7.3: Nanostructured lane micropattern with gold circles. **a)** Geometry of a linear lane pattern with a length of 80 µm and a width of 18 µm. The gold circles have a radius of 300 nm and are arranged in a hexagonal pattern with the lattice constant increasing linearly along the x-direction. The gold circles are drawn as yellow circles, and each cell of the lattice is color-coded with its gold area percentage. **b)** AFM image (top) and two line profiles (bottom) of larger gold circles on a COC substrate fabricated with electron beam lithography. The AFM image shows that the height of the circles of around 12 nm is slightly higher than the 3 nm thick titanium adhesion layer and the 7 nm thick evaporated gold layer. The small difference is most likely due to a step in the fabrication process where DMSO dissolves some COC on the substrate surface. **c)** RFLM image of cells adhered to an array of lane patterns. The image shows that the cells adhered only to the lane patterns. Most patterns were occupied with several cells (yellow rectangles), a few of the structures were left unoccupied (blue rectangles), and only one pattern was occupied with only one cell (green rectangle), indicating a non-optimum seeding density. Scale bar: 250 µm. **d)** SEM image of a cell on a micropattern with gold circles on the passivated COC substrate. It can be seen that the cell adhered only to the individual islands, while it is repelled by the passivated substrate. Scale bar: 2 µm

In summary, it was shown that e-beam litography on COC substrates allows the fabrication of nanostructured micropatterns with (1) stable and strongly cell repellent passivated areas; (2) allow chemical functionalization of the cytophilic areas; (3) allow a precise and reproducible variation of the density of the density of the available adhesion area. Substrates with gradients in the spacing of adhesive sites have been used successfully to study changes of cellular behavior along the gradients [342, 343]. Furthermore, in this section it was shown that time-lapse images series of cells on arrays of these patterns can be acquired with RFLM under cell culturing conditions.

8 Conclusion and Outlook

Deriving quantitative information from image data is becoming a critical technology in biomedical sciences. Due to the recent advances in computational methods, image analysis of microscopy images now allows the time-resolved measurement of multiple cellular phenotypes in high-throughput. Traditionally, images of cells are recorded with conventional light microscopes. However, more recently, novel and unconventional techniques for cell microscopy have drawn attention [344]. LM is one of these emerging techniques and capable of label-free live-cell imaging with a wide FOV [65]. LM systems often sacrifice some of the optical resolution that a conventional microscope provides in order to achieve some unique advantages such as versatility, compactness, cost-efficiency, and portability. This trade-off allows LM systems to be used in scenarios where conventional microscopes are not a viable option. Compact LM techniques are, for example, especially promising for the use in cell culture, where image-based monitoring of critical phenotypic parameters like cell growth and motility has the potential to assist greatly in ensuring the consistency of cell line characteristic traits and cell culture routines.

The scope of this thesis was the development of an LM technique for phenotypic monitoring of cell growth and motility. Unlike most DHM-based LM techniques which rely on the computational reconstruction of in-focus images, the presented RFLM technique is based on extracting information on cell growth and motility directly from the recorded low-coherence interference patterns using suitable image analysis.

First, it was shown that foregoing the computational reconstruction allows designing extremely compact setups for live-cell imaging due to the lower demands on the coherence of the light source. In these setups, an LED illuminates the sample in transmission mode and a digital image sensor placed in contact directly beneath the sample records the resulting low-coherence interference patterns of the cells. It was demonstrated that these interference patterns contain footprints of the cells since the shapes of the intensity maxima resemble the shapes of the cells in this configuration. The presented results show that this footprint enables the identification and localization of the cells and that this footprint contains information of the shape on the cells. One technical advantage of using this approach is that it allows minimizing the inevitable heat dissipation caused by the image sensor during image acquisition since the technique does not rely on the acquisition of multiple images such as the super-resolution and phase retrieval techniques that are frequently employed in DHM-based techniques. Furthermore, it was demonstrated

that the technique is capable to image the cells under stable environmental conditions inside standard cell culture incubators. Finally, several setups were presented that are capable of live-cell imaging using standard culture flasks and of performing parallelized measurements in order to be able to monitor cell growth and motility during culturing, as well as in cell-based assays.

In order to extract image-based metrics for cell growth and motility from the recorded RFLM image data, suitable image analysis methods were developed and verified. ***Figure 8.1*** summarizes the results of this quantitative analysis of critical phenotypic parameters of the cells.
A machine learning technique based on cell detection with a fully convolutional network (FCN) and the generation of cell trajectories and lineages with moral lineage tracing (MLT) was used to analyze cell number and motility on the level of individual cells. ***Figure 8.1 a&b*** illustrate that this single cell analysis allows calculating numerous image-based metrics for the quantitative analysis of cell migration and proliferation. The trajectories were used to calculate the cell speed, the cell speed distribution, the confinement ratio, the diffusion coefficient D_α, and

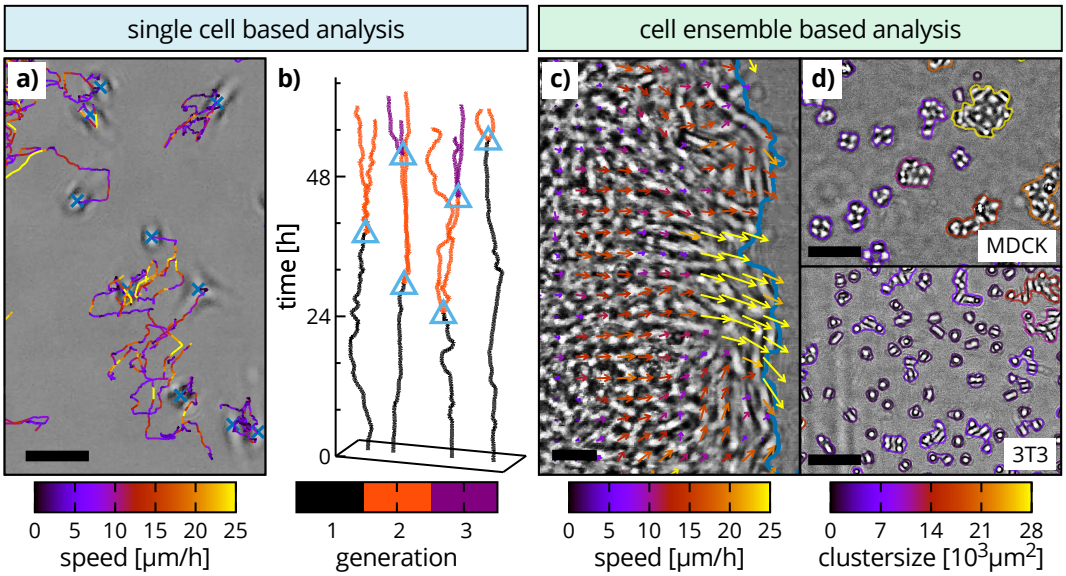

Figure 8.1: Analysis of cell growth and motility using RFLM images and image-based metrics. **a)** The image shows a section of an RFLM image showing individually migrating NIH-3T3 fibroblasts. The superimposed lines depict the trajectories of the cells. The line-color corresponds to the speed of the cells (calculated over a 22 min interval). Scale bar: 100 µm. **b)** The graph shows four examples of lineages of NIH-3T3 cells. The results illustrate that the lineages give insights into cellular heterogeneity, as the time between cell divisions (highlighted with turquoise triangles) varies between the different cells. **c)** Determination of collective cell migration in a scratch wound assay using PIV. The background image shows a layer of NIH-3T3 cells and a cell-free area on the right. The colored arrows correspond to the PIV-velocity field, and the blue line indicates the outlines of the cell layer. Scale bar: 100 µm. **d)** The images show the results of the automatically detected cell covered substrate area for a sample with MDCK and NIH-3T3 cells, respectively. The outlines of the detected area are color-coded with the cluster size. The results illustrate the different clustering behavior: MDCK cells prefer to grow in close contact with their neighbors, whereas the NIH-3T3 cells tend to avoid contact with other cells. Scale bar: 200 µm.

the exponent α as metrics for the cell motility. The lineages provide the cell number and hence the proliferation, but in addition, also allow assessing the heterogeneity of a cell population. ***Figure 8.1 c&d*** illustrate the results of the image analysis methods that were developed to obtain metrics for cell ensembles. The achieved detection and segmentation of the cell covered substrate area enables the determination of the population doubling times, the cell cluster shape, and the cluster size distribution. Furthermore, collective cell migration can be determined by calculating the front velocity of the two converging cell layers in the scratch wound assay. Additionally, particle image velocimetry (PIV) can be used to obtain flow fields describing the collective cell migration in cell layers and patches.

Subsequently, the introduced RFLM setups and image-based metrics were used to monitor cell growth and motility during culturing and in cell-based assays. First, it was shown that the presented image analysis captures key aspects of the characteristic phenotypic traits of cell lines. To this end, distinct phenotypic profiles for three different cell lines were generated based on growth, mean squared displacement (MSD), and cell clustering metrics. These phenotypic profiles can be tracked over serial passages to ensure the consistency of cell line specific characteristic traits during culturing. ***Figure 8.2 a&b*** summarize the results of using RFLM for the quantitative analysis of key aspects in culturing cell lines. Population doubling times (PDT) and cell migration were monitored during the culture period and tracked over serial passages. Additionally, an RFLM-based method to assess the variations of the cell density over the entire substrate area of culture flasks was presented. This method provides a tool that can aid to avoid phenotypic drift during culturing by ensuring that the cells are seeded in a fashion that minimizes the heterogeneity in the cellular microenvironment.

Secondly, the image-based metrics were used to demonstrate that the technique is capable of measuring the dose-dependent phenotypic response of cells to the exposure with biochemical agents in parallelized measurements. First, the analysis of the cell covered substrate area and the FCN cell detection were used to assess the cell seeding density and its spatial uniformity since these factors can significantly affect the measured drug response [47, 50]. Subsequently, cell growth and motility of several established and primary cell lines were monitored to measure the dose-dependent response to treatment with a variety of different biochemical agents. ***Figure 8.2 c&d*** summarize two key results of using the technique for cell-based assays: (1) The technique provides the time-resolved drug response, which allows calculating measures such as normalized growth rates. Using such measures minimizes the effect of changes in drug response during the assay period on the obtained dose-response curves [295]. (2) The technique is multiplex as it provides multiple readout parameters such as proliferation and motility. The results of the performed drug-screening experiments demonstrate the efficacy of the technique for label-free phenotypic drug-screening.

Finally, it was shown that the technique is not limited to the analysis of eukaryotic cells. Bacterial microcolonies were successfully detected, segmented, and tracked. Multiple image-based metrics for colony morphology were introduced, which in combination with a linear discriminant analysis enabled the discrimination between microcolonies of different bacterial strains.

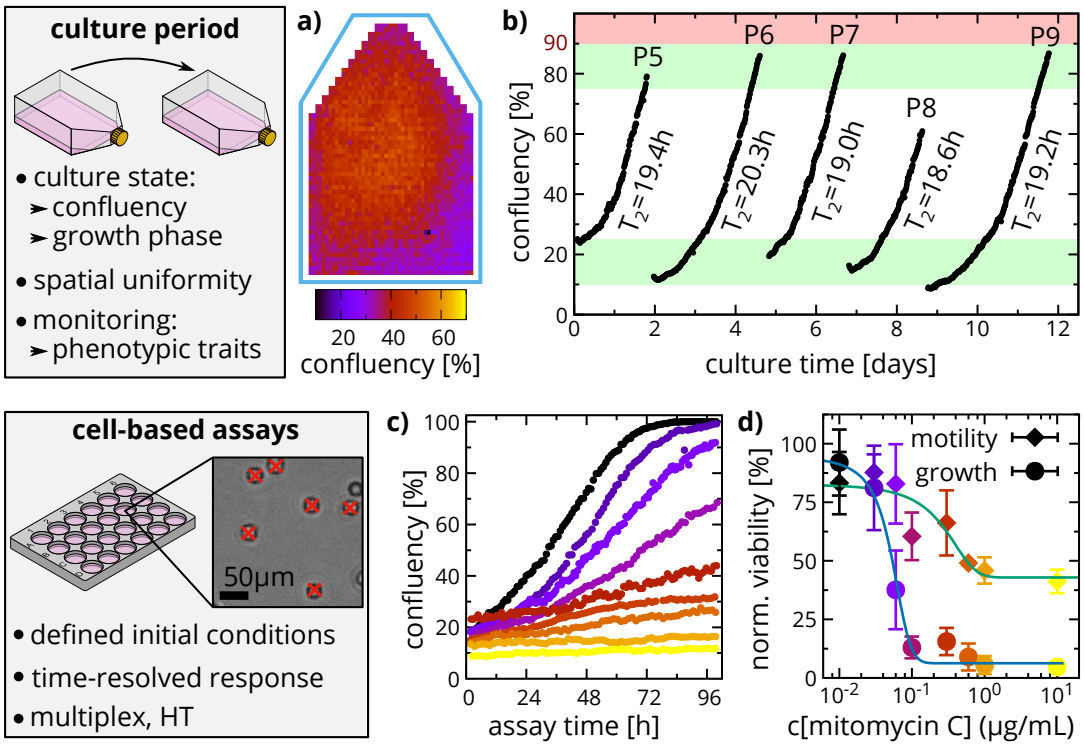

Figure 8.2: Using RFLM for quantitative phenotypic analysis of cells during culturing (top panel) and in cell-based assays (bottom panel). **a)** The graph depicts the confluency at different positions in the flask. This analysis allows an assessment of the uniformity of the seeding density in the flask to avoid phenotypic drift due to a heterogeneous cellular microenvironment. **b)** Monitoring the confluency of a cell culture facilitates a consistent routine of serial passaging (passages P5-P9 in the green confluency ranges). Furthermore, critical phenotypic parameters such as the PDTs can be tracked over the culture period to detect changes in cell line characteristic traits. **c)** In addition to cell line monitoring, RFLM also allows parallelized multiplex cell-based assays. The seeding density in the multiwell plates is determined to avoid bias in the measured drug response due to a non-uniform seeding density. The time-resolved determination of multiple phenotypic parameters such as the confluency (shown in the graph) and the motility allows generating dose-response curves, as shown in **d)**.

In conclusion, the presented technique provides an easy-to-use system for monitoring of cell growth and motility based on label-free in-situ live-cell imaging using lensless microscopy and image-based metrics.
Therefore, the technique has great potential to aid in efforts to increase standards and reproducibility in experiments that rely on using cultured cell lines. Monitoring cell growth and motility during culturing does not only provide quantitative data to ensure the consistency of cell line characteristic traits. This data could also be used in a machine-readable form for online resource databases such as the Cellosaurus [345] to improve inter-study comparability. Furthermore, the data provides valuable input for *in silico* models of cell growth dynamics, which are increasingly integrated into *in vitro* experiments and employed in cell culture optimization [116, 117, 119, 120, 346].

In addition, the technique provides a convenient and inexpensive tool for high-throughput live-cell measurements using standard multiwell plates in scenarios where conventional automated

high-end microscopes are either not available or impractical to employ. Since the technique is not limited to eukaryotic cells it also provides a viable option for, e.g., antimicrobial susceptibility testing. Further applications could include imaging cells growing in three-dimensional cell cultures, which are becoming increasingly popular [81]. Especially the analysis of the shape of cell-spheroids [347] is promising since the footprint of such larger objects in the recorded interference patterns should be easily detectable even at larger vertical distances from the image sensor.

Future perspectives include extending the image analysis with further metrics. For tissue analysis, it has been shown that it is a viable approach to create phenotypic profiles consisting of hundreds of image-based metrics for morphology, topology, and texture [282]. Such an analysis might be feasible for RFLM images as well since differences in texture and topology are discernible by eye in the shown images for different cell lines.
A further promising extension of the analysis is to extract information on the morphology and state of individual cells from their interference patterns [73]. In this regard, deep learning holds great promise to analyze live-cell imaging data [348–350]. Using fluorescence cell cycle or apoptosis markers to record RFLM images complemented with corresponding fluorescence microscopy images might provide a powerful approach to generate extensive training data sets for machine learning techniques to enable the detection of mitosis and apoptosis in RFLM images.

Materials and Methods

Used cell lines: NIH-3T3 (RRID:CVCL_0594) and HeLa (RRID:CVCL_0030) cell lines were acquired from DSMZ (Leibniz Institute DSMZ, Braunschweig, Germany); the HuH7 (RRID:CVCL_0336) cell line from Institut für angewandte Zellkultur (Munich, Germany); and the A549 (RRID:CVCL_0023) and MDCK.2 (RRID:CVCL_B034) cell lines from ATCC. The primary melanoma cell line was kindly provided by the University Hospital Zürich, Department of Dermatology. It was established from patient biopsy of melanoma metastases using the selective adherence method [351] and included in the URPP biobank, University Hospital Zürich, Department of Dermatology. Clinical diagnosis of the tumor material was confirmed by histology and immunohistochemistry.
All shown results are from experiments after the cell lines were tested negative for mycoplasma with the Venor GeM OneStep Kit (Minerva Biolabs, Berlin, Germany)

Used bacterial strains: E. coli: BZB1011; B. subtilis: NCIB 3610

Long-term measurements for RFLM-DHM area correlation: HeLa and 3T3 cells were cultivated in DMEM, A549 cells in MEM medium (C.C.Pro GmbH, Oberdorla, Germany), supplemented with 10 % FBS (Gibco, Thermo Fisher Scientific, Waltham, USA) and 2 mM L-Glutamine. For the measurements, the cells were seeded with a density of 1–2 $\times 10^4$ cells mm^{-2} in T-25 flasks with a bottom thickness of 1 mm (Sarstedt, Nümbrecht, Germany). After letting the cells adhere for 4 h the medium was exchanged with Leibovitz L-15 medium (C.C.Pro) supplemented with 10 % FBS and 2 mM L-Glutamine.

Experiments for cell line characterization: Media composition for culturing and experiments: 3T3 cells were grown in DMEM Glutamax + 10 % FBS, A549 cells in MEM Glutamax + 10 % FBS and HuH7 cells in RPMI 1640 Glutamax + 10 % FBS + 5 mM HEPES + 1 mM sodium pyruvate. The cells were seeded in an eight chamber microscopy slide with a bottom thickness of 180 µm (μ-Slide 8 Well w/ ibiTreat coating, Ibidi, Martinsried, Germany). Four of the chambers were seeded with 300 µl of cell suspension with 3×10^3 cells ml^{-1} for the tracking measurements. The other four chambers were seeded with 300 µl of cell suspension with 4×10^4 cells ml^{-1} for the growth and PIV measurements. The measurements were performed in a standard CO_2 incubator at 5 % CO_2 and 95 % humidity. The passage number was below 30 for the 3T3 and A549 cells and below 36 for the HuH7 cells.

Experiments for comparison between RFLM and brightfield/fluorescence microscopy: Tracking of 3T3 cells with fluorescently labeled nuclei: 1 ml of a cell suspension with 3×10^4 cells ml^{-1} in DMEM medium was seeded in a petri dish (μ-Dish 35 mm high w/ ibiTreat coating, Ibidi, Martinsried, Germany). After 4 hours adhesion time in a CO_2 incubator the medium was replaced with L15 medium supplemented with 10 % FBS, 0.5 % penicillin/streptomycin (Gibco) and 25 nM Hoechst 33342 (Invitrogen, Carlsbad, USA). After 1 h image acquisition was started. Preparation of sample for PIV: 1 ml of a cell suspension with 1×10^5 cells ml^{-1} of 3T3 cells in DMEM medium was seeded in a petri dish (μ-Dish 35 mm high, Ibidi, Martinsried, Germany). After 6 hours adhesion time in a CO_2 incubator the medium was replaced with Leibovitz L-15 Glutamax medium (Gibco) supplemented with 10 % FBS.

Cell line monitoring experiments: The primary melanoma cell line and the NIH-3T3 cell line were grown inside standard T-25 flasks with a bottom thickness of 1 mm (Sarstedt, Nümbrecht, Germany) and monitored in a standard CO_2 incubator at 5 % CO_2 and 95 % humidity. The NIH-3T3 cells were cultured in DMEM Glutamax + 10 % FBS after being thawed from a vial with 70 % medium, 20 % FBS, and 10 % DMSO. The primary cell line was cultured in RPMI 1640 Glutamax + 10 % FBS + 1 mM sodium pyruvate after being thawed from a vial with 70 % medium, 20 % FBS, and 10 % DMSO. For both cell lines, the initial medium the cells were frozen in, was replaced with the respective culture medium the day after thawing the cells.

Scratch wound + proliferation assays with human primary melanoma cells: Culture medium: RPMI 1640 + 10 % FBS + 1 mM 2 mM L-Glutamine + 2 mM sodium pyruvate.
Compound solutions:

- *pepstatin A:* Solved in DMSO. The final DMSO concentration in the medium was 0.4 % for all samples of the dilution series.
- *T-5224:* Solved in DMSO. The final DMSO concentration in the medium was 0.1 % for all samples of the dilution series.
- *neocuproine:* Solved in DMSO. The final DMSO concentration in the medium was 0.008 % for all samples of the dilution series.
- *BMS-754807:* Solved in DMSO. The final DMSO concentration in the medium was 0.1 % for all samples of the dilution series.

Preparation of scratches: 300 µL of a cell suspension was pipetted into each chamber of an 8-chamber slide (μ-Slide 8 Well w/ ibiTreat coating, Ibidi, Martinsried, Germany). The seeding densities were 2.5×10^5 ml^{-1} for the MAPK resistant cell line and 2.4×10^5 ml^{-1} for the MAPK sensitive cell line. After about 24 h a scratch wound was created with a p200 pipette tip. Each chamber was rinsed three times with prewarmed medium. Finally, the medium containing the compounds was added, and imaging started. In the case of pepstatin A, the medium was exchanged in the chambers 3 h before the creation of the scratch wound and replaced with the medium containing pepstatin A. After creation of the scratch wound, the regular culture medium was used.
Preparation of proliferation assays: 300 µL of a cell suspension was pipetted into each chamber of an 8-chamber slide (μ-Slide 8 Well w/ ibiTreat coating, Ibidi, Martinsried, Germany). The

seeding densities were $4 \times 10^4\,\mathrm{ml}^{-1}$ for the MAPK resistant cell line and $5.3 \times 10^4\,\mathrm{ml}^{-1}$ for the MAPK sensitive cell line. After letting the cells adhere for several hours, the medium was replaced with the medium containing the compounds was added, and imaging started. In the case of pepstatin A, the medium containing the pepstatin A was replaced again after three further hours with the regular culture medium.

Scratch wound assays with different media supplements: One silicone insert (Cat.No 80209, Ibidi, Martinsried, Germany) were placed into each well of an 8-chamber slide (μ-Slide 8 Well w/ ibiTreat coating, Ibidi, Martinsried, Germany). Subsequently, 70 µl were of a suspension of NIH-3T3 cells ($9 \times 10^5\,\mathrm{ml}^{-1}$) was pipetted into each of the two insert-wells. The DMEM medium contained 10 % FBS and 2 mM L-Glutamine. After an incubation time of about 24 h, the inserts were removed. Each chamber was rinsed twice with prewarmed medium. Finally, the chambers were filled with 400 µM medium containing various concentrations of the two supplements (FBS and the supplement of unknown composition), and image acquisition was started.

Experiments with Mitomycin C: The experiments with the MDCK cells were performed in 8-chamber slides (μ-Slide 8 Well w/ ibiTreat coating, Ibidi, Martinsried, Germany). Medium: DMEM + 10 % FBS + 2 mM L-Glutamine. 300 µl cell suspension with a density of $2.5 \times 10^4\,\mathrm{ml}^{-1}$ was seeded into each chamber. After overnight incubation, the medium was exchanged with medium that contained different concentrations of mitomycin C. After 2 h of incubation, the mitomycin C medium was removed and the chambers rinsed with PBS. Subsequently, fresh medium (without mitomycin C) was added into the chambers.
The experiments with the NIH-3T3 cells were performed analogously, but in 24-Well plates (Eppendorf cell imaging plates) and with an adjusted volume of the cell suspension.

Growth inhibition and cytotoxicity measurements: Cell line: HeLa; Medium: DMEM + 10 % FBS + 1 % penicilin-streptomycin
Compound solutions:

- *Docetaxel:* Solved in PBS + DMSO. The final DMSO concentration in the medium was 0.25 % for all samples of the dilution series.
- *Etoposide:* Solved in PBS + DMSO. The final DMSO concentration in the medium was 1 % for all samples of the dilution series.

RFLM-assay: 1.5×10^4 cells suspended in 270 µl medium were seeded into each chamber of an 8-chamber slides (μ-Slide 8 Well w/ ibiTreat coating, Ibidi, Martinsried, Germany) and incubated overnight (37 °C, 5 % CO_2). Subsequently, 30 µl of the compound solutions were added, and image acquisition was started.
MTT-assay: 5×10^3 cells suspended in 90 µl medium and seeded into a 96-well plate. The outer wells were used as blanks. The well plate was incubated overnight (37 °C, 5 % CO_2). Subsequently, 10 µl of the compound solutions were added. After 45 h, 10 µl of $5\,\mathrm{mg\,ml}^{-1}$ MTT in PBS was added. After 3 h of further incubation, the medium was aspirated, and the cells were dissolved in pure DMSO (for 5 min in the incubator). Finally, the absorption at 550 nm was measured with a plate reader for each well.

Preparation of nanostructured micropatterns:

- *Cleaning:* A #1.5 COC coverslip (Cat.No: 10813, Ibidi, Germany) was cleaned with isopropanol and sonication for 2 min. Subsequently, the coverslip submerged in a beaker filled with isopropanol for a few seconds. The coverslip is dried with N_2.
- *Coating:* PMMA 500k in MIBK is spin-coated onto the coverslip (1 s at 800 RPM + 30 s at 5000 RPM). Subsequently, the sample is baked overnight at 95 °C. The whole procedure is repeated with PMMA 996k in MIBK.
- *Application of conductive layer:* 5 nm of chromium are deposited on the coverslip
- *E-beam lithography:* A Raith E-line system was used with for exposure with the following parameters: acceleration voltage: 20 kV; aperture: 30 µm; dose: 580 µC cm^{-2}
- *Removal of chromium layer:* the coverslips are submerged in a beaker with Chrome-etch Selectipur for ca. 10 s. Subsequently, the slide is cleaned by successive submersion in two beakers with H_2O dest. for ca. 10 s then and dried with N_2
- *Development:* The coverslip is submerged in a beaker filled with PMMA-developer (Isopropanol:MIBK, 3:1) at room temperature for 30 s. Subsequently, the coverslip is rinsed in a beaker filled with isopropanol for 20 s and then dried with N_2.
- *Evaporation:* 3 nm of titanium followed by 7 nm of gold at a rate of 1 Å s^{-1}
- *Lift-off:* The coverslip is sonicated in a beaker filled with DMSO at room temperature until the lift-off is completed. Subsequently, the coverslip is cleaned by serial submersion for 10 s in three beakers filled with H_2O dest. and one beaker filled with isopropanol. Finally, the coverslip is dried with N_2.

Bibliography

[1] Abhisek Mitra, Lopa Mishra, and Shulin Li. Technologies for deriving primary tumor cells for use in personalized cancer therapy. *Trends in biotechnology*, 31(6):347–354, 2013.

[2] Zhihua Song, Jun Cai, Yanxia Liu, Dongxin Zhao, Jun Yong, Shuguang Duo, Xijun Song, Yushan Guo, Yang Zhao, Han Qin, et al. Efficient generation of hepatocyte-like cells from human induced pluripotent stem cells. *Cell research*, 19(11):1233, 2009.

[3] Faye H Chen, Kathleen T Rousche, and Rocky S Tuan. Technology insight: adult stem cells in cartilage regeneration and tissue engineering. *Nature Reviews Rheumatology*, 2 (7):373, 2006.

[4] Elisa Michelini, Luca Cevenini, Laura Mezzanotte, Andrea Coppa, and Aldo Roda. Cell-based assays: fuelling drug discovery. *Analytical and bioanalytical chemistry*, 398(1): 227–238, 2010.

[5] Michael C Alley, Dominic A Scudiero, Anne Monks, Miriam L Hursey, Maciej J Czerwinski, Donald L Fine, Betty J Abbott, Joseph G Mayo, Robert H Shoemaker, and Michael R Boyd. Feasibility of drug screening with panels of human tumor cell lines using a microculture tetrazolium assay. *Cancer research*, 48(3):589–601, 1988.

[6] Hans G Drexler, Yoshinobu Matsuo, and Roderick AF MacLeod. Continuous hematopoietic cell lines as model systems for leukemia–lymphoma research. *Leukemia research*, 24 (11):881–911, 2000.

[7] AG Souza, ICC Ferreira, K Marangoni, VAF Bastos, and VA Goulart. Advances in cell cul-ture: more than a century after cultivating cells. *Journal of Biotechnology & Biomaterials*, 6:1–4, 2016.

[8] Fernando Amat, William Lemon, Daniel P Mossing, Katie McDole, Yinan Wan, Kristin Branson, Eugene W Myers, and Philipp J Keller. Fast, accurate reconstruction of cell lineages from large-scale fluorescence microscopy data. *Nature methods*, 11(9):951, 2014.

[9] Fabian Zanella, James B Lorens, and Wolfgang Link. High content screening: seeing is believing. *Trends in biotechnology*, 28(5):237–245, 2010.

[10] Erik Meijering, Oleh Dzyubachyk, Ihor Smal, et al. Methods for cell and particle tracking. *Methods Enzymol*, 504(9):183–200, 2012.

[11] Andrey Kan. Machine learning applications in cell image analysis. *Immunology and cell biology*, 95(6):525–530, 2017.

[12] Bo Huang, Hazen Babcock, and Xiaowei Zhuang. Breaking the diffraction barrier: super-resolution imaging of cells. *Cell*, 143(7):1047–1058, 2010.

[13] Misha B Ahrens, Michael B Orger, Drew N Robson, Jennifer M Li, and Philipp J Keller. Whole-brain functional imaging at cellular resolution using light-sheet microscopy. *Nature methods*, 10(5):413, 2013.

[14] Pierre Marquet, Benjamin Rappaz, Pierre J Magistretti, Etienne Cuche, Yves Emery, Tristan Colomb, and Christian Depeursinge. Digital holographic microscopy: a noninvasive contrast imaging technique allowing quantitative visualization of living cells with subwavelength axial accuracy. *Optics letters*, 30(5):468–470, 2005.

[15] Anne E Carpenter, Thouis R Jones, Michael R Lamprecht, Colin Clarke, In Han Kang, Ola Friman, David A Guertin, Joo Han Chang, Robert A Lindquist, Jason Moffat, et al. Cellprofiler: image analysis software for identifying and quantifying cell phenotypes. *Genome biology*, 7(10):R100, 2006.

[16] B. Alberts, A. Johnson, J. Lewis, D. Morgan, M. Raff, K. Roberts, and P. Walter. *Molecular Biology of the Cell, Sixth Edition:*. Taylor & Francis Group, 2014. ISBN 9781317563754. URL `https://books.google.de/books?id=jK6UBQAAQBAJ`.

[17] Evan Z Macosko, Anindita Basu, Rahul Satija, James Nemesh, Karthik Shekhar, Melissa Goldman, Itay Tirosh, Allison R Bialas, Nolan Kamitaki, Emily M Martersteck, et al. Highly parallel genome-wide expression profiling of individual cells using nanoliter droplets. *Cell*, 161(5):1202–1214, 2015.

[18] R Ian Freshney. *Culture of animal cells: A manual of basic technique and specialized applications*. New York: Wiley-Sons, 2010.

[19] Douglas Hanahan and Robert A Weinberg. Hallmarks of cancer: the next generation. *cell*, 144(5):646–674, 2011.

[20] Zhiwei Wang, Yiwei Li, Dejuan Kong, Sanjeev Banerjee, Aamir Ahmad, Asfar Sohail Azmi, Shadan Ali, James L Abbruzzese, Gary E Gallick, and Fazlul H Sarkar. Acquisition of epithelial-mesenchymal transition phenotype of gemcitabine-resistant pancreatic cancer cells is linked with activation of the notch signaling pathway. *Cancer research*, 69(6): 2400–2407, 2009.

[21] Sylvia Julien Grille, Alfonso Bellacosa, John Upson, Andres J Klein-Szanto, Frans Van Roy, Whaseon Lee-Kwon, Mark Donowitz, Philip N Tsichlis, and Lionel Larue. The protein kinase akt induces epithelial mesenchymal transition and promotes enhanced motility and invasiveness of squamous cell carcinoma lines. *Cancer research*, 63(9):2172–2178, 2003.

[22] Raghu Kalluri and Robert A Weinberg. The basics of epithelial-mesenchymal transition. *The Journal of clinical investigation*, 119(6):1420–1428, 2009.

[23] Claire Lifan Chen, Ata Mahjoubfar, Li-Chia Tai, Ian K Blaby, Allen Huang, Kayvan Reza Niazi, and Bahram Jalali. Deep learning in label-free cell classification. *Scientific reports*, 6:21471, 2016.

[24] David J Logan, Jing Shan, Sangeeta N Bhatia, and Anne E Carpenter. Quantifying co-cultured cell phenotypes in high-throughput using pixel-based classification. *Methods*, 96:6–11, 2016.

[25] Miroslav Hejna, Aparna Jorapur, Jun S Song, and Robert L Judson. High accuracy label-free classification of single-cell kinetic states from holographic cytometry of human melanoma cells. *Scientific reports*, 7(1):11943, 2017.

[26] Juan C Caicedo, Sam Cooper, Florian Heigwer, Scott Warchal, Peng Qiu, Csaba Molnar, Aliaksei S Vasilevich, Joseph D Barry, Harmanjit Singh Bansal, Oren Kraus, et al. Data-analysis strategies for image-based cell profiling. *Nature methods*, 14(9):849, 2017.

[27] Gurvinder Kaur and Jannette M Dufour. Cell lines: Valuable tools or useless artifacts, 2012.

[28] Helmut Franke, Hans-Joachim Galla, and Carsten T Beuckmann. Primary cultures of brain microvessel endothelial cells: a valid and flexible model to study drug transport through the blood–brain barrier in vitro. *Brain Research Protocols*, 5(3):248–256, 2000.

[29] Kiertisin Dharmsathaphorn and James L Madara. [24] established intestinal cell lines as model systems for electrolyte transport studies. In *Methods in enzymology*, volume 192, pages 354–389. Elsevier, 1990.

[30] David D Allen, Raúl Caviedes, Ana María Cárdenas, Takeshi Shimahara, Juan Segura-Aguilar, and Pablo A Caviedes. Cell lines as in vitro models for drug screening and toxicity studies. *Drug development and industrial pharmacy*, 31(8):757–768, 2005.

[31] Uri Ben-David, Benjamin Siranosian, Gavin Ha, Helen Tang, Yaara Oren, Kunihiko Hinohara, Craig A Strathdee, Joshua Dempster, Nicholas J Lyons, Robert Burns, et al. Genetic and transcriptional evolution alters cancer cell line drug response. *Nature*, page 1, 2018.

[32] Vivien Marx. Cell-line authentication demystified, 2014.

[33] Peyton Hughes, Damian Marshall, Yvonne Reid, Helen Parkes, Cohava Gelber, et al. The costs of using unauthenticated, over-passaged cell lines: how much more data do we need? *Biotechniques*, 43(5):575–588, 2007.

[34] John R Masters and Glyn N Stacey. Changing medium and passaging cell lines. *Nature protocols*, 2(9):2276–2284, 2007.

[35] Wolfgang Wagner, Anthony D Ho, and Martin Zenke. Different facets of aging in human mesenchymal stem cells. *Tissue Engineering Part B: Reviews*, 16(4):445–453, 2010.

[36] HT Nguyen, M Geens, and C Spits. Genetic and epigenetic instability in human pluripotent stem cells. *Human reproduction update*, 19(2):187–205, 2012.

[37] Simona Negrini, Vassilis G Gorgoulis, and Thanos D Halazonetis. Genomic instabilityan evolving hallmark of cancer. *Nature reviews Molecular cell biology*, 11(3):220, 2010.

[38] Daniel Stockholm, Rachid Benchaouir, Julien Picot, Philippe Rameau, Thi My Anh Neildez, Gabriel Landini, Corinne Laplace-Builhé, and Andras Paldi. The origin of phenotypic heterogeneity in a clonal cell population in vitro. *PloS one*, 2(4):e394, 2007.

[39] John R Masters. Hela cells 50 years on: the good, the bad and the ugly. *Nature Reviews Cancer*, 2(4):315, 2002.

[40] Jennie P Mather and Penelope E Roberts. *Introduction to cell and tissue culture: theory and technique*. Springer Science & Business Media, 1998.

[41] Harry Rubin. Degrees and kinds of selection in spontaneous neoplastic transformation: an operational analysis. *Proceedings of the National Academy of Sciences*, 102(26):9276–9281, 2005.

[42] Hannah K Wilson, Scott G Canfield, Michael K Hjortness, Sean P Palecek, and Eric V Shusta. Exploring the effects of cell seeding density on the differentiation of human pluripotent stem cells to brain microvascular endothelial cells. *Fluids and Barriers of the CNS*, 12(1):13, 2015.

[43] Hayden G Coon. Clonal stability and phenotypic expression of chick cartilage cells in vitro. *Proceedings of the National Academy of Sciences*, 55(1):66–73, 1966.

[44] Valério M Portela, Gustavo Zamberlam, and Christopher A Price. Cell plating density alters the ratio of estrogenic to progestagenic enzyme gene expression in cultured granulosa cells. *Fertility and sterility*, 93(6):2050–2055, 2010.

[45] Elena Postnikova, Yu Cong, Lisa Evans DeWald, Julie Dyall, Shuiqing Yu, Brit J Hart, Huanying Zhou, Robin Gross, James Logue, Yingyun Cai, et al. Testing therapeutics in cell-based assays: Factors that influence the apparent potency of drugs. *PloS one*, 13(3): e0194880, 2018.

[46] Tatsuya Osaki, Tatsuto Kageyama, Yuka Shimazu, Dina Mysnikova, Shintaro Takahashi, Shinichi Takimoto, and Junji Fukuda. Flatbed epi relief-contrast cellular monitoring system for stable cell culture. *Scientific Reports*, 7(1):1897, 2017.

[47] Mario Niepel, Marc Hafner, Mirra Chung, and Peter K Sorger. Measuring cancer drug sensitivity and resistance in cultured cells. *Current Protocols in Chemical Biology*, pages 55–74, 2017.

[48] Marina Wright Muelas, Fernando Ortega, Rainer Breitling, Claus Bendtsen, and Hans V Westerhoff. Rational cell culture optimization enhances experimental reproducibility in cancer cells. *Scientific reports*, 8(1):3029, 2018.

[49] Raziur Rahman, Saugato Rahman Dhruba, Kevin Matlock, Carlos De-Niz, Souparno Ghosh, and Ranadip Pal. Evaluating the consistency of large-scale pharmacogenomic studies. *Briefings in Bioinformatics*, 2018.

[50] Yifeng He, Qiujing Zhu, Mo Chen, Qihong Huang, Wenjing Wang, Qing Li, Yuting Huang, and Wen Di. The changing 50% inhibitory concentration (ic50) of cisplatin: a pilot study on the artifacts of the mtt assay and the precise measurement of density-dependent chemoresistance in ovarian cancer. *Oncotarget*, 7(43):70803, 2016.

[51] Christos Hatzis, Philippe L Bedard, Nicolai J Birkbak, Andrew H Beck, Hugo JWL Aerts, David F Stern, Leming Shi, Robert Clarke, John Quackenbush, and Benjamin Haibe-Kains. Enhancing reproducibility in cancer drug screening: how do we move forward? *Cancer research*, 74(15):4016–4023, 2014.

[52] Leonard P Freedman, Mark C Gibson, Stephen P Ethier, Howard R Soule, Richard M Neve, and Yvonne A Reid. Reproducibility: changing the policies and culture of cell line authentication. *Nature methods*, 12(6):493–497, 2015.

[53] Benjamin Rappaz, Billy Breton, Etienne Shaffer, and Gerardo Turcatti. Digital holographic microscopy: a quantitative label-free microscopy technique for phenotypic screening. *Combinatorial chemistry & high throughput screening*, 17(1):80–88, 2014.

[54] Anna Mölder, Mikael Sebesta, Mats Gustafsson, Lennart Gisselson, A Gjörloff Wingren, and Kersti Alm. Non-invasive, label-free cell counting and quantitative analysis of adherent cells using digital holography. *Journal of Microscopy*, 232(2):240–247, 2008.

[55] Olivier Debeir, Philippe Van Ham, Robert Kiss, and Christine Decaestecker. Tracking of migrating cells under phase-contrast video microscopy with combined mean-shift processes. *IEEE transactions on medical imaging*, 24(6):697–711, 2005.

[56] Pierre-Marc Juneau, Alain Garnier, and Carl Duchesne. Monitoring of adherent live cells morphology using the undecimated wavelet transform multivariate image analysis (uwt-mia). *Biotechnology and bioengineering*, 114(1):141–153, 2017.

[57] Priya Choudhry. High-throughput method for automated colony and cell counting by digital image analysis based on edge detection. *PloS one*, 11(2):e0148469, 2016.

[58] Gil Topman, Orna Sharabani-Yosef, and Amit Gefen. A method for quick, low-cost automated confluency measurements. *Microscopy and Microanalysis*, 17(6):915–922, 2011.

[59] Lee E Weiss, Silvina N Junkers, Mei Chen, Zhaozheng Yin, Michael F Sandbothe, Seungil Huh, Sungeun Eom, Ryoma Bise, Elvira Osuna-Highley, Takeo Kanade, et al. An engineered approach to stem cell culture: Automating the decision process for real-time adaptive subculture of stem cells. *PloS one*, 6(11):e27672, 2011.

[60] Pierre-Marc Juneau, Alain Garnier, and Carl Duchesne. Selection and tuning of a fast and simple phase-contrast microscopy image segmentation algorithm for measuring myoblast growth kinetics in an automated manner. *Microscopy and microanalysis*, 19(4):855–866, 2013.

[61] Nicolas Jaccard, Lewis D Griffin, Ana Keser, Rhys J Macown, Alexandre Super, Farlan S Veraitch, and Nicolas Szita. Automated method for the rapid and precise estimation of adherent cell culture characteristics from phase contrast microscopy images. *Biotechnology and bioengineering*, 111(3):504–517, 2014.

[62] Lena Kastl, Michael Isbach, Dieter Dirksen, Jürgen Schnekenburger, and Björn Kemper. Quantitative phase imaging for cell culture quality control. *Cytometry Part A*, 91(5): 470–481, 2017.

[63] Guoan Zheng, Roarke Horstmeyer, and Changhuei Yang. Wide-field, high-resolution fourier ptychographic microscopy. *Nature photonics*, 7(9):739, 2013.

[64] Alon Greenbaum, Wei Luo, Ting-Wei Su, Zoltán Göröcs, Liang Xue, Serhan O Isikman, Ahmet F Coskun, Onur Mudanyali, and Aydogan Ozcan. Imaging without lenses: achievements and remaining challenges of wide-field on-chip microscopy. *Nature methods*, 9(9):889–895, 2012.

[65] Aydogan Ozcan and Euan McLeod. Lensless imaging and sensing. *Annual review of biomedical engineering*, 18:77–102, 2016.

[66] Ray Fontaine. The state-of-the-art of mainstream cmos image sensors. In *Proceedings of the International Image Sensors Workshop*, pages 6–12, 2015.

[67] Dirk Lange, Christopher W Storment, Catharine A Conley, and Gregory TA Kovacs. A microfluidic shadow imaging system for the study of the nematode caenorhabditis elegans in space. *Sensors and Actuators B: Chemical*, 107(2):904–914, 2005.

[68] Aydogan Ozcan and Utkan Demirci. Ultra wide-field lens-free monitoring of cells on-chip. *Lab on a Chip*, 8(1):98–106, 2008.

[69] Yichen Wu and Aydogan Ozcan. Lensless digital holographic microscopy and its applications in biomedicine and environmental monitoring. *Methods*, 2017.

[70] Mohendra Roy, Dongmin Seo, Sangwoo Oh, Ji-Woon Yang, and Sungkyu Seo. A review of recent progress in lens-free imaging and sensing. *Biosensors and Bioelectronics*, 88: 130–143, 2017.

[71] Zoltán Göröcs and Aydogan Ozcan. On-chip biomedical imaging. *IEEE reviews in biomedical engineering*, 6:29–46, 2013.

[72] Cheng Yang, Haowen Ma, Xu Cao, Xia Hua, Xiaofeng Bu, Limin Zhang, Tao Yue, and Feng Yan. Resolution-enhanced lensless color shadow imaging microscopy based on large field-of-view submicron-pixel imaging sensors. In *Proceedings of the IEEE Conference on Computer Vision and Pattern Recognition Workshops*, pages 2246–2253, 2018.

[73] Guoxiao Li, Rongbiao Zhang, Ning Yang, Changsheng Yin, Mingji Wei, Yecheng Zhang, and Jian Sun. An approach for cell viability online detection based on the characteristics of lensfree cell diffraction fingerprint. *Biosensors and Bioelectronics*, 107:163–169, 2018.

[74] Gerhard Gstraunthaler and Toni Lindl. *Zell-und Gewebekultur: allgemeine Grundlagen und spezielle Anwendungen*. Springer-Verlag, 2013.

[75] Lucas G Chase, Uma Lakshmipathy, Luis A Solchaga, Mahendra S Rao, and Mohan C Vemuri. A novel serum-free medium for the expansion of human mesenchymal stem cells. *Stem cell research & therapy*, 1(1):8, 2010.

[76] T.D. Pollard, W.C. Earnshaw, J. Lippincott-Schwartz, and G. Johnson. *Cell Biology E-Book*. Elsevier Health Sciences, 2016. ISBN 9780323400022. URL `https://books.google.de/books?id=Th1uDQAAQBAJ`.

[77] Katy Phelan and Kristin M May. Basic techniques in mammalian cell tissue culture. *Current protocols in cell biology*, 66(1):1–1, 2015.

[78] Maureen A Harrison and Ian F Rae. *General techniques of cell culture*. Cambridge University Press, 1997.

[79] Nitya Ramkumar and Buzz Baum. Coupling changes in cell shape to chromosome segregation. *Nature Reviews Molecular Cell Biology*, 17(8):nrm–2016, 2016.

[80] John W Haycock. 3d cell culture: a review of current approaches and techniques. In *3D cell culture*, pages 1–15. Springer, 2011.

[81] Mark W Tibbitt and Kristi S Anseth. Hydrogels as extracellular matrix mimics for 3d cell culture. *Biotechnology and bioengineering*, 103(4):655–663, 2009.

[82] Corine M Beaufort, Jean CA Helmijr, Anna M Piskorz, Marlous Hoogstraat, Kirsten Ruigrok-Ritstier, Nicolle Besselink, Muhammed Murtaza, Wilfred FJ van IJcken, Anouk AJ Heine, Marcel Smid, et al. Ovarian cancer cell line panel (occp): clinical importance of in vitro morphological subtypes. *PloS one*, 9(9):e103988, 2014.

[83] Fumiko Matsuoka, Ichiro Takeuchi, Hideki Agata, Hideaki Kagami, Hirofumi Shiono, Yasujiro Kiyota, Hiroyuki Honda, and Ryuji Kato. Morphology-based prediction of osteogenic differentiation potential of human mesenchymal stem cells. *PloS one*, 8(2): e55082, 2013.

[84] Richard Kasprowicz, Rakesh Suman, and Peter OToole. Characterising live cell behaviour: Traditional label-free and quantitative phase imaging approaches. *The international journal of biochemistry & cell biology*, 84:89–95, 2017.

[85] Dagmar Beier, Peter Hau, Martin Proescholdt, Annette Lohmeier, Jörg Wischhusen, Peter J Oefner, Ludwig Aigner, Alexander Brawanski, Ulrich Bogdahn, and Christoph P Beier. Cd133+ and cd133- glioblastoma-derived cancer stem cells show differential growth characteristics and molecular profiles. *Cancer research*, 67(9):4010–4015, 2007.

[86] June L Biedler, Lawrence Helson, and Barbara A Spengler. Morphology and growth, tumorigenicity, and cytogenetics of human neuroblastoma cells in continuous culture. *Cancer research*, 33(11):2643–2652, 1973.

[87] Laure Cayrefourcq, Thibault Mazard, Simon Joosse, Jérôme Solassol, Jeanne Ramos, Eric Assenat, Udo Schumacher, Valérie Costes, Thierry Maudelonde, Klaus Pantel, et al. Establishment and characterization of a cell line from human circulating colon cancer cells. *Cancer research*, 75(5):892–901, 2015.

[88] Desirae L Deskins, Dikshya Bastakoty, Sarika Saraswati, Andrew Shinar, Ginger E Holt, and Pampee P Young. Human mesenchymal stromal cells: identifying assays to predict potency for therapeutic selection. *Stem cells translational medicine*, 2(2):151–158, 2013.

[89] Alessandro Bertolo, Marco Mehr, Tiziana Janner-Jametti, Ursula Graumann, Niklaus Aebli, Martin Baur, Stephen J Ferguson, and Jivko V Stoyanov. An in vitro expansion score for tissue-engineering applications with human bone marrow-derived mesenchymal stem cells. *Journal of tissue engineering and regenerative medicine*, 10(2):149–161, 2016.

[90] Herta Reile, Herbert Birnböck, Günther Bernhardt, Thilo Spruß, and Helmut Schönenberger. Computerized determination of growth kinetic curves and doubling times from cells in microculture. *Analytical biochemistry*, 187(2):262–267, 1990.

[91] Felix Buggenthin, Carsten Marr, Michael Schwarzfischer, Philipp S Hoppe, Oliver Hilsenbeck, Timm Schroeder, and Fabian J Theis. An automatic method for robust and fast cell detection in bright field images from high-throughput microscopy. *BMC bioinformatics*, 14(1):297, 2013.

[92] Edwin F Juarez, Roy Lau, Samuel H Friedman, Ahmadreza Ghaffarizadeh, Edmond Jonckheere, David B Agus, Shannon M Mumenthaler, and Paul Macklin. Quantifying

differences in cell line population dynamics using cellpd. *BMC systems biology*, 10(1):92, 2016.

[93] Sébastien Benzekry, Clare Lamont, Afshin Beheshti, Amanda Tracz, John ML Ebos, Lynn Hlatky, and Philip Hahnfeldt. Classical mathematical models for description and prediction of experimental tumor growth. *PLoS computational biology*, 10(8):e1003800, 2014.

[94] Alessandro Bertolo, Armin Gemperli, Marco Gruber, Benjamin Gantenbein, Martin Baur, Tobias Pötzel, and Jivko Stoyanov. In vitro cell motility as a potential mesenchymal stem cell marker for multipotency. *Stem cells translational medicine*, 4(1):84–90, 2015.

[95] Peter Friedl. Prespecification and plasticity: shifting mechanisms of cell migration. *Current opinion in cell biology*, 16(1):14–23, 2004.

[96] Germán Reig, Eduardo Pulgar, and Miguel L Concha. Cell migration: from tissue culture to embryos. *Development*, 141(10):1999–2013, 2014.

[97] Ryan J Petrie, Andrew D Doyle, and Kenneth M Yamada. Random versus directionally persistent cell migration. *Nature reviews Molecular cell biology*, 10(8):538, 2009.

[98] Pernille Rørth. Collective cell migration. *Annual Review of Cell and Developmental*, 25: 407–429, 2009.

[99] Peter Friedl and Darren Gilmour. Collective cell migration in morphogenesis, regeneration and cancer. *Nature reviews Molecular cell biology*, 10(7):445, 2009.

[100] Denis Wirtz, Konstantinos Konstantopoulos, and Peter C Searson. The physics of cancer: the role of physical interactions and mechanical forces in metastasis. *Nature Reviews Cancer*, 11(7):512, 2011.

[101] Matthias L Zorn, Anna-Kristina Marel, Felix J Segerer, and Joachim O Rädler. Phenomenological approaches to collective behavior in epithelial cell migration. *Biochimica et Biophysica Acta (BBA)-Molecular Cell Research*, 1853(11):3143–3152, 2015.

[102] Laurence Petitjean, Myriam Reffay, Erwan Grasland-Mongrain, Mathieu Poujade, Benoıt Ladoux, Axel Buguin, and Pascal Silberzan. Velocity fields in a collectively migrating epithelium. *Biophysical journal*, 98(9):1790–1800, 2010.

[103] Bart Smeets, Ricard Alert, Jiří Pešek, Ignacio Pagonabarraga, Herman Ramon, and Romaric Vincent. Emergent structures and dynamics of cell colonies by contact inhibition of locomotion. *Proceedings of the National Academy of Sciences*, 113(51):14621–14626, 2016.

[104] Mae L Woods, Carlos Carmona-Fontaine, Chris P Barnes, Iain D Couzin, Roberto Mayor, and Karen M Page. Directional collective cell migration emerges as a property of cell interactions. *PLoS One*, 9(9):e104969, 2014.

[105] Shanmiao Gou, Tao Liu, Chunyou Wang, Tao Yin, Kai Li, Ming Yang, and Jing Zhou. Establishment of clonal colony-forming assay for propagation of pancreatic cancer cells with stem cell properties. *Pancreas*, 34(4):429–435, 2007.

[106] Chien-Lin Chen and Hong-Chen Chen. Functional suppression of e-cadherin by protein kinase cδ. *Journal of cell science*, 122(4):513–523, 2009.

[107] Tarek MA Elsaba, Luisa Martinez-Pomares, Adrian R Robins, Simon Crook, Rashmi Seth, Darryl Jackson, Amy McCart, Andrew R Silver, Ian PM Tomlinson, and Mohammad Ilyas. The stem cell marker cd133 associates with enhanced colony formation and cell motility in colorectal cancer. *PloS one*, 5(5):e10714, 2010.

[108] Chenfei Zhou, Jun Ji, Qu Cai, Min Shi, Xuehua Chen, Yingyan Yu, Zhenggang Zhu, and Jun Zhang. Mta2 enhances colony formation and tumor growth of gastric cancer cells through il-11. *BMC cancer*, 15(1):343, 2015.

[109] Muthu Subash Kavitha, Takio Kurita, Soon-Yong Park, Sung-Il Chien, Jae-Sung Bae, and Byeong-Cheol Ahn. Deep vector-based convolutional neural network approach for automatic recognition of colonies of induced pluripotent stem cells. *PloS one*, 12(12): e0189974, 2017.

[110] Ryuji Kato, Megumi Matsumoto, Hiroto Sasaki, Risako Joto, Mai Okada, Yurika Ikeda, Kei Kanie, Mika Suga, Masaki Kinehara, Kana Yanagihara, et al. Parametric analysis of colony morphology of non-labelled live human pluripotent stem cells for cell quality control. *Scientific reports*, 6, 2016.

[111] MJ Vilela, ML Martins, NS Renato, L Cazares, F Lattanzio, M Ward, and OJ Semmes. Proteomic and fractal analysis of a phenotypic transition in the growth of human breast cells in culture. *Journal of Statistical Mechanics: Theory and Experiment*, 2007(12): P12006, 2007.

[112] Juliane Zimmermann, Brian A Camley, Wouter-Jan Rappel, and Herbert Levine. Contact inhibition of locomotion determines cell–cell and cell–substrate forces in tissues. *Proceedings of the National Academy of Sciences*, 113(10):2660–2665, 2016.

[113] Alberto Puliafito, Lars Hufnagel, Pierre Neveu, Sebastian Streichan, Alex Sigal, D Kuchnir Fygenson, and Boris I Shraiman. Collective and single cell behavior in epithelial contact inhibition. *Proceedings of the National Academy of Sciences*, 109(3):739–744, 2012.

[114] Dapeng Bi, Xingbo Yang, M Cristina Marchetti, and M Lisa Manning. Motility-driven glass and jamming transitions in biological tissues. *Physical Review X*, 6(2):021011, 2016.

[115] Kathryn A Rosowski, Aaron F Mertz, Samuel Norcross, Eric R Dufresne, and Valerie Horsley. Edges of human embryonic stem cell colonies display distinct mechanical properties and differentiation potential. *Scientific reports*, 5:14218, 2015.

[116] N Garijo, R Manzano, R Osta, and MA Perez. Stochastic cellular automata model of cell migration, proliferation and differentiation: Validation with in vitro cultures of muscle satellite cells. *Journal of theoretical biology*, 314:1–9, 2012.

[117] Paul Van Liedekerke, MM Palm, N Jagiella, and Dirk Drasdo. Simulating tissue mechanics with agent-based models: concepts, perspectives and some novel results. *Computational Particle Mechanics*, 2(4):401–444, 2015.

[118] Sebastian Aland, Haralambos Hatzikirou, John Lowengrub, and Axel Voigt. A mechanistic collective cell model for epithelial colony growth and contact inhibition. *Biophysical journal*, 109(7):1347–1357, 2015.

[119] Yuki Kagawa and Masahiro Kino-oka. An in silico prediction tool for the expansion culture of human skeletal muscle myoblasts. *Royal Society open science*, 3(10):160500, 2016.

[120] JJ Vaca-González, ML Gutiérrez, JM Guevara, and DA Garzón-Alvarado. Cellular automata model for human articular chondrocytes migration, proliferation and cell death: an in vitro validation. *In silico biology*, 12(3-4):83–93, 2017.

[121] Fangfang Du, Xiaohong Wu, Yanjun Liu, Teng Wang, Xiaowei Qi, Yong Mao, Li Jiang, Yifei Zhu, Yun Chen, Ruiyu Zhu, et al. Acquisition of paclitaxel resistance via pi3k-dependent epithelial-mesenchymal transition in a2780 human ovarian cancer cells. *Oncology reports*, 30(3):1113–1118, 2013.

[122] Samuel Baron. *Medical microbiology*. University of Texas Medical Branch at Galveston, Galveston, Tex, 1996. ISBN 978-0963117212.

[123] Stuart B. Levy and Bonnie Marshall. Antibacterial resistance worldwide: causes, challenges and responses. *Nature Medicine*, 10:S122 EP –, Nov 2004. URL `http://dx.doi.org/10.1038/nm1145`.

[124] Laura JV Piddock. The crisis of no new antibioticswhat is the way forward? *The Lancet infectious diseases*, 12(3):249–253, 2012.

[125] Richard J Fair and Yitzhak Tor. Antibiotics and bacterial resistance in the 21st century. *Perspectives in medicinal chemistry*, 6:PMC–S14459, 2014.

[126] Iruka N Okeke, Rosanna W Peeling, Herman Goossens, Raymond Auckenthaler, Stuart S Olmsted, Jean-François de Lavison, Barbara L Zimmer, Mark D Perkins, and Katarina Nordqvist. Diagnostics as essential tools for containing antibacterial resistance. *Drug resistance updates*, 14(2):95–106, 2011.

[127] Marina R Pulido, Meritxell García-Quintanilla, Reyes Martín-Peña, José Miguel Cisneros, and Michael J McConnell. Progress on the development of rapid methods for antimicrobial susceptibility testing. *Journal of Antimicrobial Chemotherapy*, 68(12):2710–2717, 2013.

[128] Julian Davies and Dorothy Davies. Origins and evolution of antibiotic resistance. *Microbiology and molecular biology reviews*, 74(3):417–433, 2010.

[129] Angela HAM Van Hoek, Dik Mevius, Beatriz Guerra, Peter Mullany, Adam Paul Roberts, and Henk JM Aarts. Acquired antibiotic resistance genes: an overview. *Frontiers in microbiology*, 2:203, 2011.

[130] Clayton W Hall and Thien-Fah Mah. Molecular mechanisms of biofilm-based antibiotic resistance and tolerance in pathogenic bacteria. *FEMS microbiology reviews*, 41(3):276–301, 2017.

[131] Niels Høiby, Thomas Bjarnsholt, Michael Givskov, Søren Molin, and Oana Ciofu. Antibiotic resistance of bacterial biofilms. *International journal of antimicrobial agents*, 35 (4):322–332, 2010.

[132] E.R.S. Hodges and Guild of Natural Science Illustrators (U.S.). *The Guild Handbook of Scientific Illustration*. Wiley, 2003. ISBN 9780471360117. URL `https://books.google.de/books?id=gD8pWkA6TcwC`.

[133] Qinnan Zhang, Liyun Zhong, Ping Tang, Yingjie Yuan, Shengde Liu, Jindong Tian, and Xiaoxu Lu. Quantitative refractive index distribution of single cell by combining phase-shifting interferometry and afm imaging. *Scientific reports*, 7(1):2532, 2017.

[134] Jurgen Stephan, Felix Keber, Valentin Stierle, Joachim O Radler, and Philipp Paulitschke. Single-cell optical distortion correction and label-free 3d cell shape reconstruction on lattices of nanostructures. *Nano letters*, 17(12):8018–8023, 2017.

[135] Myung K Kim. Principles and techniques of digital holographic microscopy. *SPIE Reviews*, 1(1):018005, 2010.

[136] Adam D Douglass and Ronald D Vale. Single-molecule imaging of fluorescent proteins. *Methods in cell biology*, 85:113–125, 2008.

[137] Samuel A Latt and G Stetten. Spectral studies on 33258 hoechst and related bisbenzimidazole dyes useful for fluorescent detection of deoxyribonucleic acid synthesis. *Journal of Histochemistry & Cytochemistry*, 24(1):24–33, 1976.

[138] Karen G Porter and Yvette S Feig. The use of dapi for identifying and counting aquatic microflora. *Limnology and oceanography*, 25(5):943–948, 1980.

[139] Roger Y Tsien. The green fluorescent protein, 1998.

[140] Daniel L Coutu and Timm Schroeder. Probing cellular processes by long-term live imaging–historic problems and current solutions. *J Cell Sci*, 126(17):3805–3815, 2013.

[141] Ellen C Jensen. Use of fluorescent probes: their effect on cell biology and limitations. *The Anatomical Record*, 295(12):2031–2036, 2012.

[142] Katherine B Abbitt, G Ed Rainger, and Gerard B Nash. Effects of fluorescent dyes on selectin and integrin-mediated stages of adhesion and migration of flowing leukocytes. *Journal of immunological methods*, 239(1-2):109–119, 2000.

[143] Linliang Yin, Wei Wang, Shaopeng Wang, Fenni Zhang, Shengtao Zhang, and Nongjian Tao. How does fluorescent labeling affect the binding kinetics of proteins with intact cells? *Biosensors and Bioelectronics*, 66:412–416, 2015.

[144] Jaroslav Icha, Michael Weber, Jennifer C Waters, and Caren Norden. Phototoxicity in live fluorescence microscopy, and how to avoid it. *Bioessays*, 39(8), 2017.

[145] Eugene Hecht. *Optics*. Pearson Education, 2016.

[146] Sri Rama Prasanna Pavani, Michael A Thompson, Julie S Biteen, Samuel J Lord, Na Liu, Robert J Twieg, Rafael Piestun, and WE Moerner. Three-dimensional, single-molecule fluorescence imaging beyond the diffraction limit by using a double-helix point spread function. *Proceedings of the National Academy of Sciences*, 106(9):2995–2999, 2009.

[147] Mark A Neifeld. Information, resolution, and space–bandwidth product. *Optics letters*, 23(18):1477–1479, 1998.

[148] Dennis Gabor. A new microscopic principle, 1948.

[149] Leonid Yaroslavsky. *Digital holography and digital image processing: principles, methods, algorithms*. Springer Science & Business Media, 2013.

[150] Ulf Schnars and Werner Jüptner. Direct recording of holograms by a ccd target and numerical reconstruction. *Applied optics*, 33(2):179–181, 1994.

[151] Ting-Chung Poon and Jung-Ping Liu. *Introduction to modern digital holography: with MATLAB*. Cambridge University Press, 2014.

[152] Jorge Garcia-Sucerquia, Wenbo Xu, Stephan K Jericho, Peter Klages, Manfred H Jericho, and H Jürgen Kreuzer. Digital in-line holographic microscopy. *Applied optics*, 45(5):836–850, 2006.

[153] Manfred H Jericho and H Jürgen Kreuzer. Point source digital in-line holographic microscopy digital in-line holographic microscopy. In *Coherent Light Microscopy*, pages 3–30. Springer, 2011.

[154] Ceyhun Akcay, Pascale Parrein, and Jannick P Rolland. Estimation of longitudinal resolution in optical coherence imaging. *Applied Optics*, 41(25):5256–5262, 2002.

[155] L Repetto, E Piano, and C Pontiggia. Lensless digital holographic microscope with light-emitting diode illumination. *Optics letters*, 29(10):1132–1134, 2004.

[156] Klaus D Mielenz. On the diffraction limit for lensless imaging. *Journal of research of the National Institute of Standards and Technology*, 104(5):479, 1999.

[157] Damien P Kelly, Bryan M Hennelly, Nitesh Pandey, Thomas J Naughton, and William T Rhodes. Resolution limits in practical digital holographic systems. *Optical Engineering*, 48(9):095801, 2009.

[158] Yan Hao and Anand Asundi. Resolution analysis of a digital holography system. *Applied optics*, 50(2):183–193, 2011.

[159] Temitope E Agbana, Hai Gong, Abena S Amoah, Vitaly Bezzubik, Michel Verhaegen, and Gleb Vdovin. Aliasing, coherence, and resolution in a lensless holographic microscope. *Optics letters*, 42(12):2271–2274, 2017.

[160] Patrik Langehanenberg, Björn Kemper, and Gert von Bally. Autofocus algorithms for digital-holographic microscopy. In *European Conference on Biomedical Optics*, page 6633_13. Optical Society of America, 2007.

[161] Elena Stoykova, Hoonjong Kang, and Jiyung Park. Twin-image problem in digital holography-a survey. *Chinese Optics Letters*, 12(6):060013, 2014.

[162] Loic Denis, Corinne Fournier, Thierry Fournel, and Christophe Ducottet. Twin-image noise reduction by phase retrieval in in-line digital holography. In *Wavelets XI*, volume 5914, page 59140J. International Society for Optics and Photonics, 2005.

[163] Yoav Shechtman, Yonina C Eldar, Oren Cohen, Henry Nicholas Chapman, Jianwei Miao, and Mordechai Segev. Phase retrieval with application to optical imaging: a contemporary overview. *IEEE signal processing magazine*, 32(3):87–109, 2015.

[164] Sang-Hyuk Lee, Yohai Roichman, Gi-Ra Yi, Shin-Hyun Kim, Seung-Man Yang, Alfons Van Blaaderen, Peter Van Oostrum, and David G Grier. Characterizing and tracking single colloidal particles with video holographic microscopy. *Optics Express*, 15(26):18275–18282, 2007.

[165] Fook Chiong Cheong, Bhaskar Jyoti Krishnatreya, and David G Grier. Strategies for three-dimensional particle tracking with holographic video microscopy. *Optics express*, 18(13):13563–13573, 2010.

[166] Xiao Yu, Jisoo Hong, Changgeng Liu, and Myung K Kim. Review of digital holographic microscopy for three-dimensional profiling and tracking. *Optical engineering*, 53(11): 112306, 2014.

[167] Frank Dubois, Catherine Yourassowsky, Olivier Monnom, J-C Legros, Olivier Debeir, Philippe Van Ham, Robert Kiss, and Christine Decaestecker. Digital holographic microscopy for the three-dimensional dynamic analysis of in vitro cancer cell migration. *Journal of biomedical optics*, 11(5):054032, 2006.

[168] Kersti Alm, Zahra El-Schich, Maria Falck Miniotis, Anette Gjörloff Wingren, Birgit Janicke, and Stina Oredsson. Cells and holograms–holograms and digital holographic microscopy as a tool to study the morphology of living cells. In *Holography-Basic Principles and Contemporary Applications*. Intech, 2013.

[169] Benjamin Rappaz, Alexander Barbul, Yves Emery, Rafi Korenstein, Christian Depeursinge, Pierre J Magistretti, and Pierre Marquet. Comparative study of human erythrocytes by digital holographic microscopy, confocal microscopy, and impedance volume analyzer. *Cytometry Part A*, 73(10):895–903, 2008.

[170] Nicolas Pavillon, Jonas Kühn, Corinne Moratal, Pascal Jourdain, Christian Depeursinge, Pierre J Magistretti, and Pierre Marquet. Early cell death detection with digital holographic microscopy. *PloS one*, 7(1):e30912, 2012.

[171] Pierre Marquet, Christian Depeursinge, and Pierre J Magistretti. Review of quantitative phase-digital holographic microscopy: promising novel imaging technique to resolve neuronal network activity and identify cellular biomarkers of psychiatric disorders. *Neurophotonics*, 1(2):020901, 2014.

[172] Björn Kemper, Andreas Bauwens, Angelika Vollmer, Steffi Ketelhut, Patrik Langehanenberg, Johannes Muthing, Helge Karch, and Gert von Bally. Label-free quantitative cell division monitoring of endothelial cells by digital holographic microscopy. *Journal of Biomedical Optics*, 15(3):036009, 2010.

[173] Yann Cotte, Fatih Toy, Pascal Jourdain, Nicolas Pavillon, Daniel Boss, Pierre Magistretti, Pierre Marquet, and Christian Depeursinge. Marker-free phase nanoscopy. *Nature Photonics*, 7(2):113, 2013.

[174] Birgit Janicke, Andreas Kårsnäs, Peter Egelberg, and Kersti Alm. Label-free high temporal resolution assessment of cell proliferation using digital holographic microscopy. *Cytometry Part A*, 91(5):460–469, 2017.

[175] Wenbo Xu, MH Jericho, IA Meinertzhagen, and HJ Kreuzer. Digital in-line holography for biological applications. *Proceedings of the National Academy of Sciences*, 98(20): 11301–11305, 2001.

[176] Xiquan Cui, Lap Man Lee, Xin Heng, Weiwei Zhong, Paul W Sternberg, Demetri Psaltis, and Changhuei Yang. Lensless high-resolution on-chip optofluidic microscopes

for caenorhabditis elegans and cell imaging. *Proceedings of the National Academy of Sciences*, 105(31):10670–10675, 2008.

[177] Chao Han, Shuo Pang, Danielle V Bower, Patrick Yiu, and Changhuei Yang. Wide field-of-view on-chip talbot fluorescence microscopy for longitudinal cell culture monitoring from within the incubator. *Analytical chemistry*, 85(4):2356–2360, 2013.

[178] Eric R Fossum, Donald B Hondongwa, et al. A review of the pinned photodiode for ccd and cmos image sensors. *IEEE J. Electron Devices Soc*, 2(3):33–43, 2014.

[179] D. Durini. *High Performance Silicon Imaging: Fundamentals and Applications of CMOS and CCD Sensors*. Woodhead Publishing series in electronic and optical materials. Elsevier Science & Technology, 2014. ISBN 9780857095985. URL `https://books.google.de/books?id=2FPqnQEACAAJ`.

[180] Abbas El Gamal and Helmy Eltoukhy. Cmos image sensors. *IEEE Circuits and Devices Magazine*, 21(3):6–20, 2005.

[181] Waheb Bishara, Ting-Wei Su, Ahmet F Coskun, and Aydogan Ozcan. Lensfree on-chip microscopy over a wide field-of-view using pixel super-resolution. *Optics express*, 18(11): 11181–11191, 2010.

[182] Onur Mudanyali, Derek Tseng, Chulwoo Oh, Serhan O Isikman, Ikbal Sencan, Waheb Bishara, Cetin Oztoprak, Sungkyu Seo, Bahar Khademhosseini, and Aydogan Ozcan. Compact, light-weight and cost-effective microscope based on lensless incoherent holography for telemedicine applications. *Lab on a Chip*, 10(11):1417–1428, 2010.

[183] Alon Greenbaum, Uzair Sikora, and Aydogan Ozcan. Field-portable wide-field microscopy of dense samples using multi-height pixel super-resolution based lensfree imaging. *Lab on a Chip*, 12(7):1242–1245, 2012.

[184] Wei Luo, Alon Greenbaum, Yibo Zhang, and Aydogan Ozcan. Synthetic aperture-based on-chip microscopy. *Light: Science & Applications*, 4(3):e261, 2015.

[185] Daniel WE Noom, Kjeld SE Eikema, and Stefan Witte. Lensless phase contrast microscopy based on multiwavelength fresnel diffraction. *Optics letters*, 39(2):193–196, 2014.

[186] Richard Stahl, Geert Vanmeerbeeck, Gauthier Lafruit, Roeland Huys, Veerle Reumers, Andy Lambrechts, Chao-Kang Liao, Chin-Chun Hsiao, Masayuki Yashiro, Masashi Takemoto, et al. Lens-free digital in-line holographic imaging for wide field-of-view, high-resolution and real-time monitoring of complex microscopic objects. In *Imaging, Manipulation, and Analysis of Biomolecules, Cells, and Tissues XII*, volume 8947, page 89471F. International Society for Optics and Photonics, 2014.

[187] Wei Luo, Yibo Zhang, Zoltán Göröcs, Alborz Feizi, and Aydogan Ozcan. Propagation phasor approach for holographic image reconstruction. *Scientific reports*, 6:22738, 2016.

[188] Yair Rivenson, Yichen Wu, Hongda Wang, Yibo Zhang, Alborz Feizi, and Aydogan Ozcan. Sparsity-based multi-height phase recovery in holographic microscopy. *Scientific reports*, 6:37862, 2016.

[189] Anwar Hussain, Yicheng Li, Diyi Liu, Cuifang Kuang, and Xu Liu. On-chip microscopy using random phase mask scheme. *Scientific reports*, 7(1):14768, 2017.

[190] Ayan Sinha, Justin Lee, Shuai Li, and George Barbastathis. Lensless computational imaging through deep learning. *Optica*, 4(9):1117–1125, 2017.

[191] Yichen Wu, Yair Rivenson, Yibo Zhang, Zhensong Wei, Harun Günaydin, Xing Lin, and Aydogan Ozcan. Extended depth-of-field in holographic imaging using deep-learning-based autofocusing and phase recovery. *Optica*, 5(6):704–710, 2018.

[192] Serhan O Isikman, Waheb Bishara, Sam Mavandadi, W Yu Frank, Steve Feng, Randy Lau, and Aydogan Ozcan. Lens-free optical tomographic microscope with a large imaging volume on a chip. *Proceedings of the National Academy of Sciences*, 108(18):7296–7301, 2011.

[193] Evelien Mathieu, Colin D Paul, Richard Stahl, Geert Vanmeerbeeck, Veerle Reumers, Chengxun Liu, Konstantinos Konstantopoulos, and Liesbet Lagae. Time-lapse lens-free imaging of cell migration in diverse physical microenvironments. *Lab on a Chip*, 16(17): 3304–3316, 2016.

[194] John Weidling, Serhan O Isikman, Alon Greenbaum, Aydogan Ozcan, and Elliot L Botvinick. Lens-free computational imaging of capillary morphogenesis within three-dimensional substrates. *Journal of biomedical optics*, 17(12):126018, 2012.

[195] Alon Greenbaum, Yibo Zhang, Alborz Feizi, Ping-Luen Chung, Wei Luo, Shivani R Kandukuri, and Aydogan Ozcan. Wide-field computational imaging of pathology slides using lens-free on-chip microscopy. *Science translational medicine*, 6(267):267ra175–267ra175, 2014.

[196] C Allier, S Morel, R Vincent, L Ghenim, F Navarro, M Menneteau, T Bordy, L Hervé, O Cioni, X Gidrol, et al. Imaging of dense cell cultures by multiwavelength lens-free video microscopy. *Cytometry Part A*, 91(5):433–442, 2017.

[197] Ting-Wei Su, Sungkyu Seo, Anthony Erlinger, and Aydogan Ozcan. High-throughput lensfree imaging and characterization of a heterogeneous cell solution on a chip. *Biotechnology and bioengineering*, 102(3):856–868, 2009.

[198] Mohendra Roy, Geonsoo Jin, Dongmin Seo, Myung-Hyun Nam, and Sungkyu Seo. A simple and low-cost device performing blood cell counting based on lens-free shadow imaging technique. *Sensors and Actuators B: Chemical*, 201:321–328, 2014.

[199] Yuan Fang, Ningmei Yu, Runlong Wang, and Dong Su. An on-chip instrument for white blood cells classification based on a lens-less shadow imaging technique. *PloS one*, 12(3): e0174580, 2017.

[200] Xiaohui Zhang, Imran Khimji, Umut Atakan Gurkan, Hooman Safaee, Paolo Nicolas Catalano, Hasan Onur Keles, Emre Kayaalp, and Utkan Demirci. Lensless imaging for simultaneous microfluidic sperm monitoring and sorting. *Lab on a Chip*, 11(15):2535–2540, 2011.

[201] Ivan Pushkarsky, Yunbo Liu, Westbrook Weaver, Ting-Wei Su, Onur Mudanyali, Aydogan Ozcan, and Dino Di Carlo. Automated single-cell motility analysis on a chip using lensfree microscopy. *Scientific reports*, 4:4717, 2014.

[202] Monika E Dolega, Cédric Allier, Srikanth Vinjimore Kesavan, Sophie Gerbaud, Frédérique Kermarrec, Pierre Marcoux, Jean-Marc Dinten, Xavier Gidrol, and Nathalie Picollet-DHahan. Label-free analysis of prostate acini-like 3d structures by lensfree imaging. *Biosensors and Bioelectronics*, 49:176–183, 2013.

[203] Sang Bok Kim, Hojae Bae, Jae Min Cha, Sang Jun Moon, Mehmet R Dokmeci, Donald M Cropek, and Ali Khademhosseini. A cell-based biosensor for real-time detection of cardiotoxicity using lensfree imaging. *Lab on a Chip*, 11(10):1801–1807, 2011.

[204] Yoshiaki Maeda, Hironori Dobashi, Yui Sugiyama, Tatsuya Saeki, Tae-kyu Lim, Manabu Harada, Tadashi Matsunaga, Tomoko Yoshino, and Tsuyoshi Tanaka. Colony fingerprint for discrimination of microbial species based on lensless imaging of microcolonies. *PloS one*, 12(4):e0174723, 2017.

[205] Geonsoo Jin, In-Hwa Yoo, Seung Pil Pack, Ji-Woon Yang, Un-Hwan Ha, Se-Hwan Paek, and Sungkyu Seo. Lens-free shadow image based high-throughput continuous cell monitoring technique. *Biosensors and Bioelectronics*, 38(1):126–131, 2012.

[206] Srikanth Vinjimore Kesavan, Fabrice P Navarro, Mathilde Menneteau, Frederique Mittler, Brigitte David-Watine, Nelly Dubrulle, Spencer L Shorte, Bernard Chalmond, Jean-Marc Dinten, and Cedric P Allier. Real-time label-free detection of dividing cells by means of lensfree video-microscopy. *Journal of biomedical optics*, 19(3):036004–036004, 2014.

[207] Lynsey A Penwill, Gwendoline E Batten, Stefania Castagnetti, and Andrew M Shaw. Growth phenotype screening of schizosaccharomyces pombe using a lensless microscope. *Biosensors and Bioelectronics*, 54:345–350, 2014.

[208] Mohendra Roy, Geonsoo Jin, Jeong-Hoon Pan, Dongmin Seo, Yongha Hwang, Sangwoo Oh, Moonjin Lee, Young Jun Kim, and Sungkyu Seo. Staining-free cell viability measurement technique using lens-free shadow imaging platform. *Sensors and Actuators B: Chemical*, 224:577–583, 2016.

[209] Guoan Zheng, Seung Ah Lee, Yaron Antebi, Michael B Elowitz, and Changhuei Yang. The epetri dish, an on-chip cell imaging platform based on subpixel perspective sweeping microscopy (spsm). *Proceedings of the National Academy of Sciences*, 108(41):16889–16894, 2011.

[210] Sina Wäldchen, Julian Lehmann, Teresa Klein, Sebastian Van De Linde, and Markus Sauer. Light-induced cell damage in live-cell super-resolution microscopy. *Scientific reports*, 5:15348, 2015.

[211] Tigran V Galstian. *Smart mini-cameras*. CRC press, 2013.

[212] H Rhodes, D Tai, Y Qian, D Mao, V Venezia, Wei Zheng, Z Xiong, CY Liu, KC Ku, S Manabe, et al. The mass production of bsi cmos image sensors. In *International Image Sensor Workshop*, volume 2009, pages 27–32, 2009.

[213] Kyusam Lim, Hwangyoung So, Sejin Kang, Jeonghun Kim, and Suki Kim. 3 megapixel camera signal processor for mobile camera applications. In *Electronics, Circuits and Systems, 2006. ICECS'06. 13th IEEE International Conference on*, pages 886–889. IEEE, 2006.

[214] Tobias Pärr. In Situ Timelapse Reconstruction-Free Monitoring of Confluence with a Lensfree, Ultra Small, Low Cost Microscopic Setup. Master's thesis, Ludwig Maximilians Universität München, Germany, 2016.

[215] David J Stephens and Victoria J Allan. Light microscopy techniques for live cell imaging. *Science*, 300(5616):82–86, 2003.

[216] Konstantin J. Ditzel. Time-dependent drug response in multiparametric viability assay based on lensless microscopy. Master's thesis, Ludwig Maximilians Universität München, Germany, 2018.

[217] Emily L Deer, Jessica González-Hernández, Jill D Coursen, Jill E Shea, Josephat Ngatia, Courtney L Scaife, Matthew A Firpo, and Sean J Mulvihill. Phenotype and genotype of pancreatic cancer cell lines. *Pancreas*, 39(4):425, 2010.

[218] Anja Torsvik, Daniel Stieber, Per Øyvind Enger, Anna Golebiewska, Anders Molven, Agnete Svendsen, Bengt Westermark, Simone P Niclou, Thale Kristin Olsen, Martha Chekenya Enger, et al. U-251 revisited: genetic drift and phenotypic consequences of long-term cultures of glioblastoma cells. *Cancer medicine*, 3(4):812–824, 2014.

[219] Morgan Harris. Phenotypic changes in cell culture. In *Genomic Adaptability in Somatic Cell Specialization*, pages 79–95. Springer, 1989.

[220] L Yao, CS Bestwick, Lara Anne Bestwick, N Maffulli, and Richard Malcolm Aspden. Phenotypic drift in human tenocyte culture. *Tissue engineering*, 12(7):1843–1849, 2006.

[221] Camila Bonazza, Sheila Siqueira Andrade, Joana Tomomi Sumikawa, Fabrício Pereira Batista, Edgar J Paredes-Gamero, Manoel JBC Girão, Maria Luiza V Oliva, and Rodrigo Aquino Castro. Primary human uterine leiomyoma cell culture quality control: some properties of myometrial cells cultured under serum deprivation conditions in the presence of ovarian steroids. *PloS one*, 11(7):e0158578, 2016.

[222] Manuela Natoli, Bruno D Leoni, Igea DAgnano, Flavia Zucco, and Armando Felsani. Good caco-2 cell culture practices. *Toxicology in vitro*, 26(8):1243–1246, 2012.

[223] Berend Snijder and Lucas Pelkmans. Origins of regulated cell-to-cell variability. *Nature reviews Molecular cell biology*, 12(2):119, 2011.

[224] Chiho Ikebe and Ken Suzuki. Mesenchymal stem cells for regenerative therapy: optimization of cell preparation protocols. *BioMed research international*, 2014, 2014.

[225] Céline Martin, Éric Olmos, Marie-Laure Collignon, Natalia De Isla, Fabrice Blanchard, Isabelle Chevalot, Annie Marc, and Emmanuel Guedon. Revisiting msc expansion from critical quality attributes to critical culture process parameters. *Process Biochemistry*, 59:231–243, 2017.

[226] Ichiro Sekiya, Benjamin L Larson, Jason R Smith, Radhika Pochampally, Jian-Guo Cui, and Darwin J Prockop. Expansion of human adult stem cells from bone marrow stroma: conditions that maximize the yields of early progenitors and evaluate their quality. *Stem cells*, 20(6):530–541, 2002.

[227] RJ Geraghty, A Capes-Davis, JM Davis, J Downward, RI Freshney, I Knezevic, R Lovell-Badge, JRW Masters, J Meredith, GN Stacey, et al. Guidelines for the use of cell lines in biomedical research. *British journal of cancer*, 111(6):1021, 2014.

[228] Sang Bok Kim, Kyo-in Koo, Hojae Bae, Mehmet R Dokmeci, Geraldine A Hamilton, Anthony Bahinski, Sun Min Kim, Donald E Ingber, and Ali Khademhosseini. A mini-microscope for in situ monitoring of cells. *Lab on a Chip*, 12(20):3976–3982, 2012.

[229] Di Jin, Dennis Wong, Junxiang Li, Zhang Luo, Yiran Guo, Bifeng Liu, Qiong Wu, Chih-Ming Ho, and Peng Fei. Compact wireless microscope for in-situ time course study of large scale cell dynamics within an incubator. *Scientific reports*, 5:18483, 2015.

[230] Jinho Kim, Beverley M Henley, Charlene H Kim, Henry A Lester, and Changhuei Yang. Incubator embedded cell culture imaging system (emsight) based on fourier ptychographic microscopy. *Biomedical optics express*, 7(8):3097–3110, 2016.

[231] Gary Bradski and Adrian Kaehler. *Learning OpenCV: Computer vision with the OpenCV library*. " O'Reilly Media, Inc.", 2008.

[232] Markus Rempfler, Sanjeev Kumar, Valentin Stierle, Philipp Paulitschke, Bjoern Andres, and Bjoern H Menze. Cell lineage tracing in lens-free microscopy videos. In *International Conference on Medical Image Computing and Computer-Assisted Intervention*, pages 3–11. Springer, 2017.

[233] Markus Rempfler, Valentin Stierle, Konstantin Ditzel, Sanjeev Kumar, Philipp Paulitschke, Bjoern Andres, and Bjoern H Menze. Tracing cell lineages in videos of lens-free microscopy. *Medical Image Analysis*, 2018.

[234] Judith R Mourant, James P Freyer, Andreas H Hielscher, Angelia A Eick, Dan Shen, and Tamara M Johnson. Mechanisms of light scattering from biological cells relevant to noninvasive optical-tissue diagnostics. *Applied optics*, 37(16):3586–3593, 1998.

[235] Erik Meijering, Oleh Dzyubachyk, Ihor Smal, et al. 9 methods for cell and particle tracking. *Methods in enzymology*, 504(9):183–200, 2012.

[236] Joost B Beltman, Athanasius FM Marée, and Rob J De Boer. Analysing immune cell migration. *Nature Reviews Immunology*, 9(11):789–798, 2009.

[237] Dávid Selmeczi, Liang Li, Lykke II Pedersen, SF Nrrelykke, Peter H Hagedorn, Stephan Mosler, Niels B Larsen, Edward C Cox, and Henrik Flyvbjerg. Cell motility as random motion: A review. *The European Physical Journal Special Topics*, 157(1):1–15, 2008.

[238] Stefan Thurner, Nikolaus Wick, Rudolf Hanel, Roland Sedivy, and Lukas Huber. Anomalous diffusion on dynamical networks: a model for interacting epithelial cell migration. *Physica A: Statistical Mechanics and its Applications*, 320:475 – 484, 2003. ISSN 0378-4371. doi: https://doi.org/10.1016/S0378-4371(02)01598-4. URL `http://www.sciencedirect.com/science/article/pii/S0378437102015984`.

[239] Eldad Kepten, Aleksander Weron, Grzegorz Sikora, Krzysztof Burnecki, and Yuval Garini. Guidelines for the fitting of anomalous diffusion mean square displacement graphs from single particle tracking experiments. *PLoS One*, 10(2):e0117722, 2015.

[240] Tatiane Souza Vilela Podestá, Tiago Venzel Rosembach, Anésia Aparecida dos Santos, and Marcelo Lobato Martins. Anomalous diffusion and q-weibull velocity distributions in epithelial cell migration. *PloS one*, 12(7):e0180777, 2017.

[241] Sri Ram Krishna Vedula, Man Chun Leong, Tan Lei Lai, Pascal Hersen, Alexandre J Kabla, Chwee Teck Lim, and Benoît Ladoux. Emerging modes of collective cell migration induced by geometrical constraints. *Proceedings of the National Academy of Sciences*, 109 (32):12974–12979, 2012.

[242] Kevin Doxzen, Sri Ram Krishna Vedula, Man Chun Leong, Hiroaki Hirata, Nir S Gov, Alexandre J Kabla, Benoit Ladoux, and Chwee Teck Lim. Guidance of collective cell migration by substrate geometry. *Integrative biology*, 5(8):1026–1035, 2013.

[243] Simon Garcia, Edouard Hannezo, Jens Elgeti, Jean-François Joanny, Pascal Silberzan, and Nir S Gov. Physics of active jamming during collective cellular motion in a monolayer. *Proceedings of the National Academy of Sciences*, 112(50):15314–15319, 2015.

[244] Rosemairy L Mendes, Anésia A Santos, ML Martins, and MJ Vilela. Cluster size distribution of cell aggregates in culture. *Physica A: Statistical Mechanics and its Applications*, 298(3):471–487, 2001.

[245] Jiafeng Geng, Mena Aioub, Mostafa A El-Sayed, and Bridgette A Barry. Uv resonance raman study of apoptosis, platinum-based drugs, and human cell lines. *ChemPhysChem*, 2018.

[246] Ioan Notingher. Raman spectroscopy cell-based biosensors. *Sensors*, 7(8):1343–1358, 2007.

[247] Megan L Gelsinger, Laura L Tupper, and David S Matteson. Cell line classification using electric cell-substrate impedance sensing (ecis). *arXiv preprint arXiv:1710.09821*, 2017.

[248] Lionel Blanchet, Jan AM Smeitink, Sjenet E Van Emst-De Vries, Caroline Vogels, Mina Pellegrini, An I Jonckheere, Richard JT Rodenburg, Lutgarde MC Buydens, Julien Beyrath, Peter HGM Willems, et al. Quantifying small molecule phenotypic effects using mitochondrial morpho-functional fingerprinting and machine learning. *Scientific reports*, 5:8035, 2015.

[249] Christoph Schreiber, Felix J Segerer, Ernst Wagner, Andreas Roidl, and Joachim O Rädler. Ring-shaped microlanes and chemical barriers as a platform for probing single-cell migration. *Scientific reports*, 6:26858, 2016.

[250] Steven Busschots, Sharon OToole, John J OLeary, and Britta Stordal. Non-invasive and non-destructive measurements of confluence in cultured adherent cell lines. *MethodsX*, 2: 8–13, 2015.

[251] C Kent Osborne, Kimberly Hobbs, and Jeffrey M Trent. Biological differences among mcf-7 human breast cancer cell lines from different laboratories. *Breast cancer research and treatment*, 9(2):111–121, 1987.

[252] Francis Jacob, Sheri Nixdorf, Neville F Hacker, and Viola A Heinzelmann-Schwarz. Reliable in vitro studies require appropriate ovarian cancer cell lines. *Journal of ovarian research*, 7(1):60, 2014.

[253] Anita Bandrowski, Matthew Brush, Jeffery S Grethe, Melissa A Haendel, David N Kennedy, Sean Hill, Patrick R Hof, Maryann E Martone, Maaike Pols, Serena C Tan, et al. The resource identification initiative: A cultural shift in publishing. *Journal of Comparative Neurology*, 524(1):8–22, 2016.

[254] Sachiko Sato, Ann Rancourt, Yukiko Sato, and Masahiko S Satoh. Single-cell lineage tracking analysis reveals that an established cell line comprises putative cancer stem cells and their heterogeneous progeny. *Scientific reports*, 6:23328, 2016.

[255] MH Gail and Ch W Boone. Cell-substrate adhesivity: a determinant of cell motility. *Experimental cell research*, 70(1):33–40, 1972.

[256] A Tremel, A Cai, N Tirtaatmadja, BD Hughes, GW Stevens, KA Landman, and AJ OConnor. Cell migration and proliferation during monolayer formation and wound healing. *Chemical Engineering Science*, 64(2):247–253, 2009.

[257] Matthew J Simpson, Kai-Yin Lo, and Yung-Shin Sun. Quantifying the roles of random motility and directed motility using advection-diffusion theory for a 3t3 fibroblast cell migration assay stimulated with an electric field. *BMC systems biology*, 11(1):39, 2017.

[258] Anna Q Cai, Kerry A Landman, and Barry D Hughes. Multi-scale modeling of a wound-healing cell migration assay. *Journal of Theoretical Biology*, 245(3):576–594, 2007.

[259] Daniel Campos, Vicenç Méndez, and Isaac Llopis. Persistent random motion: Uncovering cell migration dynamics. *Journal of theoretical biology*, 267(4):526–534, 2010.

[260] Richard B Dickinson and Robert T Tranquillo. Optimal estimation of cell movement indices from the statistical analysis of cell tracking data. *AIChE Journal*, 39(12):1995–2010, 1993.

[261] Claus Metzner, Christoph Mark, Julian Steinwachs, Lena Lautscham, Franz Stadler, and Ben Fabry. Superstatistical analysis and modelling of heterogeneous random walks. *Nature communications*, 6, 2015.

[262] David Selmeczi, Stephan Mosler, Peter H Hagedorn, Niels B Larsen, and Henrik Flyvbjerg. Cell motility as persistent random motion: theories from experiments. *Biophysical journal*, 89(2):912–931, 2005.

[263] MH Ernst and PGJ Van Dongen. Scaling laws in aggregation: fragmentation models with detailed balance. *Physical Review A*, 36(1):435, 1987.

[264] Fumio Oosawa. Size distribution of protein polymers. *Journal of theoretical biology*, 27 (1):69–86, 1970.

[265] TA Witten Jr and Leonard M Sander. Diffusion-limited aggregation, a kinetic critical phenomenon. *Physical review letters*, 47(19):1400, 1981.

[266] SG Alves and ML Martins. Cluster–cluster aggregation with particle replication and chemotaxy: a simple model for the growth of animal cells in culture. *Journal of Statistical Mechanics: Theory and Experiment*, 2010(09):P09012, 2010.

[267] Hwanseok Jang, Jacob Notbohm, Bomi Gweon, Youngbin Cho, Chan Young Park, Sun-Ho Kee, Jeffrey J Fredberg, Jennifer H Shin, and Yongdoo Park. Homogenizing cellular tension by hepatocyte growth factor in expanding epithelial monolayer. *Scientific Reports*, 7:45844, 2017.

[268] Somanna A Kollimada, Ankur H Kulkarni, Aniket Ravan, and Namrata Gundiah. Advancing edge speeds of epithelial monolayers depend on their initial confining geometry. *PloS one*, 11(4):e0153471, 2016.

[269] Aarthi Ramesh, Aishwarya Pattabhi, and Maddaly Ravi. Assays used in vitro to study cancer cell lines. *Life Science Research*, 1(01):19–24, 2016.

[270] Otília Menyhárt, Hajnalka Harami-Papp, Saraswati Sukumar, Reinhold Schäfer, Luca Magnani, Oriol de Barrios, and Balázs Győrffy. Guidelines for the selection of functional assays to evaluate the hallmarks of cancer. *Biochimica et Biophysica Acta (BBA)-Reviews on Cancer*, 1866(2):300–319, 2016.

[271] Daniel F Gilbert and Oliver Friedrich. *Cell Viability Assays*. Springer, 2017.

[272] G Sitta Sittampalam, Nathan P Coussens, K Brimacombe, A Grossman, M Arkin, D Auld, C Austin, J Baell, B Bejcek, TDY Chung, et al. Assay guidance manual. 2004.

[273] Helga HJ Gerets, Stéphane Dhalluin, and Franck A Atienzar. Multiplexing cell viability assays. In *Mammalian Cell Viability*, pages 91–101. Springer, 2011.

[274] Terry L Riss, Richard A Moravec, and Andrew L Niles. Cytotoxicity testing: measuring viable cells, dead cells, and detecting mechanism of cell death. In *Mammalian Cell Viability*, pages 103–114. Springer, 2011.

[275] Daniel F Gilbert and Michael Boutros. A protocol for a high-throughput multiplex cell viability assay. In *High-Throughput RNAi Screening*, pages 75–84. Springer, 2016.

[276] Tina M Hallis, Andrew L Kopp, Jasmin Gibson, Connie S Lebakken, Michael Hancock, Kaitlyn Vandenheuvel-Kramer, and Tammy Turek-Etienne. An improved β-lactamase reporter assay: multiplexing with a cytotoxicity readout for enhanced accuracy of hit identification. *Journal of biomolecular screening*, 12(5):635–644, 2007.

[277] Kelli Solly, Xiaobo Wang, Xiao Xu, Berta Strulovici, and Wei Zheng. Application of real-time cell electronic sensing (rt-ces) technology to cell-based assays. *Assay and drug development technologies*, 2(4):363–372, 2004.

[278] Charles R Keese, Joachim Wegener, Sarah R Walker, and Ivar Giaever. Electrical wound-healing assay for cells in vitro. *Proceedings of the National Academy of Sciences*, 101(6): 1554–1559, 2004.

[279] Biao Xi, Naichen Yu, Xiaobo Wang, Xiao Xu, and Yama Abassi. The application of cell-based label-free technology in drug discovery. *Biotechnology journal*, 3(4):484–495, 2008.

[280] Aabid Shariff, Joshua Kangas, Luis Pedro Coelho, Shannon Quinn, and Robert F Murphy. Automated image analysis for high-content screening and analysis. *Journal of biomolecular screening*, 15(7):726–734, 2010.

[281] Michael Boutros, Florian Heigwer, and Christina Laufer. Microscopy-based high-content screening. *Cell*, 163(6):1314–1325, 2015.

[282] Zi Di, Maarten JD Klop, Vasiliki-Maria Rogkoti, Sylvia E Le Dévédec, Bob van de Water, Fons J Verbeek, Leo S Price, and John HN Meerman. Ultra high content image analysis and phenotype profiling of 3d cultured micro-tissues. *PLoS One*, 9(10):e109688, 2014.

[283] Juan C Caicedo, Shantanu Singh, and Anne E Carpenter. Applications in image-based profiling of perturbations. *Current opinion in biotechnology*, 39:134–142, 2016.

[284] Leonard P Freedman, Iain M Cockburn, and Timothy S Simcoe. The economics of reproducibility in preclinical research. *PLoS biology*, 13(6):e1002165, 2015.

[285] Florian Prinz, Thomas Schlange, and Khusru Asadullah. Believe it or not: how much can we rely on published data on potential drug targets? *Nature reviews Drug discovery*, 10(9):712–712, 2011.

[286] C Glenn Begley and Lee M Ellis. Drug development: Raise standards for preclinical cancer research. *Nature*, 483(7391):531–533, 2012.

[287] C Glenn Begley and John PA Ioannidis. Reproducibility in science: improving the standard for basic and preclinical research. *Circulation research*, 116(1):116–126, 2015.

[288] Aimo Kannt and Thomas Wieland. Managing risks in drug discovery: reproducibility of published findings. *Naunyn-Schmiedeberg's archives of pharmacology*, 389(4):353–360, 2016.

[289] Leonard P Freedman and James Inglese. The increasing urgency for standards in basic biologic research. *Cancer research*, 2014.

[290] Vanicha Vichai and Kanyawim Kirtikara. Sulforhodamine b colorimetric assay for cytotoxicity screening. *Nature protocols*, 1(3):1112, 2006.

[291] Y Nefedova, TH Landowski, and WS Dalton. Bone marrow stromal-derived soluble factors and direct cell contact contribute to de novo drug resistance of myeloma cells by distinct mechanisms. *Leukemia*, 17(6):1175, 2003.

[292] Carmen Garrido, Patrick Ottavi, Annie Fromentin, Arlette Hammann, André-Patrick Arrigo, Bruno Chauffert, and Patrick Mehlen. Hsp27 as a mediator of confluence-dependent resistance to cell death induced by anticancer drugs. *Cancer Research*, 57(13):2661–2667, 1997.

[293] Marie-ThéRéSe Dimanche-Boitrel, Hélène Pelletier, Philippe Genne, Jean-Michel Petit, Christian Le Grimellec, Pierre Canal, Claude Ardiet, Gérard Bastian, and Bruno Chauffert. Confluence-dependent resistance in human colon cancer cells: role of reduced drug accumulation and low intrinsic chemosensitivity of resting cells. *International journal of cancer*, 50(5):677–682, 1992.

[294] Carol E Cass. Density-dependent resistance to puromycin in cell cultures. *Journal of cellular physiology*, 79(1):139–146, 1972.

[295] Marc Hafner, Mario Niepel, and Peter K Sorger. Alternative drug sensitivity metrics improve preclinical cancer pharmacogenomics. *Nature biotechnology*, 35(6):500, 2017.

[296] Mohammad Fallahi-Sichani, Saman Honarnejad, Laura M Heiser, Joe W Gray, and Peter K Sorger. Metrics other than potency reveal systematic variation in responses to cancer drugs. *Nature chemical biology*, 9(11):708, 2013.

[297] Leonard A Harris, Peter L Frick, Shawn P Garbett, Keisha N Hardeman, B Bishal Paudel, Carlos F Lopez, Vito Quaranta, and Darren R Tyson. An unbiased metric of antiproliferative drug effect in vitro. *Nature methods*, 13(6):497, 2016.

[298] Chun-Chi Liang, Ann Y Park, and Jun-Lin Guan. In vitro scratch assay: a convenient and inexpensive method for analysis of cell migration in vitro. *Nature protocols*, 2(2): 329–333, 2007.

[299] Reza Riahi, Yongliang Yang, Donna D Zhang, and Pak Kin Wong. Advances in wound-healing assays for probing collective cell migration. *Journal of laboratory automation*, 17 (1):59–65, 2012.

[300] Stuart T Johnston, Esha T Shah, Lisa K Chopin, DL Sean McElwain, and Matthew J Simpson. Estimating cell diffusivity and cell proliferation rate by interpreting incucyte zoom assay data using the fisher-kolmogorov model. *BMC systems biology*, 9(1):38, 2015.

[301] Philip K Maini, DL Sean McElwain, and David I Leavesley. Traveling wave model to interpret a wound-healing cell migration assay for human peritoneal mesothelial cells. *Tissue engineering*, 10(3-4):475–482, 2004.

[302] Mathieu Poujade, Erwan Grasland-Mongrain, A Hertzog, J Jouanneau, Philippe Chavrier, Benoît Ladoux, Axel Buguin, and Pascal Silberzan. Collective migration of an epithelial monolayer in response to a model wound. *Proceedings of the National Academy of Sciences*, 104(41):15988–15993, 2007.

[303] Markus Basan, Jens Elgeti, Edouard Hannezo, Wouter-Jan Rappel, and Herbert Levine. Alignment of cellular motility forces with tissue flow as a mechanism for efficient wound healing. *Proceedings of the National Academy of Sciences*, 110(7):2452–2459, 2013.

[304] Xavier Trepat and Jeffrey J Fredberg. Plithotaxis and emergent dynamics in collective cellular migration. *Trends in cell biology*, 21(11):638–646, 2011.

[305] James EN Jonkman, Judith A Cathcart, Feng Xu, Miria E Bartolini, Jennifer E Amon, Katarzyna M Stevens, and Pina Colarusso. An introduction to the wound healing assay using live-cell microscopy. *Cell adhesion & migration*, 8(5):440–451, 2014.

[306] Damian Stichel, Alistair M Middleton, Benedikt F Müller, Sofia Depner, Ursula Klingmüller, Kai Breuhahn, and Franziska Matthäus. An individual-based model for collective cancer cell migration explains speed dynamics and phenotype variability in response to growth factors. *NPJ systems biology and applications*, 3(1):5, 2017.

[307] Florian Milde, Davide Franco, Aldo Ferrari, Vartan Kurtcuoglu, Dimos Poulikakos, and Petros Koumoutsakos. Cell image velocimetry (civ): boosting the automated quantification of cell migration in wound healing assays. *Integrative Biology*, 4(11):1437–1447, 2012.

[308] Matthew J Simpson, Katrina K Treloar, Benjamin J Binder, Parvathi Haridas, Kerry J Manton, David I Leavesley, DL Sean McElwain, and Ruth E Baker. Quantifying the roles of cell motility and cell proliferation in a circular barrier assay. *Journal of the Royal Society Interface*, 10(82):20130007, 2013.

[309] Wang Jin, Esha T Shah, Catherine J Penington, Scott W McCue, Lisa K Chopin, and Matthew J Simpson. Reproducibility of scratch assays is affected by the initial degree of confluence: experiments, modelling and model selection. *Journal of theoretical biology*, 390:136–145, 2016.

[310] Hans-Jürgen Heidebrecht, Bernadette Kainz, Roland Schopf, Klaus Godl, Züleyha Karcier, Ulrich Kulozik, and Beatrix Förster. Isolation of biofunctional bovine immunoglobulin g from milk-and colostral whey with mixed-mode chromatography at lab and pilot scale. *Journal of Chromatography A*, 2018.

[311] Maria Tomasz. Mitomycin c: small, fast and deadly (but very selective). *Chemistry & biology*, 2(9):575–579, 1995.

[312] David M Graham, Tomas Andersen, Lisa Sharek, Gunes Uzer, Katheryn Rothenberg, Brenton D Hoffman, Janet Rubin, Martial Balland, James E Bear, and Keith Burridge. Enucleated cells reveal differential roles of the nucleus in cell migration, polarity, and mechanotransduction. *J Cell Biol*, pages jcb–201706097, 2018.

[313] Sham Tlili, Estelle Gauquelin, Brigitte Li, Olivier Cardoso, Benoît Ladoux, Hélène Delanoë-Ayari, and François Graner. Collective cell migration without proliferation: density determines cell velocity and wave velocity. *Royal Society open science*, 5(5):172421, 2018.

[314] Brenda N Vo, Christopher C Drovandi, Anthony N Pettitt, and Graeme J Pettet. Melanoma cell colony expansion parameters revealed by approximate bayesian computation. *PLoS computational biology*, 11(12):e1004635, 2015.

[315] A Patrícia Bento, Anna Gaulton, Anne Hersey, Louisa J Bellis, Jon Chambers, Mark Davies, Felix A Krüger, Yvonne Light, Lora Mak, Shaun McGlinchey, et al. The chembl bioactivity database: an update. *Nucleic acids research*, 42(D1):D1083–D1090, 2014.

[316] Marc Hafner, Mario Niepel, Mirra Chung, and Peter K Sorger. Growth rate inhibition metrics correct for confounders in measuring sensitivity to cancer drugs. *Nature methods*, 13(6):521, 2016.

[317] Stevan Z Knezevic, Jens C Streibig, and Christian Ritz. Utilizing r software package for dose-response studies: the concept and data analysis. *Weed Technology*, 21(3):840–848, 2007.

[318] David L Morse, Heather Gray, Claire M Payne, and Robert J Gillies. Docetaxel induces cell death through mitotic catastrophe in human breast cancer cells. *Molecular cancer therapeutics*, 4(10):1495–1504, 2005.

[319] KR Hande. Etoposide: four decades of development of a topoisomerase ii inhibitor. *European journal of cancer*, 34(10):1514–1521, 1998.

[320] Yukihiko Aikawa, Kimiko Morimoto, Tetsuya Yamamoto, Hisaaki Chaki, Akira Hashiramoto, Hirokazu Narita, Shuichi Hirono, and Shunichi Shiozawa. Treatment of arthritis with a selective inhibitor of c-fos/activator protein-1. *Nature biotechnology*, 26 (7):817, 2008.

[321] Joan M Carboni, Mark Wittman, Zheng Yang, Francis Lee, Ann Greer, Warren Hurlburt, Stephen Hillerman, Carolyn Cao, Glenn H Cantor, Janet Dell-John, et al. Bms-754807, a small molecule inhibitor of insulin-like growth factor-1r/ir. *Molecular cancer therapeutics*, pages 1535–7163, 2009.

[322] Malgorzata Borowiak, Wallis Nahaboo, Martin Reynders, Katharina Nekolla, Pierre Jalinot, Jens Hasserodt, Markus Rehberg, Marie Delattre, Stefan Zahler, Angelika Vollmar, et al. Photoswitchable inhibitors of microtubule dynamics optically control mitosis and cell death. *Cell*, 162(2):403–411, 2015.

[323] L Barth Reller, Melvin Weinstein, James H Jorgensen, and Mary Jane Ferraro. Antimicrobial susceptibility testing: a review of general principles and contemporary practices. *Clinical infectious diseases*, 49(11):1749–1755, 2009.

[324] Irith Wiegand, Kai Hilpert, and Robert EW Hancock. Agar and broth dilution methods to determine the minimal inhibitory concentration (mic) of antimicrobial substances. *Nature protocols*, 3(2):163, 2008.

[325] CP Allier, G Hiernard, V Poher, and JM Dinten. Bacteria detection with thin wetting film lensless imaging. *Biomedical optics express*, 1(3):762–770, 2010.

[326] Yeon Hwa Kwak, Junhee Lee, Junghoon Lee, Soo Hwan Kwak, Sangwoo Oh, Se-Hwan Paek, Un-Hwan Ha, and Sungkyu Seo. A simple and low-cost biofilm quantification method using led and cmos image sensor. *Journal of microbiological methods*, 107:150–156, 2014.

[327] Jae Hee Jung and Jung Eun Lee. Real-time bacterial microcolony counting using on-chip microscopy. *Scientific reports*, 6:21473, 2016.

[328] Yoshiaki Maeda, Yui Sugiyama, Atsushi Kogiso, Tae-Kyu Lim, Manabu Harada, Tomoko Yoshino, Tadashi Matsunaga, and Tsuyoshi Tanaka. Colony fingerprint-based discrimination of staphylococcus species with machine learning approaches. *Sensors*, 18(9):2789, 2018.

[329] Tatjana Lamparter. Area dependent dynamic response to antibiotics of bacterial microcolonies grown on agar. Master's thesis, Ludwig Maximilians Universität München, Germany, 2018.

[330] Anders Blomberg. Measuring growth rate in high-throughput growth phenotyping. *Current opinion in biotechnology*, 22(1):94–102, 2011.

[331] Ana Margarida Sousa, Idalina Machado, Ana Nicolau, and Maria Olívia Pereira. Improvements on colony morphology identification towards bacterial profiling. *Journal of microbiological methods*, 95(3):327–335, 2013.

[332] Xingyu Jiang, Derek A Bruzewicz, Amy P Wong, Matthieu Piel, and George M Whitesides. Directing cell migration with asymmetric micropatterns. *Proceedings of the National Academy of Sciences*, 102(4):975–978, 2005.

[333] Kristopher A Kilian, Branimir Bugarija, Bruce T Lahn, and Milan Mrksich. Geometric cues for directing the differentiation of mesenchymal stem cells. *Proceedings of the National Academy of Sciences*, 2010.

[334] Peter JF Röttgermann, Kenneth A Dawson, and Joachim O Rädler. Time-resolved study of nanoparticle induced apoptosis using microfabricated single cell arrays. *Microarrays*, 5(2):8, 2016.

[335] Didier Falconnet, Gabor Csucs, H Michelle Grandin, and Marcus Textor. Surface engineering approaches to micropattern surfaces for cell-based assays. *Biomaterials*, 27(16): 3044–3063, 2006.

[336] Jian Tang, Rong Peng, and Jiandong Ding. The regulation of stem cell differentiation by cell-cell contact on micropatterned material surfaces. *Biomaterials*, 31(9):2470–2476, 2010.

[337] Sang-Hee Yoon and Mohammad RK Mofrad. Cell adhesion and detachment on gold surfaces modified with a thiol-functionalized rgd peptide. *Biomaterials*, 32(30):7286–7296, 2011.

[338] Roman Glass, Martin Möller, and Joachim P Spatz. Block copolymer micelle nanolithography. *Nanotechnology*, 14(10):1153, 2003.

[339] Roman Lutz, Kristopher Pataky, Neha Gadhari, Mattia Marelli, Juergen Brugger, and Matthias Chiquet. Nano-stenciled rgd-gold patterns that inhibit focal contact maturation induce lamellipodia formation in fibroblasts. *PloS one*, 6(9):e25459, 2011.

[340] Peter JF Röttgermann, Samira Hertrich, Ida Berts, Max Albert, Felix J Segerer, Jean-François Moulin, Bert Nickel, and Joachim O Rädler. Cell motility on polyethylene glycol block copolymers correlates to fibronectin surface adsorption. *Macromolecular bioscience*, 14(12):1755–1763, 2014.

[341] Xavi Illa, Olga Ordeig, Detlef Snakenborg, Albert Romano-Rodríguez, Richard G Compton, and Jörg P Kutter. A cyclo olefin polymer microfluidic chip with integrated gold microelectrodes for aqueous and non-aqueous electrochemistry. *Lab on a Chip*, 10(10): 1254–1261, 2010.

[342] Marco Arnold, Vera C Hirschfeld-Warneken, Theobald Lohmuller, Patrick Heil, Jacques Blummel, Elisabetta A Cavalcanti-Adam, Mónica López-García, Paul Walther, Horst Kessler, Benjamin Geiger, et al. Induction of cell polarization and migration by a gradient of nanoscale variations in adhesive ligand spacing. *Nano letters*, 8(7):2063–2069, 2008.

[343] Mats Hulander, Anders Lundgren, Lars Faxälv, TL Lindahl, Anders Palmquist, Mattias Berglin, and H Elwing. Gradients in surface nanotopography used to study platelet adhesion and activation. *Colloids and Surfaces B: Biointerfaces*, 110:261–269, 2013.

[344] Euan McLeod and Aydogan Ozcan. Unconventional methods of imaging: computational microscopy and compact implementations. *Reports on Progress in Physics*, 79(7):076001, 2016.

[345] Amos Bairoch. The cellosaurus, a cell-line knowledge resource. *Journal of biomolecular techniques: JBT*, 2018.

[346] Yoonseok Kam, Katarzyna A Rejniak, and Alexander RA Anderson. Cellular modeling of cancer invasion: integration of in silico and in vitro approaches. *Journal of cellular physiology*, 227(2):431–438, 2012.

[347] Rasheena Edmondson, Jessica Jenkins Broglie, Audrey F Adcock, and Liju Yang. Three-dimensional cell culture systems and their applications in drug discovery and cell-based biosensors. *Assay and drug development technologies*, 12(4):207–218, 2014.

[348] David A Van Valen, Takamasa Kudo, Keara M Lane, Derek N Macklin, Nicolas T Quach, Mialy M DeFelice, Inbal Maayan, Yu Tanouchi, Euan A Ashley, and Markus W Covert. Deep learning automates the quantitative analysis of individual cells in live-cell imaging experiments. *PLoS computational biology*, 12(11):e1005177, 2016.

[349] Dai Kusumoto, Mark Lachmann, Takeshi Kunihiro, Shinsuke Yuasa, Yoshikazu Kishino, Mai Kimura, Toshiomi Katsuki, Shogo Itoh, Tomohisa Seki, and Keiichi Fukuda. Automated deep learning-based system to identify endothelial cells derived from induced pluripotent stem cells. *Stem cell reports*, 10(6):1687–1695, 2018.

[350] Christoph Sommer, Rudolf Hoefler, Matthias Samwer, and Daniel W Gerlich. A deep learning and novelty detection framework for rapid phenotyping in high-content screening. *Molecular biology of the cell*, 28(23):3428–3436, 2017.

[351] Marieke IG Raaijmakers, Daniel S Widmer, Melanie Maudrich, Tabea Koch, Alice Langer, Anna Flace, Claudia Schnyder, Reinhard Dummer, and Mitchell P Levesque. A new live-cell biobank workflow efficiently recovers heterogeneous melanoma cells from native biopsies. *Experimental dermatology*, 24(5):377–380, 2015.

[352] F. Pedregosa, G. Varoquaux, A. Gramfort, V. Michel, B. Thirion, O. Grisel, M. Blondel, P. Prettenhofer, R. Weiss, V. Dubourg, J. Vanderplas, A. Passos, D. Cournapeau, M. Brucher, M. Perrot, and E. Duchesnay. Scikit-learn: Machine learning in Python. *Journal of Machine Learning Research*, 12:2825–2830, 2011.

List of Abbreviations

ADC	Analog-Digital Converter
API	Application Programming Interface
ASM	Angular Spectrum Method
CCD	Charge-Coupled Device
CMOS	Complementary Metal-Oxide-Semiconductor
DHM	Digital Holographic Microscopy
DNA	DeoxyriboNucleic Acid
EC_{50}	half maximal Effective Concentration
EMT	Epithelial-Mesenchymal Transition
FBS	Fetal Bovine Serum
FCN	Fully Convolutional Network
FFT	Fast Fourier Transform
FOV	Field Of View
GT	Ground Truth
EC_{50}	half maximal Effective Concentration
ISP	Image Signal Processor
LDA	Linear Discriminant Analysis
LED	Light-Emitting Diode
LM	Lensless Microscopy
MLT	Moral Lineage Tracing
MODA	Multiple Object Detection Accuracy
MOTA	Multiple Object Tracking Accuracy
MSD	Mean Squared Displacement
ND	Neutral Density
PCB	Printed Circuit Board
PDT	Population Doubling Time
PIV	Particle Image Velocimetry
QC	Quality Control
QPI	Quantitative Phase Imaging
RGB	Red Green Blue
RFLM	Reconstruction Free Lensless Microscopy
ROI	Region Of Interest
SBP	Space-Bandwidth Product
SD	Squared displacement
SNR	Signal-to-Noise Ratio
SOC	System On a Chip
UV	Ultra Violet

List of Publications

Associated Publications and Manuscripts

P1 Markus Rempfler, Sanjeev Kumar, Valentin Stierle, Philipp Paulitschke, Bjoern Andres, and Bjoern H Menze. Cell lineage tracing in lens-free microscopy videos. In International Conference on Medical Image Computing and Computer-Assisted Intervention, pages 311. Springer, 2017.

P2 Markus Rempfler, Valentin Stierle, Konstantin Ditzel, Sanjeev Kumar, Philipp Paulitschke, Bjoern Andres, and Bjoern H Menze. Tracing cell lineages in videos of lens-free microscopy. Medical Image Analysis, 2018.

P3 Patentanmeldung Aktenzeichen DE 10 2017 008 249.9 vom 01.09.2017. Erfinder: Paulitschke, Stierle, Menze, Rempfler: Detection of Biological Cells and Tracing of Cell Lineages. Inhaber: LMU, TUM

M1 Valentin Stierle, Tobias Paerr, Konstantin Ditzel, Markus Rempfler, Ester Porcellato, Bjoern Menze, Joachim Rädler, Philipp Paulitschke. Multiparameter Monitoring Of Cell Line Characteristics Using Lensless Microscopy
Manuscript in preparation

Further Publications

P4 Jürgen Stephan, Felix Keber, Valentin Stierle, Joachim O Rädler, and Philipp Paulitschke. Single-cell optical distortion correction and label-free 3d cell shape reconstruction on lattices of nanostructures. Nano Letters, 17(12):80188023, 2017.

P5 David Volbers, Valentin Stierle, Konstantin Ditzel, Julian Aschauer, Joachim Rädler, Madeleine Opitz, Philipp Paulitschke. Interference Disturbance Analysis Enables Single-Cell Level Growth and Mobility Characterization for Rapid Antimicrobial Susceptibility Testing. Nano Letters, 2018

Acknowledgments

I hereby would like to thank all the people, communities, and institutions that contributed in one way or another to this work, namely:

Prof. Joachim Rädler for your supervision of this work, your ideas, and your guidance.

Dr. Philipp Paulitschke for the discussions, your feedback, your support, and for giving me the freedom to follow almost any idea.

Ester Porcellato for your patience, thoroughness, and overall impressive capability to perfectly handle every task from cell culture experiments, electron beam lithography, soldering electronics, using motorized stages for positioning systems, to working with my programs and using the linux command line.

The masters students ***Christian Huber***, ***Tobias Pärr***, ***Konstantin Ditzel***, and ***Tatjana Lamparter***, it was a pleasure of working with you.

Prof. Björn Menze and ***Markus Rempfler*** for the collaboration on the cell detection and tracking.

Dr. Oliver Thorn-Seshold, ***Dr. Malgorzata Borowiak***, and ***Hans-Christian Mescheder*** for kindly providing the photostatin and the collaboration on the cytotoxicity measurements.

the ***University Hospital Zürich, Department of Dermatology*** for kindly providing the primary melanoma cell lines and corresponding compounds for growth inhibition.

Dr. Beatrix Förster for the collaboration on the scratch assay experiments with different media supplements.

Dr. Madeleine Opitz and ***Alexandra Götz*** for the collaboration on the bacteria project.

Philipp Altpeter for his patience in introducing me to working with the AFM

Gerline Schwake for helping me anytime I failed with my cell culture experiments.

Alexandra Elbakyan and Sci-Hub, ***Stack Overflow***, ***Wikipedia***, and the ***linux and open source community*** for their invaluable contribution to science and society by providing free access to information and software.

my office co-workers in the ***megaoffice 2000***, namely Matthias, Florian, Segey, and Jürgen for being the best office in the history of offices, maybe ever.

A special thank you goes to ***Jürgen*** for the discussions, for proof-reading, coffee breaks, and generally for tolerating me as an office desk-neighbour for several years. Also sorry for turning you into a coffee-addict.

A big thank you goes to ***Alexandra*** for being the best proofreader you can wish for.

Ricarda for the chats when I needed a break and was looking for someone to bother.

David for joint Netto-Expeditions.

our research group

my ***coworkers*** at the chair.

Further thanks goes to everyone who took part in joint recreational water-related activities characterized by short spatio-temporal distance to the workplace.

and finally my ***Friends and Family***

Appendix

Table of Contents

1 Derivations

1.1 Diffraction Formalism

If we plug the Ansatz

$$\psi\left(x,y,z,t\right)=\psi_p\left(x,y;z\right)e^{i\omega_0 t} \tag{1}$$

for the complex amplitude of the diffracted wave at a plane at a distance z from the aperture into the scalar wave equation

$$\nabla^2\psi=\frac{1}{\nu^2}\frac{\partial^2\psi}{\partial t^2} \tag{2}$$

we obtain the differential equation

$$\frac{\partial^2\psi_p}{\partial x^2}+\frac{\partial^2\psi_p}{\partial y^2}+\frac{\partial^2\psi_p}{\partial z^2}+k_0^2\psi_p=0 \tag{3}$$

This differential equation is subject to the initial condition

$$\Psi_{p0}\left(x,y\right)=\Psi_p\left(x,y,z=0\right)=A\times T\left(x,y\right) \tag{4}$$

After applying the Fourier transform

$$\mathcal{F}\{\psi_p\left(x,y;z\right)\}=\iint\limits_{-\infty}^{+\infty}\psi_p\left(x,y;z\right)e^{ik_x x}e^{ik_y y}dxdy=\Psi_p\left(k_x,k_y;z\right) \tag{5}$$

the differential equation simplifies to

$$\frac{d^2\Psi_p}{dz^2}+k_0\left(1-\frac{k_x^2}{k_0^2}-\frac{k_y^2}{k_0^2}\right)\Psi_p=0 \tag{6}$$

with the initial condition $\mathcal{F}\{\psi_{p0}\}=\Psi_{p0}$. The solution is then

$$\Psi_p\left(k_x,k_y;z\right)=\Psi_{p0}\left(k_x,k_y\right)\exp\left(-ik_0\sqrt{1-k_x^2/k_0^2-k_y^2/k_0^2}z\right) \tag{7}$$

The solution for the complex amplitude can be obtained by applying the inverse Fourier transform:

$$\psi_p\left(x,y;z\right)=\frac{1}{4\pi}\iint\limits_{-\infty}^{+\infty}\Psi_{p0}\left(k_x,k_y\right)\exp\left(-ik_0\sqrt{1-k_x^2/k_0^2-k_y^2/k_0^2}z\right)e^{-ik_x x}e^{-ik_y y}dk_x dk_y \tag{8}$$

Under the paraxial approximation, i.e. $k_x^2+k_y^2\ll k0^2$, the Taylor expansion of the square root term up to the second order gives

$$\psi_p\left(x,y;z\right)=\frac{1}{4\pi}\iint\limits_{-\infty}^{+\infty}\Psi_{p0}\left(k_x,k_y\right)\exp\left(-ik_0 z\left(1-\frac{k_x^2+k_y^2}{2k_0^2}\right)\right)e^{-ik_x x}e^{ik_y y}dk_x dk_y \tag{9}$$

With the definition of the *spatial frequency transfer function in Fourier optics*

$$H\left(k_x,k_y;z\right)=e^{-ik_0 z}\exp\left(i\left(1-\frac{k_x^2+k_y^2}{2k_0^2}\right)\right) \tag{10}$$

and its Fourier transform

$$h(x,y;z) = \mathcal{F}\{H(k_x,k_y;z)\} \tag{11}$$

$$= e^{-ik_0 z}\frac{ik_0}{2\pi z}\exp\left[-\frac{ik_0}{2z}\left(x^2+y^2\right)\right] \tag{12}$$

this equation can be written as

$$\psi_p(x,y;z) = \mathcal{F}^{-1}\{\Psi_{p0}(k_x,k_y)\,H(k_x,k_y;z)\} \tag{13}$$

$$= \psi_{p0}(x,y) * h(x,y;z) \tag{14}$$

$$= e^{-ik_0 z}\frac{ik_0}{2\pi z}\iint_{-\infty}^{+\infty}\Psi_{p0}(x',y')\exp\left\{-\frac{ik_0}{2z}\left[(x-x')^2+(y-y')^2\right]\right\}dx'dy' \tag{15}$$

1.2 Hologram of a Point Aperture

The field distribution of the plain reference wave at the detector plane is given by $\psi_r = a\exp(-ik_0 z_0)$. We model the pinhole aperture with a delta function $\delta(x,y)$. According to Fresnel diffraction (equation 14), the object wave can be written as

$$\psi_o(x,y;z) = \delta(x,y) * h(x,y;z) \tag{16}$$

$$= \delta(x,y) * \exp(-ik_0 z_0)\frac{ik_0}{2\pi z_0}\exp\left[-\frac{ik_0}{2z_0}\left(x^2+y^2\right)\right] \tag{17}$$

$$= \exp(-ik_0 z_0)\frac{ik_0}{2\pi z_0}\exp\left[-\frac{ik_0}{2z_0}\left(x^2+y^2\right)\right] \tag{18}$$

For the transparency function T_h of the recorded hologram, we hence obtain

$$T_h(x,y) = |\psi_r(x,y)+\psi_o(x,y)|^2 \tag{19}$$

$$= a^2 + \left(\frac{k_0}{2\pi z_0}\right) + a\frac{-ik_0}{2\pi z_0}\exp\left[\frac{ik_0}{2z_0}\left(x^2+y^2\right)\right] + a\frac{ik_0}{2\pi z_0}\exp\left[-\frac{ik_0}{2z_0}\left(x^2+y^2\right)\right] \tag{20}$$

2 Setups and Setup Characterization

2.1 Timing of the Image Acquisition Steps

The times required for the different processes during the acquisition of an image with the custom CMOS camera module were measured to assess their effect on heat generation and to characterize the setup. For each image, three frames with a resolution of 2592x1944 were acquired in the YUYV format and subsequently averaged. The times were measured by using the Linux programs *unbuffer* and *ts* and calling *fswebcam* with the verbose option. Both the time required for the initialization (opening the camera device, applying the settings, and initiating memory mapping) and the total acquisition time were measured. On average, *fswebcam* needed (5236 ± 10) ms to acquire an image. Of this time, (225 ± 3) ms were needed on average for the initialization. The times required to acquire the individual frames were further analyzed with a custom C++ program using the chrono timing library from the C++ standard library. For each frame, the program waited that the camera signaled that a frame was ready by using the *select()* function. Subsequently, the program transfers the data from the camera to the PC by calling the *v4l2_ioctl()* function of the *v4l* library with the *VIDIOC_DQBUF* request. ***Table 1*** summarizes the time required for these two operations both for the first frame of each acquisition, and the next ten frames. On average, the first frame required (3962 ± 49) ms and the subsequent frames (488 ± 2) ms. The time needed to acquire three frames with *fswebcam* is 5011 ms (total time - initialization time), which is consistent with the 4938 ms measured with the custom program. The difference of 73 ms is most likely needed to average the images, a task that is not included in the custom program.

Table 1: Duration of image acquisition. The measurement was repeated ten times. The times of the first and subsequent frames were determined with a custom C++ program. All times are in milli seconds.

	fswebcam (total)	**fswebcam (initialization)**	**first frame**	**next frames (10 frame average)**
	5241	222	3978	482
	5263	222	3978	490
	5234	223	3978	489
	5240	231	3978	490
	5230	225	3978	481
	5233	229	3822	490
	5231	226	3978	487
	5228	223	3978	487
	5230	225	3978	488
	5230	225	3977	488
mean	5236	225	3962	488
stdev	10	3	49	2

2.2 Temperature Sensor Slide

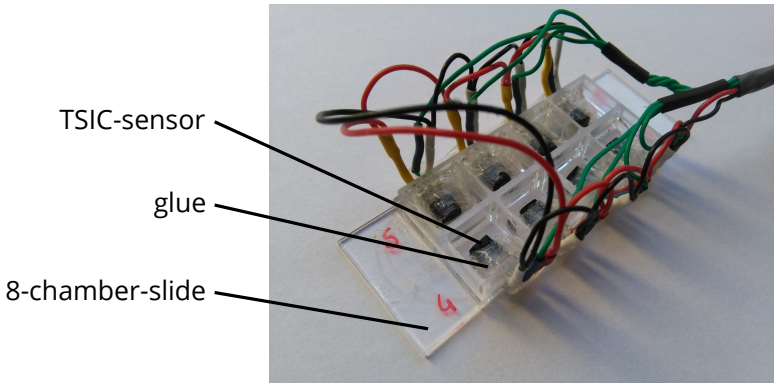

Figure 1: 8-chamber slide with TSIC temperature sensors. The pins of the sensors are covered in hot glue to protect them from the liquid in the chamber. The chambers were filled with deionized MilliQ water to simulate realistic conditions (here shown without water). The slide was closed with its lid during measurements.

2.3 Image Reconstruction in Dense Cell Layers

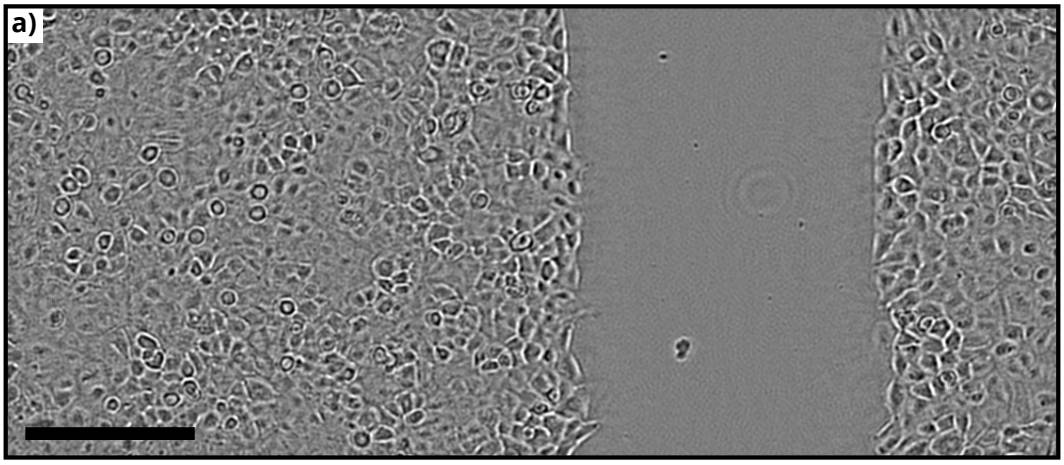

Figure 2: Example of an amplitude image of a dense cell layer acquired with the lensless DHM setup. The image shows a scratch wound in a layer of A549 cells. Scale bar: 250 µm. This demonstrates that the used multi-height acquisition approach allows to reconstruct high-quality images even for dense cell layers since individual cells are still discernible within the layer.

2.4 Setup for Culture Dishes

For an early proof-of-concept and the initial RFLM live-cell imaging experiments presented in this thesis, a setup was designed for the acquisition of time-lapsed image series of cells growing inside standard 35 mm cell culture dishes. In this setup, the camera, the LED, and the sample were enclosed in a polytetrafluoroethylene (PTFE) housing, as shown in ***Figure 3***. The dish

was placed directly on top of the image sensor, and the distance between the LED and the sample was 45 mm. The setups were placed inside a Galaxy 14S incubator (New Brunswick Scientific, Edison, USA) for live-cell imaging experiments.

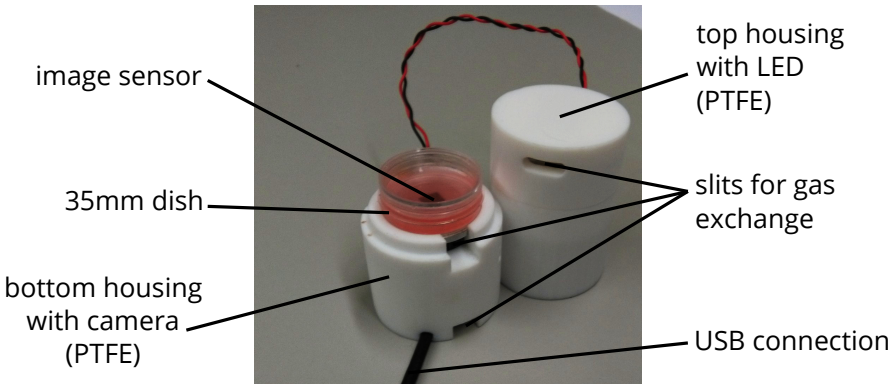

Figure 3: RFLM setup for live-cell imaging of cell populations growing inside standard 35 mm culture dishes. The sensor, the LED, the image sensor, and the dish are inside of a PTFE housing to shield the image sensor from background light. Slits in the housing allow the exchange of gas.

3 Image Processing and Analysis

3.1 RFLM Background Correction

The RFLM micrographs are acquired as RGB images with 8 bit per color channel. All channels with an intensity histogram with a mean and a width within a given range are averaged to a single channel 8 bit image i_1. The openCV function *GaussianBlur* (kernel>128 pixel) is applied to a copy of the image i_1 to obtain a map of the background b_1 that contains the low spatial frequencies. The background map b_1 is subtracted from the image i_1 to obtain the image i_2. The range of i_2 is then normalized by mapping its minimum to zero and its maximum to 255. As a last step openCVs contrast limited adaptive histogram equalization (CLAHE) is applied to i_2 to obtain the background corrected RFLM image.

3.2 PIV Analysis

A reduced stack of images was created by taking only every nth frame of the original time-lapse image sequence. The choice of n was based on how fast the cells moved. For the NIH-3T3 and HuH7 cells, n was chosen so that the time difference between two frames of the reduced stack was around 16 min. For the slower A549 cells it was around 40 min. The ImageJ plugin "PIV" was used in conjunction with a custom macro to calculate the displacement field for each pair of consecutive frames of the reduced image stack. The velocity field was obtained by dividing the vectors of the PIV displacement field by the time difference between the two frames it was calculated from. For each velocity field, the corresponding mask of the detected foreground area was loaded. If a grid point of the velocity field was inside the foreground area, it was used

for the calculations, and if the point was outside, it was discarded. For each of the obtained velocity fields, the average x and y component, as well as the average absolute value of the field vectors, was calculated. By calculating for each grid point the average vector of all velocity fields from the sequence a time-averaged field is obtained.

3.3 Features for Discrimination of Bacterial Microcolonies

The following metrics for the colony morphology were calculated for each microcolony detected in the RFLM images. Here, A denotes the area of the colony, L the length of the outline of the detected area, l_{maj} the major axis of the detected area, l_{min} the minor axis of the detected area. G is the gray value of the pixels. Further quantities used for the calculation of the metrics include:

$$\Sigma = \sum_{area} G(x,y) \tag{21}$$

$$x_0 = \frac{1}{\Sigma} \sum_{area} G(x,y)\, x \tag{22}$$

$$y_0 = \frac{1}{\Sigma} \sum_{area} G(x,y)\, y \tag{23}$$

$$mu_{20} = \frac{1}{\Sigma} \sum_{area} G(x,y)\, (x - x0)^2 \tag{24}$$

$$mu_{02} = \frac{1}{\Sigma} \sum_{area} G(x,y)\, (y - y0)^2 \tag{25}$$

$$mu_{30} = \frac{1}{\Sigma} \sum_{area} G(x,y)\, (x - x0)^3 \tag{26}$$

$$mu_{03} = \frac{1}{\Sigma} \sum_{area} G(x,y)\, (y - y0)^3 \tag{27}$$

- surface to volume ratio: A/L
- sphericity: $\frac{2\times\sqrt{A\pi}}{L}$
- ellipticity: $\frac{l_{maj}-l_{min}}{l_{maj}}$
- roundness: $\frac{4A}{l_{maj}^2}$
- the largest value of the minimum distance of all points of the outline of the contour to the minimum enclosing rectangle of the contour
- distance of the geometrical center to the center of mass
- $\sqrt{m_{20}^2 + m_{02}^2}$
- $\sqrt{m_{30}^2 + m_{03}^2}$
- mean of the histogram of gray values

- variance of the histogram of gray values
- skewness of the histogram of gray values
- entropy of the histogram of gray values

3.4 Gray Value Level Based Cell Detection

An early version of the cell detection was based on analyzing gray value levels (GVL) and geometrical shapes. This analysis used the following steps:

Detection: The function *adaptiveThreshold()* was used to obtain binary masks containing the regions with gray values over (M_O) and under (M_U) appropriate local thresholds, respectively.
Size filtering: areas with a size above and below selected size-thresholds were removed.
Shape filtering I: areas with a hole were removed from the mask M_O, but filled in the mask M_U.
Shape filtering II: the fraction of the detected areas and the areas of their bounding boxes was calculated. If the fraction was below a selectable value, the corresponding area was removed from the masks. This step is also illustrated in ***Figure 4 b***.
Gray value distribution: For areas in M_O with a circularity below a choosable number the orientation of the major axis was determined. The mean gray values in two rectangles with a size of $8\,\mu m \times 25\,\mu m$ were calculated. The long axis of the rectangles was parallel to the orientation of the detected area. The distance of the center of the rectangles to the major axis was 15 µm. If the respective mean values did not match the criteria shown in ***Figure 4 c***, the areas were removed from the masks.

Figure 5 a compares the results of the previously described GVL-based cell detection with the FCN cell detection. The shown data corresponds to four measurements with NIH-3T3 cells conducted in parallel with the dish-setups presented in ***Appendix 2.4***. 1 ml of cell suspension was seeded with a concentration of $3.5\,ml^{-1}$ into a petri dish (μ-Dish 35 mm high w/ ibiTreat coating, Ibidi, Martinsried, Germany). The medium in the dishes contained 0.5 % FBS. To two of the four dishes, FBS was added after about 12 h to a final concentration of 10 % FBS in the medium. The number of detected cells is about three times smaller than the number of cells detected by the FCN. However, for both methods, an increase in cell number can be observed after about 12 h. This indicates that although the GVL-based detection performs poorly, it can still be used for a qualitative analysis of proliferation. Unlike the FCN detection, the GVL based detection provides information about orientation, shape, and brightness of the interference pattern of the detected cells.

The results of the GVL-based detection were used for a simple tracking. Therefore, cells in subsequent frames were linked based on the distance to the nearest neighbors in the previous three frames. The results of the MSD_{1h} calculated from the simple tracking and the MLT for the four measurements are shown in ***Figure 5 b***. The curves show good agreement between the two methods. This indicates, that while the GVL-based detection misses about two-thirds of the cells detected by the FCN, the remainder of the detected cells still allows obtaining comparable results for the cell motility.

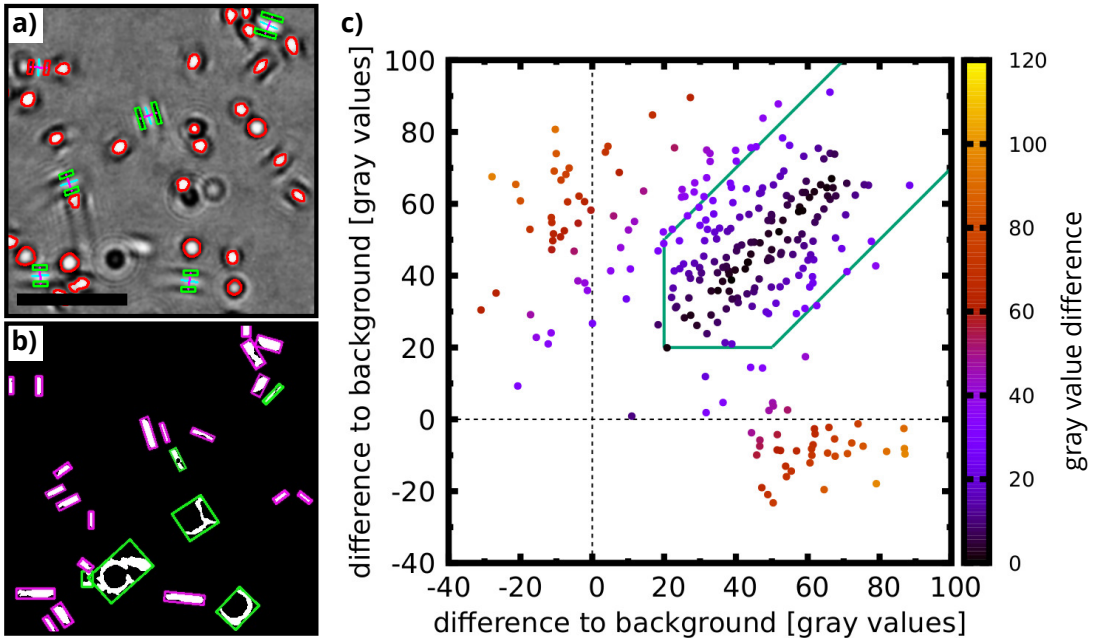

Figure 4: Gray Value Level based cell detection. **a)** RFLM image of cells, scale bar: 200 µm. The outlines of areas with gray values above a local threshold and a circularity above a threshold are drawn with red lines. The symmetry of the interference pattern of detected areas with a circularity below the threshold is analyzed by calculating the gray values inside the green rectangles. The long axis of the rectangles is parallel to the orientation of the central maximum (major axis). **b)** Geometrical analysis of the detected areas for filtering out false positives. The fraction of the detected area and the area of its bounding box is calculated. If this fraction is below a given threshold, the corresponding areas are discarded. **c)** The plot shows the mean gray value in the two rectangles from a) plotted against each other for all detected areas with an elongated shape. The difference between the two means is color-coded. Areas with a gray value distribution that lies outside the region indicated with the green lines are discarded. An example of such a case is highlighted in a) with the red rectangles.

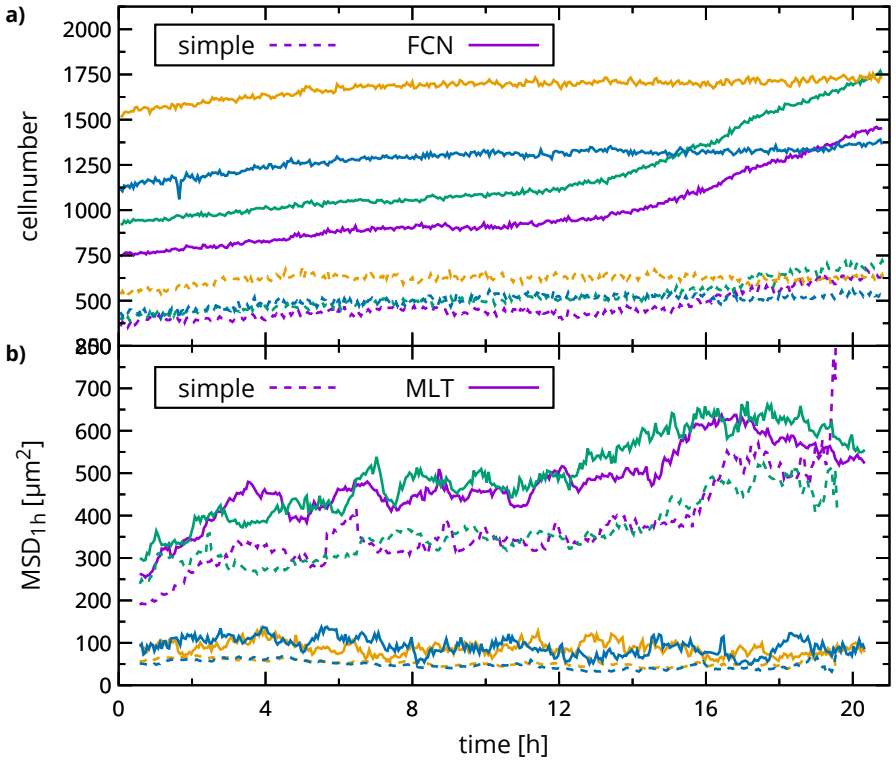

Figure 5: Comparison of the results of the GVL based cell detection and tracking with results from the FNC detection and MLT. **a)** The graph shows the number of detected cells with the FNC detection and the GVL-based detection (simple) against time. Four measurements with NIH-3T3 cells were conducted simultaneously. To two of the four dishes with an initial FBS concentration of 0.5 %, FBS was added after about 12 h to achieve a final FBS concentration of 10 % in the medium. The number of detected cells is about three times smaller for the GVL-based detection. However, the same order and trends of the different samples can be observed for both methods. **b)** The MSD_{1h} is calculated from the MLT output and from a simple nearest neighbor tracking that uses the results of the GVL-based cell detection. Here, the values, trends, and the order of the different samples agree very well between the two different methods.

3.5 Comparison of FCN Cell Detection with Fluorescence Microscopy

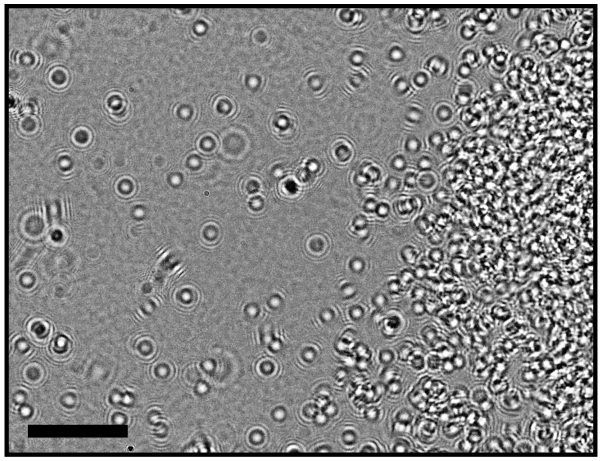

Figure 6: Nonuniform cell density in the experiments performed for comparing the results of the FCN detection with the cell detection in the corresponding fluorescence microscopy images. The image shows an example of NIH-3T3 cells seeded in the well of a multiwell plate. It can be seen, that the cell density is highly non-uniform. Scale bar: 500 µm

3.6 Extrapolation of the Correction Factor

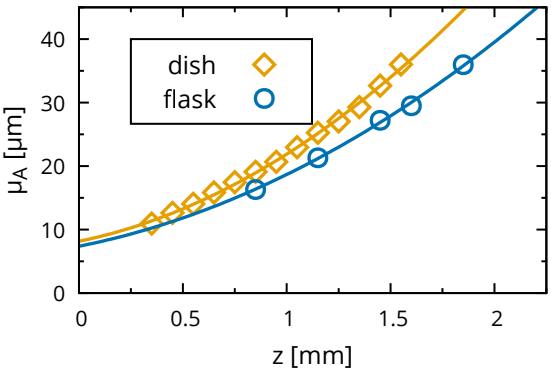

Figure 7: The graph shows a plot of the correction factor μ_A obtained from RFLM images acquired at different sample-sensor distances z. Here, z corresponds to the distance of the substrate surface to the surface of the cover glass of the image sensor. The cells were placed in culture flasks and dishes. The interference pattern spreads with increasing z, resulting in larger values for the correction factor μ_A. The data was fitted with second-order polynomials to be able to extrapolate the correction factor for arbitrary sample sensor distances in the interval $0\,\text{mm} < z < 2\,\text{mm}$.

4 Data Analysis and Processing

The program Gnuplot (version 5.0) was used for all performed fits. It was also used to create all used frequency distributions and histograms by using the *smooth frequency* option. Gnuplot was also used for data averaging by using the *unique acsplines* option.
The output of the MLT was analyzed with a custom C++ program. The generated lineages were post-processed by pruning any branches with less than five localizations. Also, any traces shorter than 1 h were discarded.
The cluster analysis was performed with a custom python script using the *LinearDiscriminantAnalysis* function and the *PCA* function from the scikit learn library [352]. The Voronoi segmentation was performed with numpys *Voronoi* function.

4.1 Calculation of Cell Displacement

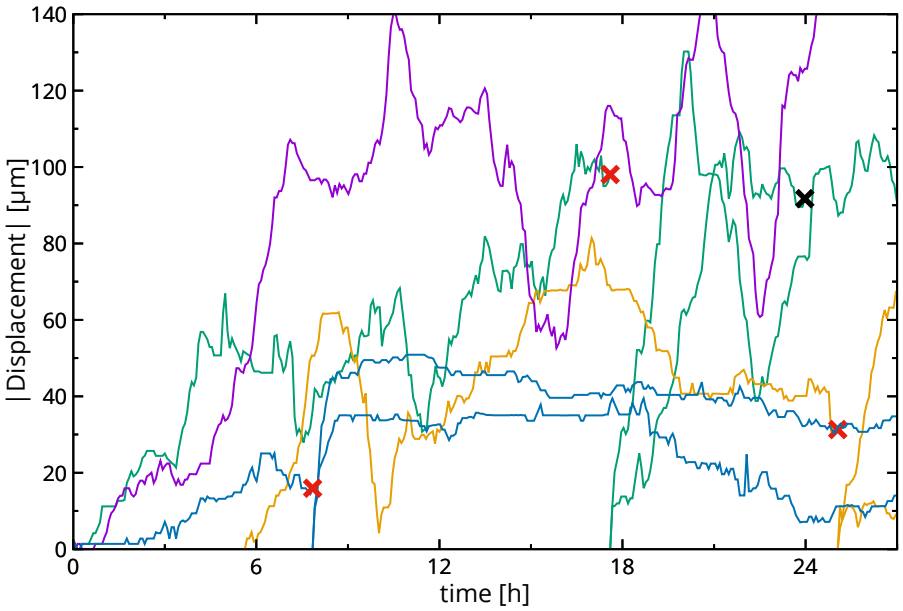

Figure 8: Calculation of cell displacement. The graph shows the absolute value of the cell displacement, i.e., the distance between the cells current position and its initial position. The shown data are example trajectories obtained by tracking NIH-3T3 cells with the FCN cell detection and MLT. Trajectories can start at the beginning of the measurement or at a later time point, e.g., when a cell migrates into the field of view (FOV) or if a cell erroneously was not detected in the beginning (yellow curve). Trajectories can end if the cell migrates out of the FOV or if the tracking algorithm loses the cell (black cross). Trajectories are also terminated when the cell divides (red crosses). The trajectories of the two daughter cells then start with a displacement of zero (red dots).

4.2 Determination of Normalized Growth Rates

The growth rate of a cell population is the increase of cells per time interval $\dot{N}(t) = \frac{dN(t)}{dt}$. The relative/normalized growth rate is then $\frac{\dot{N}(t)}{N(t)}$. For a population with a PDT T_2, the normalized

growth rate μ during the log phase of growth is just $\mu = \frac{\ln(2)}{T_2}$. The normalized growth rate can be determined by fitting an exponential function to the part of the growth curve which corresponds to the log phase of growth. However, the determination of the fit interval is subjective, and in drug screening experiments the assumption of exponential growth is not necessarily fulfilled. To address these issues, the following approach is used here to determine the normalized growth rate: For each data-point of the growth curve, a 3rd order polynomial is fitted over the interval containing the data-point and its n preceding and n successive data points. This procedure is also illustrated in ***Figure 9 a***. Each of the original data-points is then replaced with the best fit value for that point to obtain a smooth curve as an approximation

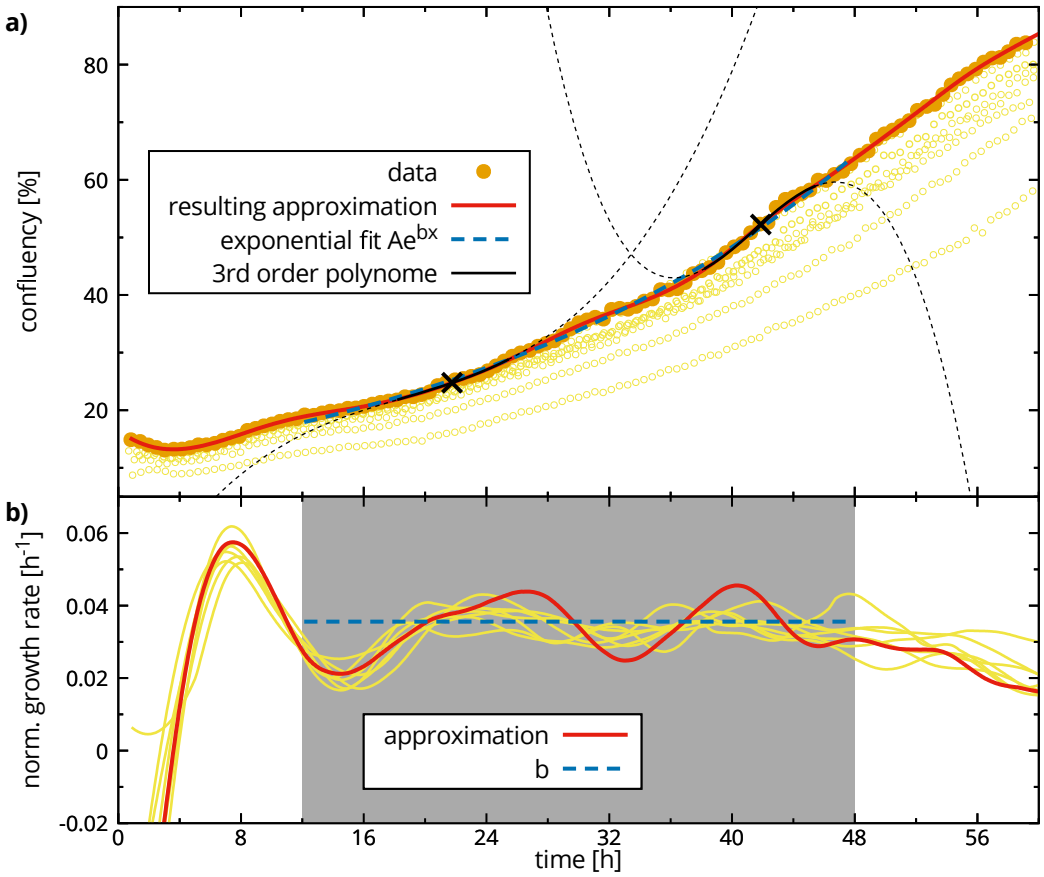

Figure 9: Determination of the normalized growth rates for eight growth curves of NIH-3T3 cells. **a)** The graph shows the confluency against time. The growth curve drawn with filled circles illustrates the data approximation scheme: For each data-point, the interval containing the preceding n and successive n data-points is fitted with a third order polynomial. Here, these fits are shown for the two data-points highlighted with the black crosses. The fit interval is indicated with the solid line of the polynomial. Replacing all data-points with the corresponding best fit values gives a smooth approximation of the data. The slope of the approximation divided by the y-value of the approximation corresponds to the normalized growth rate, which is plotted in **b)** against time. The constant growth rates over the interval highlighted by the gray background correspond to exponential growth. The normalized growth rate obtained from an exponential fit applied to the growth curve over the same interval is included as a dashed blue line.

to the data. Additionally, this procedure yields the slope of the approximated curve for each data-point. This slope, divided by the approximated y-value, corresponds to the normalized growth rate, which is shown in ***Figure 9 b***. In the plot of the normalized growth rate against time the log phase of growth is visible as the region with a constant normalized growth rate. The normalized growth rates can be averaged over a suitable time interval to obtain a measure of proliferation.

4.3 Comparison of MLT Tracks with Fluorescence Tracks

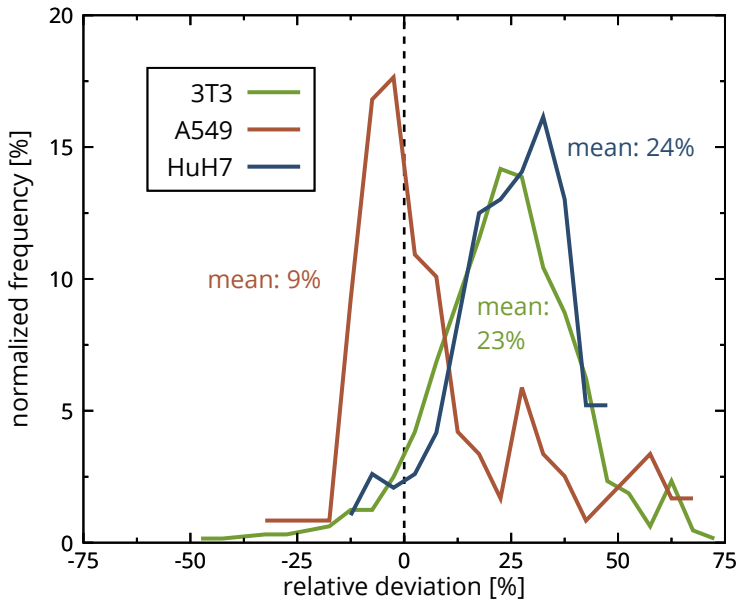

Figure 10: Analysis of the deviations between the MSD_{1h} determined with MLT and the MSD_{1h} determined from the corresponding fluorescence microscopy images. The relative deviations $((MSD_{1h}{}^{FLUO} - MSD_{1h}{}^{MLT})/MSD_{1h}{}^{FLUO})$ for all time-points from several different measurements were binned into 5 % intervals. The graph shows a plot of the resulting normalized frequency distributions of the relative deviations for measurements with the cell lines NIH-3T3, A549, and HuH7. The frequency distributions show that for the NIH-3T3 and HuH7 cells, the MSD_{1h} from the fluorescence microscopy data is about 25 % higher than the MSD_{1h} determined with MLT. However, for the slower A549 cells, the MLT gives values for the MSD_{1h} which are about 10 % higher than the ones obtained from the fluorescence microscopy data.

5 Cell Line Monitoring and Phenotypic Characterization

5.1 Calculation of Image-Based Metrics for Motility & Migration

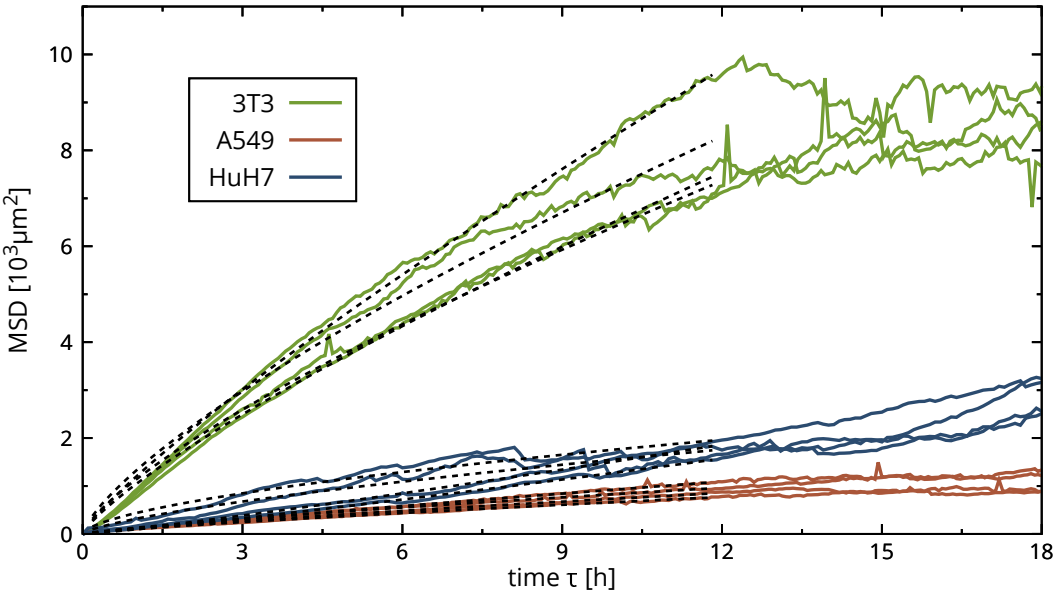

Figure 11: Determination of the diffusion coefficient D_α and the exponent α as image-based metrics for the cell motility for the purpose of phenotypic cell profiling. The plot shows the MSD for four representative measurements of each of the cell lines NIH-3T3, HuH7, and A549 against time. The anomalous diffusion equation $MSD(\tau) = D_\alpha \tau^\alpha$ was fitted over the interval from zero to τ=12 h. The resulting best-fit curves are included in the graph with dashed black lines over the corresponding fit interval.

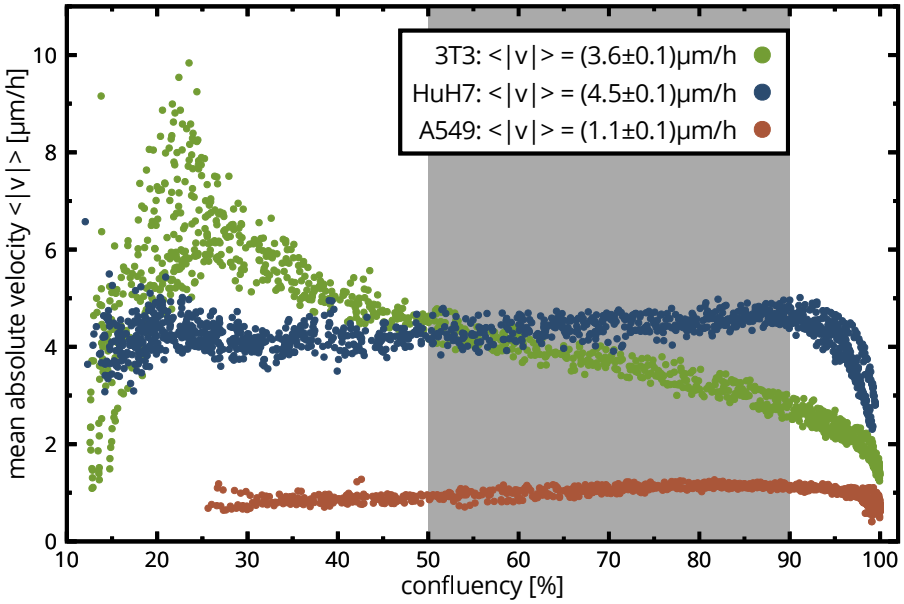

Figure 12: Quantification of collective cell migration. The graph shows the mean absolute velocity of the cells calculated from the velocity field determined with PIV plotted against the confluency. The data corresponds to four measurements for each cell line. The data points in the highlighted confluency range from 50–90 % were averaged to give a measure to compare the cell lines with regard to the collective cell migration. It is also noteworthy that the collective cell migration of the NIH-3T3 cells decreases over the whole confluency range, whereas the collective cell migration remains mostly constant for the two endothelial cell lines. The collective cell migration declines rapidly upon reaching 100 % confluency for all cell lines. The larger scattering of the mean velocities of the NIH-3T3 cells below 25 % confluency can be attributed to the tendency of the NIH-3T3 cells not to form clusters. Hence, the area that could be included in the PIV analysis was smaller when compared to the two endothelial cell lines, resulting in larger statistical variations.

5.2 Calculation of Image-Based Metrics for Cell Clustering

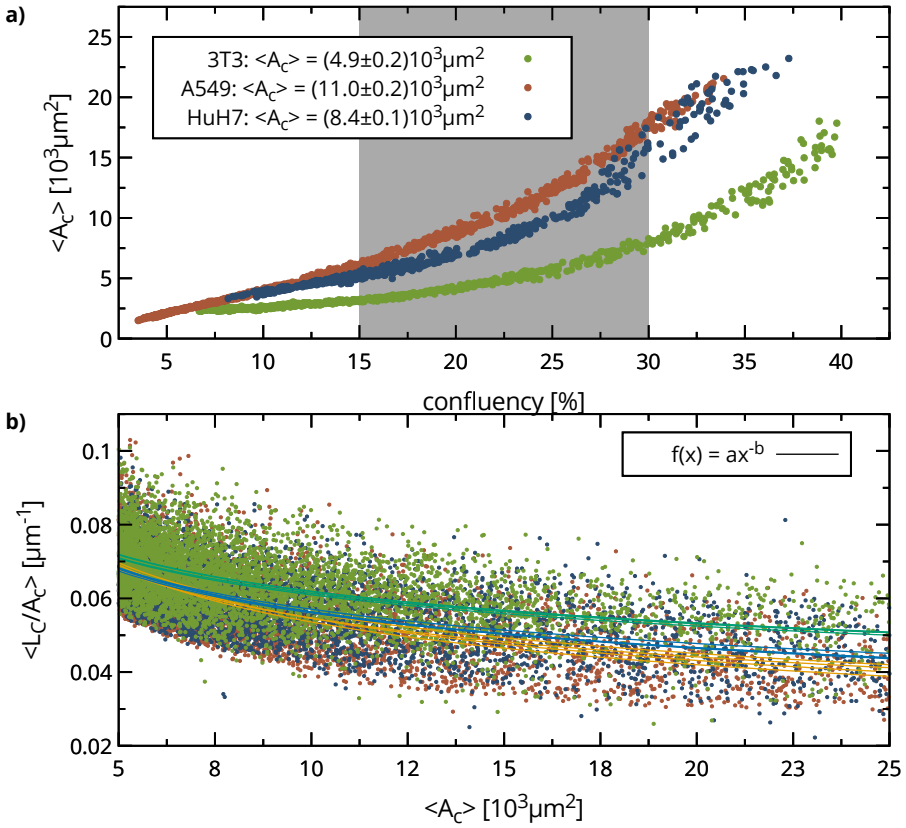

Figure 13: Quantification of cell clustering. **a)** shows a plot of the mean cell cluster size against the confluency for three different cells lines (NIH-3T3, A549, HuH7). Four measurements are shown for each cell line. The mean cell cluster size increases with increasing confluencies. For all cell lines, the cells were seeded with the same seeding densities. Clear differences between the cell lines are observable for the development of the mean cluster size A_c. The gray area highlights the interval that was used to calculate the average of the mean cluster size $<A_c>$, which was subsequently used for the phenotypic cell line profiling. **b)** Parametrization of cluster morphology. The plot shows the ratio between the length of the cluster outline L_C and the cluster area A_C in dependence of A_C. This ratio provides a measure for the compactness of the cells clusters. Clusters with protrusions have a higher value than more circular clusters. The plot includes every 50th data point of the measurements. The function $f(x) = ax^{-b}$ was used as a phenomenological fit to the data. The fit parameters a and b were used as image based metrics to create the phenotypic profiles for the different cell lines. Note that for a circle $L/A = 2\pi r/\pi r^2 = 2/r \rightarrow \frac{L}{A}(A) = \sqrt{4\pi/A}$ and that for a square with side length a $L/A = 4a/a^2 = 4/a \rightarrow \frac{L}{A}(A) = 4/\sqrt{A}$.

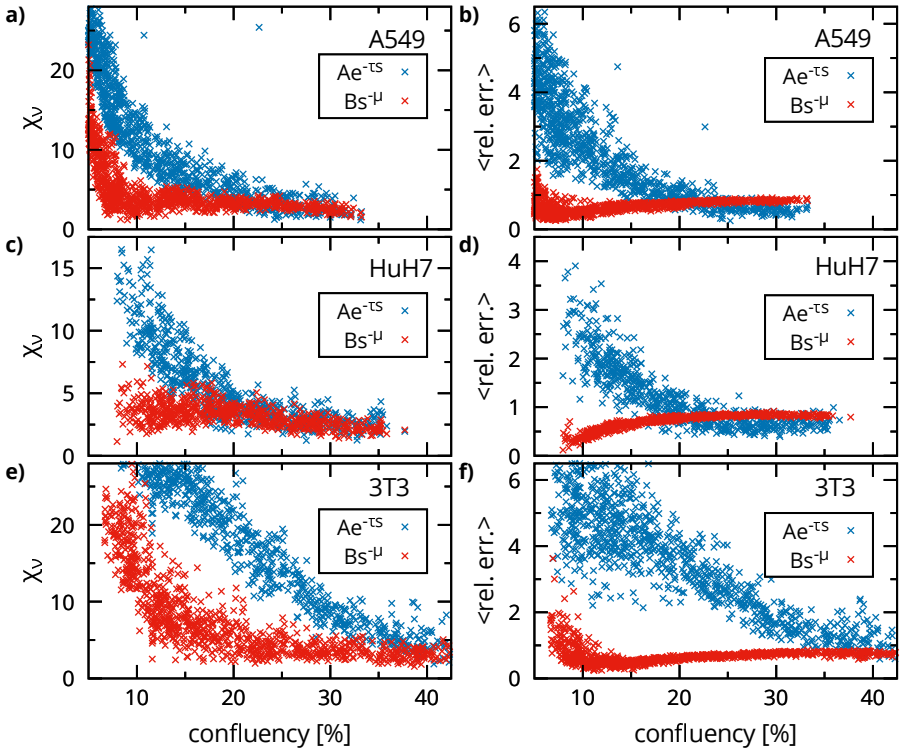

Figure 14: Dynamics of cell clustering: The cell cluster size distribution was determined in each frame and fitted with a power law decay and an exponential function. The plots show the reduced chi-square (left column) and the relative error (right column) as measures for the fit quality against the confluency. The data shows four measurements of samples with A459 cells (**a**), **b**), HuH7 cells (**c**), **d**)) and NIH-3T3 cells (**e**) **f**)). The data shows that for the A549 and HuH7 cells, there seems to be a transition from an exponential size distribution to a power law decay: Approximately the same chi-squared is obtained for both fits, but for higher confluencies, using the power law fit results in a lower relative fit error. Such a transition can not be observed for the fit errors of the NIH-3T3 cells.

5.3 Correlations Between Image-Based Metrics

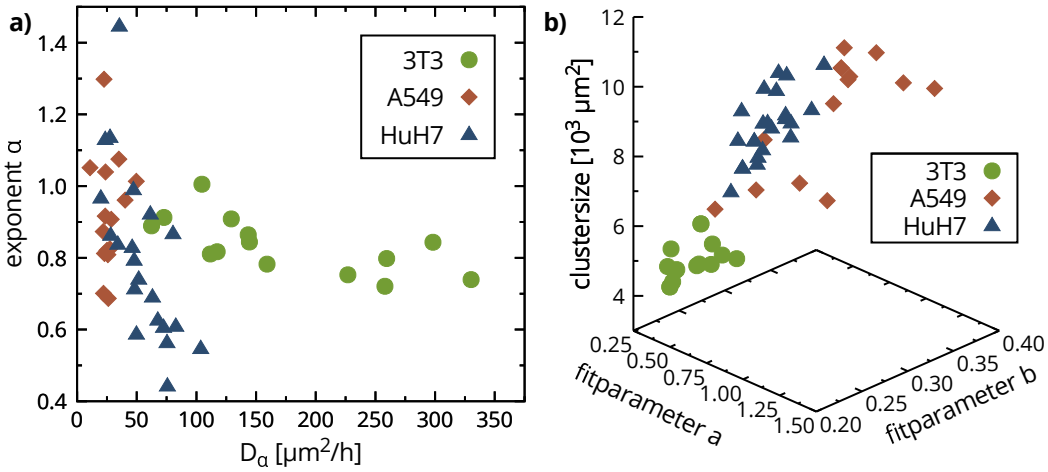

Figure 15: Correlations between different image-based metrics. **a)** The graph shows a plot of the exponent α against the diffusion coefficient D_α. These two metrics were extracted from measurements with the three different cell lines A549, HuH7, and NIH-3T3. The data was obtained by fitting the anomalous diffusion equation $MSD(\tau) = D_\alpha \tau^\alpha$ to the MSD data, as shown in ***Figure 11***. The graph shows that the metrics α and D_α are correlated. **b)** The graph shows a three dimensional plot of the three cell-clustering metrics mean cluster size A_C, fit parameter a, and fit parameter b. The metrics are plotted against each other for the three-different cell lines A549, HuH7, and NIH-3T3. The metrics were determined according to ***Figure 13***. Like in a), it can be seen that the metrics are correlated with each other.

5.4 Composition of Feature Vectors for Phenotypic Profiles

To create the phenotypic profiles for the three cell lines A549, HuH7, and NIH-3T3, the image-based metrics PDT (T_2), mean velocity of the collective cell migration ($< |\vec{v}| >$), diffusion coefficient D_α, the exponent α, the mean cluster size $< A_C >$, and the two fit parameters a and b, were pooled from different measurements. In the performed cell tracking experiments, the cells were typically seeded at a very low density. Consequently, such experiments often ended before the cells formed closed cell patches (due to depletion of the medium). Thus, the collective cell migration could not be assessed. Vice versa, cells were seeded at higher densities for experiments to measure growth and collective cell migration. In these experiments, the assessment of cell clustering was typically not possible, as there were only a few larger clusters. However, in some measurements, all presented metrics could be determined all at once. The following tables summarize the results different measurements (all performed with the 8-chamber slide setup) and the corresponding determined metrics. N/A means that the determination of the corresponding metric was not feasible in that particular measurement. In some cases, fewer than eight chambers could be used for analysis due to malfunctions of the image sensors. The metrics in the table-cells with a green background were used to construct the feature vectors that were used for the LDA.

type	pos	FBS [%]	T_2 [h]	$< \|\vec{v}\| >$ [µm h^{-1}]	D_α [µm^2 h^{-1}]	alpha	$<A_C>$ [µm^2]	a (fit)	b (fit)
G	1	10	18.1	3.21	N/A	N/A	4931	0.446	-0.216
G	2	10	24.5	3.47	N/A	N/A	5517	0.425	-0.213
G	3	10	18.4	3.41	N/A	N/A	5052	0.423	-0.210
G	4	10	18.5	3.61	N/A	N/A	4900	0.444	-0.214
G	5	10	19.8	3.54	N/A	N/A	4619	0.441	-0.212
G	6	10	16.8	3.67	N/A	N/A	4466	0.431	-0.211
G	7	10	16.8	3.64	N/A	N/A	4466	0.431	-0.211
T	1	10	21.1	3.90	129.2	0.91	5072	0.517	-0.229
T	2	10	19.6	4.27	143.4	0.86	5018	0.508	-0.228
T	3	10	19.7	4.32	104.7	1.01	5160	0.628	-0.252
T	4	10	19.6	3.96	159.2	0.78	5053	0.556	-0.236
T	5	10	20.8	4.19	117.4	0.82	5286	0.585	-0.243
T	6	10	21.7	4.20	111.7	0.81	6173	0.510	-0.232
T	7	10	21.5	3.71	72.8	0.91	6173	0.510	-0.232
T	7	10	21.9	3.51	62.4	0.89	5603	0.551	-0.238
T	1	10	24.9	N/A	259.4	0.80	N/A	N/A	N/A
T	2	10	35.4	N/A	298.2	0.84	N/A	N/A	N/A
T	3	10	28.8	N/A	330.2	0.74	N/A	N/A	N/A
T	4	10	30.7	N/A	258.0	0.72	N/A	N/A	N/A
T	5	10	34.6	N/A	226.9	0.75	N/A	N/A	N/A
T	7	10	28.1	N/A	144.4	0.84	N/A	N/A	N/A

Table 2: NIH-3T3 cells: G = growth measurement, T = tracking measurement

type	pos	FBS [%]	T_2 [h]	$< \|\vec{v}\| >$ [µm h^{-1}]	D_α [µm^2 h^{-1}]	alpha	$<A_C>$ [µm^2]	a (fit)	b (fit)
T	1	10	19.7	1.38	28.6	0.91	10286	1.007	-0.314
T	2	10	19.8	1.31	27.5	0.83	10258	1.363	-0.351
T	3	10	20.1	1.28	25.1	0.82	10357	1.008	-0.315
T	4	10	20.1	1.24	26.1	0.69	11152	0.981	-0.314
T	5	10	19.2	1.32	25.8	0.81	10327	1.231	-0.338
T	6	10	20.4	1.33	22.0	0.87	10542	0.962	-0.313
T	7	10	19.5	1.32	22.1	0.70	10542	0.962	-0.313
T	8	10	19.9	1.29	10.8	1.05	11069	1.106	-0.329
M	1	10	N/A	N/A	35.0	1.08	N/A	N/A	N/A
M	2	10	N/A	N/A	40.3	0.96	N/A	N/A	N/A
M	3	10	N/A	N/A	49.6	1.01	N/A	N/A	N/A
M	5	10	N/A	N/A	22.6	1.30	N/A	N/A	N/A
M	6	10	N/A	N/A	23.8	1.04	N/A	N/A	N/A
M	7	10	N/A	N/A	23.6	0.92	N/A	N/A	N/A
M	8	10	N/A	N/A	22.9	0.81	N/A	N/A	N/A
G	1	10	32.9	N/A	N/A	N/A	7153	0.797	-0.294
G	2	10	41.7	N/A	N/A	N/A	6969	0.652	-0.270
G	3	10	38.4	N/A	N/A	N/A	6463	0.523	-0.246
G	4	10	36.2	N/A	N/A	N/A	6686	0.901	-0.308
G	5	10	18.7	N/A	N/A	N/A	9493	0.929	-0.310
G	6	10	18.7	N/A	N/A	N/A	8420	0.680	-0.274
G	7	10	20.4	N/A	N/A	N/A	8420	0.680	-0.274
M	1	10	20.0	1.06	N/A	N/A	N/A	N/A	N/A
M	2	10	20.2	1.10	N/A	N/A	N/A	N/A	N/A
M	4	10	18.8	1.27	N/A	N/A	N/A	N/A	N/A
M	5	10	19.7	1.14	N/A	N/A	N/A	N/A	N/A
M	6	10	19.7	1.07	N/A	N/A	N/A	N/A	N/A
M	7	10	20.1	0.99	N/A	N/A	N/A	N/A	N/A

Table 3: A549 cells: G = growth measurement, T = tracking measurement

type	pos	FBS [%]	T_2 [h]	$< \|\vec{v}\| >$ [µm h^{-1}]	D_α [µm^2 h^{-1}]	alpha	$<A_C>$ [µm^2]	a (fit)	b (fit)
G	1	2.5	22.0	3.20	N/A	N/A	9154	0.756	-0.285
G	2	2.5	21.3	3.16	N/A	N/A	9900	0.679	-0.274
G	3	2.5	21.0	3.18	N/A	N/A	9282	0.610	-0.261
G	4	2.5	22.8	4.28	N/A	N/A	8938	0.685	-0.272
G	5	10	23.4	3.91	N/A	N/A	8556	0.784	-0.286
G	6	10	27.1	4.07	N/A	N/A	9061	0.760	-0.285
G	7	10	23.1	3.93	N/A	N/A	9061	0.760	-0.285
G	8	10	26.1	3.53	N/A	N/A	10350	0.728	-0.282
G	1	2.5	22.8	3.55	N/A	N/A	10319	0.766	-0.285
G	2	2.5	22.8	3.89	N/A	N/A	8949	0.783	-0.287
G	3	2.5	22.4	3.65	N/A	N/A	9340	0.855	-0.298
G	4	2.5	23.8	3.22	N/A	N/A	10651	0.902	-0.304
G	5	10	21.6	4.47	N/A	N/A	8476	0.608	-0.257
G	6	10	22.0	4.61	N/A	N/A	8427	0.656	-0.267
G	7	10	22.6	4.36	N/A	N/A	8427	0.656	-0.267
G	8	10	22.3	4.42	N/A	N/A	8182	0.686	-0.271
G	1	2.5	24.2	3.23	N/A	N/A	8813	0.718	-0.276
G	2	2.5	23.4	3.37	N/A	N/A	7990	0.676	-0.268
G	3	2.5	22.5	3.35	N/A	N/A	7778	0.670	-0.268
G	4	2.5	22.5	3.07	N/A	N/A	8943	0.699	-0.275
G	5	10	23.5	4.32	N/A	N/A	9877	0.732	-0.279
G	6	10	20.5	4.38	N/A	N/A	7675	0.622	-0.260
G	7	10	23.6	4.37	N/A	N/A	7675	0.622	-0.260
G	8	10	23.9	4.33	N/A	N/A	7007	0.587	-0.253
T	1	2.5	N/A	N/A	51.6	0.74	N/A	N/A	N/A
T	2	2.5	N/A	N/A	23.6	1.13	N/A	N/A	N/A
T	3	2.5	N/A	N/A	27.6	1.14	N/A	N/A	N/A
T	4	2.5	N/A	N/A	46.1	0.83	N/A	N/A	N/A
T	5	10	N/A	N/A	63.2	0.69	N/A	N/A	N/A
T	6	10	N/A	N/A	75.7	0.44	N/A	N/A	N/A
T	7	10	N/A	N/A	19.8	0.97	N/A	N/A	N/A
T	1	2.5	N/A	N/A	103.6	0.55	N/A	N/A	N/A
T	2	2.5	N/A	N/A	61.4	0.92	N/A	N/A	N/A
T	3	2.5	N/A	N/A	80.3	0.87	N/A	N/A	N/A
T	4	2.5	N/A	N/A	35.5	1.45	N/A	N/A	N/A
T	5	10	N/A	N/A	75.3	0.56	N/A	N/A	N/A
T	6	10	N/A	N/A	48.1	0.71	N/A	N/A	N/A
T	7	10	N/A	N/A	49.8	0.59	N/A	N/A	N/A
T	1	2.5	N/A	N/A	47.1	0.99	N/A	N/A	N/A
T	2	2.5	N/A	N/A	47.8	0.79	N/A	N/A	N/A
T	3	2.5	N/A	N/A	82.7	0.61	N/A	N/A	N/A
T	4	2.5	N/A	N/A	67.6	0.63	N/A	N/A	N/A
T	5	10	N/A	N/A	34.1	0.84	N/A	N/A	N/A
T	6	10	N/A	N/A	72.5	0.61	N/A	N/A	N/A
T	7	10	N/A	N/A	28.2	0.86	N/A	N/A	N/A

Table 4: HuH7 cells: G = growth measurement, T = tracking measurement

The dimensionality reduction of the feature vector

$$\vec{F} = (T_2; < |\vec{v}| >; D_\alpha; \alpha; < A_C >; a; b) \tag{28}$$

to the two dimensional space (with vector $\vec{v}_{LDA}$) by the LDA is given by $\vec{v}_{LDA} = \hat{A}\vec{F}$ where

$$\hat{A} = \begin{bmatrix} -1.99563493e-01 & 6.53753389e-02 \\ -2.41419968e+00 & 1.19281699e+00 \\ -8.61607466e-03 & 4.06210280e-03 \\ -2.83437173e+00 & -3.45869885e-01 \\ -1.27799717e-04 & 6.04820991e-04 \\ -1.09963112e+01 & -2.61811513e+01 \\ -1.05333049e+02 & -1.78541775e+02 \end{bmatrix} \tag{29}$$

5.5 Calculation of Motility for Cell Line Monitoring

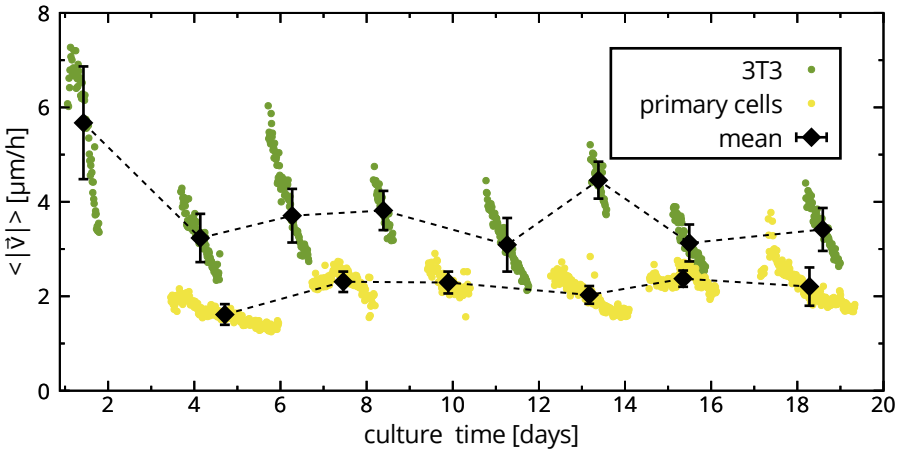

Figure 16: Tracking of cell migration of cell cultures over several passages. PIV-analysis was used to determine the average of the absolute velocities of the flow field for each frame. The standard fibroblast cell line NIH-3T3 and a human primary melanoma cell line were used as example cell lines. The graph shows a plot of the average of the mean velocity against the culture time. The shown data corresponds to confluencies above 40 % to ensure a sufficiently large area of cell patches exhibiting correlated motion and thus does not cover the whole culture period. The data points were averaged over each passage-interval to obtain a measure for comparison of cell migration between different passages. The cell migration of the NIH-3T3 cells decreases with increasing confluency, as also shown in ***Figure 12***. Due to this dependency, the migration of the NIH-3T3 cells varies stronger between different passages, as the cells were passaged at different confluencies.

6 Drug Screening Experiments

6.1 Morphological Response of MDCK Cells to Mitomycin C

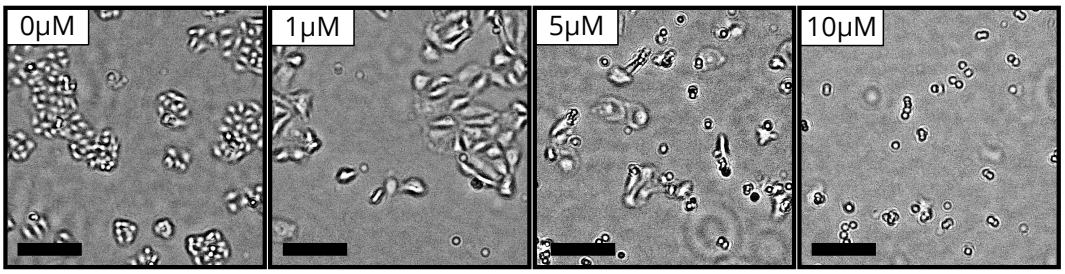

Figure 17: The images illustrate the morphological changes in MDCK cells after treatment with different concentrations of mitomycin C. The control (0 µM) shows the regular morphology. At a concentration of 1 µM, a substantially increased apparent cell size can be observed. The sample treated with 5 µM shows a mix of cells exhibiting an increased size and cells that are rounded up. At a concentration of 10 µM, only round contracted cells can be observed, indicating cell death. Scale bar: 250 µm

6.2 Determination of PST Concentrations

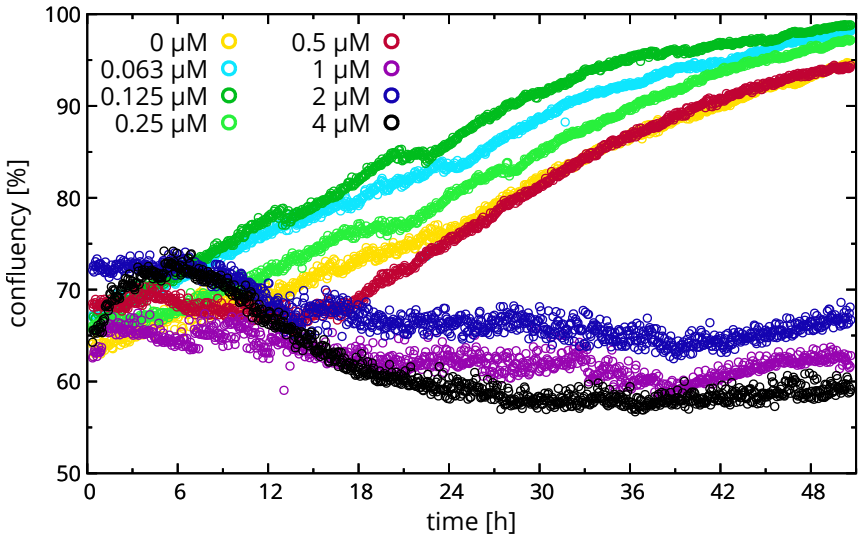

Figure 18: Dose-dependent antiproliferative effect of the PST. A549 cells were exposed to different concentrations of the PST. The PST was sustained in the active state through illumination with 10 s pulses of UV light in 4 min intervals over the duration of the whole measurement. The graph shows the measured growth curves of the proliferation. Treatment with PST in concentrations of 1 µM or more entirely suppressed proliferation, whereas no inhibitory effect with respect to the control was observed for concentrations of 1 µM or less.

6.3 Area Detection in Flasks after Seeding

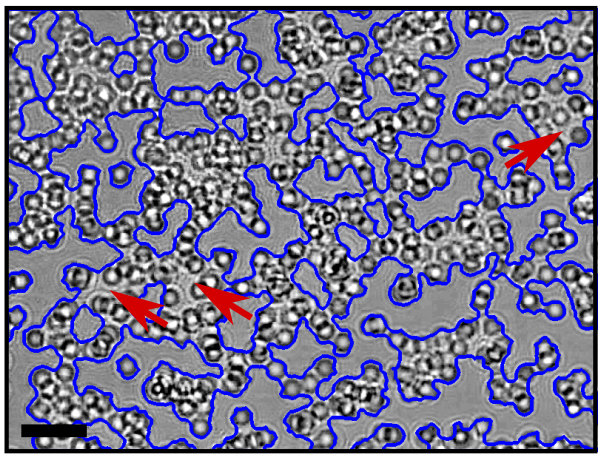

Figure 19: To determine the uniformity of the cell density inside the culture flasks, the confluency was determined spatially resolved over the whole substrate area of the flask. To this end, the flask was imaged with the scanning-setup about 2 h-3 h after seeding. The image shows that the cells were not spread out on the substrate yet at that time. This lead to an overestimation of the detected cell covered substrate area, as the image shows. The outlines of the detected areas are included as blue lines. The red arrows highlight regions that have been erroneously detected as cell covered substrate area. Scale bar: 250 µm